

UNIVERSITY OF BIRMINGHAM

GALACTIC ARCHAEOLOGY WITH HIGH TEMPORAL RESOLUTION

by

EMMA WILLETT

A thesis submitted to the University of Birmingham for the degree of

DOCTOR OF PHILOSOPHY

Solar and Stellar Physics Group

School of Physics and Astronomy

College of Engineering and Physical Sciences

University of Birmingham

September 2023

UNIVERSITY OF BIRMINGHAM

University of Birmingham Research Archive
e-theses repository



This unpublished thesis/dissertation is under a Creative Commons Attribution 4.0 International (CC BY 4.0) licence.

You are free to:

Share — copy and redistribute the material in any medium or format

Adapt — remix, transform, and build upon the material for any purpose, even commercially.

The licensor cannot revoke these freedoms as long as you follow the license terms.

Under the following terms:



Attribution — You must give appropriate credit, provide a link to the license, and indicate if changes were made. You may do so in any reasonable manner, but not in any way that suggests the licensor endorses you or your use.

No additional restrictions — You may not apply legal terms or technological measures that legally restrict others from doing anything the license permits.

Notices:

You do not have to comply with the license for elements of the material in the public domain or where your use is permitted by an applicable exception or limitation.

No warranties are given. The license may not give you all of the permissions necessary for your intended use. For example, other rights such as publicity, privacy, or moral rights may limit how you use the material.

Unless otherwise stated, any material in this thesis/dissertation that is cited to a third-party source is not included in the terms of this licence. Please refer to the original source(s) for licencing conditions of any quotes, images or other material cited to a third party.

© Copyright by EMMA WILLETT, 2023

This work is licensed under a Creative Commons “Attribution 4.0 International” license.



ABSTRACT

The study of the formation and evolution of the Milky Way has entered a golden era. Galactic archaeology, enabled by high-precision astrometry and spectroscopy, has equipped us with rich maps of our Galaxy's kinematic and chemical structures. The next step is to build up a detailed chronology of the events and processes through which these structures formed. Asteroseismology – the study and interpretation of stellar oscillations – provides tight constraints on fundamental stellar parameters for thousands of evolved low-mass stars. From these, we obtain robust age estimates, which can be used as a cosmic clock. This thesis presents three works on the application of asteroseismology to Galactic archaeology.

First, new catalogues of stellar age estimates, combined with kinematic and chemical constraints, are presented. These catalogues sample the full history of the Galactic disc and probe the stellar halo, providing the basis for detailed studies of the Milky Way. This is demonstrated in the second work, in which one of these catalogues is applied to the question of the radial metallicity gradient of the thin disc. The results represent strong observational constraints for models of Galactic evolution and dynamical processes. Finally, a new technique to infer helium abundance from the luminosity of low-mass, core helium-burning field stars is described. This constrains the relative enrichment of helium and heavier elements in the Galaxy, with strong implications for stellar age determination.

These works demonstrate the potential for studies of the Milky Way with asteroseismic constraints. Though there are many open questions, it is clear that asteroseismology has a role to play in their solution and is paving the way to Galactic archaeology with high temporal resolution.

To Dad – thanks for helping me find this path.

To George – thanks for holding my hand, especially on the steep parts.

ACKNOWLEDGEMENTS

I am immensely grateful to my primary supervisor Andrea Miglio for his support and mentorship over the last few years. I am also very grateful to Bill Chaplin who stepped in after Andrea's move to Bologna, and to Amaury Triaud in his role as co-supervisor.

The Solar and Stellar Physics group at the University of Birmingham has been a delight! The PhD students, postdoctoral researchers and staff who have come and gone during my time here have made this a place where I have loved working – even in the hard parts. Thanks go especially to Ted Mackereth, Alex Lyttle, Martin Nielsen, Guy Davies and Warrick Ball for always patiently answering even the most convoluted of questions.

The School of Physics and Astronomy at Birmingham and my extended group of collaborators in Bologna and beyond have accommodated me in unusual circumstances, and I'm grateful for their support. I'd also like to extend my thanks to Daisuke Kawata and Sean McGee for such an interesting and enjoyable viva.

Last, but never least, I thank my family for their love and encouragement. Mum, Dad and Kate – thanks for feeding me when I visit, listening to me complain and showing me you're proud. And to my fiancé George... I couldn't have done it without you – you're a good one.

CONTENTS

Abstract i

Acknowledgements v

Contents vii

List of Figures xi

List of Tables xxi

1 Introduction, Motivation and Outline 1

2 The Milky Way and Galactic Archaeology 5

2.1 Galaxy formation and evolution 6

2.2 The Milky Way as a galaxy 7

2.3 Stars in the Milky Way: kinematics 10

2.3.1 Stars in the disc and the halo 12

2.3.2 Separating components 13

2.3.3 Temporal evolution 14

2.4 Stars in the Milky Way: chemistry 15

2.4.1 Element production in stars 16

2.4.2 Chronology from chemistry 18

2.4.3 Spatial variation 20

2.4.4 *Ex situ* stars 21

2.5 Putting it together: Galactic archaeology . . . 21
2.5.1 From observations to data: astrometry . . . 21
2.5.2 From observations to data: spectroscopy . . . 23
2.5.3 Applications . . . 25
2.5.4 The importance of temporal constraints . . . 26

3 Stars and Stellar Evolution **29**
3.1 The evolution of a Sun-like star . . . 29
3.1.1 The main sequence and sub-giant phase . . . 30
3.1.2 The ascent of the red giant branch . . . 32
3.1.3 Beyond the red giant branch: The helium flash and core helium burning 32
3.1.4 Advanced evolution . . . 33
3.2 Asteroseismology . . . 34
3.2.1 Stellar oscillaions . . . 34
3.2.2 Asteroseismic parameters and scaling relations . . . 36
3.2.3 Applying asteroseismology . . . 38
3.3 The ages of stars . . . 39
3.3.1 Estimating ages . . . 39
3.3.2 Limitations of stellar modes . . . 41

4 Asteroseismic Ages For 17000 Stars in *Kepler*, K2 and TESS **43**
4.1 Introduction and motivation . . . 43
4.2 Observational constraints . . . 45
4.2.1 Asteroseismic constraints . . . 45
4.2.2 Astrometric constraints . . . 47
4.2.3 Spectroscopic constraints . . . 48
4.2.4 Samples . . . 49
4.3 Inferring stellar and orbital parameters . . . 49
4.3.1 Stellar parameters . . . 50

4.3.2 Orbital parameters . . . 60
4.4 Applications . . . 63
4.4.1 Kinematic properties . . . 63
4.4.2 Chemical abundances and chemically selected populations . . . 68
4.4.3 Stellar physics . . . 71
4.4.4 Chemical clocks . . . 74
4.5 Summary and conclusions . . . 77

5 Evolution of the Thin Disc Radial Metallicity Gradient 81
5.1 Introduction . . . 81
5.2 Observational constraints . . . 85
5.2.1 Asteroseismic, Spectroscopic and Astrometric Constraints . . . 85
5.2.2 Inferred Stellar and Orbital Parameters . . . 86
5.2.3 Thin disc selection . . . 87
5.3 The metallicity gradient in bins of age . . . 89
5.4 A hierarchical Bayesian approach . . . 94
5.5 Discussion . . . 96
5.5.1 Results of this work . . . 96
5.5.2 Stars older than 10 Gyr . . . 98
5.5.3 Possible sources of bias . . . 99
5.5.4 Comparison to literature . . . 101
5.6 Conclusions . . . 107

6 Milky Way Helium Enrichment Constrained by Red Clump Stars 109
6.1 Introduction and motivation . . . 109
6.2 Observational constraints . . . 114
6.2.1 Asteroseismic, spectroscopic and astrometric constraints . . . 114
6.2.2 Red clump selection . . . 114
6.2.3 Stellar parameters . . . 115

6.3 Method . . . 116
6.3.1 Model grid . . . 116
6.3.2 Helium abundance inference . . . 120
6.3.3 Analysis . . . 120
6.3.4 Validation with mock data . . . 124
6.4 Results and Discussion . . . 125
6.4.1 Low-α stars . . . 125
6.4.2 High-α stars . . . 127
6.4.3 Comparison to literature . . . 127
6.5 Summary and conclusions . . . 129

7 Summary and Outlook **131**
7.1 Summary . . . 131
7.2 Outlook . . . 132

References **135**

A Appendix to Chapter 4 **153**
A.1 Asteroseismic pipeline comparison for K2 targets . . . 153
A.2 Identifying nyquist-affected $\nu_{\rm max}$ . . . 153
A.3 Comparing $\Delta\nu$ and L results in *Kepler* and TESS . . . 153
A.4 Mass loss in *Kepler* . . . 157

B Appendix to Chapter 5 **159**
B.1 Effect of [Fe/H] error inflation . . . 159
B.2 Sensitivity to the $Z_{\rm max}$ cut . . . 159
B.3 Effect of $R_{\rm g}$ or $R_{\rm Gal}$ . . . 160

LIST OF FIGURES

1.1 Top: William and Caroline Herschel's qualitative map of the Milky Way. The Sun is marked by the large star in the centre. Adapted from Herschel (1785) Bottom: Colour view of the sky based on *Gaia* eDR3 (Gaia Collaboration et al., 2021). 4

2.1 A view of the Milky Way with the components we discuss in this chapter labelled. The position of the Sun is indicated by the white ⊙ symbol. This figure was generated using `mwplot`, and the image in the background is modified from an image by ESA/Gaia/DPAC. 8

2.2 Velocity distribution of stars in the Solar neighbourhood, showing the halo (black points) and disc (blue density map). Figure reproduced from Helmi (2020). 13

2.3 Energy vs. angular momentum for disc (coloured contours) and halo (white points) stars. Globular clusters are shown by white circles and the location of the debris of the *Gaia*-Enceladus merger (Helmi et al., 2018) is indicated by the red box. Figure reproduced from Massari, Koppelman, and Helmi (2019). . . . 14

2.4 α element abundance vs. iron abundance (see Chapter 4 for description of dataset). The blue and orange lines indicate the positions of the plateau, knee and downward slope described in the text. The dashed green lines show an approximate separation between the halo (low-metallicity, left) and thick (high-α, upper right) and thin (low-α, lower right) discs. 19

3.1 Evolutionary track of a solar-mass, solar-metallicity star from the main sequence to the end of core helium-burning. The evolution from the main sequence (A) to the tip of the red giant branch (E) is shown in black, the rapid evolution during helium ignition in grey, and the core helium-burning (CHeB) phase in red. The inset plot shows an enlarged view of the region containing the red giant branch bump (D) and the start of quiescent CHeB. 31

3.2 Power spectrum of the low-luminosity red giant KIC 12008916, computed with 1335 days (left) or 70 days (right) of *Kepler data.* The Gaussian envelope of the power excess due to the oscillations and the frequency of maximum oscillation power (at its peak) are marked in purple, and the large frequency spacing between the radial $l = 1$ modes is shown in red. Modes of angular degree $l = 0, 1, 2$ and 3 are indicated by red squares, green triangles with bars, blue pentagons and yellow hexagons, respectively. Figure reproduced from Davies and Miglio (2016). . . . 36

3.3 Age vs. mass for a simulated population of red giants, coloured by metallicity. The large, labelled points correspond to observational results from red giants in open and globular clusters. Figure reproduced from Miglio et al. (2017). 39

3.4 Percentage change in age at the end of the main sequence for models of low-mass stars due to changes in the model chemistry (grey), microphysics (yellow), macrophysics (green) and rotation (blue). Of particular interest to this discussion are the grey bars corresponding to a change in the initial helium abundance of ± 0.03 ($Y+, Y-$) and an increase in $\Delta Y/\Delta Z$ by 3 with respect to the solar values. Figure reproduced from Lebreton, Goupil, and Montalbán (2014a), where a full definition of the other sources of uncertainty may be found. 42

4.1 Location of stars in our samples in Galactic coordinates. Green, blue and orange points show stars with reliable ages from *Kepler*, K2 and TESS, respectively. Stars with reliable data but ages which do not pass our tests are shown in the background (black points). This figure was generated using `mwplot`, and the image in the background is modified from an image by ESA/Gaia/DPAC. 50

4.2 Location of stars in our sample in left-handed Galactocentric coordinates (top) and Galactocentric cylindrical coordinates (bottom). The colours are the same as Figure 4.1. 51

4.3 Average α element abundance [α/M] for APOGEE samples or [α/Fe] for the GALAH sample vs. [Fe/H]. The grey lines show the division between high-, low- and intermediate α populations used in Section 4.4.2. 52

4.4 Stellar mass vs. radius from PARAM where $\Delta\nu$ (top) or L (bottom) are used as an observational constraint. Stars flagged for unreliable $\Delta\nu$ are shown in red (see Section 4.3.1 for a description of the flag). 54

4.5 Distribution of the fractional uncertainty on age from PARAM where $\Delta\nu$ (filled) or L (open) are used as an observational constraint for *Kepler* (top), K2 (middle) and TESS (bottom). The area under each histogram integrates to one. 55

4.6 Difference between stellar masses obtained from scaling relations when $T_{\rm eff}$ is shifted by 50 K vs. original mass. The cases where $\Delta\nu$ (dark) or L (light) are used as an observational constraint are shown. 58

4.7 Difference between stellar masses obtained from scaling relations using luminosity when the correction to the *Gaia* parallax zero-point offset is changed from a constant 17 μas (L_{17}) to the correction proposed by Lindegren et al. (2021) ($L_{\rm Ldg}$). The difference is shown as a function of the L_{17} mass and coloured according to the distance from the inverse of the *Gaia* parallax, with a constant zero-point correction of 17 μas. 59

4.8 Stellar mass obtained from PARAM vs. that from scaling relations where $\Delta\nu$ (top) or L bottom are used as an observational constraint. Stars with masses that may be dominated by the priors imposed in PARAM are shown in purple (see Section 4.3.1 for a description of the flag). 61

4.9 HRD showing stars flagged for unreliable $\Delta\nu$ (red) and with masses that may be dominated by the priors imposed in PARAM are shown (purple; see Section 4.3.1 for a description of the flags). The full sample is shown in the background (blue). 62

4.10 Toomre diagram for stars with reliable ages in the K2 (top), Kepler and TESS (bottom) samples. The colours are the same as Figure 4.1. 64

4.11 Energy vs. Z-component of angular momentum for stars with reliable ages. The colours are the same as Figure 4.1. 64

4.12 Maximum vertical excursion vs. guiding radius for K2 stars with reliable ages. . 65

4.13 Guiding radius (middle left) and maximum vertical excursion (bottom left) vs. stellar mass for K2 stars with reliable ages. The distributions of M_* (top left), R_g (top right) and Z_{max} (bottom right) are shown using kernel density estimates in bins of stellar age. The area under each distribution integrates to one. 67

4.14 Tangential (middle left) and vertical (bottom left) velocity components vs. radial velocity component for K2 stars with reliable ages. The distributions of V_R (top left), V_T (top right) and V_Z (bottom right) are shown using kernel density estimates in bins of stellar age. The area under each distribution integrates to one. 69

4.15 [α/M] vs. [Fe/H] in bins of guiding radius and maximum vertical excursion (main panel; as shown in Figure 4.12 for K2 stars with reliable ages. Also shown are the stars binned only by R_g (bottom panel) or Z_{max} (right panel). Stars are coloured according to age bin. 70

4.16 Distributions of logarithmic age for stars in the high- and low- and intermediate α regions of the [α/M] vs. [Fe/H] plane (as shown in Figure 4.3) The results are shown for likely-RGB stars from K2 (top) and *Kepler* (bottom) with reliable ages (see Section 4.4.3 for a description of the RGB selection). The area under each histogram integrates to one. 72

4.17 [Mg/Mn] vs. [Al/Fe] (top) and [α/Fe] vs. [Fe/H] (middle) for K2 stars with reliable ages. Likely-RGB stars are shown in colour in the foreground (see Section 4.4.3 for a description of the RGB selection) and the full sample is shown in the background (black points). Stars are divided, according to the grey lines in the top panel, into *in situ* low-α (light blue) *in situ* high-alpha (dark blue) and *ex situ* (purple) populations. Also shown are the distributions of logarithmic age for these three populations (bottom). 73

4.18 Top: HRD showing our selection for RGB (blue) and CHeB (yellow) stars. The full sample is shown in the background (black). Bottom: Mass distributions corresponding to the RGB and CHeB selections. 75

4.19 [C/N] vs. [Fe/H] in bins of guiding radius and maximum vertical excursion (main panel; as shown in Figure 4.12 for K2 stars with reliable ages. Also shown are the stars binned only by R_g (bottom panel) or Z_{max} (right panel). . . 76

4.20 [C/N] vs. [Fe/H] for *Kepler* (green points), TESS (orange points) and K2 (blues contours) stars with reliable ages. 76

4.21 Abundance ratios vs. age for four elements commonly used in chemical clocks, from different nucleosynthetic channels: yttrium (left; light s-process), barium (right; heavy s-process), magnesium (top; α element) and Aluminium (left; odd-Z element). The stars shown have reliable ages from the K2-GALAH cross-match and the likely-RGB sample is shown in blue points in the foreground. The grey line shows the relationship between the yttrium chemical clocks and age found by Casamiquela et al. (2021). 77

5.1 Location of stars in our sample in left-handed Galactocentric cartesian coordinates (top) and Galactocentric cylindrical coordinates (bottom). The green points show the stars in the thin disc, and the full sample is shown in the background (black points). 86

5.2 Distribution of the uncertainty on guiding radius (top) and fractional uncertainty on age (bottom) in the full sample (grey line) and thin disc (filled green). The area under each histogram integrates to one. 88

5.3 Average α element abundance [α/M] vs. [Fe/H]. The high- and low-α sequences were separated along the red line, with the high-α population (grey) removed from the analysis. of the remaining low-α population, stars with $Z_{\rm max} \geq 0.5$ kpc were also removed (black). The final thin disc sample is shown in green. 89

5.4 [Fe/H] vs. $R_{\rm g}$ in six bins of age. The thin disc sample is shown in black points, binned according to the median age of each star. The green line shows the best-fitting radial metallicity gradient from the MCMC analysis, with a filled region representing 1σ of the intrinsic spread. 91

5.5 Corner plot (Foreman-Mackey, 2016) showing the joint and marginalised sampled posterior distributions of the fit parameters φ in the age bin $2\,{\rm Gyr} \leq \tau < 4\,{\rm Gyr}$ for one step in the MC (one realisation of τ). 92

5.6 A probabilistic graphical model of the hierarchical Bayesian model (HBM). The properties of individual stars are shown inside the rectangle, and the hyperparameters are shown outside. Grey nodes represent observables and their respective observational uncertainties are given by the small black nodes. . . . 96

5.7 Evolution of the fit parameters as a function of stellar age. The grey points show the best-fitting value and 68% credible interval in each bin from the MCMC analysis (plotted against the median age of the population in the bin). The green line and filled region show the result and 68% credible interval from the HBM. The dashed blue line and filled region show the HBM result when stars older than 10 Gyr are excluded from the analysis. 97

5.8 Results of the MCMC analysis for the oldest stars in our sample. The green line and filled region in the background show the result when including all stars with $\tau \geq 10\,\mathrm{Gyr}$, the long-dashed blue line and filled region (which are almost identical to the green) show the result of the analysis excluding stars with $\tau \geq 13.6\,\mathrm{Gyr}$, and the short-dashed orange line and filled region show the result based on only those stars. 100

5.9 [Fe/H] vs. R_g in five bins of age. The orange and white points show the high-quality and plausible samples from the OCCAM survey (Myers et al., 2022), respectively. The blue points are the results of the MCM chemo-dynamical simulation (Minchev, Chiappini, and Martig, 2013, 2014), with the underlying chemical evolution model of Chiappini (2009) shown by the blue line and filled region. The green line shows the best-fitting radial metallicity gradient from the MCMC analysis of this work, with a filled region representing 1σ of the intrinsic spread. 106

5.10 Same as Figure 5.9 for two age bins with the thin disc sample shown in black points, binned according to the median age of each star. 107

6.1 Main panel: the evolutionary track of a 1 $M_\odot$, solar metallicity model with $Y = 0.28$, showing the evolution from the MS to the tip of the RGB in black, the helium flash in grey and the CHeB phase in red. Inset panel: a closer view of the CHeB phase, and the same phase for a track of $Y = 0.31$. Grey points are positions of 100 EEPs (see Section 6.3.1) obtained by sampling the track uniformly in fractional age. 112

6.2 Evolutionary tracks of the CHeB phase for models of different M and Y, with $[\mathrm{Fe/H}] = 0.0$. Models with $M = 0.6 M_\odot$ are excluded from our analysis as their luminosity distributions when sampled uniformly in fractional age, are not easily separable between the Y coordinates. The tracks are shown on separate axes for clarity, given the overlap in T_{eff}. 113

6.3 Evolutionary tracks of the CHeB phase for models of different [Fe/H] and Y, with $M = 1.0\mathrm{M}_{\odot}$. 113

6.4 HRD showing stars flagged as RC members with low- (green) or high- (blue) α element abundance, compared to the full sample (black). 115

6.5 Average α element abundance [α/M] vs. [Fe/H]. The high- and low-α sequences were separated along the grey line. The colours are the same as Figure 6.4. . . . 116

6.6 Distributions of selected observables and uncertainties in the low- (filled green) or high- (filled blue) α RC samples and the full sample (black). From top to bottom: [Fe/H], showing also the rescaled metallicity of the high-α population (dark blue; see Section 6.2.3), mass, fractional uncertainty on mass, luminosity, fractional uncertainty on luminosity. The young α-rich stars are visible in the high-α distribution as the long tail above $\sim 1.1\,\mathrm{M}_{\odot}$. 117

6.7 Luminosity distributions from model EEPs (top panel; see Section 6.3.1) and inferred from models including sources of uncertainty (middle panel). The middle panel shows the effect of the observational uncertainty on M and [Fe/H] (filled) and with the addition of unknown $\mathcal{T}$ (fine unfilled). The bold black distribution shows the luminosity realisations of KIC 2449327. The bottom panel shows the distribution of Y arising from the inclusion of the uncertainty on M and [Fe/H] (filled) and with the addition of unknown $\mathcal{T}$ (bold black). Vertical lines correspond to the Y values of the four models. 119

6.8 Median values of Y and Z inferred for observed (top) and mock (bottom) low-α datasets. The calibrated solar value $(Y_{\odot}, Z_{\odot})$ is shown in the top panel by the black $\odot$ symbol, and the input relationship Y (Z) as the black line in the bottom panel. 121

6.9 Distribution of median values of Y in three metallicity bins inferred from 1000 realisations of the observables. 123

6.10 Results obtained from one set of bins for the observed low-α data. Bins plotted at the average Y and Z with 1σ error bars and are coloured by the median M of the binned population. Contours show the position of the median Y and Z for individual stars (top panel of Figure 6.8). The calibrated solar value $(Y_\odot, Z_\odot)$ is shown by the black $\odot$ symbol. The best fitting Y (Z) is shown by the solid green line, and with $\Delta Y/\Delta Z + 0.1$ by the dashed green line (see Section 6.4.1). 126

6.11 Same as Figure 6.10, but for the mock data. The input Y (Z) is shown by the solid black line and the best fitting result by the dashed black line. 127

6.12 Same as Figure 6.10, but for the high-α sample. The five lowest mass bins are marked by diamonds. The best fitting Y (Z) for the whole high-α sample is shown by the blue line, the result from the low-α sample by the green line and an approximate fit to the lowest mass bins by the dashed purple line. 128

A.1 Difference between $\nu_{\rm max}$ (*top*) and $\Delta\nu$ (*bottom*) from independent BHM and COR pipelines, relative to combined uncertainty. Stars with reliable ages are shown in the foreground with blue points. Stars with reliable data but which do not pass our tests on age are shown as black points in the background. 154

A.2 $\nu_{\rm max}$ vs. $\Delta\nu$ for the K2-BHM-APOGEE sample. Stars removed as a result of the cuts described in Section 4.2.1 are shown in red. 154

A.3 Same as Figure 4.4, but for *Kepler* targets. 155

A.4 Same as Figure 4.4, but for TESS targets. 156

A.5 Same as Figure 4.18, but for *Kepler* targets. 157

B.1 The [Fe/H] component of the intrinsic spread constrained by our HBM using the published [Fe/H] uncertainties (green) or inflating them as in Chapter 4 (dashed blue). 160

B.2 Evolution of the fit parameters as a function of stellar age. The grey points and green line and filled region show the best-fitting value and 68% credible interval in each bin from the MCMC analysis (plotted against the median age of the population in the bin) and the result and 68% credible interval from the HBM from the original analysis. The black points and short-dashed orange line and filled region show the same but for a sample including stars with a wider range of $Z_{\rm max}$. The long-dashed blue line and filled region show the HBM result for a narrower $Z_{\rm max}$ range. 161

B.3 [Fe/H] distributions for samples including stars with a wider (short-dashed orange) or narrower (long-dashed blue) range of $Z_{\rm max}$ than the original analysis (green). The area under each histogram integrates to one. 162

B.4 [Fe/H] vs. $R_{\rm Gal}$ in six bins of age. The thin disc sample is shown in black points, binned according to the median age of each star. The dashed blue line and filled region show the results from the MCMC analysis using $R_{\rm Gal}$. For comparison, the green line and filled region show the results using $R_{\rm g}$ (plotted against $R_{\rm g}$). . 162

B.5 Evolution of the fit parameters as a function of stellar age. The grey points and green line and filled region show the best-fitting value and 68% credible interval in each bin from the MCMC analysis (plotted against the median age of the population in the bin) and the result and 68% credible interval from the HBM from the original analysis using $R_{\rm g}$. The black points and dashed blue line and filled region show the same using $R_{\rm Gal}$. 163

B.6 Evolution of the gradient with age for the full sample (green) and excluding stars with $R_{\rm g} < R_{\rm Gal,\,min}$ (dashed blue). 164

LIST OF TABLES

4.1 Summary of reliable targets in datasets with different observational constraints. See text for descriptions of the criteria for reliable data and age, τ. 57

5.1 The median and 68% credible interval for each parameter from the MCMC analysis in bins of age (left) and the HBM, evaluated at the median age, $\tau_{\rm med}$ of each bin population (right); m is the gradient, b is the [Fe/H] offset at $R_{\rm g} = 8$ kpc, and S is the component of the intrinsic spread in the [Fe/H] direction. 93

Chapter 1

INTRODUCTION, MOTIVATION AND OUTLINE

... the Galaxy is nothing else but a mass of innumerable stars planted together in clusters.

Galileo Galilei[1]

In the 400 years since Galileo first trained his telescope on the stars of the Milky Way, astronomers have been bringing them into clearer focus. The first qualitative map of our Galaxy, made by William and Caroline Herschel in the 1780s (Herschel, 1785), and the most recent, based upon *Gaia* data released in 2020 (Gaia Collaboration et al., 2021), show the product of these efforts (Figure 1.1), but there is still much we do not know.

The Milky Way is, of course, *the* Galaxy, and inherently fascinating to us. It is the stage upon which the whole history of our Solar System has played out – albeit one that is too vast to comfortably imagine. The Sun has made its long journey around the Galactic centre roughly 20 times now but in all of human history, we have witnessed less than 0.1% of one of these orbits[2].

Since Edwin Hubble measured the distance to Andromeda in the 1920s (Hubble, 1929), we have known that the Milky Way is also *a* galaxy. We now have observations of a vast number of others – some apparently like our own, and some which appear very different. We have seen some of the earliest galaxies to emerge after the formation of the Universe (Robertson et al., 2023), used them to infer the existence of dark matter (Corbelli and Salucci, 2000), and glimpse

[1] Galilei (1610), Translated. E. S. Carlos, 1880;
https://archive.org/search.php?query=external-identifier%3A%22urn%3Aoclc%3Arecord%3A1157216996%22

[2] Assuming a circular orbit of radius 8 kpc, a circular velocity of 220 km s^{-1} and that the Sun is 4.5 Gyr old

them interacting with each other in complicated dances (Stephan, 1881; Pontoppidan et al., 2022). So why, then, should we continue to study the Milky Way?

Because for all these other galaxies, we see only a snapshot of how they looked when the light we observe left them on its long journey to our telescopes. From these snapshots, we can interpret their bulk properties and compile rough chronologies, but the detail with which we can resolve individual stars and stellar populations in the Milky Way remains unique. A full theory of the formation and evolution of galaxies still eludes us, but the rubble of the Milky Way's history lies all around. Today we are beginning to dig through it and piece together our Galaxy's past so that we can better understand all galaxies' pasts.

To do this, we build up a picture of the Milky Way's *'where'*, *'what'* and *'when'* from the fossil record in the stars. Since the launch of *Gaia* in 2013, we have entered a new era for the *'where'*, mapping the positions and motions of nearly 1% of the Galaxy's population with unprecedented precision (Gaia Collaboration et al., 2016, 2023c). Numerous[3] large-scale spectroscopic surveys are uncovering the *'what'* – the chemical compositions of stars that tells us what the Milky Way was made of when they formed. Age information for enough of these stars to constrain the *'when'* is now becoming a reality, thanks to observations from CoRoT (Baglin et al., 2006), *Kepler* (Borucki et al., 2010; Gilliland et al., 2010; Howell et al., 2014) and TESS (Ricker et al., 2015). Combining and interpreting this information is the aim of Galactic archaeology.

Perhaps the first Galactic archaeologist was Nancy Grace Roman who, in the 1950s, identified a relationship between the chemistry and velocity dispersions of stars (Roman, 1950). In the intervening decades, both theoretical models and observational data have vastly improved and, especially in the last 20 years, significant progress has been made. We are starting to unpick the complicated relationship between the thick disc, halo and the Milky Way's past interactions with other galaxies. However, the biggest open challenge remains the resolution of chronology.

We need a high-precision clock to construct a detailed timeline, with which we can measure the evolution of our Galaxy and apply the findings to other galaxies. Asteroseismology – the

[3]Too many to list here, see e.g. Section 5.1.

study and interpretation of stellar oscillations – is providing the way forward. By enabling both stringent tests of models of stellar evolution and tight constraints on fundamental stellar properties, asteroseismology is paving the way to robust estimates of the ages of thousands of stars.

In this thesis, I present three works connected to this topic. In Chapter 4 I will describe new catalogues of stellar ages from asteroseismology, combined with kinematic and chemical constraints. These ages are thoroughly tested for quality and demonstrated in simple applications in Galactic archaeology and stellar evolution. In Chapter 5 I will show a specific application of one of these catalogues to the question of the radial metallicity gradient of the thin disc, providing strong constraints on the disc's chemical and dynamical evolution. Finally, in Chapter 6 I will introduce a new method to constrain helium enrichment in the Milky Way, which remains a significant source of uncertainty in the stellar models upon which age estimates are based. These three chapters can be read as stand-alone papers – Chapter 5 is published (Willett et al., 2023) and Chapters 4 and 6, where I am also first author, will be submitted in the coming weeks. I will first present an overview of some background theory concerning galaxies and the Milky Way (Chapter 2) and stellar evolution and asteroseismology (Chapter 3). A summary and future prospects for these topics are given in Chapter 7.

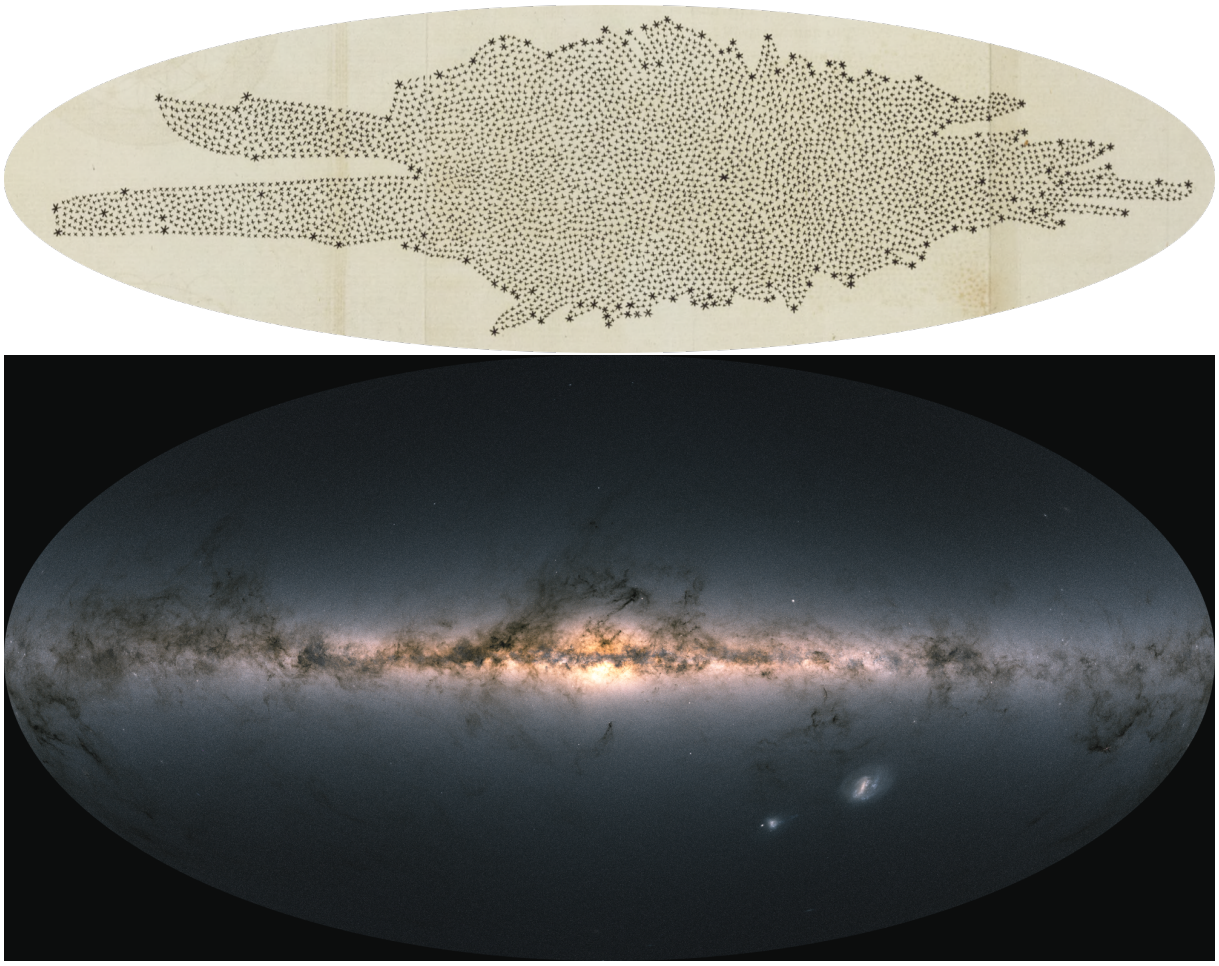


Figure 1.1: Top: William and Caroline Herschel's qualitative map of the Milky Way. The Sun is marked by the large star in the centre. Adapted from Herschel (1785)
Bottom: Colour view of the sky based on *Gaia* eDR3 (Gaia Collaboration et al., 2021). From https://sci.esa.int/web/gaia/-/the-colour-of-the-sky-from-gaia-s-early-data-release-3

Chapter 2

THE MILKY WAY AND GALACTIC ARCHAEOLOGY

This section will introduce some important features of galaxies in general and the Milky Way (MW) in particular. In Section 2.1 we will discuss how galaxies form and will focus on the main properties of the MW in Section 2.2. We then provide more detail on the characteristics of the stars in our Galaxy in terms of their kinematics (Section 2.3) and chemistry (Section 2.4) Finally, Section 2.5 provides some practical insight into Galactic archaeology and gives specific context for the work of Chapter 5. First, we will very briefly review the state of the Universe before galaxy formation, based on Liddle (2015).

The study of galaxies is intrinsically linked to the study of the nature of the Universe because they arise in the aftermath of the Universe's beginning. The currently accepted cosmological model is ΛCDM (White and Rees, 1978) which predicts that all the structure we observe today – including galaxies – can ultimately be traced back to tiny density fluctuations in the very early Universe. These small perturbations became imprinted on the fabric of the Universe during the rapid period of inflation which followed the Big Bang and, eventually, they collapsed under their own gravity, creating potential wells into which dark matter fell. After the decoupling of baryonic matter and radiation, it too collapsed into these wells, creating the sites for the formation of the first galaxies.

Before decoupling, the baryonic matter underwent changes which created the ingredients

from which early galaxies formed. Initially a 'soup' of free particles, a couple of minutes after the Big Bang the Universe had cooled enough that the mean photon energy fell below the binding energy of light nuclei, allowing protons and neutrons to fuse for the first time. This formation of the first nuclei set the balance of elements in the primordial gas and theoretical predictions of $\sim 24\%$ helium (by mass) with a very small amount of lithium are born out by observations today (Workman et al., 2022). After a further few hundred thousand years, the Universe was cool enough to allow electrons to bind to these nuclei (known as the epoch of recombination) and it is these atoms from which the first galaxies were built.

2.1 Galaxy formation and evolution

The details of the emergence of Galactic discs remain very unclear and are an area of active research using cosmological hydrodynamical simulations. From the observational constraints available from the Milky Way and other galaxies, it seems likely that, as proposed by Searle and Zinn (1978), the primordial gas fragmented as it collapsed, forming irregularly shaped clouds which fragmented further or merged together deep in the potential wells formed by the collapse of the dark matter. These clumps of gas tugged at each other, imparting rotation through mutual torques, and interacted. The gas was not collisionless, so the clumps lost energy in such interactions, but their angular momentum was roughly conserved and the gas fell into flatter, more disc-like structures (Sparke and Gallagher, 2007). The gas in these early discs was compressed and, eventually, stars began to form.

Though early galaxies were disc-dominated, observations reveal a variety of morphologies in the Universe today. These can be roughly grouped into three categories (Hubble, 1982), though these are by no means distinct.

- Evolved disc-dominated galaxies are generally called spiral galaxies, because they are usually threaded by a structure of arms and arcs, wrapping outwards from the centre of the disc. Star formation occurs in the disc and at the centre of the galaxy is a spherical component – the bulge – which may be traversed by an elongated overdensity – the bar –

which rotates as a solid body. The whole system lies within a spherical stellar halo (and a dark matter halo, though we will not discuss that here) which contains a small fraction of the total stellar mass of the galaxy.

- Elliptical galaxies have a much simpler structure, with no disc component. They are roughly spherical or ellipsoidal in shape, and their brightness decreases smoothly from the centre to the edge. They contain relatively little gas compared to spiral galaxies and have little or no ongoing star formation.

- Irregular galaxies are, as the name suggests, characterised by a lack of common characteristics. They are generally non-symmetric and show only weak structure, if any.

We get hints of how this diversity arose from the early galaxies by considering the environments in which spirals and ellipticals are found today. The relative abundance of ellipticals increases as we look closer to the centre of galaxy clusters, which qualitatively supports the idea proposed by Toomre (1977) that ellipticals are formed in the interaction and merger of other galaxies. The details of such interactions are studied extensively today, and we generally differentiate between 'major' and 'minor' events based on the mass ratio of the participants. If the mass of one galaxy dominates the other, then its properties and structure are likely to remain relatively unchanged and the merger is a minor one. In the more violent major mergers, galactic structures can be disrupted or destroyed altogether.

2.2 The Milky Way as a galaxy

Figure 2.1 shows the main features of the MW which are not, in general, dissimilar to other similar (in terms of mass, size, chemistry etc.) galaxies observed today. There are many of these similar galaxies – roughly half of the stars in the Universe live in galaxies 'like' ours. The Sun is stuated ~ 25 pc from the plane of the disc, ~ 8 kpc from the Galactic centre. From this position, we have a unique opportunity to view some of the 10^{11} stars in our Galaxy up close, but our view is also restricted by being unable to 'zoom out' and consider the big picture. In

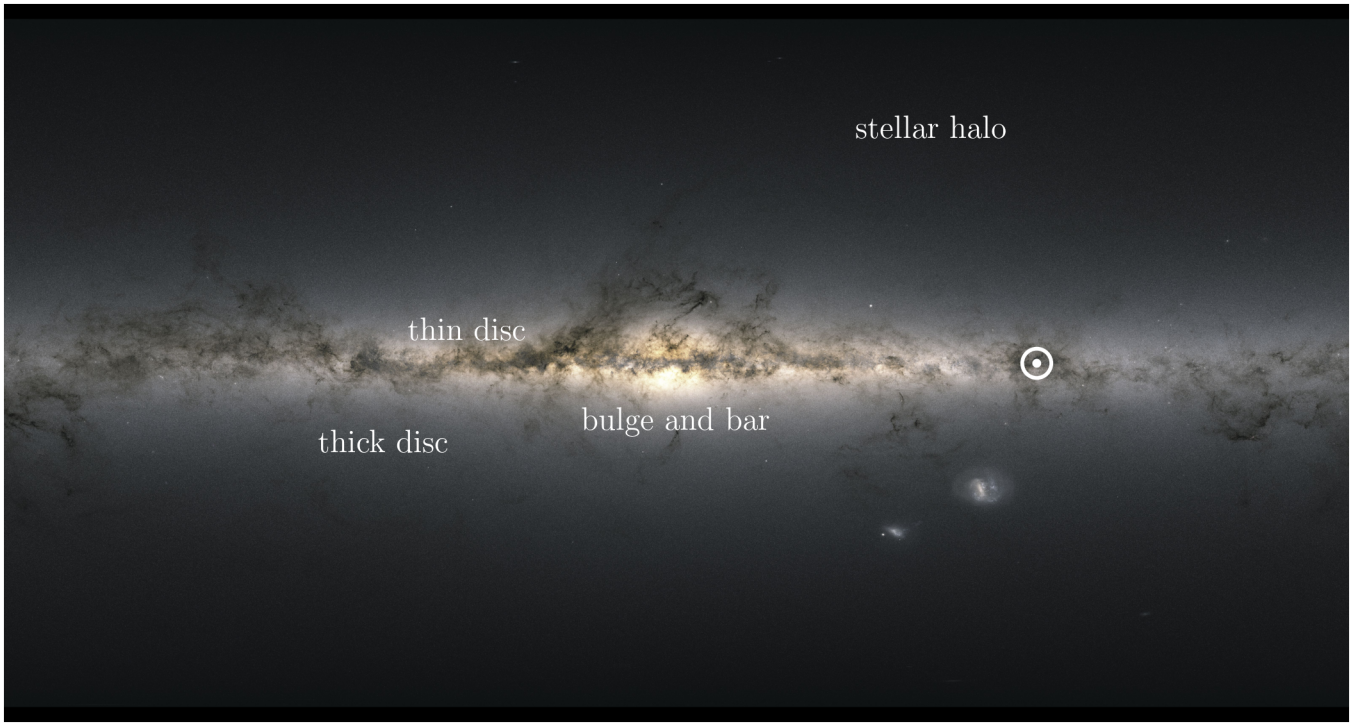


Figure 2.1: A view of the Milky Way with the components we discuss in this chapter labelled. The position of the Sun is indicated by the white ⊙ symbol and the frame covers 30×16 kpc. This figure was generated using `mwplot`[a], and the image in the background is modified from an image by ESA/Gaia/DPAC.
[a] https://milkyway-plot.readthedocs.io/en/latest/index.html

addition, many lines of sight are obscured by interstellar dust, making finding out what the MW really looks like a challenge.

Considering first the disc, we might expect to have a good understanding of our closest component, but many important details are still unclear. For example, the physical nature of the spiral arms of disc galaxies in general is not well understood. Two main schools of thought are divided between long-lived, stationary density waves (Lin and Shu, 1964; Bertin and Lin, 1996) and transient structures, likely induced by tidal forces from satellite galaxies (Sellwood and Carlberg, 1984; Dobbs et al., 2010). The MW provides only weak constraints, as even the number of arms in our own disc is not confirmed. The prevailing view is that there are four main arms (e.g. Reid et al., 2014; Camargo, Bonatto, and Bica, 2015), but the picture is complicated by a sensitivity to the age of the tracer chosen. While four arms may be visible in young populations, some older tracers tend towards just two (e.g. Drimmel, 2000; Gaia Collaboration et al., 2023b). This sensitivity arises from the fact that there is a connection

between the location or passage of the spiral arms and star formation, though the mechanism is also not well understood.

Our view out of the galactic plane is less obscured, so it has been known for a long time that the MW's disc is really better described as two discs. Star counts revealed that a single exponential drop-off is not sufficient to fit the observed stellar population (Gilmore and Reid, 1983) and recent results suggest scale heights of ~ 300 pc and ~ 1 kpc for the two superimposed components (Jurić et al., 2008), which are fairly typical values for MW-like galaxies. The question of the origin of and distinction between these 'thin' and 'thick' components is open, and we will revisit it several times in this chapter. Finally, the MW's disc does not seem to be completely flat but rather flared and warped in the outer regions (e.g. Chrobáková, Nagy, and López-Corredoira, 2022), which may be a result of an ongoing interaction with a satellite galaxy (Poggio et al., 2020).

The centre of the MW is dominated by the bulge and bar which, like the disc, pose many challenges to our understanding of their structure and origin. For example, it is not yet clear whether the MW's bulge is 'classical' – formed very early as a result of mergers – or a 'pseudobulge' – formed by secular processes in the disc (see Kormendy and Kennicutt, 2004, for more detailed descriptions). Heavy dust obscuration also makes a view of the bar difficult, so its length and pattern speed are diagnosed by looking for evidence of resonances in the stars in the disc instead (see Section 2.3.3). This indirect approach is not, so far, conclusive (e.g. Wegg, Gerhard, and Portail, 2015; Monari et al., 2017).

The stellar halo, though sparsely populated, is the most extended visible structure of the MW, reaching ~ 40 kpc from the Galactic centre (GC). It contains $\sim 1\%$ of the total stellar mass of the MW, much of it grouped together in globular clusters, but provides a rich history of the assembly of our Galaxy – if we know how to read it. The halo is the MW component where galaxies disrupted in mergers with the MW are most likely to have deposited their stars (Helmi, 2020). The most dramatic example is the Sagittarius dwarf galaxy, which has orbited the GC at least once (Johnston et al., 1999), and possibly many (Ibata et al., 1997) times, forming an elongated stream which extends hundreds of degrees (e.g. Yanny et al., 2009). In addition to

such *ex situ* stars (formed outside the MW), we shall see in the next section that the halo also contains stars formed *in situ* which were disrupted from the early stellar disc by these mergers. Taken together these provide the observational constraints for identifying the building blocks of the MW today.

2.3 Stars in the Milky Way: kinematics

When mapping the MW, it may be natural to measure everything relative to our position, but when we study the Galaxy as a whole it is more convenient to use a Galactocentric coordinate system through which we move as the Sun orbits the GC. All the other stars we observe are also moving, so the position we observe them in today does not necessarily correspond to where they were born or where they spend most of their time. For this reason, though the component parts of the MW have different spatial distributions, measurements of positions alone are not always sufficient to identify the structure to which a given star belongs.

To untangle this, we require a set of parameters which describe the 'type', rather than the instantaneous state of an orbit. These parameters should also vary slowly compared to the orbital timescale. Below we will briefly introduce and motivate the use of 'action-angle coordinates', which provide a solution to our problem. A more complete derivation may be found in Binney and Tremaine (2008), upon which this summary is based. We consider stars as particles that move in the Galactic potential, Φ, which we will initially assume is both static and axisymmetric. The motions of our star particles are described by the Hamiltonian, $\mathcal{H}$, a function of positions, $\mathbf{q}$, and momenta, $\mathbf{p}$, which describes the total energy of the particle:

$$\mathcal{H}\left(\mathbf{q}, \mathbf{p}\right) = K + V, \tag{2.1}$$

where K and V are the kinetic and potential energies, respectively. The temporal evolution of $\mathbf{q}$ and $\mathbf{p}$ is then given by the Hamiltonian equations:

$$\dot{\mathbf{q}} = \frac{\partial \mathcal{H}}{\partial \mathbf{p}}; \quad \dot{\mathbf{p}} = -\frac{\partial \mathcal{H}}{\partial \mathbf{q}}. \tag{2.2}$$

For our assumption of an axisymmetric potential, cylindrical coordinates are a convenient choice and the general positions and momenta become (for unit mass) positions, $\mathbf{x} = R, \phi, Z$ and velocities $\mathbf{v} = v_R, v_\phi, v_Z$. The Hamiltonian and Hamiltonian equations are now

$$\mathcal{H} = \frac{\mathbf{v}^2}{2} + \phi\,(\mathbf{x})\,; \quad \dot{\mathbf{x}} = \mathbf{v}; \text{ and } \dot{\mathbf{v}} = -\frac{\partial \Phi}{\partial \mathbf{x}}, \tag{2.3}$$

where the latter is the gravitational force on a particle of unit mass.

However, as described above, $\mathbf{x}$ and $\mathbf{v}$ don't give us the best overall view of the Galaxy. We define instead new coordinates $(\boldsymbol{\theta}, \mathbf{J})$, where we require that the actions, J_i are constant over time and that the angles, θ_i vary linearly with time. We may now write:

$$\dot{\mathbf{J}} = -\frac{\partial \mathcal{H}}{\partial \boldsymbol{\theta}} = 0; \quad \dot{\boldsymbol{\theta}} = \frac{\partial \mathcal{H}}{\partial \mathbf{J}} = \Omega = \text{constant}. \tag{2.4}$$

In general,

$$J_i = \frac{1}{2\pi} \oint_{\text{orbit}} p_i \, dq_i, \tag{2.5}$$

and, specifically for the case of cylindrical coordinates, we have a radial action,

$$J_R = \frac{1}{2\pi} \oint_{\text{orbit}} v_R \, dR, \tag{2.6}$$

an azimuthal action,

$$J_\phi = \frac{1}{2\pi} \oint_{\text{orbit}} v_\phi R \, d\phi = \frac{1}{2\pi} \oint_{\text{orbit}} L_Z \, d\phi = L_Z, \tag{2.7}$$

and a vertical action

$$J_Z = \frac{1}{2\pi} \oint_{\text{orbit}} v_Z \, dZ. \tag{2.8}$$

These three actions may be more intuitively understood in terms of the quantities derived from them, which are used in Chapters 4 and 5:

- J_ϕ describes the average circular motion of the particle. This is characterised by a 'guiding

radius' R_g which is the average distance from the GC, i.e. the radius of a circular orbit of angular momentum L_Z.

- J_R describes the amount of radial motion about the circular orbit, in other words, the deviation of the orbit from a circle. This is described by the eccentricity, $e = \left(R_{\rm apo} - R_{\rm peri}\right) / \left(R_{\rm apo} + R_{\rm peri}\right)$, where $R_{\rm apo}$ and $R_{\rm peri}$ are the apocentre and pericentre radii of the orbit, respectively. For a circular orbit $e = J_R = 0$.

- J_Z is similar to J_R but in the vertical direction, so $J_Z = 0$ for a flat orbit in the plane of the disc. We characterise J_Z with $Z_{\rm max}$, which is a measurement of the maximum vertical excursion of the orbit from the Galactic plane.

We use these quantities, in addition to the orbital energy, E, to characterise the orbits of stars throughout this thesis.

2.3.1 Stars in the disc and the halo

In this thesis, we are primarily concerned with stars in the MW's disc. As we saw in Section 2.2, this is where star formation occurs – in the MW the rate is $\sim 1.6\,{\rm M}_\odot\,{\rm yr}^{-1}$ – and stars are born with flat, circular orbits (i.e. low J_R and J_Z) in the thin disc. The thick disc has a greater vertical extent because its stars have larger J_Z (and J_R), providing a potential discriminator between stars which belong to the two populations and raising the question of *nature* vs. *nurture*: were the thick disc stars born with these hotter orbits, or did they evolve to this point – and if the latter, how? However, the kinematic properties are found to vary smoothly between the two discs, so a meaningful separation based on kinematic information alone is a challenge. The discs do show differences in chemistry, hinting at different formation channels, and this is revisited in later sections of this chapter.

While the orbits of stars in the disc are dominated by rotation, halo star orbits are more randomly distributed. These stars can travel far above the plane of the disc, but some can still be found close to the Sun as they traverse the Galactic plane on their long journey around the

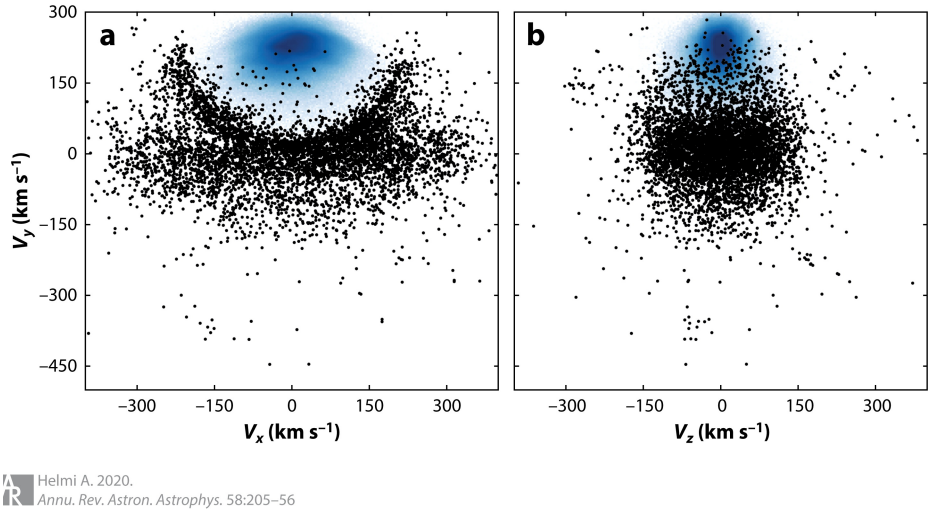


Figure 2.2: Velocity distribution of stars in the Solar neighbourhood, showing the halo (black points) and disc (blue density map). Figure reproduced from Helmi (2020).

GC. This means that some stars in the Solar neighbourhood may be of *ex situ* origin and can be studied in even quite local samples.

2.3.2 Separating components

Though the spatial distribution of stars in the two discs and the halo is different, the components are superimposed and stars from any of them can pass through the space close to the Sun at any time. In addition, the halo contains further substructures related to the buildup of the MW through mergers. Below, we give two examples of how kinematics can help us to uncover to which component the stars we observe belong.

One widely used method to separate halo from disc stars is to consider their velocities. Figure 2.2 shows the Cartesian components of the velocities of stars in the Solar neighbourhood. Halo stars (black points) are separated from the disc (blue density map) by selecting those with velocities which are significantly different from the local standard of rest (the mean motion of material close to the Sun). For disc stars, v_X and v_Z are centred on 0 km s^{-1} and the bulk rotation is seen in the v_Y axis. For halo stars, the rotational component is greatly diminished. We see a group of stars centred on $v_Y = 0$ km s^{-1} and a 'banana' shape formed of stars disrupted from the thick disc.

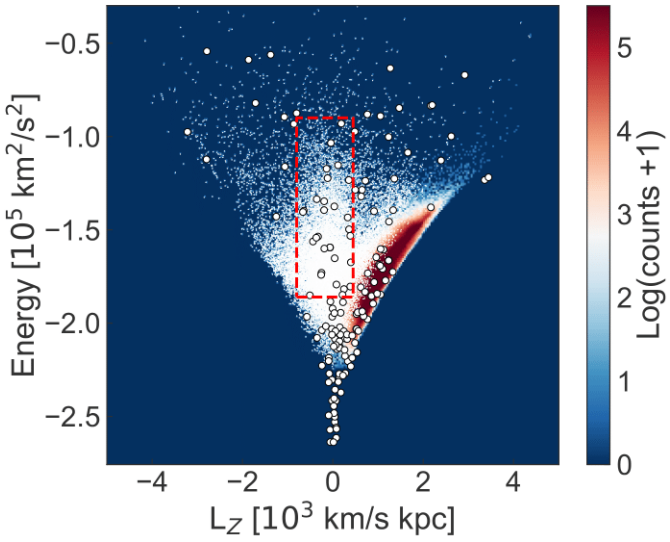


Figure 2.3: Energy vs. angular momentum for disc (coloured contours) and halo (white points) stars. Globular clusters are shown by white circles and the location of the debris of the *Gaia*-Enceladus merger (Helmi et al., 2018) is indicated by the red box. Figure reproduced from Massari, Koppelman, and Helmi (2019).

The energy-angular momentum plane is also commonly used. Figure 2.3 shows this plane for Galactic disc (coloured contours) and halo (white points) stars, as well as globular clusters (white circles). The concentration of stars on the right-hand side corresponds to the disc, and we see a wide range of both E and L_Z for halo stars. Under the assumption of a static, axisymmetric potential, both E and L_Z should be conserved, so remnants of merger events should be grouped together in distinct substructures in this plane. However, in the real MW, these assumptions do not hold perfectly and the features become 'fuzzier' over time. The red box in Figure 2.3 indicates the location of debris from the *Gaia-Enceladus* merger (Helmi et al., 2018).

2.3.3 Temporal evolution

So far in this chapter, we have seen that orbital actions are conserved in static, axisymmetric potentials, but also that the MW contains significant non-axisymmetric components (the bar and the spiral arms). This means that the Galactic potential changes with time, and so the actions change too – though slowly compared to the orbital timescale. This is the secular evolution of the disc and the processes which alter the actions fall into two categories (Sellwood and Binney, 2002; Schönrich and Binney, 2009a).

- 'Blurring' affects J_R and J_Z, making orbits more eccentric and increasing their vertical extent. This process is also known as orbital heating.

- 'Churning' affects J_ϕ, changing L_Z and, therefore, the average size of the orbit. It shifts stars away from the (radial) position of their birth and is thought to be roughly an order of magnitude stronger than blurring in the MW (Frankel et al., 2020).

Both processes are more important for stars in an orbital resonance with one of the non-axisymmetric features of the disc. For a star with initial orbital frequency Ω_0 and radial oscillation frequency κ_0 in a galaxy with a spiral arm of frequency Ω_s, the important resonances include the 'corotation resonance', $\Omega_0 = \Omega_s$, which will cause churning, and the 'Lindblad resonance', $\kappa_0 = \pm m\,(\Omega_s - \Omega_0)$, which will cause radial blurring (Binney and Tremaine, 2008). As we saw in Section 2.2, spiral structures in a galactic disc may be short-lived, so a star might experience multiple resonances with different structures during its lifetime.

We have already mentioned features of the MW which may be attributed to non-secular processes at work in, or rather on, the Galaxy (e.g. the build-up of the bulge and the warp of the disc). Further discussion based on simulations may be found in e.g. Villalobos and Helmi (2008) and Bird et al. (2013), but is beyond the scope of this thesis.

2.4 Stars in the Milky Way: chemistry

We saw in the previous section that the kinematic properties of stars can help us go some way towards untangling the structure and history of the MW, but that the picture becomes less clear over time as orbits are affected by dynamical processes in the Galaxy. In this section, we explore the independent constraints provided by the chemical compositions of stars.

In most cases, we start by making an important assumption: that the chemical abundances we measure in stars today are the same as in the gas cloud where the star was born. On the face of it, this seems unlikely as we know (and will see in more detail in Chapter 3) that stars fuse light elements to heavier ones during their lifetimes. However, fusion occurs in, or at least close to, the stellar core and our observations are of the surface abundances. For this reason,

the assumption works well in general. Exceptions arise in cases where the surface abundance of one or more elements changes as a result of processes of stellar evolution (see Section 3.1.1) but for most elements, most of the time, this is not important.

While it is possible to directly measure the chemical composition of gas in the MW or of gas and stars in other galaxies under certain conditions, this can only provide us with a snapshot, either of the MW today or a distant galaxy at the time the light we observe was emitted. Building up a coherent picture of galaxy evolution is, therefore, very challenging as not all systems evolve in the same way. However, the MW once again offers us a special opportunity to study chemical evolution as a function of time, by considering stars of different ages. Under our assumptions, the chemical composition of a given star tells us the composition of the Galaxy at the time and in the location where the star was born. Stellar ages pose their own set of challenges, which are explored in Chapter 3, and require detailed observations not available in other galaxies. In the rest of this section, we give an overview of Galactic chemical evolution, as told by the stars.

2.4.1 Element production in stars

If stars represent the make-up of the Galaxy at the time and location of their birth, and not all stars have the same chemical composition, we infer that the MW was not made of the same material at all times and in all locations in its history. In this section, we will see that stars are not only the messenger but also the mechanism of this change as we present a summary of element production processes, based primarily on Burbidge et al. (1957), Pagel (2009), and Bovy (in preparation). We also adopt the astronomical standard of describing all elements heavier than helium as 'metals'.

We saw earlier that only a few elements were present in the early Universe: hydrogen, helium and lithium were all produced by Big Bang nucleosynthesis. Beryllium and boron form mainly through the breakup of heavier elements upon collision with a cosmic ray, but all other elements are formed by stars. This can happen during their life, as a result of quiescent fusion, or death, in explosive nucleosynthesis, and the elements are released back into the interstellar medium (ISM) before or as the star dies. The next generation of stars then form from this material,

which is enriched in the products of the generation before, and therefore have different surface abundances.

The make-up of the ISM can also change due to the accretion of gas from outside the Galaxy either from the intergalactic medium, IGM, or a companion galaxy. Even the stellar products do not necessarily enrich the region where the star was born – we have already seen how stars move during their lifetime – or where it died since it is possible for the material to be ejected from the disc in a 'Galactic fountain' and reenter the MW somewhere else entirely.

However, here we are primarily interested in element production in stars, which can be divided into four main formation channels.

- Type II supernovae (SNeII): Massive stars ($M \gtrapprox 8\,\mathrm{M}_\odot$) fuse elements up to iron in their cores and surrounding shells. Beyond iron, however, fusion is no longer exothermic so the process halts and the source of energy production in the star shuts down. Without this internal support, the star collapses, rebounds and explodes. This core-collapse supernova releases the material formed inside the star by fusion but also generates enough energy to allow elements up to zinc to be produced. The result is that $\sim 90\%$ of metals in the Universe are produced by SNeII. Of particular interest for Galactic archaeology are the α-elemtents (formed by the α fusion ladder) for which SNeII are the dominant formation mechanism.

- Type Ia supernovae (SNeIa): Stars of lower mass end their lives as a white dwarf (WD). If isolated, WDs are stable, but they can become unstable due to interactions with other stars – whether by the accretion of mass from a giant companion or merging with another WD. Though the mechanism is not yet fully understood (Leung and Nomoto, 2021), these interactions result in a SN. Once again, the explosion produces iron peak elements, and in total $\sim 99\%$ of metals in the Universe form between these SN channels.

Elements heavier than zinc are not produced in SN explosions, but rather by a process of repeated neutron capture and β-decay (where a neutron is converted to a proton, and an electron and antineutrino are ejected).

- Slow (s-process) neutron capture: Neuton capture occurs slowly compared to the timescale of β-decay during core helium burning in massive stars and helium shell burning during the ascent of the asymptotic giant branch. The products are ejected by stellar winds or released in a SN and account for $\sim$ 50% of elements heavier than zinc. This channel is also a significant producer of carbon and nitrogen, but we will see in the next chapter that these elements are also affected by processes of stellar evolution, so they are generally less useful for Galactic archaeology.

- Rapid (r-process) neutron capture: In a very neutron-rich environment, neutron capture may happen rapidly compared to β-decay, which accounts for the other $\sim$ 50% of elements heavier than zinc. However, where such sites occur in the Universe is still rather unclear. Neutron star mergers certainly play a role, but it is not currently thought that these alone can explain the observational data (Thielemann et al., 2011).

2.4.2 Chronology from chemistry

We have now seen that elements in the Galaxy are produced in different formation channels and, in most cases, multiple channels contribute to the production of a given element. These channels are inherently linked to stellar evolution and, therefore, the timescales on which they occur are linked to stellar lifetimes. As we will see in the next chapter, it is not only the ultimate fate of a star which is determined by its initial mass, but also the timescales on which it evolves.

Massive stars have short lifetimes compared to the timescales of Galactic evolution ($\lessapprox$ 40 Myr) and, therefore, SNII are assumed to occur 'promptly' after the start of star formation in a system. This means that the elements produced in this channel are released ~directly into the ISM and build up over time. WDs are the end product of low-mass stars and, therefore, their formation takes longer ($\sim$ 1 Gyr), so there is a delay between the start of element production by SNII and SNIa. The timescales associated with element production by neutron capture are less clear, given that the s-process occurs in stars of a range of masses and the sites of the r-process are not well understood. However, it is clear that the relative abundance of elements in a system must change over time, in a way which depends on the star formation history and the distribution

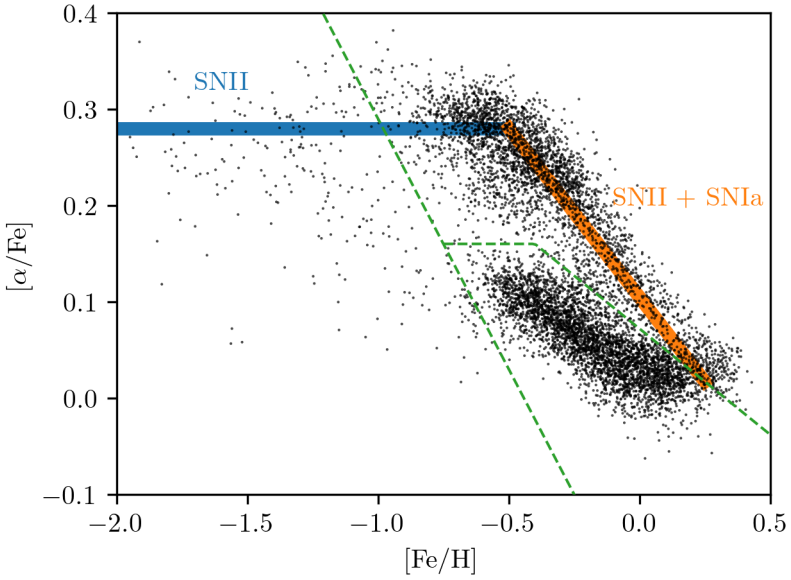


Figure 2.4: α element abundance vs. iron abundance (see Chapter 4 for description of dataset). The blue and orange lines indicate the positions of the plateau, knee and downward slope described in the text. The dashed green lines show an approximate separation between the halo (low-metallicity, left) and thick (high-α, upper right) and thin (low-α, lower right) discs.

of stellar masses in that system.

Therefore, the balance of elements we observe contains a wealth of information about the star formation rate (SFR) and initial mass function (the distribution of initial stellar masses; IMF) of the Galaxy. As an example, in Figure 2.4 we compare the abundances of α-elements and iron, using data described in Chapter 4. We use the notation [Fe/H] and [α/Fe] to denote the relative abundances of iron and hydrogen and an average over several α elements and iron, respectively. This is described in more detail in Section 2.5.2. We overlay a schematic showing the main features of this plot in the context of the present discussion and summarise them below.

At low [Fe/H] there is a plateau. These stars, therefore, formed at a time when the relative abundance of α-elements and iron was constant – with both increasing at the same rate. This indicates that both the α-elements and iron are being produced by, and only by, the same formation channel: SNeII and therefore these stars formed early, before the start of element production by SNeIa. At intermediate [Fe/H] there is a knee, followed by a downward slope. The position of the knee indicates the point at which SNeIa start to contribute to element production, as beyond this point iron is produced more rapidly than the α-elements.

From the height of the plateau, we can learn about the IMF of the system: an IMF which favours massive stars will generate a large abundance of α-elements, leading to a high plateau. The position of the knee in the [Fe/H] axis gives a hint to the SFR: if the system forms stars very rapidly, many SNeII will occur in the time before SNeIa start to contribute iron, and the knee will be found at higher [Fe/H]. In less massive systems, the SFR is generally lower and, therefore, the knee is seen at lower [Fe/H]. Iron enrichment is also slower, leading to a shallower downward slope.

From these features we can infer, in general terms, the type of system in which the stars formed. In Figure 2.4 we see more structure than is captured by our simple schematic, indicating that multiple star formation events contribute to the stellar population of the MW today.

2.4.3 Spatial variation

So far, we have seen what can be learned from the chemical abundances averaged over the whole system. There is also information to be gained from a more detailed investigation of how the abundances change as a function of position and Galactic component.

In Figure 2.4 we show cuts to highlight the regions of the [α/Fe]-[Fe/H] plane which are usually associated with halo, thick and thin disc stars. In the case of the discs, chemistry provides a clearer separation than is achievable in kinematic planes. In broad terms, the thin disc has lower α-element abundances, while the thick disc is more α-enriched, populating the knee and downward slope in Figure 2.4. This strongly suggests that the two discs have different formation channels, the details of which are not yet fully understood. This is an open topic in Galactic archaeology, and we will revisit it toward the end of this chapter.

In addition, in many disc galaxies, a higher metallicity (traced by a range of elements) is observed in the centre of the disc, compared to the edge (Aller 1942; Searle 1971; Pagel and Edmunds 1981 and see Magrini et al. 2016 and references threin for recent results). This is an indication that the disc formed from the inside out because the centre of the disc is more enriched in heavy elements, produced by more generations of stars, than the disc edge. The details of the [Fe/H] gradient in the MW are the main focus of Chapter 5.

2.4.4 *Ex situ* stars

As we have seen, structures in the [α/Fe]-[Fe/H] plane indicate the characteristics of the system in which the stars were born. With this information, we can infer that not all of the stars present in the MW today were born here. These accreted stars are thought to have formed in a system of lower mass than the MW since they form a sequence with a lower metallicity knee and shallower slope than the *in situ* population.

Making a robust selection of these stars based on α and iron abundances alone is challenging but in the last decade, many new chemical planes have been demonstrated as useful diagnostics of *ex situ* stars (e.g. Hawkins et al., 2015; Horta et al., 2023). In Chapter 4 we use [Mg/Mn] vs. [Al/Fe], which uses the comparison of elements from different formation channels to isolate *ex situ* stars: magnesium is an α-element, manganese is a pure tracer of SNeIa and aluminium is an odd-Z element, which has been shown to be less abundant in low-mass galaxies (Das, Hawkins, and Jofré, 2020).

2.5 Putting it together: Galactic archaeology

This section will give an overview of how the data required to understand the kinematics and chemistry of stars is obtained. We will then draw together the two strands of our discussion so far to show how kinematics and chemistry can be combined to throw light on the MW's history. We close this chapter by outlining the necessity for chronological information in our picture of the Galaxy.

2.5.1 From observations to data: astrometry

The measurement of the positions and motions of stars is known as astrometry and is one of the oldest branches of astronomy. In modern observations, we measure six quantities:

- The right ascension, α, describes the azimuthal coordinate on the celestial sphere.

- The declination, δ measures the angular distance from the celestial equator and is positive in the Northern hemisphere.
- The proper motions, μ_α and μ_δ are the projected motions in the directions of α and δ. Together they describe the motion perpendicular to the line of sight.
- The motion along the line of sight, μ_R, is usually called the radial velocity (RV) and, unlike the other parameters, is generally much better constrained by spectroscopy.
- The parallax, ϖ, is the apparent motion of the star caused by the Earth's passage around the Sun. When measured in arcseconds it is related to the distance to the star, D measured in parsecs, by $D = 1/\varpi$.

The astrometric observables used in this thesis were obtained by the *Gaia* mission (Gaia Collaboration et al., 2016), which has heralded a new era in Galactic archaeology with full astrometric information available for almost 1.5 billion sources so far (Gaia Collaboration et al., 2023c). Though this is less than 1% of the total Galactic population, it is still an improvement of many orders of magnitude over the data previously available.

To obtain orbital characteristics from astrometric observations, we must model the motion of the star in the Galactic potential, Φ, which requires us to make some assumptions.

- First, that the system is in a steady state and that the potential in the Galaxy does not change with time.
- Second, the system is axisymmetric, meaning that we assume the Galaxy is well mixed and stars have had sufficient time to orbit away from their birth position so $\partial/\partial\phi = 0$.
- Finally, the system is collisionless and stars are separated by large distances compared to their size, meaning that their motion is controlled by Φ.

We also require a model of Φ itself which is constrained by observations of, for example, the velocity dispersion of stellar populations and the Galactic rotation curve (e.g. Bovy, 2015).

Even with these simplifications, computing actions and other orbital characteristics is, in general, very computationally expensive and can only be achieved numerically in most potentials.

This is because, in most orbits, the frequency of the oscillations in R and Z are not integer multiples of the orbital frequency. This means that the orbit does not 'close' and when a star returns to its starting position in ϕ it is not at the same radial or vertical coordinate. The result is that the integrals of Equations 2.6 - 2.8 cannot be simply computed. In the orbital computations of this work we make another assumption to overcome this, called the Stäckel fudge (Binney, 2012). In this case, we approximate the MW's potential with at Stäckel potential (de Zeeuw, 1985) and make a coordinate transformation to elliptical coordinates. Under this transformation, the Stäckel potential may be written

$$\Phi_S(u, v) = \frac{U(u) - V(v)}{\sinh^2 u + \sin^2 v}. \tag{2.9}$$

Since U and V depend only on one variable each, the integrals become tractable and this allows the orbits of many stars to be computed quickly with only a small loss in accuracy compared to the full, (assumed) potential which is, itself, only an approximation of the true MW (Mackereth and Bovy, 2018).

2.5.2 From observations to data: spectroscopy

Spectroscopic observations provide us with astrophysical stellar parameters and the RV. In spectroscopy, the light from a star passes through a telescope and into a spectrograph, which disperses the components of different wavelengths, revealing the absorption lines present in the stellar spectrum. These absorption lines are created when an atom in the star's atmosphere absorbs a photon emitted by the interior, with the precise energy required to excite it to a higher, discrete energy level. This means that we see lines at different wavelengths and with different characteristics, depending on the chemical makeup and physical conditions of the stellar atmosphere.

By comparing the absorption lines present in the spectrum to the known wavelengths of lines corresponding to a given element, we can reveal the species present in the stellar atmosphere. The strength of a line depends on the number of absorptions corresponding to that specific energy

transition, which is affected by the balance of atoms in the lower and higher energy states. This depends on the temperature at the surface, $T_{\rm eff}$, and the total number of atoms present (i.e. the abundance of the element in the star). The absorption lines are also not perfectly narrow; all have a finite width corresponding to the uncertainty in the energy of the transition as a result of the finite lifetime of the excited state. Beyond this 'natural' broadening, the conditions in the stellar atmosphere can also contribute to broader lines. At higher pressures, collisions between excited atoms and other particles are more frequent, which effectively shortens the lifetime of the excited state and results in broader lines. The line width can, therefore, be used to constrain the surface gravity, $\log g$. In addition, all the lines will be red- or blue-shifted as a result of the motion of the star along the line of sight. From this global shift, the RV is measured.

In this thesis, there are two notations used to describe chemical abundances. The mass fractions of hydrogen, helium and metals are labelled X, Y, and Z, respectively and $X+Y+Z = 1$. We use this when discussing stellar evolution and helium abundance in Chapters 3 and 6. We have already seen notation of the form [A/B], which describes the abundance of element A relative to B via the logarithmic ratio of the number density, compared to the Sun:

$$[\mathrm{A/B}] = \log_{10}\left(\frac{N_\mathrm{A}}{N_\mathrm{B}}\right)_* - \log_{10}\left(\frac{N_\mathrm{A}}{N_\mathrm{B}}\right)_\odot , \tag{2.10}$$

where N_A and N_B are the numbers of A and B nuclei per unit volume of the stellar photosphere, respectively. In particular, [Fe/H] is often used as a tracer for the total stellar metallicity (for historical reasons as there are many iron lines present in most stellar spectra) and [α/Fe] is an average over several α elements. In α-enriched stars, however, iron does not provide a good proxy for the full metal abundance. One approach to combat this (for example, when comparing to models as in Chapter 6) is to rescale the observed [Fe/H] to account for the additional metallicity contributed by the α enrichment, relative to the solar α abundance. Salaris, Chieffi, and Straniero (1993) demonstrate this, showing that stellar evolutionary tracks are from α enhanced models can be reproduced by tracks of solar-α with a rescaled metallicity.

2.5.3 Applications

We have now seen how we can infer some of the properties and history of the MW from the available observations. In Chapter 5 we combine chemistry and kinematics explicitly to investigate the change in metallicity radially through the disc. We discuss extensively the relationship of the spread observed around the radial metallicity gradient and radial migration, and the advantages of the guiding radius compared to the Galactocentric radius. In this section, we provide additional background to two other specific applications where we benefit from the combination of kinematics and spectroscopy which are relevant to the work in Chapters 4 - 6, but which are explained in less detail there.

Identifying *ex situ* stars

There are many methods in the literature for identifying stars born outside the MW, which have led to the identification of a wide range of substructures (see Helmi, 2020, for a review). In Chapter 4 we touch briefly upon this topic, using the [Mg/Mn]-[Al/Fe] plane to identify stars of *ex situ* origin. However, we can further refine this selection by reinforcing the chemical information with kinematics recalling that we saw in Section 2.3 that orbital actions and properties based on them are approximately conserved. For our purposes, it's enough to recognise that higher eccentricity stars are more likely to be members of accreted populations (Mackereth et al., 2019b) and we, therefore, combine a cut in eccentricity with the chemical selection to strengthen our result.

Identifying the thin disc

The main problem here is to understand what is meant by the names thin and thick disc, as any true separation between them should be based on their formation history, not only how they appear today. Unfortunately, the formation of the discs is still poorly constrained. The main scenarios (Helmi, 2020) for the formation of the thick disc are minor merger(s) which led to heating of an *in situ* thinner disc (Quinn, Hernquist, and Fullagar, 1993) or deposited their debris

directly into a hot, disc-like structure (Abadi et al., 2003); a more gas-rich and turbulent disc in the past, in which stars were formed on hotter orbits than they are today (Brook et al., 2004; Bird et al., 2013); or migration from the early thin disc (Schönrich and Binney, 2009b). In these scenarios, the thick disc forms either earlier than the thin disc or outside the MW, giving rise to a different kinematic and chemical mixture and accounting for the two sequences in the [α/Fe]-[Fe/H] plane we see today.

Though it now seems likely that orbital migration alone would not have been able to produce the thick disc we see today (Minchev et al., 2012), the true solution is probably some combination of two or more of the scenarios above (Gallart et al., 2019), which left overlapping imprints on the chemistry and kinematics of the stellar populations. Since, as yet, it is not possible to definitively identify members of the thick disc (and so remove them from a thin disc sample) we take a pragmatic approach in Chapter 5, selecting cold orbits with a somewhat arbitrary (though motivated) cut in $Z_{\rm max}$ and a conservative cut in the chemical plane, removing stars where the high- and low-α sequences overlap. The best we can do to verify the results obtained from these selections is to test our sensitivity to the details which, in this case, indicates that our findings are robust (Appendix B.2). In Chapter 6 we consider high- and low-α stars separately, but since we do not seek to separate the two discs specifically, a simple chemical cut is suitable

2.5.4 The importance of temporal constraints

We have not yet discussed the third constraint in our picture of the MW, the '*when*'. In the course of this chapter we have mentioned, in varying levels of detail, several open questions about the structure and history of our Galaxy which would be illuminated by high-quality chronological information, and we expand on them below.

Building up a timeline of the MW's merger history

The time of a merger is roughly indicated by the age of the youngest stars in the *ex situ* population (Helmi et al., 2018). It's also possible for a merger to trigger a starburst (a period of rapid star formation) in the larger galaxy (e.g. Renaud, Segovia Otero, and Agertz, 2022) and again, the

ages of stars formed in such an event provide a constraint on the time of the merger.

Understanding the formation of the bulge

Robust ages would be useful to differentiate between the classical and pseudobulge scenarios. In the classical case the bulge members should be exclusively old because the bulge is built early in the Galaxy's formation, while in the pseudobulge scenario, secular processes are expected to mix younger stars into the bulge. At present the observations are difficult to explain with either of these scenarios (Nataf, 2016).

Untangling the formation of the discs

The different scenarios for the formation of the discs presented in the previous section not only predict different chemical and kinematic properties of the stellar populations of the disc but also different star formation histories. Identifying the presence and nature of any breaks in the star formation of the discs could, therefore, provide a much-needed diagnostic. In addition, by comparison to the times of known accretion events, it is possible to build up a picture of which components of the Galaxy were already formed and may have been disrupted in the merger (e.g. Gallart et al., 2019).

The choice of tracer for the passage of time in the MW is also important. For robust inference, we ideally require long-lived objects – to trace the full history of the Galaxy – which are numerous and luminous enough to be seen in all Galactic domains. While any constraint is of benefit, a precision of $\sim$ 10% is expected to herald significant breakthroughs (Miglio et al., 2017). In the next chapter, we will see that low-mass red giant stars in the field are an ideal tool and that asteroseismology is paving the way to the required data volume and quality.

Chapter 3

STARS AND STELLAR EVOLUTION

In Chapter 2 we saw how much can be learned about the Galaxy from studying the stars in it. In this chapter, we will consider these stars in a little more detail, discussing important aspects of their evolution in Section 3.1 and the field of asteroseismology in Section 3.2. In Section 3.3 we will focus on methods of estimating stellar ages, thus obtaining the third constraint for our study of the Milky Way, and mention some specific challenges associated with stellar modelling. This section will specifically motivate the work included in Chapters 4 and 6

3.1 The evolution of a Sun-like star

The discussion of stellar evolution given here is very incomplete, focusing only on a few evolutionary phases which are of specific interest in the later chapters of this thesis. More detailed descriptions of these processes may be found in Kippenhahn (2012), upon which most of the summary presented in this section is based.

For our purposes it is enough to know that stars form from the collapse of gas clouds in the interstellar medium (ISM), increasing in temperature as they do so until the core of the resulting ball of gas is hot and dense enough to ignite hydrogen fusion, and a star is born. To understand the processes at play as this star evolves, it is necessary to consider the mechanisms which transport the energy released by this fusion to the stellar surface, from where it can radiate away and we may observe it. Radiation, convection and conduction all play a role – though

the latter only in cases where the stellar interior has become degenerate. Whether radiation or convection dominates in a given region depends on the local temperature gradient. If it is too steep, radiation is not sufficient to transport all the energy outwards, and the region becomes convectively unstable. The specific points where this occurs depend on the interplay of the properties of the gas, including the opacity, which describes how opaque the gas is to radiation of a given wavelength. This in turn depends on the mean molecular weight, μ. Convection is an important process inside stars as, because it requires the physical movement of the stellar gas, it can mix and redistribute the elements present in the stellar interior and potentially change the abundance measures at the surface.

3.1.1 The main sequence and sub-giant phase

After hydrogen ignites in the core, the star has entered the 'main sequence' (MS). This is the longest phase of its lifetime and the Sun is currently about halfway through. The duration of this phase is strongly mass dependent: $\tau_{\rm MS} \propto M/L\,(M) \propto M^{-(\gamma-1)}$, where $\gamma \sim 4$ (Kippenhahn, 2012). For a star of $1\,{\rm M}_\odot$ $\tau_{\rm MS} \sim 9\,{\rm Gyr}$, and it is around an order of magnitude shorter for a $2\,{\rm M}_\odot$ star. As hydrogen is fused to helium, μ increases and there is a corresponding increase in the luminosity, $L \propto \mu^{15/2} M^{11/2}$, shifting the star from A to B in Figure 3.1. It's this connection between L and μ which means that the initial helium abundance of a star has a significant impact on its main sequence lifetime. This is addressed further in Chapter 6.

As well as the MS lifetime, the fusion mechanism also depends on the stellar mass. Below $\sim 1.2\,{\rm M}_\odot$, fusion takes place via the slow combination of protons in the pp-chain. In more massive stars, the CNO cycle occurs – helium is still the end product, but isotopes of carbon, nitrogen and oxygen are involved in the reaction sequence as catalysts and produced as byproducts. This mechanism is more sensitive to temperature, resulting in more centrally concentrated energy generation and a convective core. The exact boundaries of the convective region are rather ill-defined, however, since packets of material approaching the theoretical edge of the convective region do not lose momentum instantaneously and instead carry on travelling for some distance. This process of 'overshooting' can effectively extend the burning region, mixing new hydrogen

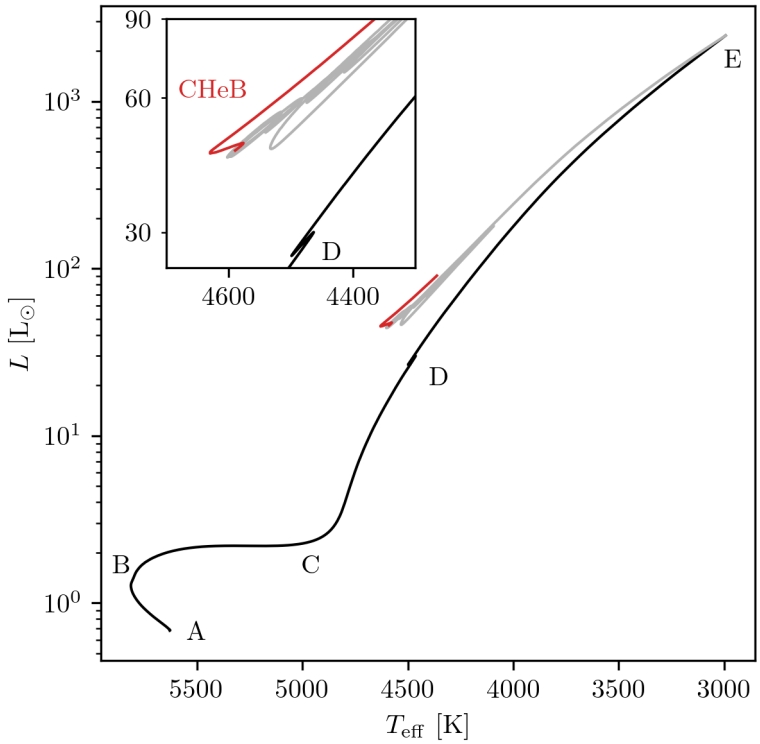


Figure 3.1: Evolutionary track of a solar-mass, solar-metallicity star from the main sequence to the end of core helium-burning. The evolution from the main sequence (A) to the tip of the red giant branch (E) is shown in black, the rapid evolution during helium ignition in grey, and the core helium-burning (CHeB) phase in red. The inset plot shows an enlarged view of the region containing the red giant branch bump (D) and the start of quiescent CHeB.

fuel into the core and extending the MS lifetime as a result. The strength and description of overshooting in this, and other, phases of stellar evolution is one of the many open challenges in stellar physics.

When the core is eventually depleted of hydrogen, the MS phase ends. The temperature of the, now inert, core is too low to ignite helium fusion, but the surrounding layers of the star are hot enough for hydrogen fusion to continue in a shell. During this 'sub-giant' phase, the shell becomes thinner as hydrogen in the envelope is depleted, and the outer layers of the star cool, moving the star to the right in Figure 3.1. As they cool, they become more opaque, resulting in the formation of a thick convective layer.

3.1.2 The ascent of the red giant branch

Thus, when the star reaches the bottom of the red giant branch (RGB) it has a small, inert helium core, a hydrogen-burning shell and a deep convective envelope. As the core continues to gain mass from the shell, it starts to contract and the star becomes more luminous, moving from *C* to *E* in Figure 3.1. The outer layers also expand and the convective layer reaches deeper into the interior, eventually drawing products from the MS core fusion to the surface. This is known as the first dredge-up, and is responsible for a change in the surface abundances of carbon and nitrogen meaning, as mentioned in Section 2.4.1, that they are no longer representative of the birth environment of the star. We revisit this again, briefly, in Section 4.4.3.

Eventually, the convective envelope recedes, and the hydrogen-burning shell moves outwards. There is a chemical discontinuity which marks the deepest extent of the convective region, at the boundary between the mixed and unmixed material. As the shell crosses this there is a temporary drop in luminosity, called the RGB-bump, (point D, Figure 3.1) before the ascent of the RGB continues.

3.1.3 Beyond the red giant branch: The helium flash and core helium burning

What happens to the star next depends on its mass, though the exact boundaries are also affected by chemical composition. For stars above $\sim 1.8\,M_\odot$ the core will eventually attain the temperature needed to ignite helium fusion. In less massive stars, the central density continues to increase as the core mass grows until eventually it becomes degenerate. The core is now efficiently cooled by electron conduction, with the effect that helium ignition is delayed until it reaches a critical mass of $\sim 0.5\,M_\odot$, regardless of total stellar mass (Girardi, 2016).

At this point, helium fusion ignites, slightly off-centre, causing a rapid temperature increase. There is no corresponding drop in pressure in the degenerate core, so the nuclear reaction rate increases and the star enters a thermal runaway phase, known as the helium flash. Eventually, the degeneracy is lifted in the layer where ignition occurred. However, the layer inside this

is still degenerate and so the process repeats in a series of sub-flashes which, over $\sim 10\,\mathrm{Myr}$ gradually lift the degeneracy closer and closer to the centre of the star. When the degeneracy is lifted throughout the core the star enters the phase of quiescent helium burning (Figure 3.1).

Stars which ignite helium in a flash all reach this point with very similar core masses, and therefore very similar luminosities. This results in an observational overdensity of stars at this point in the Hertzsprung–Russell diagram (HRD), known as the red clump (RC). The slightly more massive stars which ignited helium in a non-degenerate environment are slightly less luminous and form the secondary red clump (SRC) while at still larger masses, the core mass is greater and the CHeB phase luminosity increases again. RC stars are the focus of Chapter 6, and a more detailed description of their properties with respect to helium abundance is given there.

3.1.4 Advanced evolution

The details of the subsequent phases of evolution are beyond the scope of our discussion here until stars reach the end of their lives and enrich the ISM through the processes described in Section 2.4.1.

For stars of $M \lessapprox 8\,\mathrm{M}_\odot$, hydrogen and helium fusion continues in shells around an inert core as the star ascends the asymptotic giant branch (AGB). The evolution during this phase is complicated due to the interaction of the two burning shells. The energy produced by each varies significantly in response to the other, leading to 'thermal pulses'. The star also experiences significant mass loss as its outer layers become more diffuse and eventually the shell burning is extinguished. What remains is a white dwarf (WD) which gradually cools and illuminates the clouds of gas from its outer envelope, now known as a planetary nebula.

More massive stars undergo several further, increasingly rapid, phases of core and shell fusion until they reach iron. At this point, no further energy can be released from fusion, the internal support for the star is removed and a core-collapse supernova follows.

3.2 Asteroseismology

This section gives a very brief overview of the study of pulsations in solar-like oscillators, based primarily on Chaplin and Miglio (2013), providing background for the quantities used in later chapters.

3.2.1 Stellar oscillaions

Oscillations in the Sun and similar stars are excited and damped by near-surface convection. The pulsation modes resonate in cavities in the stellar interior and are affected by the conditions there. The observation of these resonant frequencies can, therefore, provide a diagnostic for the stellar structure, enabling us to 'see' inside stars in a way which is not possible with traditional observations.

These 'solar-like' oscillators are just one of many classes of variable stars, and their study is only a few decades old since the amplitude of the pulsations is small (a few tens to hundreds of parts per million (ppm) for RGs, e.g. Yu et al., 2018). Observations are primarily based on space-based photometry from missions such as CoRoT (Baglin et al., 2006), Kepler/ K2 (Borucki et al., 2010; Gilliland et al., 2010; Howell et al., 2014) and TESS (Ricker et al., 2015). The angular behaviour of the modes is described in terms of spherical harmonics, characterised by the angular degree, l; the number of nodes on the stellar surface, the azimuthal order, m; the orientation of the nodes on the surface, and the radial order, n; the number of nodes in the radial direction. A full description of the oscillation modes and their properties is not included here, as we aim only to motivate the use of some specific parameters as diagnostics of the bulk properties of stars.

The conditions in a star give rise to two types of standing waves, differentiated by the nature of the restoring force. 'p-modes' are acoustic in nature and are restored by pressure, while in 'g-modes' the restoring force is gravity. Since g-modes cannot propagate in convective regions, they are confined to the deep interior and are generally hard to observe in Sun-like and RG stars. If the resonant cavities of the p- and g-modes are sufficiently close, however, 'modes of mixed

character' may be observed at the stellar surface, but both these and g-modes themselves are beyond the scope of the discussion here.

In the description of solar-like oscillations, we assume that the stellar interior is adiabatic and, therefore, no energy is exchanged between the wave and the fluid in which it propagates. We may then write the sound speed as

$$c_s = \left(\Gamma_1 \frac{P}{\rho}\right)^{\frac{1}{2}} \propto \left(\frac{T}{\mu}\right)^{\frac{1}{2}}, \tag{3.1}$$

where P, ρ and T are the pressure, density and temperature of the gas and Γ_1 is the first adiabatic exponent: $\Gamma_1 = (\partial \ln P / \partial \ln \rho)_{\rm ad}$. Since the resonant oscillations are confined to a cavity, the location of this cavity dictates which regions of the stellar interior a given mode is sensitive to. Towards the outer layers of a star, the density drops rapidly and we infer a critical frequency, below which a mode will be reflected:

$$\nu_{\rm ac} = \frac{1}{4\pi} \frac{c_s}{H}, \tag{3.2}$$

where $H \propto T/g$ is the scale height of the gas, which varies with the temperature and gravitational acceleration (Lamb, 1932; Christensen-Dalsgaard, 2014).

In the interior, c_s increases with depth and the propagating mode is refracted away from the centre. Total internal reflection occurs at the 'Lamb frequency':

$$S_l^2 = l\,(l+1) \left(\frac{c_s}{r}\right)^2, \tag{3.3}$$

where r is the distance to the centre of the star (Hekker and Christensen-Dalsgaard, 2017, and references therein) This shows us that modes of lower angular degree probe deeper inside the star, with the radial $l = 0$ modes passing through the centre.

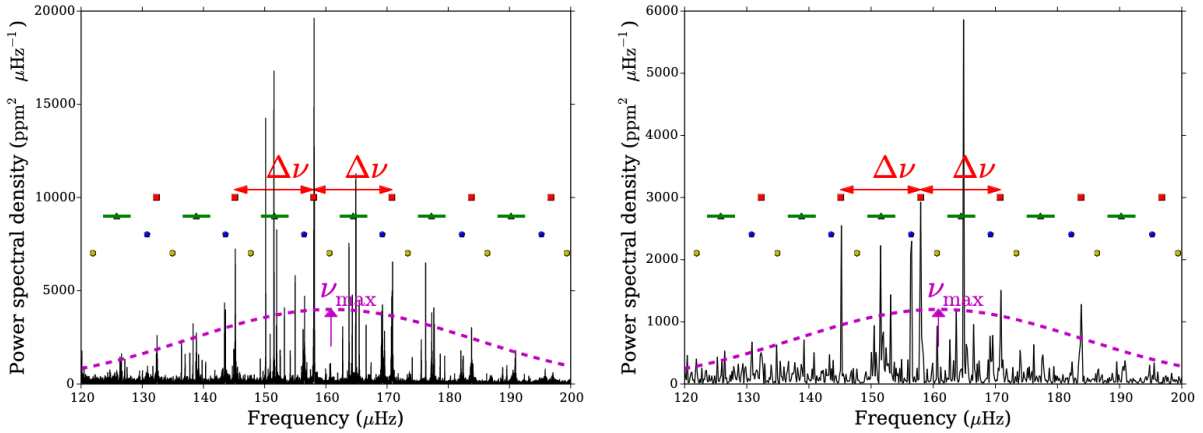


Figure 3.2: Power spectrum of the low-luminosity red giant KIC 12008916, computed with 1335 days (left) or 70 days (right) of *Kepler data.* The Gaussian envelope of the power excess due to the oscillations and the frequency of maximum oscillation power (at its peak) are marked in purple, and the large frequency spacing between the radial $l = 1$ modes is shown in red. Modes of angular degree $l = 0, 1, 2$ and 3 are indicated by red squares, green triangles with bars, blue pentagons and yellow hexagons, respectively. Figure reproduced from Davies and Miglio (2016).

3.2.2 Asteroseismic parameters and scaling relations

We will now consider the population of oscillation frequencies in a given star, as shown by the power spectrum in Figure 3.2. We observe two distinct characteristics from which we may infer the bulk properties of the star. These are the 'global' asteroseismic parameters:

- $\nu_{\rm max}$, the frequency of maximum oscillation power which is found at the peak of the Gaussian envelope of the power excess due to the oscillations.

- $\Delta\nu$, the large frequency separation, which characterises the regular spacing of the modes.

The information available from the spectrum is clearly much richer than these two quantities, but a more detailed discussion of the individual mode frequencies is not needed for our discussion here.

$\nu_{\rm max}$ has been found to scale with the acoustic cut-off frequency $\nu_{\rm ac}$ (Kjeldsen and Bedding, 1995), so we have that

$$\nu_{\rm max} \propto \nu_{\rm ac} \propto gT^{-\frac{1}{2}} \propto MR^{-2}T_{\rm eff}^{-\frac{1}{2}} \tag{3.4}$$

or, as is more common, scaled to the solar values:

$$\frac{\nu_{\max}}{\nu_{\max,\odot}} = \frac{M}{M_\odot}\left(\frac{R}{R_\odot}\right)^{-2}\left(\frac{T_{\rm eff}}{T_{\rm eff,\odot}}\right)^{-\frac{1}{2}}, \tag{3.5}$$

where, since $\nu_{\rm ac}$ is constrained by the surface properties of the star, we switch to the effective temperature $T_{\rm eff}$ and M and R are the stellar mass and radius, respectively. $\nu_{\max,\odot} = 3090\,\mu$Hz (Huber et al., 2011), and $\nu_{\max}$ decreases from $\sim 10^3$ to $\sim 10\,\mu$Hz from the MS to the RGB tip. The full theoretical basis for this relation is an area of ongoing research (e.g. Belkacem et al., 2011).

To understand $\Delta\nu$, we first assume that we are working at high radial order in the 'asymptotic limit' $l/n \to 0$ (Tassoul, 1980). We then approximate the frequencies in the spectrum to first order as

$$\nu_{n,l} \approx \left(n + \frac{l}{2} + \varepsilon\right)\Delta\nu, \tag{3.6}$$

where ε is some constant offset. We see that $\Delta\nu_{n,l} = \nu_{n,l} - \nu_{n-1,l} \approx \Delta\nu$ as $\Delta\nu$ is approximately the same for all l under our assumption. Observationally, we estimate $\Delta\nu$ as an average of the the separations $\Delta\nu_{n,l}$ visible in the spectrum and find that

$$\langle\Delta\nu_{n,l}\rangle \propto \langle\rho\rangle^{\frac{1}{2}}, \tag{3.7}$$

so we have

$$\frac{\Delta\nu}{\Delta\nu_\odot} = \left(\frac{M}{M_\odot}\right)^{\frac{1}{2}}\left(\frac{R}{R_\odot}\right)^{\frac{-3}{2}}, \tag{3.8}$$

(Ulrich, 1986; Belkacem et al., 2013), with $\Delta\nu_\odot = 135\,\mu$Hz (Huber et al., 2011). The caveat here is that the asymptotic limit is not strictly valid as $n \sim 20$ for the MS, $\lessapprox 15$ for the RGB and ~ 8 for the RC (Mosser, 2015). There are, therefore, ongoing efforts to investigate and constrain an evolutionary-state dependent correction to the relation in Equation 3.8 (e.g. Miglio et al., 2012, 2016).

This complication aside, we can combine Equations 3.5 and 3.8 in the 'asteroseismic scaling

relations' for stellar mass and radius:

$$\frac{M_*}{M_\odot} = \left(\frac{\nu_{\rm max}}{\nu_{\rm max,\odot}}\right)^3 \left(\frac{\Delta\nu}{\Delta\nu_\odot}\right)^{-4} \left(\frac{T_{\rm eff}}{T_{\rm eff,\odot}}\right)^{\frac{3}{2}}, \tag{3.9}$$

$$\frac{R_*}{R_\odot} = \frac{\nu_{\rm max}}{\nu_{\rm max,\odot}} \left(\frac{\Delta\nu}{\Delta\nu_\odot}\right)^{-2} \left(\frac{T_{\rm eff}}{T_{\rm eff,\odot}}\right)^{\frac{1}{2}}. \tag{3.10}$$

By relating radius to the luminosity, L, and $T_{\rm eff}$, we may also remove the dependence on $\Delta\nu$:

$$\frac{M_*}{M_\odot} = \frac{\nu_{\rm max}}{\nu_{\rm max,\odot}} \frac{L}{L_\odot} \left(\frac{T_{\rm eff}}{T_{\rm eff,\odot}}\right)^{\frac{-7}{2}} \tag{3.11}$$

$$\frac{R_*}{R_\odot} = \sqrt{\frac{L}{L_\odot} \left(\frac{T_{\rm eff}}{T_{\rm eff,\odot}}\right)^{-4}}. \tag{3.12}$$

In general, measurements of $\nu_{\rm max}$ and $\Delta\nu$ improve with the duration of the observations used to produce the power spectrum, as the frequency precision increases (Figure 3.2).

3.2.3 Applying asteroseismology

Asteroseismology is now a well-established field, and its techniques and results have been explored in diverse applications (see Chaplin and Miglio, 2013; Aerts, 2021, for reviews). The scaling relations above give a 'direct' estimate of stellar properties (Mosser et al., 2010), which is independent of stellar models and evolutionary theory. Alternatively, the global asteroseismic parameters, or more specific information based on the individual mode frequencies, can be used to improve the comparison to stellar models in a 'grid-based' approach (e.g. Rodrigues et al., 2017). The latter has the advantage of flexibility in the definition of $\Delta\nu$, which can be calculated from the modelled frequencies in a way which mimics the approach in the observations, enabling a more robust comparison.

One important specific case in the following chapters is the impact of asteroseismology on the constraint of stellar age. We saw in Section 3.1 that stellar lifetimes are dominated by the time spent on the MS which is, in turn, related closely to the initial mass. For RGs this gives a very tight age-mass relation (Figure 3.3), and so the mass constraints from asteroseismology

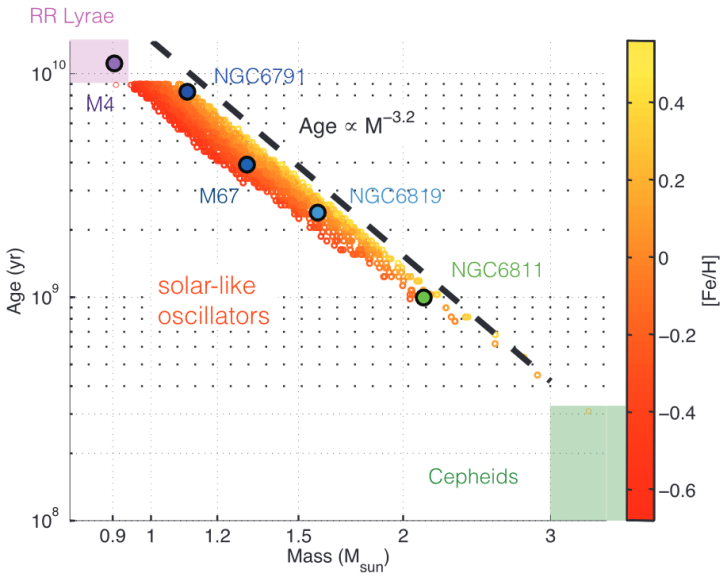


Figure 3.3: Age vs. mass for a simulated population of red giants, coloured by metallicity. The large, labelled points correspond to observational results from red giants in open and globular clusters. Figure reproduced from Miglio et al. (2017).

allow the robust estimation of ages of a large number of field stars with grid-based modelling (e.g. Miglio et al., 2021).

3.3 The ages of stars

We saw in Chapter 2 that age information provides an essential constraint for models of the formation and evolution of the Milky Way. In this section we describe how the ages of stars may be estimated – they can never be directly measured – and some limitations of the models on which these estimations are based. The main reference for this section is the review of Soderblom (2010).

3.3.1 Estimating ages

There is only one star for which the age is known both precisely and accurately: the Sun. Its age – 4567 ± 1(stat) ± 5(sys)Myr (Chaussidon, 2007) – is obtained from measurements of radioisotopes in rocks in the Solar System and, unfortunately, this technique cannot be applied to any other star. Soderblom (2010) describes this as a 'fundamental' age estimate because all

the physical processes involved are well understood and all required observations are available.

The Sun's age is the only such fundamental estimate. All other techniques fall into one of four categories:

- 'Semi-fundamental' ages may be obtained when only a few assumptions about the underlying physics are required, and the resulting estimate is not overly sensitive to the details of the assumption made. Examples are nucleocosmochronometry – the study of the decay of uranium and thorium in stars via the weak lines visible in the spectra of metal-poor thick disc and halo stars – and kinematic dating – tracing the orbits of very young populations back to a single point of formation. Ages from these methods rely on challenging observations and are only available for specific types of stars so they are not, in general, useful for Galactic archaeology.

- Model-dependent ages are estimated by comparing observable properties of stars to evolutionary models and inferring the age from the best match. This relies on the quality of the model and the observational constraints available, as well as a good understanding of any systematic effects present. As we saw in the previous section, ages from asteroseismology are model-dependent, as are those obtained by fitting isochrones to the coeval populations in open or globular clusters.

- Empirical ages rely on relationships between observed properties of stars and ages obtained from another (usually model-dependent) source, which can be calibrated and applied to stars where no other age estimate is available. In general, the physics underlying the relationships is not fully understood, so the predictive power is limited. Gyrochronology – the relationship between stellar rotation rate and age – is one example.

- Statistical ages are similar, but based on broader trends such as the age-metallicity or age-velocity dispersion relations. They rely on large high-quality training samples which, again, introduces a model dependence. Modern advances in machine learning and Bayesian statistics are increasing the availability of these kinds of ages which, if reliable training data can be obtained, represent a significant future prospect for MW studies.

Of all these techniques, it is asteroseismology which opens the door to the quantity and quality of ages needed for Galactic archaeology, with precise constraints for the mass of low-mass RGs in the field. These long-lived, luminous stars are ideal tracers for every temporal and spatial domain of the MW. In addition to the direct use of such ages, they can be used as training data for modern catalogues of machine learning-based estimates (e.g. Mackereth et al., 2019a; Anders et al., 2023). This motivates the production of high-quality catalogues, combining asteroseismic targets with the information available from spectroscopy and astrometry, such as those presented in Chapter 4.

3.3.2 Limitations of stellar modes

Despite the many advantages of asteroseismic ages, they are still fundamentally model-dependent. A detailed discussion of stellar modelling is beyond the scope of this section, but here we mention some of the key challenges relevant to the estimation of age.

Guzik (2013) provide a list of many such challenges, ranging across four broad categories

- Model inputs: including the details of the star one wished to model and the databases of nuclear reaction rates and opacities required to compute the stellar evolution.
- Physical processes: for example, the description and strength of overshooting and mixing processes in the interior and the effect of (usually) neglecting stellar rotation and magnetic fields.
- Numerical techniques: ensuring the models run efficiently and accurately over the large dynamic range associated with processes inside stars.
- Testing and constraining: methods for confronting models with observational data for a wide variety of stars.

Lebreton, Goupil, and Montalbán (2014a) investigated the effect of some of these challenges on the MS lifetime of low-mass stars. A summary of these results is presented in Figure 3.4, where it is apparent that the helium mass fraction, Y, is amongst the most significant sources of

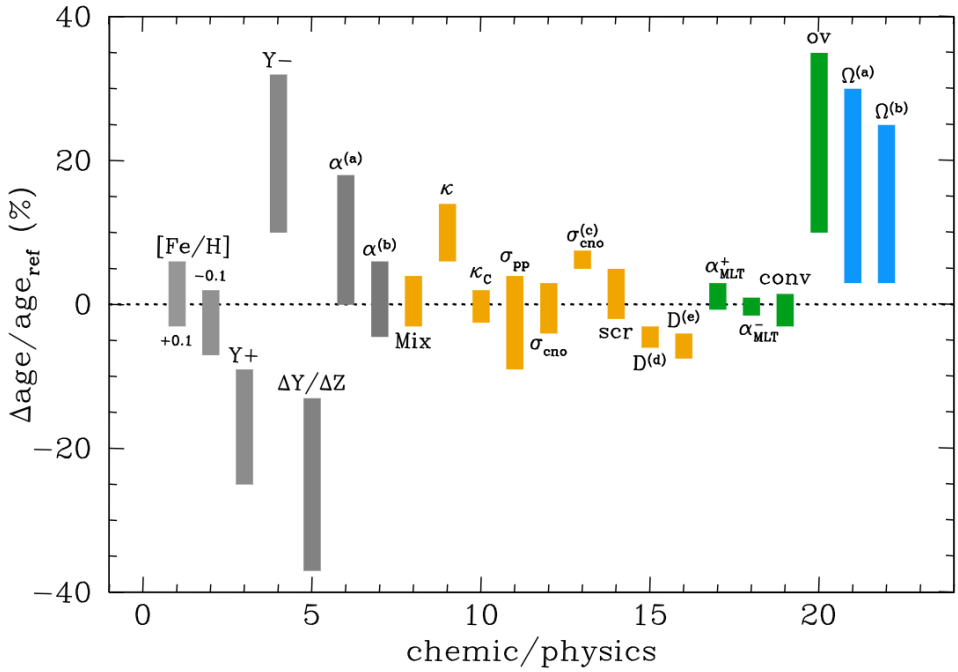


Figure 3.4: Percentage change in age at the end of the main sequence for models of low-mass stars due to changes in the model chemistry (grey), microphysics (yellow), macrophysics (green) and rotation (blue). Of particular interest to this discussion are the grey bars corresponding to a change in the initial helium abundance of ±0.03 ($Y+, Y-$) and an increase in $\Delta Y/\Delta Z$ by 3 with respect to the solar values. Figure reproduced from Lebreton, Goupil, and Montalbán (2014a), where a full definition of the other sources of uncertainty may be found.

uncertainty. The work presented in Chapter 6 is motivated by this issue, and a more detailed discussion may be found there.

Chapter 4

ASTEROSEISMIC AGES FOR 17000 STARS IN *KEPLER*, K2 AND TESS

This chapter presents a draft copy of the paper with the above title. I confirm that all writing is my own, with editorial contributions from A. Miglio. The work presented is my own, with the exception of the inferred stellar parameters from PARAM, which were provided by A. Miglio. Data are obtained from sources cited in the text. The K2 catalogue described in this chapter has been used in the work of Willett et al. (2023), presented in Chapter 5 of this thesis, Casali et al. (2023) and Grisoni et al. (in preparation).

4.1 Introduction and motivation

Long-duration, space-based photometry has provided precise asteroseismic constraints for tens of thousands of red giant (RG) stars. These constraints, when combined with measurements of effective temperature and metallicity, have paved the way for robust estimates of stellar parameters - including the mass. As a result of the tight correlation between initial stellar mass and main sequence (MS) lifetime (Miglio et al., 2017), we can now obtain age estimates for large samples of RG field stars. These reliable stellar masses and ages throw light on open questions of stellar structure and evolution as well as providing strong tests of stellar models (see e.g. Chaplin and Miglio, 2013; Aerts, 2021, for reviews). In addition, robust age estimates combined with spectroscopic and astrometric information are opening the door to understanding

the formation and evolution of the Milky Way (MW) through Galactic archaeology.

For meaningful studies of our Galaxy, we require samples which reach different Galactic domains, extending as far as possible both spatially and temporally. Low-mass RGs are excellent candidates for this work, being intrinsically luminous and long-lived, they can be seen over several kpc and probe more than 10 Gyr of MW history. Asteroseismic constraints have been used in this context in the Galactic disc (e.g. Anders et al., 2017b; Miglio et al., 2021; Willett et al., 2023) and the halo (e.g. Chaplin et al., 2020; Montalbán et al., 2021). Ages from asteroseismology have also been used to verify other age-estimation techniques, such as chemical clocks and gyrochronology of main sequence stars (e.g. Hall et al., 2021; Morel et al., 2021; Moya et al., 2022), and as training data for machine learning techniques (Mackereth et al., 2019a; Anders et al., 2023). The latter, in particular, represents a powerful way to vastly increase the sample of stars with age information available but relies on high-quality training data, and inferences made by extrapolating beyond the parameter space covered by the training set are unlikely to be reliable. For this reason, increasing the number and variety of stars with robust, homogeneously determined methods from more 'direct' methods, like asteroseismology, will support efforts to answer open questions about the MW and the stars in it on a large scale.

In this work, we present reliable ages for over 17000 stars, based on *Kepler*, K2 and TESS photometry, APOGEE and GALAH spectroscopy and *Gaia* astrometry. We show that asteroseismic results from the three photometry missions are complementary, with each representing a different compromise between precision and scale. We provide stellar and orbital parameters which are homogeneously determined across the samples, and consider in detail the sensitivity of our results to different choices of observational constraints. We also explore the applicability of each set of parameters to different problems, showing that the evolutionary phase of the star can affect the reliability of its age estimate, and provide quality flags to combat this effect.

We use our samples to explore several well-known planes in Galactic archaeology studies, showing trends with age in kinematic and chemical properties which we find to be robust against the uncertainties in the stellar parameters. Such trends may be used to constrain the dynamical and chemical evolution of the MW, and the K2 sample presented in this work has already been

utilised in this context to study the radial metallicity gradient of the thin disc (Willett et al., 2023), cerium enrichment (Casali et al., 2023) and young α-rich stars Grisoni et al. (in preparation). We also identify the stars in our sample with were likely born outside the MW and present some results on stellar evolution during the RG phase.

The rest of this paper is organised as follows: in Section 4.2 we present the observational data and describe the cross-matched samples, and we describe the inference of stellar and orbital parameters in Section 4.3. Section 4.4 presents some simple applications of our results, in both Galactic archaeology and stellar evolution. A brief summary is provided in Section 4.5.

4.2 Observational constraints

The catalogues compiled in this work are based upon asteroseismic observations from the *Kepler* (Borucki et al., 2010; Gilliland et al., 2010), K2 (Howell et al., 2014) and TESS (Ricker et al., 2015) missions. These are combined with astrometric parameters from *Gaia* DR3 (Gaia Collaboration et al., 2016, 2023c) and spectroscopically derived quantities from APOGEE DR17 (Majewski et al., 2017; Abdurro'uf et al., 2022) and GALAH DR3 (De Silva et al., 2015; Buder et al., 2021). In Sections 4.2.1 - 4.2.3 we introduce the observations, required parameters and quality flags and cross-match procedure, and describe the final samples in Section 4.2.4.

4.2.1 Asteroseismic constraints

In this work we make use of the global asteroseismic parameters $\nu_{\rm max}$, the frequency of maximum oscillation power, and $\Delta\nu$, the average large frequency separation. These parameters are related to the surface gravity and mean stellar density, respectively, so can be used to infer the stellar mass and radius (see Chaplin and Miglio, 2013). In the following sections, we outline some relevant details of each mission and how $\nu_{\rm max}$ and $\Delta\nu$ are obtained.

Kepler

The NASA *Kepler* mission provided 4 years of observations from 2009 for a single 105 $\deg^2$ field of view. Our sample is based on the catalogue of (Yu et al., 2018) which contains more than 16,000 red giants. These stars were selected from six previously published catalogues, but the lightcurves were reanalysed to produce a set of homogeneously determined $\nu_{\rm max}$ and $\Delta\nu$ values. To this catalogue, we add the 2MASS ID and magnitudes available in the *Kepler* Input Catalogue (KIC) (Brown et al., 2011).

K2

Following the failure of *Kepler*'s second reaction wheel in 2013 the mission was repurposed as K2, which went on to observe 20 campaigns around the ecliptic plane, each of 80 day. Here we use lightcurves produced by the EVEREST pipeline (Luger et al., 2018), analysed with two independent methods. The pipeline of Elsworth et al. (2020) (hereafter BHM), including the use of $\nu_{\rm max}$ determined by the deep learning method of Hon, Stello, and Yu (2018) and Hon, Stello, and Zinn (2018) as a soft prior, and then applies several layers of weak tests to exclude false results without removing real, but unusual, stars. Mosser and Appourchaux (2009) and Mosser et al. (2010) provide an alternative pipeline (hereafter COR) and, in general, the results of these two approaches agree well (see Appendix A.1). In the interest of clarity, the results presented here focus on the BHM pipeline, as Mackereth et al. (2021) found that it produces fewer false positive detections and the definition of $\Delta\nu$ is more similar to that used in our models. We add the 2MASS ID and magnitudes from the Ecliptic Plane Input Catalogue (EPIC) (Huber et al., 2016), removing cases where a single 2MASS ID is mapped to multiple K2 IDs. Because some targes were observed in multiple K2 campaigns, we also add a flag to identify the observation to be retained in our analysis, to prevent double counting when utilising our samples. We retain targets with a higher SNR on $\nu_{\rm max}$, meaning that the flag may be different for the BHM and COR pipelines.

TESS

TESS was launched in 2018 and will survey the whole sky with repeated 27 day observations of 96×24 deg sectors. In this work, we focus on the results from the southern continuous viewing zone (SCVZ), where these sectors overlap, from the first year of observations. Mackereth et al. (2021) extracted lightcurves from the full frame images, which were analysed by three asteroseismic pipelines. Here we focus on the results from the BHM pipeline.

Cuts in asteroseismic parameters

We apply two cuts in the asteroseismic observables at this stage. First, we remove targets with $\nu_{\rm max}$ more than three standard deviations below 20 μHz, as asteroseismic inferences have not been robustly tested in this domain. Second, we remove targets where $\nu_{\rm max}$ may be affected by the Nyquist frequency of the observations. Such cases are identified by comparing $\nu_{\rm max}$ and $\Delta\nu$ and removing targets where the tight correlation between these quantities is broken – i.e. where $\Delta\nu$ is too large for the measured $\nu_{\rm max}$. In practice, this means removing targets with $\Delta\nu \geq 21$ μHz (see Appendix A.2).

4.2.2 Astrometric constraints

We obtain the required astrometric constraints from *Gaia* DR3, which is based on 34 months of observations. We use five-parameter solutions $[\alpha, \delta, \varpi, \mu_\alpha, \mu_\delta]$ and, following L. Lindegren (2018), remove targets with `ruwe` > 1.4 or which are marked as binaries by the `non_single_star` flag. We also consider different corrections to the known zero-point offset in *Gaia* parallaxes (Lindegren et al., 2021). Khan et al. (2023) compared the *Gaia* parallaxes with an independent estimate based on asteroseismology and found that the correction of Lindegren et al. (2021) works well for the *Kepler* field but significantly underestimates the zero-point offset in K2 (averaged over multiple campaigns) and underestimates it in the TESS SCVZ. In this work we apply the Lindegren et al. (2021) correction to the *Kepler* and TESS sample, and use a constant correction of 17 μas for K2 (guided by the average offset found in quasars in DR3

(Lindegren et al., 2021), and the results of Khan et al. 2023). We test the sensitivity of our results to the zero-point correction in Section 4.3.1.

For the *Kepler* and K2 samples, we obtain the *Gaia* DR3 `source_id` via crossmatch to the `TMASS_PSC_XSC_BEST_NEIGHBOUR` table, removing targets with more than one neighbour or two mates. The catalogue of Mackereth et al. (2021) already contains the DR2 `source_id` so we use the `DR2_NEIGHBOURHOOD` table instead. We retained sources with smaller angular separation in cases where a single DR2 `source_id` matches multiple DR3 results. Finally, for all samples, we obtain data from the DR3 `gaia_source` table, by matching on the `source_id`.

4.2.3 Spectroscopic constraints

The main spectroscopically derived parameters required in this work are the radial velocity (RV), effective temperature and chemical abundances – specifically the metallicity[1] and average α-element abundance.

APOGEE

We cross-match each asteroseismic sample with APOGEE DR17, which uses high-resolution ($R \sim 22,500$) infra-red (IR) spectroscopy to obtain stellar parameters and abundances from 20 elements, covering a range of nucleosynthesis channels. Chemical abundances and stellar parameters are obtained from the APOGEE Stellar Parameters and Chemical Abundances Pipeline (ASPCAP) (García Pérez et al., 2016, and see Holtzman et al. (in preparation) for a full description of this pipeline as applied to APOGEE DR17). We remove targets with `STAR_BAD` or `STAR_WARN` set in `ASPCAPFLAG`, and those with any `RV_FLAG` set. In addition, when using any of the individual abundances we remove targets with the relevant `ELEM_FLAG` set. The uncertainties reported by ASPCAP reflect only the internal errors, so we enforce minimum values of $\sigma_{[\mathrm{Fe/H}]} = 0.05\,\mathrm{dex}$ and $\sigma_{T_{\mathrm{eff}}} = 50\,\mathrm{K}$ during the inference of stellar parameters (see Section 4.3.1).

[1]Throughout this work we use iron abundance as a tracer for metallicity: $[\mathrm{Fe/H}] = \log_{10}(N_{\mathrm{Fe}}/N_{\mathrm{H}})_* - \log_{10}(N_{\mathrm{Fe}}/N_{\mathrm{H}})_\odot$, where N_{Fe} and N_{H} are the numbers of iron and hydrogen nuclei per unit volume of the stellar photosphere, respectively.

Before crossmatching to APOGEE DR17, we remove duplicated observations of targets observed in multiple fields, retaining those with higher [Fe/H] SNR. We then crossmatched based on the 2MASS ID (for TESS this was first obtained from `TMASS_PSC_XSC_BEST_NEIGHBOUR` table)

GALAH

We also cross-match the K2 samples to GALAH DR3 on the 2MASS ID, another high-resolution ($R \sim 28,000$) spectroscopic survey across the visible and IR. GALAH provides abundances for up to 30 elements per star, and we use the recommended quality flags, requiring that `snr_c3_iraf == 0`, `flap_sp == 0` and `flag_fe_h == 0` for all targets, and `flag_X_fe == 0` for other abundances `X`.

4.2.4 Samples

In total, our samples contain observations of over 17000 stars. Figure 4.1 shows their positions in Galactic spherical coordinates, with the full sample shown in black and the stars with reliable ages (see Section 4.3.1) overlaid in colours corresponding to the survey. In Figure 4.2 we show positions in Galactocentric Cartesian (top panel) and cylindrical coordinates (bottom panel). Finally, the samples are shown in APOGEE chemical abundance space using the well-studied [α/M] vs. [Fe/H] plane[2] in Figure 4.3. For K2 we also show the GALAH [α/Fe] vs. [Fe/H] plane, where the much greater scatter (expected due to the larger observational uncertainties) almost obscures the separation of the high- and low-α sequences.

4.3 Inferring stellar and orbital parameters

From the observations described above, we infer stellar (Section 4.3.1) and orbital (Section 4.3.2) parameters for the stars in each sample. This section describes the assumptions made and, specifically in the case of the stellar masses and ages, the tests performed to ensure the

[2]We use [α/M] as a proxy for [α/Fe] as the differences between them (defining [α/Fe] as an average of [X/Fe] for O, Mg, Si, S, and Ca) are negligible.

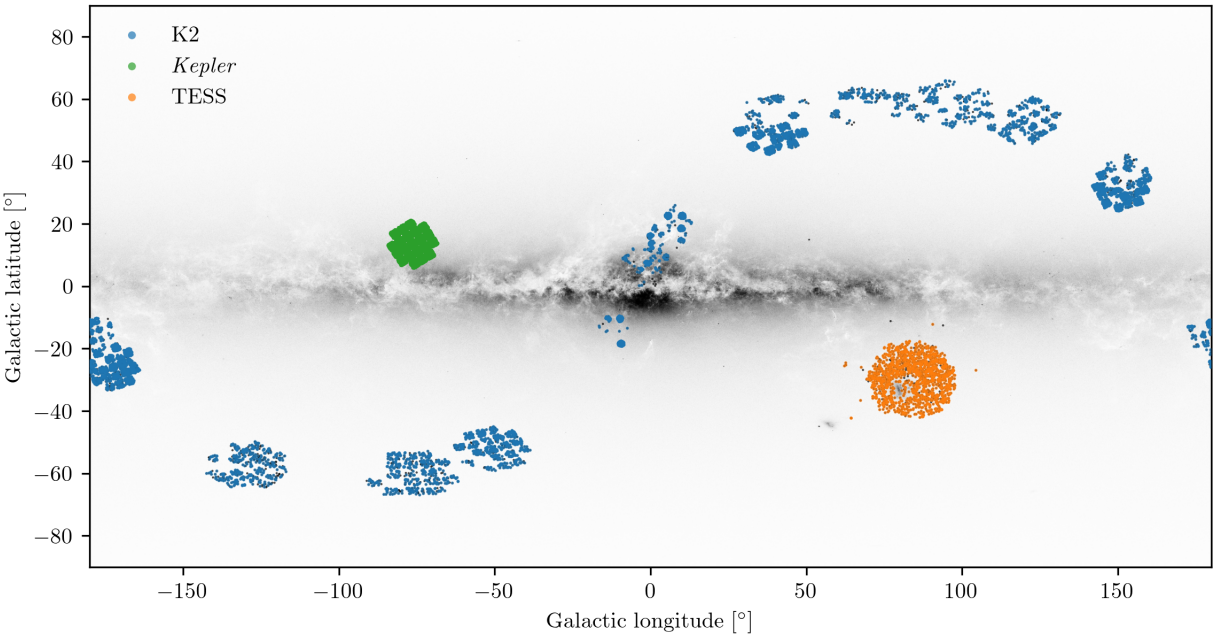


Figure 4.1: Location of stars in our samples in Galactic coordinates. Green, blue and orange points show stars with reliable ages from *Kepler*, K2 and TESS, respectively. Stars with reliable data but ages which do not pass our tests are shown in the background (black points). This figure was generated using `mwplot`[a], and the image in the background is modified from an image by ESA/Gaia/DPAC.

[a] https://milkyway-plot.readthedocs.io/en/latest/index.html

most robust results are presented. In most cases, the figures shown in this section focus on the K2-APOGEE sample, both for clarity and because the *Kepler* and TESS samples are based on those presented elsewhere. Additional figures corresponding to these samples may be found in the Appendix, where relevant.

4.3.1 Stellar parameters

Stellar masses, M_*, radii, R_*, ages, τ and distances, D are inferred using the PARAM code (da Silva et al., 2006; Rodrigues et al., 2014, 2017), which performs a Bayesian comparison between observations and a model grid. We follow the method presented in Miglio et al. (2021) using the law of Reimers (1975), with efficiency parameter $\eta = 0.2$ to estimate the mass loss at the tip of the RGB (Miglio et al., 2012). We also use their reference grid (G2), which was computed in MESA (Paxton et al., 2011, 2013, 2015, 2018, 2019; Jermyn et al., 2023) including microscopic diffusion and assuming a linear relation between the stellar helium and metal mass fraction. PARAM returns full posterior information, and we report the median and 16$^{\text{th}}$ and

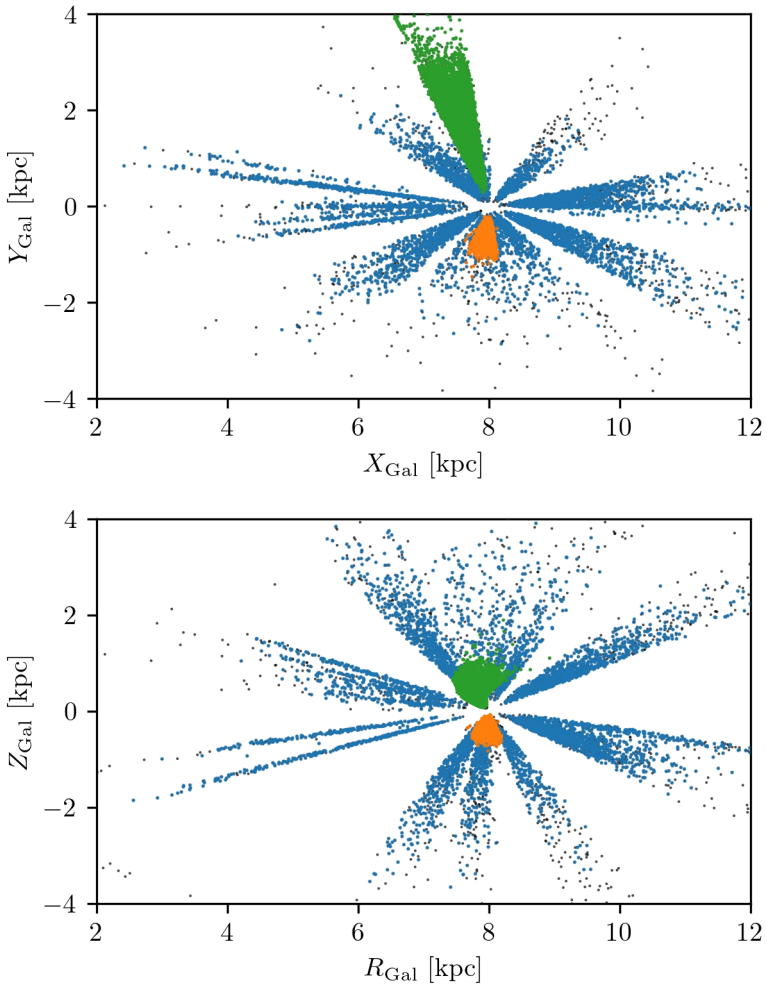


Figure 4.2: Location of stars in our sample in left-handed Galactocentric coordinates (top) and Galactocentric cylindrical coordinates (bottom). The colours are the same as Figure 4.1.

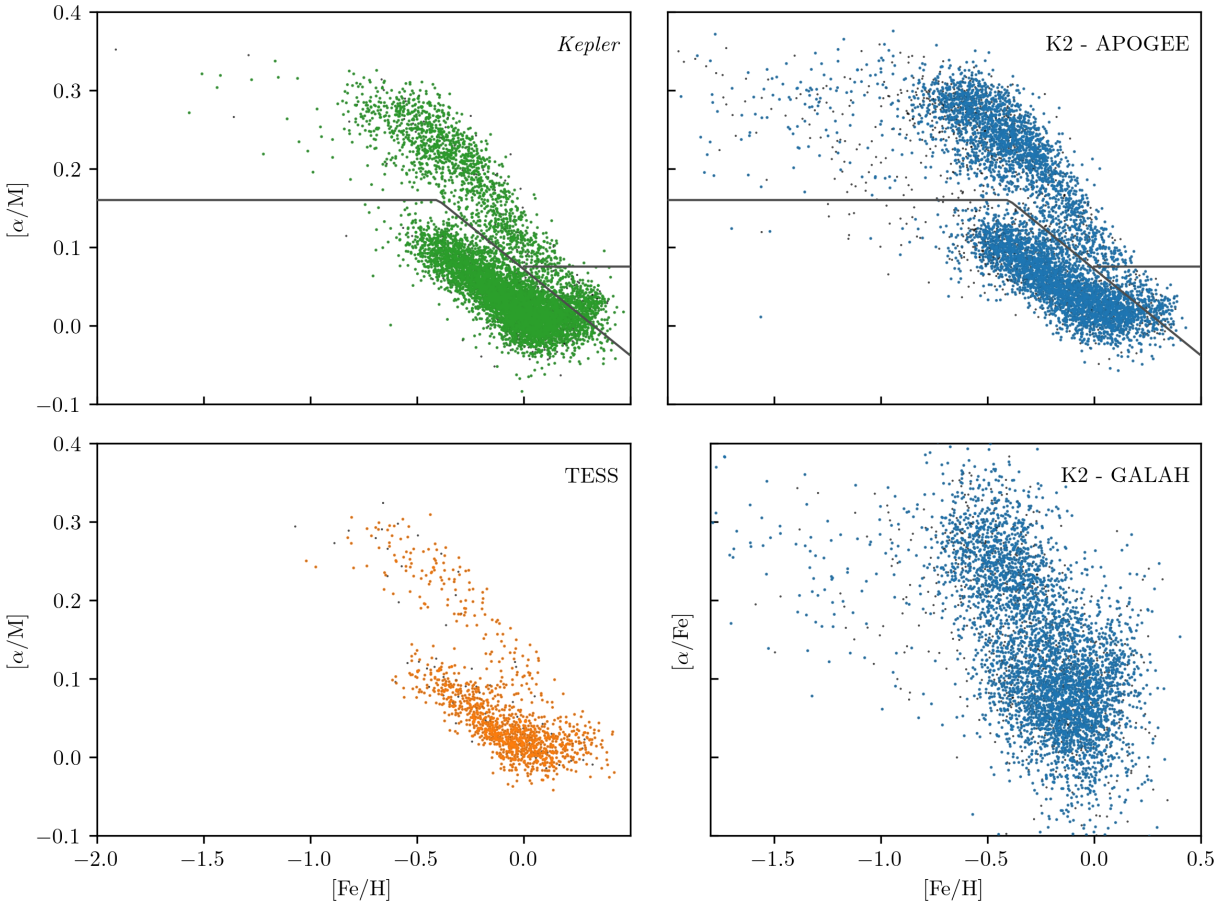


Figure 4.3: Average α element abundance [α/M] for APOGEE samples or [α/Fe] for the GALAH sample vs. [Fe/H]. The grey lines show the division between high-, low- and intermediate α populations used in Section 4.4.2.

84$^{\text{th}}$ percentiles here. Observational constraints are provided by $\nu_{\max}$, $T_{\rm eff}$, [Fe/H] and either $\Delta\nu$ or the luminosity, L, based on the (zero-point corrected) *Gaia* parallax. Finally, minimum uncertainties of $\sigma_{\rm [Fe/H]} = 0.05$ dex and $\sigma_{T_{\rm eff}} = 50$ K are imposed in the APOGEE observations, as the reported uncertainties reflect only the pipeline's internal errors. In the case of $T_{\rm eff}$, this has the additional benefit of reducing the impact of model uncertainties concerning the outer boundary conditions and near-surface convection.

For *Kepler* and K2 the luminosities were computed using extinctions from the `Bayestar19` dustmap (Green et al., 2014; Green et al., 2019) implemented in the `dustmaps` python package (Green, 2018), from which we obtain quality flags for the convergence of the fit in each pixel and the reliability of the map at the queried distance. The TESS-SCVZ lies outside the range of `Bayestar19`, so we use the `combined19` dustmap (Drimmel, Cabrera-Lavers, and López-Corredoira, 2003; Marshall et al., 2006; Green et al., 2019) implemented in `mwdust` (Bovy et al., 2016) instead. In both cases, we require that $\sigma_{\varpi}/\varpi > 5$ when using the luminosities or quantities derived from the luminosity, and few stars are also removed by the range of validity of the bolometric correction computation, performed using the code of Casagrande and VandenBerg (2014).

Using $\Delta\nu$ or L as an observational constraint

In Figure 4.4 we show the stellar mass, M_*, and radius, R_*, obtained from scaling relations based on $T_{\rm eff}$, [Fe/H], $\nu_{\max}$ and either $\Delta\nu$ or L. In the $\Delta\nu$ case (top panel) we see a strong feature with $M_* > 1.5$ and $R_* > 15$, which is not expected in descriptions of stellar evolution and is not present in the case where $\Delta\nu$ is replaced by L (bottom panel). We highlight stars which are common between the samples[3] where $|M_{*,\Delta\nu} - M_{*,L}| > 0.5 M_{*,L}$ (red points). In the $\Delta\nu$ results, this highlights the high-M_* - high-R_* feature well, and from the L results we see that these stars are members of the red clump (RC). This is an expected consequence of unreliable $\Delta\nu$ determinations for core helium burning (CHeB) stars with short-duration asteroseismic observations (Tailo et al., 2022). In Appendix A.3 we show that the situation is less significant

[3]There are some stars present in the $\Delta\nu$ sample which are removed when using L as the observational constraint due to the quality flags on the extinction and parallax, described in Section 4.3.1, above.

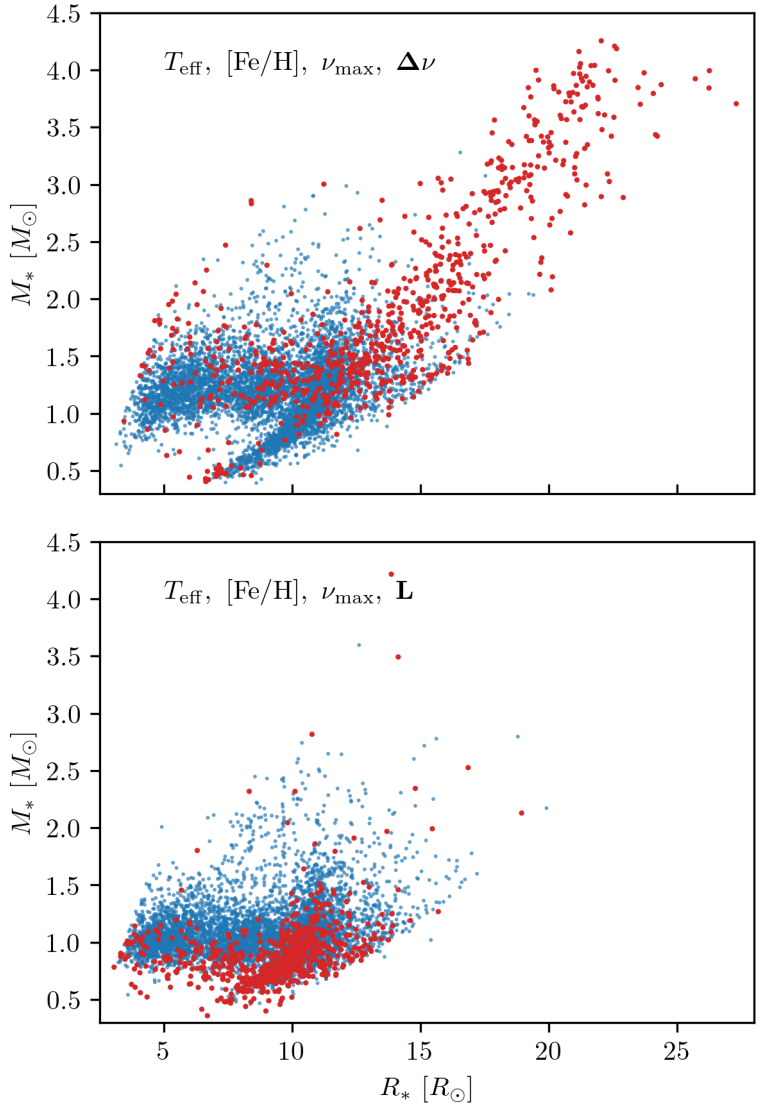


Figure 4.4: Stellar mass vs. radius from PARAM where $\Delta\nu$ (top) or L (bottom) are used as an observational constraint. Stars flagged for unreliable $\Delta\nu$ are shown in red (see Section 4.3.1 for a description of the flag).

when using the *Kepler* and TESS samples, where the observation durations are much longer than the K2 campaigns. We flag and remove stars with a high mass difference in samples where $\Delta\nu$ is an observational constraint, as their unreliably high masses will lead to erroneous, young ages.

In the remaining sample, we find that ages obtained from PARAM and $\Delta\nu$ are less precise than those from L, thanks to the exquisite precision of the *Gaia* DR3 data (Figure 4.5). However, using L as a constraint introduces other sensitivities in the results which are discussed further, below.

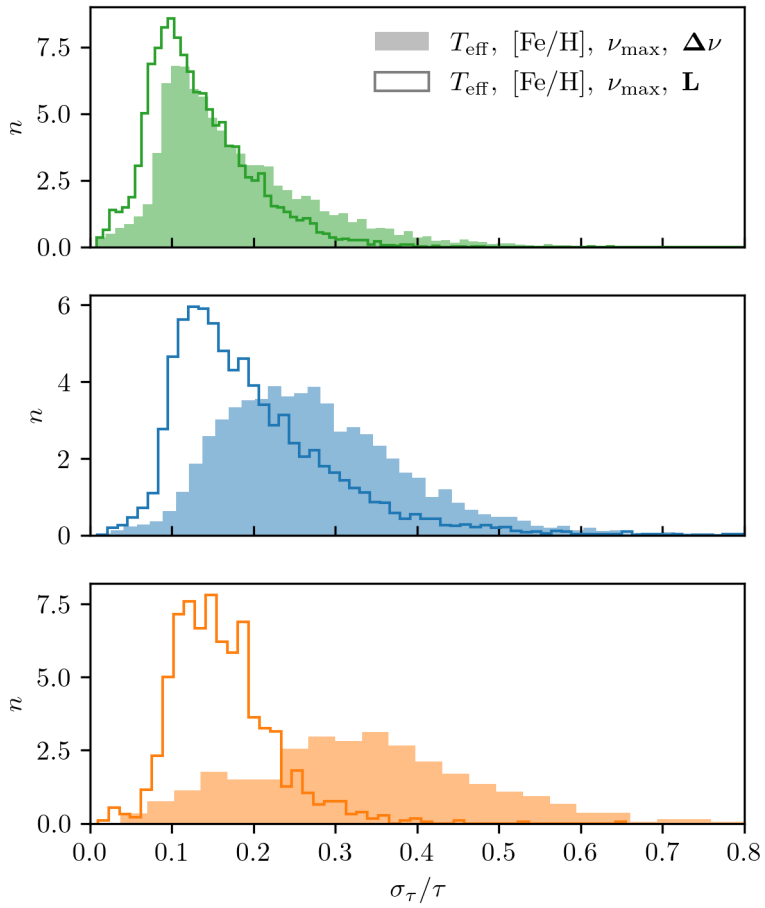


Figure 4.5: Distribution of the fractional uncertainty on age from PARAM where $\Delta\nu$ (filled) or L (open) are used as an observational constraint for *Kepler* (top), K2 (middle) and TESS (bottom). The area under each histogram integrates to one.

Table 4.1 shows a summary of the samples from different sets of observational constraints. The number of stars with reliable data is higher in the $\Delta\nu$ case because we do not require the additional checks on parallax uncertainty or dustmap flags. However, the number of stars with reliable ages in this case is smaller due to the removal of those with unreliable $\Delta\nu$ values.

Table 4.1: Summary of reliable targets in datasets with different observational constraints. See text for descriptions of the criteria for reliable data and age, τ.

Photometry source	Asteroseismology pipeline	Spectroscopy source	Observational constraint	N_* with reliable data	N_* with reliable τ
Kepler	Yu 2018	APOGEE	$\Delta\nu$	8199	7874
			L_{Ldg}	8105	7953
K2	BHM	APOGEE	$\Delta\nu$	7390	6095
			L_{17}	6929	6896
			L_{Ldg}	7004	6968
		GALAH	$\Delta\nu$	5266	4486
			L_{17}	5056	5038
	COR	APOGEE	$\Delta\nu$	7601	5751
			L_{17}	6883	6492
TESS	BHM	APOGEE	$\Delta\nu$	1398	1313
			L_{Ldg}	1398	1379

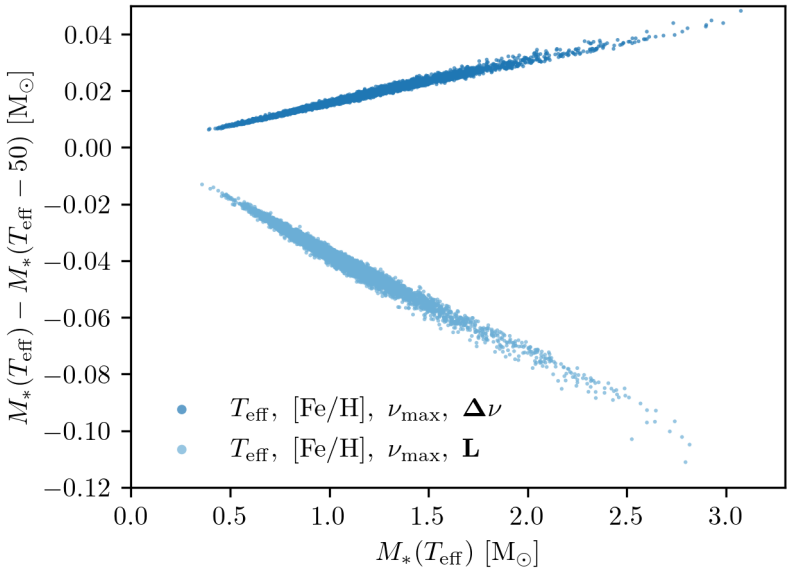


Figure 4.6: Difference between stellar masses obtained from scaling relations when $T_{\rm eff}$ is shifted by 50 K vs. original mass. The cases where $\Delta\nu$ (dark) or L (light) are used as an observational constraint are shown.

Ages from L: sensitivity to $T_{\rm eff}$ and ϖ-zeropoint

The mass (and therefore the age) from L is much more sensitive to $T_{\rm eff}$, than when derived from $\Delta\nu$. Given the known offsets (e.g. Hegedűs et al., 2023) in the temperature scales between spectroscopic surveys, this sensitivity is a limitation to the ages constrained by L. The scale of this effect is shown in Figure 4.6, where we plot the mass difference from the scaling relations using $\Delta\nu$ (dark blue) or L (light blue) caused by decreasing $T_{\rm eff}$ by 50 K. For a 1 M$_\odot$ star, the mass difference when using L is $\approx 5\%$, corresponding to an age difference of more than 1 Gyr.

Using the luminosity also introduces a sensitivity to the zero-point correction to the *Gaia* parallax. This is a further limitation and results in, effectively, data release-dependent ages. The situation is more complicated for K2, as Khan et al. (2023) found that the correction differs between K2 campaigns. In Figure 4.7 we show the difference in mass, again from the scaling relation, using the luminosity derived from $\varpi + 17\,\mu$as, L_{17}, or with ϖ corrected according to the scheme of Lindegren et al. (2021), $L_{\rm Ldg}$. Stars are coloured according to the logarithmic distance and sorted with the closest stars on top. We see that more distant stars are more sensitive to the zero-point correction, with a mass difference of up to 20% in some cases.

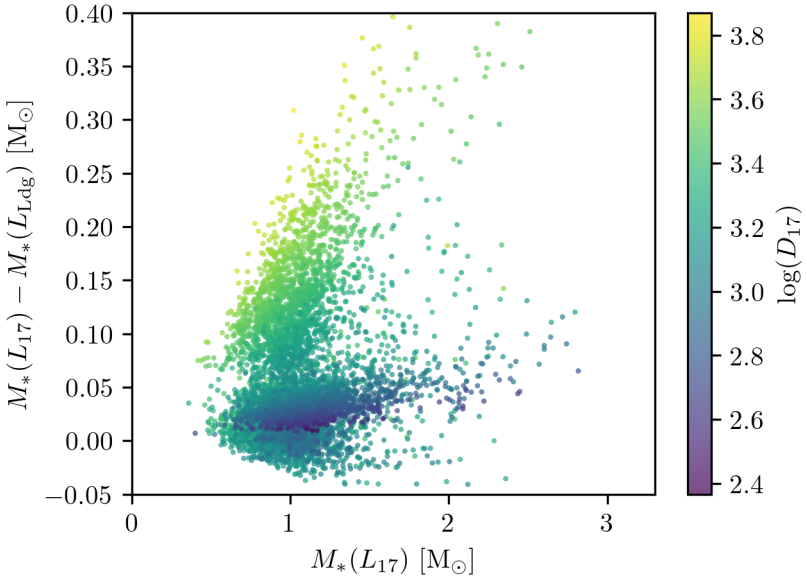


Figure 4.7: Difference between stellar masses obtained from scaling relations using luminosity when the correction to the *Gaia* parallax zero-point offset is changed from a constant 17 μas (L_{17}) to the correction proposed by Lindegren et al. (2021) ($L_{\rm Ldg}$). The difference is shown as a function of the L_{17} mass and coloured according to the distance from the inverse of the *Gaia* parallax, with a constant zero-point correction of 17 μas.

PARAM output: sensitivity to priors

Regardless of the choice of observational constraint, when using the stellar parameters output by PARAM, it is important to understand any effects which may be introduced by the model grid or choice of priors. When using the $[T_{\rm eff}, [{\rm Fe/H}], \nu_{\rm max}, L]$ as observational constraints, the stellar mass from PARAM is expected to be the same as that from the scaling relation, and any differences are a result of the priors on the mass and age enforced when we run the code. The bottom panel of Figure 4.8 shows a comparison between the two where, at $M_{\rm scaling}$ below around 0.7M$_\odot$, we see a deviation caused by the upper limit of the age prior used. We flag stars within 1σ of this limit (20 Gyr), where σ is the median fractional uncertainty of the whole population multiplied by the stellar age (purple points). We choose this estimate as the uncertainties reported on individual stars with posteriors affected by the prior will be artificially small, and this appears to select the affected stars well. We apply the same process to the results constrained by $[T_{\rm eff}, [{\rm Fe/H}], \nu_{\rm max}, \Delta\nu]$, though the affected stars are not easily identifiable in a comparison of the masses (top panel) as PARAM performs a more complex analysis than the

scaling relation in this case. In both cases, the flagged stars are potentially unreliable, and we ensure that the results presented in the rest of this paper based on PARAM output are not affected by removing them.

The majority of affected stars are in the CHeB phase, as they have experienced significant mass loss at the tip of the RGB (e.g. Miglio et al., 2021; Tailo et al., 2021), resulting in very low masses from the scaling relations. These masses cannot be reconciled with ages below the age of the Universe under our current prescription for mass loss in PARAM (see Section 4.3.1 and Matteuzzi et al. 2023). The top panel of Figure 4.9 shows the HRD for the sample with stellar parameters based on $\Delta\nu$, using the asteroseismic luminosity, $L_{\rm seis}$. The bottom panel shows stars with parameters from L_{17}. The stars flagged as having unreliable $\Delta\nu$ values are shown in red and those with parameters possibly affected by the age prior are shown in purple. There are fewer prior-affected stars shown in the $\Delta\nu$ results as there is a significant overlap with those stars already removed by the $\Delta\nu$ flag. This means that the results based on $\Delta\nu$ are less sensitive to the prior, but have fewer CHeB stars overall.

4.3.2 Orbital parameters

Orbital parameters are computed using the fast orbit estimation method of Mackereth and Bovy (2018), implemented in `galpy` (Bovy, 2015) and a left-handed Galactocentric coordinate frame. To constrain the parameters and their uncertainties, we draw samples from the covariance matrix formed by $[\alpha, \delta, \mu_\alpha, \mu_\delta]$ (from *Gaia*), RV (from APOGEE or GALAH) and either D from PARAM, when using $\Delta\nu$ to constrain the stellar parameters, or *Gaia* ϖ, when using L. In the latter case, we invert the sampled ϖ to obtain an estimate for D. We assume that the spectroscopic RV and D from PARAM are uncorrelated with each other and the other parameters, but in all other cases we utilise the correlation coefficients included in the *Gaia* catalogue.

We estimate orbital parameters including the orbital energy, E, angular momentum, L_Z, guiding radius, $R_{\rm g}$ maximum vertical excursion $Z_{\rm max}$ and eccentricity, e, and report the median and $16^{\rm th}$ and $84^{\rm th}$ percentiles. We assume that the MW is well represented by the simple Milky Way potential `MWPotential2014` (Bovy, 2015), and that the radial position of the Sun

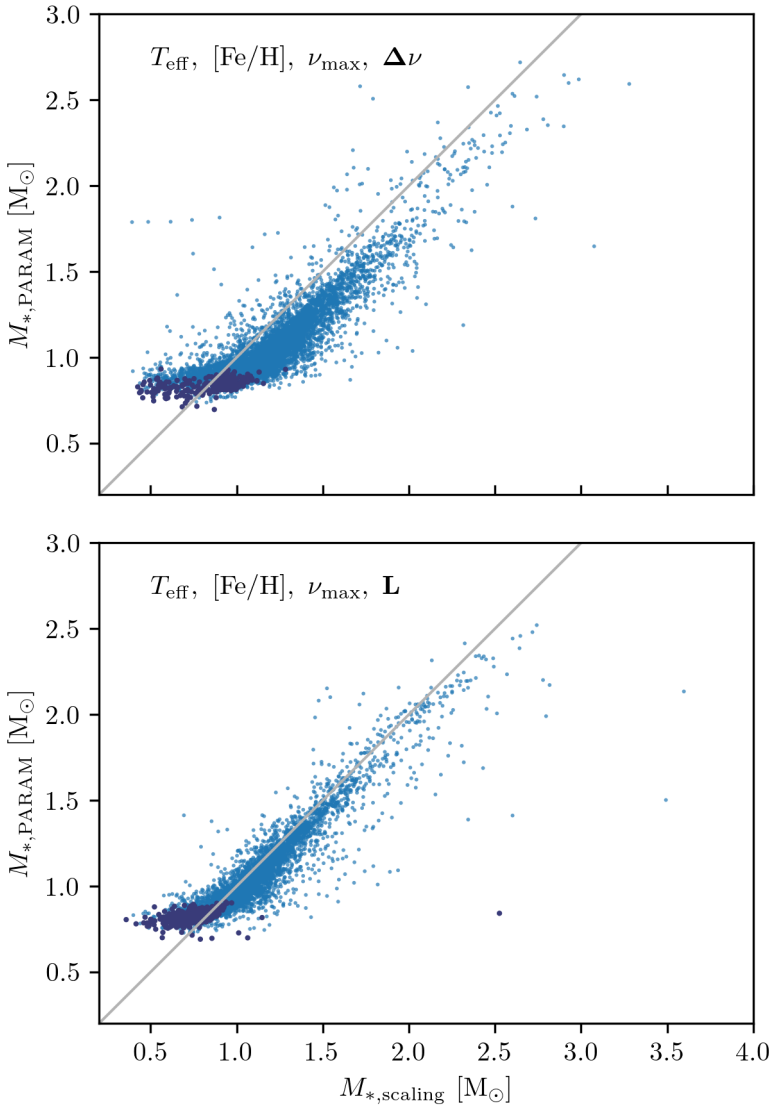


Figure 4.8: Stellar mass obtained from PARAM vs. that from scaling relations where $\Delta\nu$ (top) or L bottom are used as an observational constraint. Stars with masses that may be dominated by the priors imposed in PARAM are shown in purple (see Section 4.3.1 for a description of the flag).

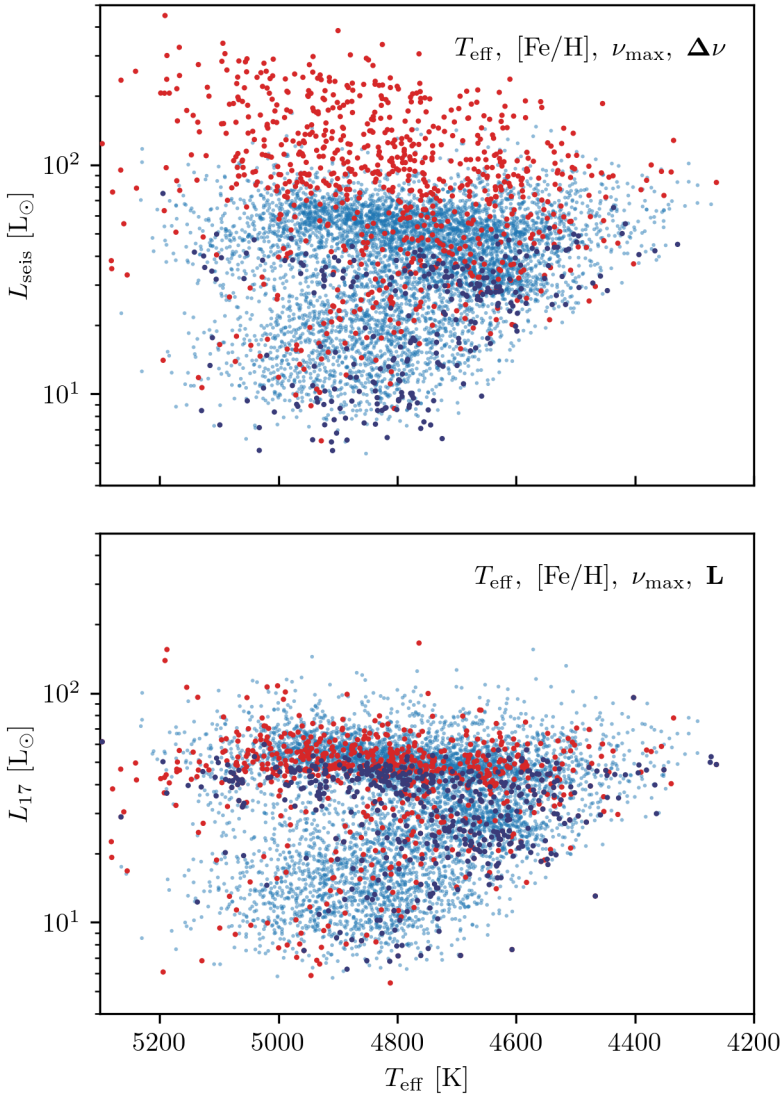


Figure 4.9: HRD showing stars flagged for unreliable $\Delta\nu$ (red) and with masses that may be dominated by the priors imposed in PARAM are shown (purple; see Section 4.3.1 for a description of the flags). The full sample is shown in the background (blue).

is $R_{\mathrm{Gal},\odot} = 8.0\,\mathrm{kpc}$, where the circular velocity is $v_{\mathrm{circ}} = 220\,\mathrm{km\,s^{-1}}$ (Bovy et al., 2012). The additional solar motion is given by $[U, V, W]_{\odot} = [-11.1, 12.24, 7.25]\mathrm{km\,s^{-1}}$ (Schönrich, Binney, and Dehnen, 2010), and the Sun's vertical offset from the Galactic plane is $Z_{\mathrm{Gal},\odot} = 20.8\,\mathrm{pc}$ (Bennett and Bovy, 2019).

4.4 Applications

In this section, we demonstrate some simple applications of the samples presented above. In all cases we show only stars with reliable ages and, unless otherwise stated, use the stellar parameters from PARAM, constrained by $[T_{\mathrm{eff}}, [\mathrm{Fe/H}], \nu_{\mathrm{max}}, \Delta\nu]$ and K2 results from the BHM-APOGEE sample.

4.4.1 Kinematic properties

First, in Figures 4.10 and 4.11 we show two commonly used kinematic planes: the Toomre diagram (velocities in Galactocentric Cartesian coordinates) and orbital energy vs. angular momentum. In both planes, we see that the TESS sample is confined to the thin disc, *Kepler* extends into the thick disc, and K2 provides some coverage of the halo (see Figure 4.10, where the grey line indicates the approximate separation of disc and halo stars). This is consistent with the chemical picture from Figure 4.3, as the low- and high-α and low-metallicity ([Fe/H] $\lessapprox -0.7$) populations map well, in broad terms, to the thin and thick discs and halo, respectively. Figure 4.11 shows that the majority of stars on retrograde orbits which are present in our samples are found in K2, which also provides better coverage of the inner Galaxy (low-energy orbits).

In many applications, it is useful to investigate spatial trends in the Galaxy and in these cases K2 is especially valuable (see Figure 4.2 for a comparison of the samples' spatial distributions). However, using the present-day positions of stars does not provide the most representative view of the processes at work in the MW, particularly for older stars, as radial migration and vertical heating move stars away from their birth positions (e.g. Schönrich and Binney, 2009a; Minchev, Chiappini, and Martig, 2013, 2014; Hayden et al., 2015; Frankel et al., 2018, 2020; Vincenzo

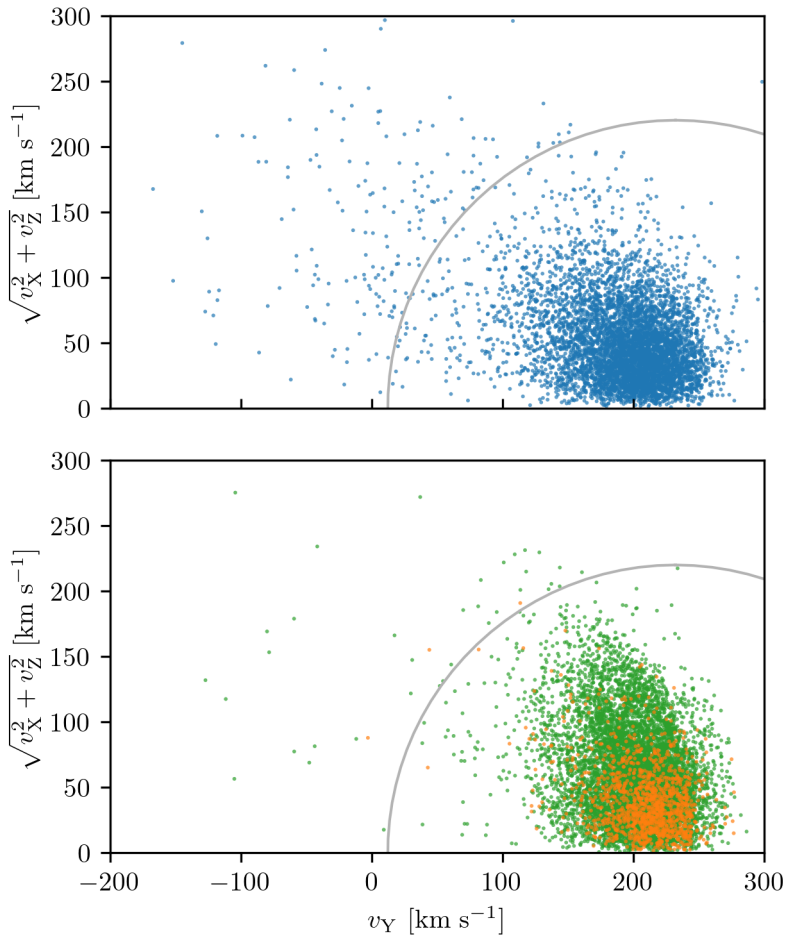


Figure 4.10: Toomre diagram for stars with reliable ages in the K2 (top), Kepler and TESS (bottom) samples. The colours are the same as Figure 4.1.

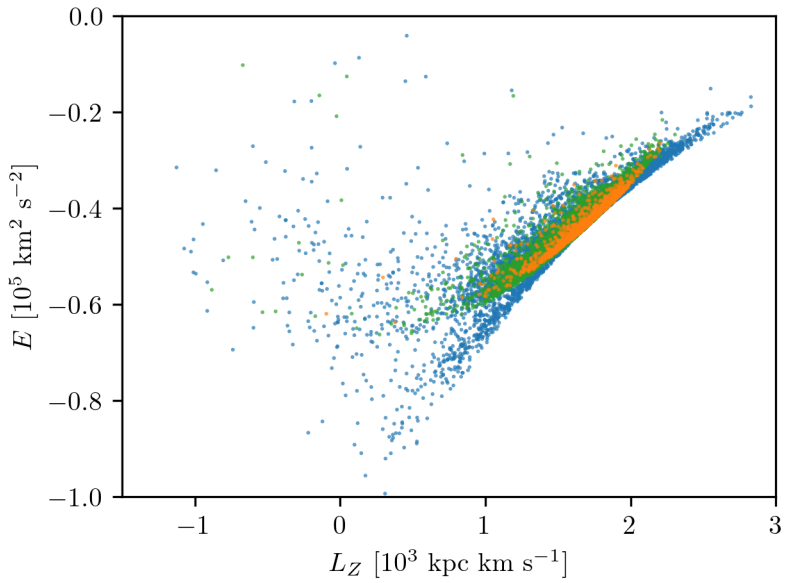


Figure 4.11: Energy vs. Z-component of angular momentum for stars with reliable ages. The colours are the same as Figure 4.1.

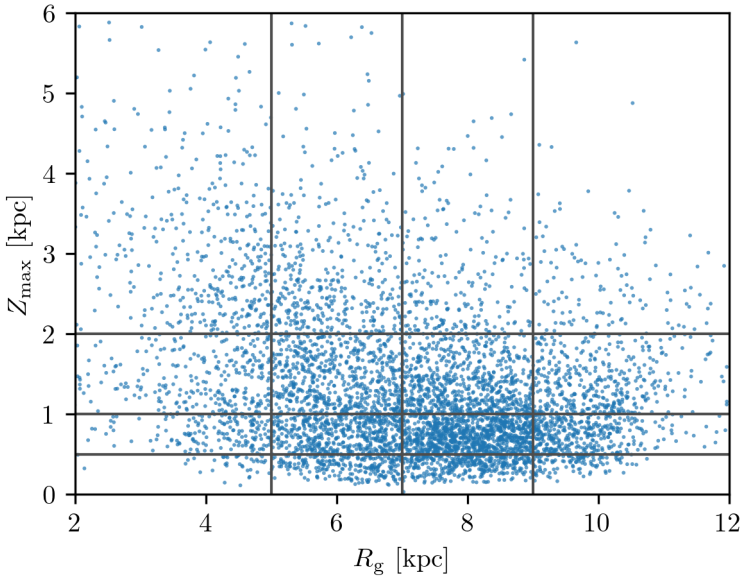


Figure 4.12: Maximum vertical excursion vs. guiding radius for K2 stars with reliable ages.

and Kobayashi, 2020; Miglio et al., 2021). This means that stars passing close to the Sun and within our observable limits today were not necessarily born nearby, and nor do they necessarily have orbits similar to the Sun. Figure 4.12 shows an alternative choice of coordinates, defined below.

The term radial migration is used to refer to two processes: blurring, the observational effect of orbital eccentricity, which results in the star being observed at different $R_{\rm Gal}$, and churning, where interactions with non-axisymmetric features in the Galactic disc result in a change of the orbital radius. Both processes are more important in older populations, as orbital eccentricity tends to increase with time due to radial heating, and the interactions which lead to churning can occur at any time so older stars are more likely to have migrated. The guiding radius $R_{\rm g}$, is the radius of a circular orbit with the same L_Z as the true orbit and therefore it mitigates against the effect of blurring, providing a better estimate of the 'average' radial position of the star. This has the effect of appearing to spread our sample further in radius, as many stars observed around $R_{\rm Gal} \approx 8$ kpc spend the majority of their orbit closer to or further from the Galactic centre. This is particularly noticeable when comparing the number of stars with $R_{\rm Gal}$ and $R_{\rm g} \approx 6$ kpc in Figures 4.2 and 4.12, where we see many more stars in the latter case, indicating that they are on more eccentric orbits and nearer to apocentre than pericentre.

In the vertical coordinate, it is useful to know how far the orbit extends from the Galactic plane, as this is the main differentiating factor between orbits which are more thin or thick disc-like. The maximum vertical extent of the stellar orbit, $Z_{\rm max}$, is also expected to increase with time as stars' orbits are heated by adiabatic (due to the secular evolution of the Galactic disc) or non-adiabatic (due to interactions with other galaxies or giant molecular clouds) processes (Ting and Rix, 2019). Figure 4.12 shows the K2 sample divided into bins in $R_{\rm g}$ and $Z_{\rm max}$, which we use to investigate chemical trends later in this section.

It's also useful to investigate how these parameters change as a function of stellar age, as this can throw light on the dynamical evolution of the MW – including radial migration and vertical heating. Figure 4.13 shows $R_{\rm g}$ and $Z_{\rm max}$ as a function of stellar mass (which is more precisely constrained than age) and also the distributions of these parameters in six bins of age:

$$\begin{aligned} \tau < 1\,\mathrm{Gyr}, \qquad & 1\,\mathrm{Gyr} \leq \tau < 2\,\mathrm{Gyr}, \\ 2\,\mathrm{Gyr} \leq \tau < 4\,\mathrm{Gyr}, \qquad & 4\,\mathrm{Gyr} \leq \tau < 6\,\mathrm{Gyr}, \\ 6\,\mathrm{Gyr} \leq \tau < 10\,\mathrm{Gyr}, \quad & 10\,\mathrm{Gyr} \leq \tau. \end{aligned}$$

These age bins increase in width to accommodate the broader age posteriors of older stars. We see clearly that older stars (of lower mass) are distributed over a wider range of both $R_{\rm g}$ and $Z_{\rm max}$, and this spread is the signature of churning and vertical heating in our sample.

In Figure 4.14 we show a similar exercise, using the velocity components in Galactocentric cylindrical coordinates. We see similar trends with age to the previous plot, with older ages corresponding to a larger dispersion. This is a result both of the kinematic heating experienced by stars in the disc and the fact that the halo population is sampled only in the older bins. The vertical velocity dispersion σ_{v_Z} has been studied as an indicator of the MW's last major merger, as it is expected that this event would have resulted in significant and rapid heating of the MW's disc at the time (e.g. Helmi et al. 2018; and see also Helmi 2020 and references therein). Our simple examination of the data in Figure 4.14 suggests that the largest change in σ_{v_Z} between age bins is between the 4 – 6 Gyr and 6 – 10 Gyr bins, consistent with a merger 10 Gyr ago (e.g.

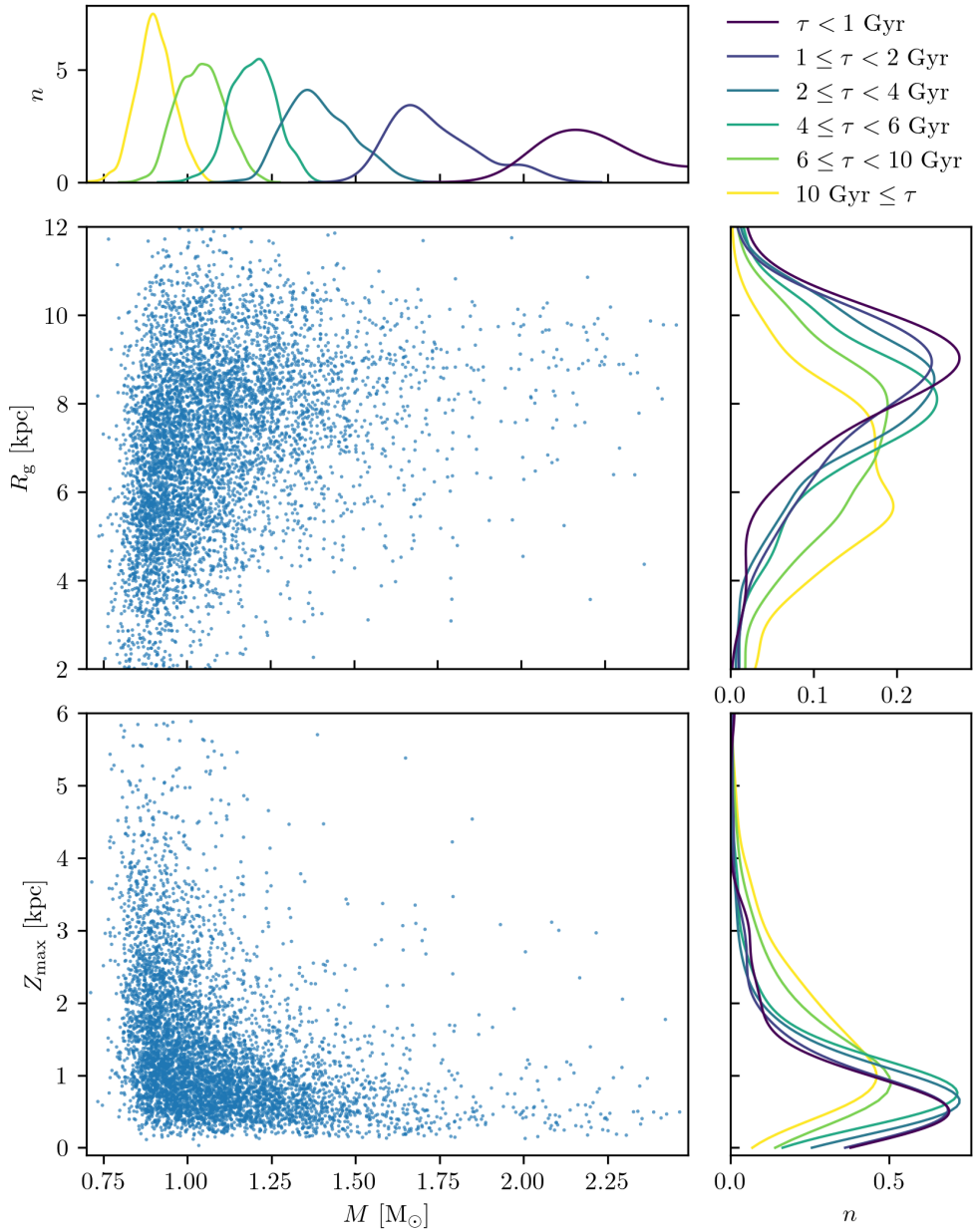


Figure 4.13: Guiding radius (middle left) and maximum vertical excursion (bottom left) vs. stellar mass for K2 stars with reliable ages. The distributions of M_* (top left), R_g (top right) and Z_{max} (bottom right) are shown using kernel density estimates in bins of stellar age. The area under each distribution integrates to one.

Gallart et al., 2019). However, since the bin width also increases here from two to four Gyr, this indication should be treated with caution and further investigation is needed to confirm whether it can really be attributed to the MW's merger history.

4.4.2 Chemical abundances and chemically selected populations

Moving beyond the kinematic properties, Figure 4.15 shows the [α/M] vs. [Fe/H] plane, in the bins of R_g and Z_{max} shown in Figure 4.12. The stars are coloured according to their age bin, and the data are sorted to show the youngest stars on top. We see clearly that the low-α sequence is dominated by younger stars and the high-α sequence is formed primarily of stars older than 6 Gyr, but there are a few apparently young stars also present. These are interesting objects and are likely the result of binary evolution and mass accretion, rather than genuinely young. Grisoni et al. (in preparation) studied these targets in more detail for this sample, and Miglio et al. (2021) investigated those present in the *Kepler* field. Overall in Figure 4.15, we see a general trend of older, high-α stars in the inner disc, and younger stars concentrated further from the Galactic centre though, as also shown in Figure 4.13, old stars are found at all R_g. We also see younger stars concentrated in the plane of the disc, while older stars tend to have orbits which extend to greater vertical distances.

In Figure 4.16 we show the age distributions of the high- and low-α sequences, as well as the 'intermediate' stars from the higher metallicity region where the sequences appear to overlap (see Figure 4.3 for the separation of these sequences). We consider only RGB stars, as CHeB stars experience significant mass-loss at the tip of the RGB, resulting in an overestimation of their age (see Section 4.4.3 for further discussion). In both the *Kepler* and K2 samples, the high-α population peaks at $\approx$ 10 Gyr, and the low-α at 6 - 7 Gyr. The peak of the intermediate population is between the two, consistent with a superposition of members of the two sequences. Warfield et al. (2021) compared ages from *Kepler* and K2 asteroseismology and found that the high-α sequence in K2 was younger than in their *Kepler* sample, but this does not appear to be the case in our data[4]. In addition, in both *Kepler* and K2, our low-α population peaks at slightly

[4]Warfield et al. (2021) separation of the high- and low-α sequences would have grouped our intermediate

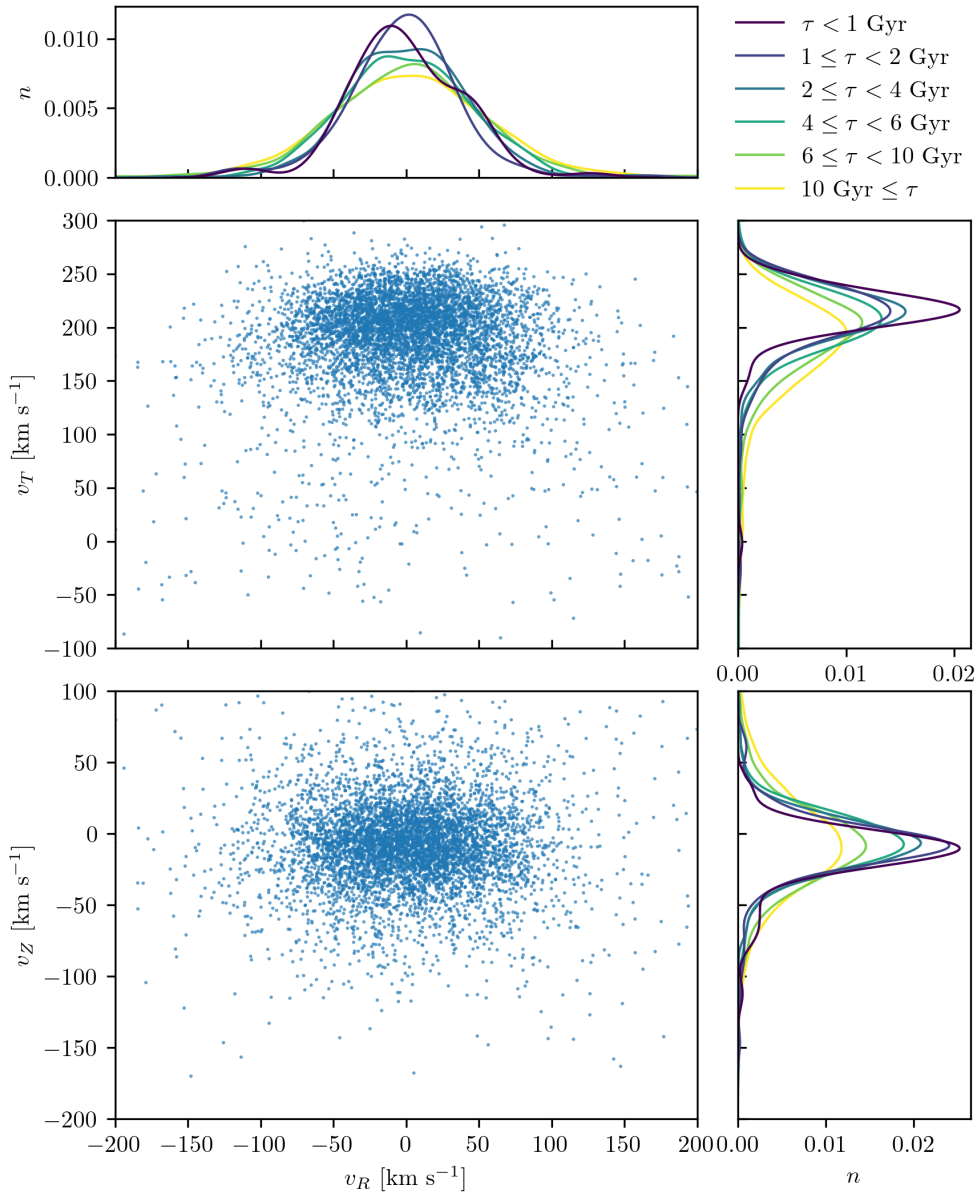


Figure 4.14: Tangential (middle left) and vertical (bottom left) velocity components vs. radial velocity component for K2 stars with reliable ages. The distributions of V_{R} (top left), V_{T} (top right) and V_{Z} (bottom right) are shown using kernel density estimates in bins of stellar age. The area under each distribution integrates to one.

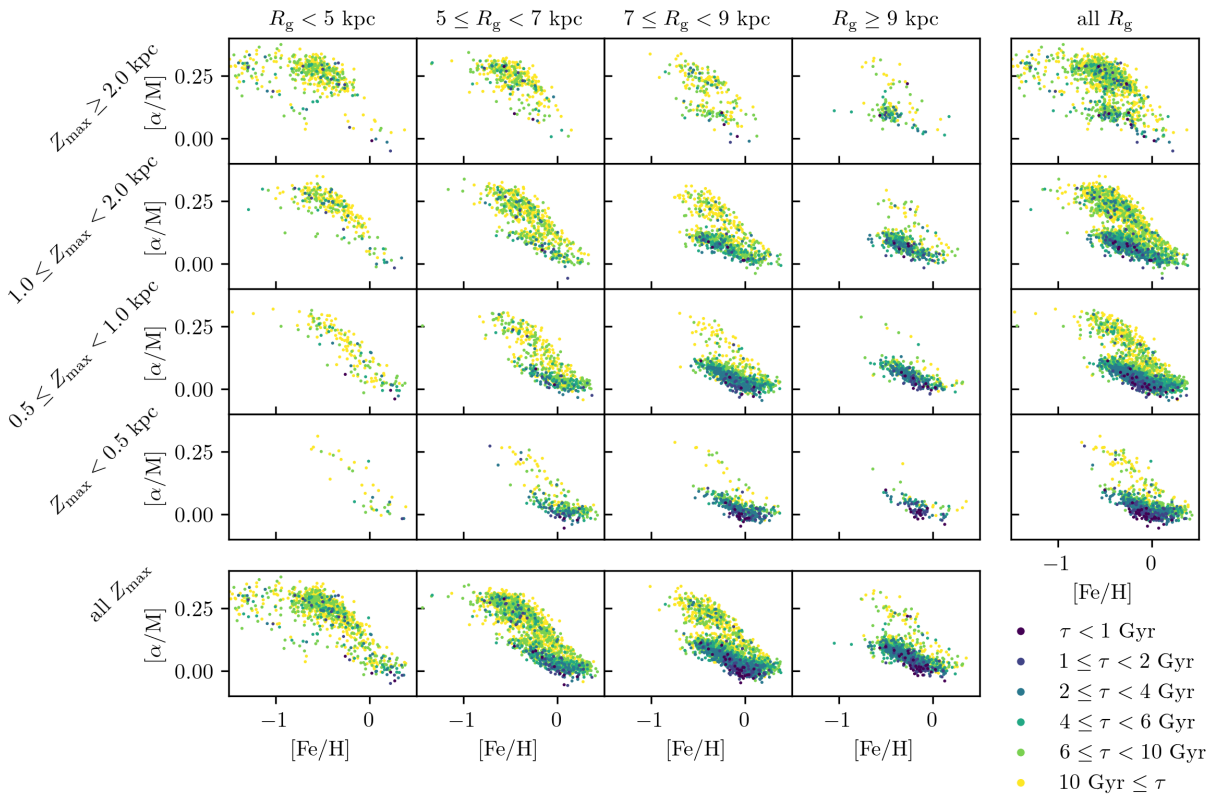


Figure 4.15: [α/M] vs. [Fe/H] in bins of guiding radius and maximum vertical excursion (main panel; as shown in Figure 4.12 for K2 stars with reliable ages. Also shown are the stars binned only by R_g (bottom panel) or Z_{max} (right panel). Stars are coloured according to age bin.

older ages, indicating a systematic difference between the ages in this work and those of Warfield et al. (2021). The age distribution of the *Kepler* high-α population agrees well, however.

Figure 4.17 shows a different separation of the K2 RGB sample and the corresponding age distributions. Das, Hawkins, and Jofré (2020) proposed the [Mg/Mn] vs. [Al/Fe] plane as a way of chemically identifying stars with a high probability of having been born outside the MW. These '*ex situ*' stars have high [Mg/Mn] and low [Al/Fe] (top panel) and lie in the expected low-metallicity, high-α region of the [α/M] vs. [Fe/H] plane (middle panel). We find that they are, on average, slightly younger than the '*in situ*' high-α stars (bottom panel), with a median age of ~ 8.6 Gyr. This is consistent with literature expectations that the *in situ* high-α population formed with higher star formation efficiency than the *ex situ* (e.g. Hawkins et al., 2014; Gallart et al., 2019; Vincenzo et al., 2019b; Das, Hawkins, and Jofré, 2020; Montalbán et al., 2021). To further refine the sample of *ex situ* stars, we introduce kinematic information and, consider stars with high eccentricity, e, as more likely to have been accreted (e.g. Mackereth et al., 2019b). From the chemically selected population of 18 stars, 6 have $e > 0.7$ with a median age of ~ 8.0 Gyr. The remaining 12 stars (with $e \leq 0.7$) have a median age of ~ 8.8 Gyr. Repeating this analysis for the *Kepler* sample, we find two stars with a median age of ~ 8.8 Gyr.

4.4.3 Stellar physics

As mentioned in the previous section, recovering robust ages for CHeB stars is challenging, due to the mass loss experienced at the tip of the RGB. We select RGB stars using cuts in L and $\log g$:

$$L < 35 L_{\odot};\ \log g > 2.6$$

and CHeB stars:

$$L \geq 35 L_{\odot};\ \log g < 2.5,$$

where these selections are not continuous in $\log g$ to reduce cross-contamination between the populations. In Figure 4.18 we show our selection and the mass distribution of the two groups

population with the low-α stars, so this cannot explain the difference in our results.

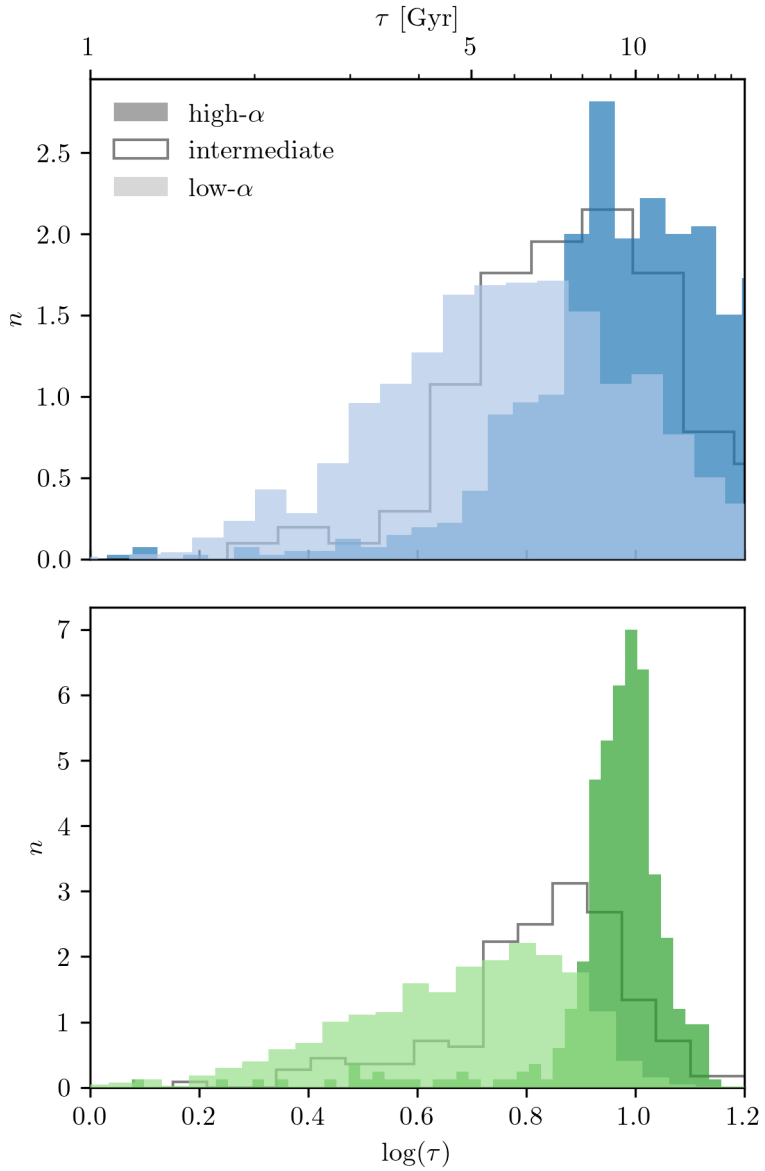


Figure 4.16: Distributions of logarithmic age for stars in the high- and low- and intermediate α regions of the [α/M] vs. [Fe/H] plane (as shown in Figure 4.3) The results are shown for likely-RGB stars from K2 (top) and *Kepler* (bottom) with reliable ages (see Section 4.4.3 for a description of the RGB selection). The area under each histogram integrates to one.

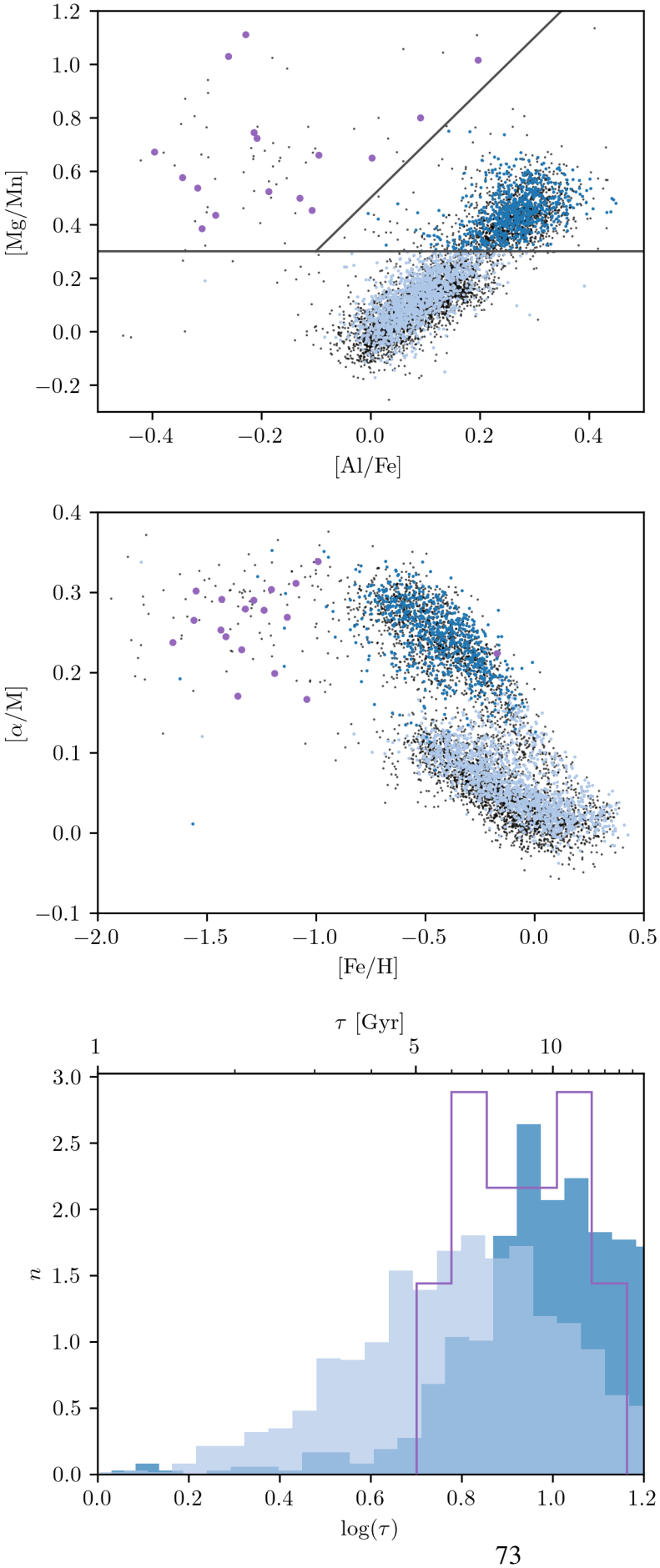


Figure 4.17: [Mg/Mn] vs. [Al/Fe] (top) and [α/Fe] vs. [Fe/H] (middle) for K2 stars with reliable ages. Likely-RGB stars are shown in colour in the foreground (see Section 4.4.3 for a description of the RGB selection) and the full sample is shown in the background (black points). Stars are divided, according to the grey lines in the top panel, into *in situ* low-α (light blue) *in situ* high-alpha (dark blue) and *ex situ* (purple) populations. Also shown are the distributions of logarithmic age for these three populations (bottom).

in the K2 sample, using masses from the scaling relation with L_{17}, to increase the number of CHeB stars in the sample and remove any effect of the PARAM priors. We select stars with $-0.5 < [\mathrm{Fe/H}] < 0.0$, to allow a comparison to the results from *Kepler* over the same metallicity range. We find that the CHeB stars have lost $\sim 0.1\,\mathrm{M}_{\odot}$ compared to the RGB population, consistent with *Kepler* (Appendix A.4 and see also Miglio et al. 2021).

K2 is also consistent with *Kepler* and TESS when we examine the [C/N] ratio as a function of stellar mass. The observed trend is a result of the first dredge-up, which brings material from the stellar interior to the surface as the star moves away from the main sequence (MS). In more massive stars the convective envelope reaches deeper and retrieves more nitrogen, which is produced in the core by CN and CNO cycle burning during the MS (e.g. Iben, 1964, 1967; Masseron and Gilmore, 2015; Martig et al., 2016). Figure 4.19 shows this relationship in the same bins of R_{g} and Z_{max} used previously, and we see changes across the Galaxy as a result of the different age demographics in each region and increased scatter at low mass due to the differences in initial chemical composition for these old stars. The full K2 sample is shown by the contours in Figure 4.20, and maps well to the *Kepler* and TESS samples.

4.4.4 Chemical clocks

Finally, in Figure 4.21, we show four 'chemical clocks' as a function of stellar age, from the K2-GALAH sample. Chemical clocks are formed by the ratio of two elements with different nucleosynthesis channels - ideally elements which individually have opposing trends with stellar age. Identifying and testing consistent and sensitive chemical clocks is a valuable application of stellar ages, as they allow ages to be inferred for large populations of stars where asteroseismic or other age determinations are not available (Moya et al., 2022). Here we show chemical clocks formed by the s-process elements yttrium and barium (which are not available in APOGEE and have an increase in abundance relative to iron in older stars) compared to the α-element magnesium and the odd-Z element aluminium (which have slightly decreasing trends relative to iron with age). Qualitatively our results agree with those reported in the literature (e.g. Casamiquela et al., 2021), and they demonstrate the utility of the GALAH sample, where

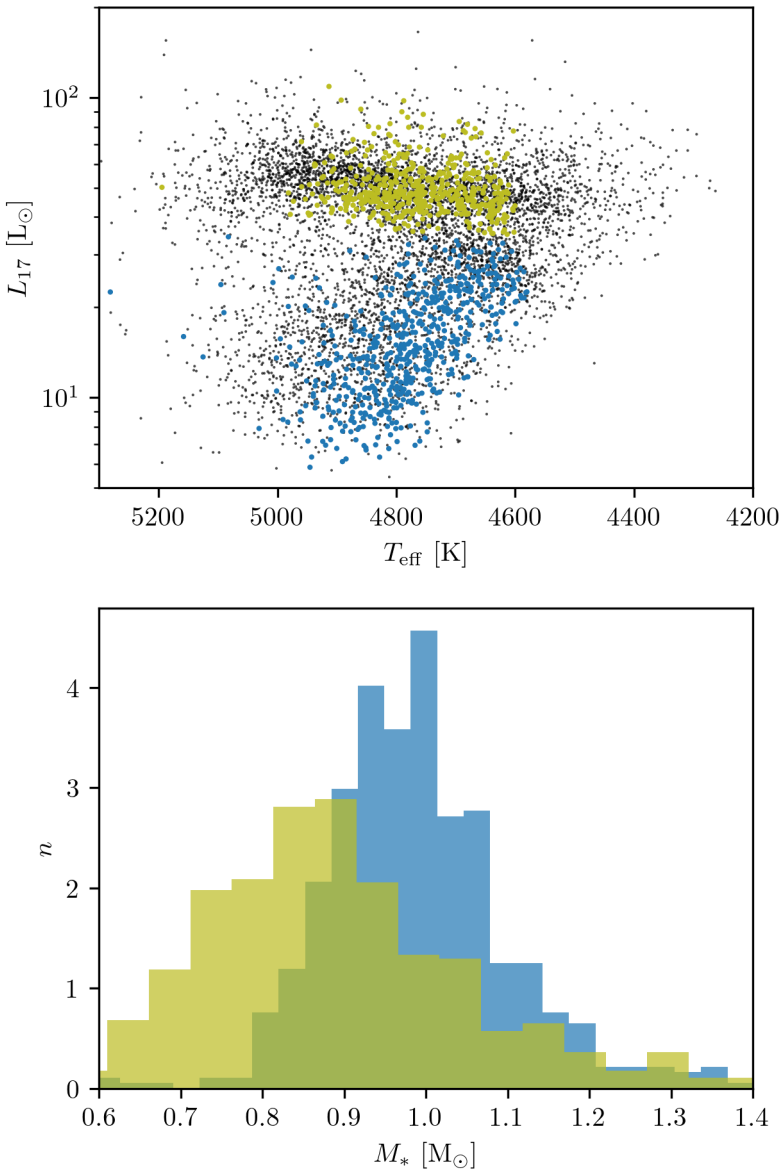


Figure 4.18: Top: HRD showing our selection for RGB (blue) and CHeB (yellow) stars. The full sample is shown in the background (black). Bottom: Mass distributions corresponding to the RGB and CHeB selections.

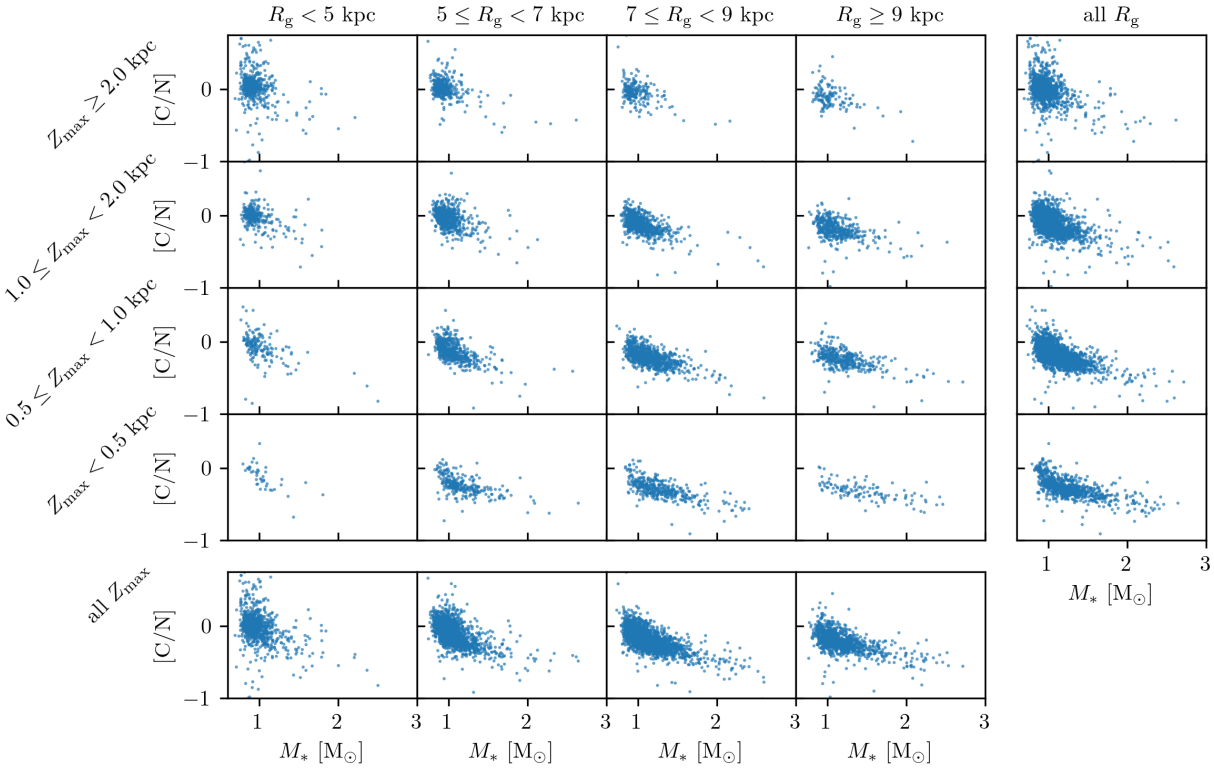


Figure 4.19: [C/N] vs. [Fe/H] in bins of guiding radius and maximum vertical excursion (main panel; as shown in Figure 4.12 for K2 stars with reliable ages. Also shown are the stars binned only by R_g (bottom panel) or Z_{max} (right panel).

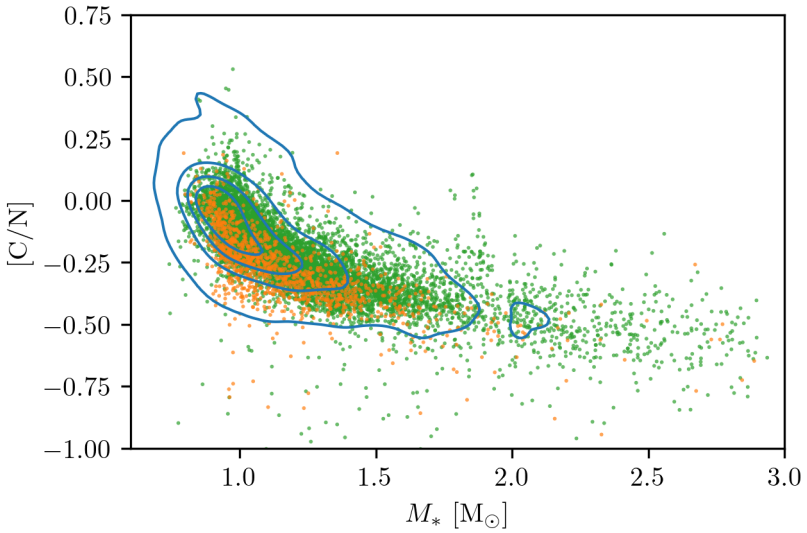


Figure 4.20: [C/N] vs. [Fe/H] for *Kepler* (green points), TESS (orange points) and K2 (blues contours) stars with reliable ages.

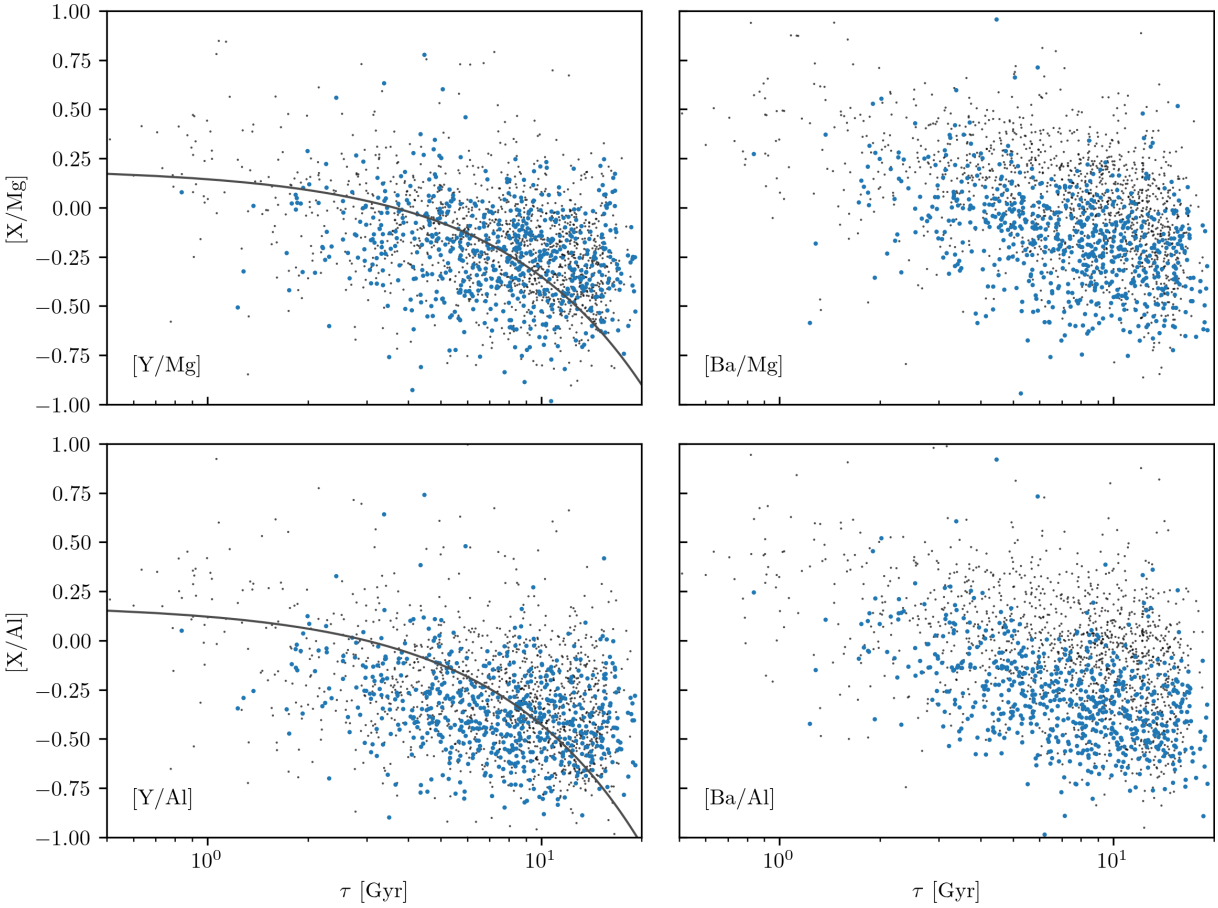


Figure 4.21: Abundance ratios vs. age for four elements commonly used in chemical clocks, from different nucleosynthetic channels: yttrium (left; light s-process), barium (right; heavy s-process), magnesium (top; α element) and Aluminium (left; odd-Z element). The stars shown have reliable ages from the K2-GALAH cross-match and the likely-RGB sample is shown in blue points in the foreground. The grey line shows the relationship between the yttrium chemical clocks and age found by Casamiquela et al. (2021).

elements form more nucleosynthesis channels can be investigated.

4.5 Summary and conclusions

We have used asteroseismology based on data from *Kepler*, K2 and TESS, combined with *Gaia* DR3 astrometry and spectroscopic constrained from APOGEE DR17 and GALAH DR3 to infer stellar and orbital parameters for over 17000 RGs. We pay specific attention to the age estimates of our samples, identifying those which are or may be unreliable for different combinations of observational constraints. In particular, we highlight stars with unreliable $\Delta\nu$ determinations

based on comparisons to *Gaia* luminosities. These are particularly relevant in K2 data due to the short duration of the observations of each campaign, and therefore important to characterise for Galactic archaeology studies where the spatial range of K2 is a benefit.

We demonstrate the suitability of different age and mass estimations in different applications including showing trends with age and mass of the orbital parameters R_g and Z_{max} and velocity components, and investigating the [α/M]-[Fe/H] plane in bins of R_g, Z_{max} and age. We also compare the age distributions of the low- and high-α populations, and the ages obtained from chemically selected *ex situ* stars.

Using conservative selections of RGB and CHeB stars, we investigate the average mass-loss experienced by stars on the RGB, finding consistent results between *Kepler* and K2 for the same metallicity range of $\sim 0.1\,M_\odot$. We find that our K2 results agree with the known relationship between stellar mass and [C/N] ratio in *Kepler* and TESS, but extend it to lower masses where the other surveys do not sample significantly. We observe greater scatter in this region, which we attribute to the greater spread of initial abundances amongst the oldest stars where the halo population is sampled. Finally, we use abundances from GALAH to show that our K2 ages agree qualitatively with results for chemical clocks based on open clusters.

These datasets, taken together, are a valuable tool for studies of Galactic archaeology and stellar evolution, and the K2 sample presented here has already been used to investigate Galactic cerium enrichment, young α-rich stars and the radial metallicity gradient in the works of Casali et al. (2023) and Willett et al. (2023) and Grisoni et al. (in preparation). The examples presented in these works represent a small fraction of the possible applications of these data which offer scope to investigate many open problems directly and to be used as training data which will extend the range of currently available machine learning-based ages.

Looking ahead, the availability of asteroseismology from the continuing TESS mission, as well as future missions including the Nancy Grace Roman Telescope (Spergel et al., 2015) and ESA's PLATO mission (Rauer et al., 2014), will be complemented by future *Gaia* data releases and upcoming spectroscopic surveys (e.g. 4MOST; de Jong et al. 2012, MOONS; Cirasuolo et al. 2014 and WEAVE; Dalton et al. 2020). PLATO, in particular, has the potential to provide

age estimates with 10% precision for a large sample of RGs (Miglio et al., 2017), which would represent a meaningful improvement over the present data.

Chapter 5

THE EVOLUTION OF THE MILKY WAY'S THIN DISC RADIAL METALLICITY GRADIENT WITH K2 ASTEROSEISMIC AGES

This chapter presents the entirety of Willett et al. (2023) with minor modification. I confirm that all writing is my own, with editorial contributions from my coauthors. The work presented is my own, with the exception of the inferred stellar parameters from PARAM, which were provided by A. Miglio. Data are obtained from sources cited in the text.

5.1 Introduction

Over the last decade, the field of Galactic archaeology has expanded rapidly, with many new discoveries concerning the formation and evolution of the Milky Way (MW). These advances have been facilitated by the availability of astrometry of unprecedented precision from *Gaia* (Gaia Collaboration et al., 2016) and several large spectroscopic surveys, such as the Apache Point Observatory Galactic Evolution Experiment (APOGEE; Majewski et al., 2017), *Gaia*-ESO (Randich et al., 2022), GALactic Archeology with HERMES (GALAH; Buder et al., 2021), the Large sky Area Multi-Object fibre Spectroscopic Telescope (LAMOST; Deng et al., 2012; Zhao et al., 2012) and the RAdial Velocity Experiment (RAVE; Steinmetz et al., 2020a,b). When combined with stellar ages, these provide meaningful tests of chemo-dynamical models of the

MW.

Many such models of spiral galaxies predict that the inner part of the disc forms earlier than the outer regions (e.g. Larson, 1976; Matteucci and Francois, 1989; Chiappini, Matteucci, and Gratton, 1997; Frankel et al., 2019), and the idea of 'inside-out' formation is now widely accepted. One of the signatures of this formation scenario is a radial metallicity[1] gradient in the Galactic disc, with higher metallicities in the centre, caused by more generations of stars which enrich the material from which the next generation form. This gradient might change with time as the disc expands and star formation proceeds unevenly. In the MW we have the opportunity to explore this evolution by using tracers of the metallicity gradient with different ages, in contrast to studies of other galaxies where, from a given tracer, we see only a snapshot of the aggregate effect (e.g. Cresci et al., 2010; Magrini et al., 2016).

In addition to its intrinsic interest as a property of the MW, the radial metallicity gradient also helps to constrain dynamical processes in the disc. If we expect that stars are born into the Galaxy with some tight relationship between their metallicity and birth radius, R_b, but the relationship in a mono-age population shows some scatter, then we may infer that some stars have moved away from R_b. This assumption breaks down in the presence of contaminants from the debris of galactic mergers of other processes, but it is an acceptable simplification in a robustly selected in-situ population. Inferring birth radii is an important step towards recovering the MW's history, and therefore tight observational constraints on the metallicity gradient are very valuable (e.g. Wielen, Fuchs, and Dettbarn, 1996; Minchev, Chiappini, and Martig, 2013; Frankel et al., 2018; Minchev et al., 2018).

There are two reasons why a star may be observed with a galactocentric radius, $R_\mathrm{Gal} \neq R_\mathrm{b}$. First, the eccentricity of the orbit naturally results in a star being observed at different R_Gal during the orbit. Stars in the disc are born onto nearly circular orbits, which increase in eccentricity over time as a result of radial heating. This process increases the radial action, J_R, and is referred to as 'blurring' (Sellwood and Binney, 2002; Schönrich and Binney, 2009a). Importantly, for

[1]Throughout this work we use iron abundance as a tracer for metallicity: $[\mathrm{Fe/H}] = \log_{10}(N_\mathrm{Fe}/N_\mathrm{H})_* - \log_{10}(N_\mathrm{Fe}/N_\mathrm{H})_\odot$, where N_Fe and N_H are the numbers of iron and hydrogen nuclei per unit volume of the stellar photosphere, respectively.

efforts to recover birth radii, blurring does not change the orbital angular momentum, L_z, so the star retains some 'kinematic memory' of its birth conditions. By considering the metallicity gradient with guiding radius, R_g (the radius of a circular orbit of the same angular momentum) we can mitigate this effect in our sample.

Second, interactions with non-axisymmetric features of the MW's disc (for example, the bar or spiral arms) can cause 'churning' (Sellwood and Binney, 2002), in which an exchange of angular momentum shifts the star into a new orbit. Frankel et al. (2020) found that this effect is roughly an order of magnitude stronger than blurring in the Galactic disc, shifting stars by up to ≈ 3 kpc over 6 Gyr on average. The change of L_z means that $R_g \neq R_b$ and R_b can only be inferred by indirect means, such as the combination of the metallicity gradient and age. Minchev, Chiappini, and Martig (2016) found that churning is necessary in their chemo-dynamical simulation in order to reproduce the observed spread of metallicity in stars of a given age. The same model also shows that the presence of churning affects the flaring of a galactic disc in a quiescent setting or during a merger (Minchev, 2016).

Constraints on migratory processes like churning require precise measurements of the metallicity gradient in populations spanning the full history of the disc. This necessitates a large sample, covering a wide range of radii, metallicities and ages. Open clusters (OCs) have been used in such studies, (Magrini et al., 2009; Casamiquela et al., 2017, 2019; Spina et al., 2021; Myers et al., 2022; Netopil et al., 2022; Spina, Magrini, and Cunha, 2022; Gaia Collaboration et al., 2023a), however, dynamical processes are thought to create a survival bias towards high-metallicity OCs, obscuring the underlying chemical evolution of the Galaxy (Lynga and Palous, 1987; Anders et al., 2017b; Spina et al., 2021). Cepheid variables can be used to probe the present-day gradient, as they provide an excellent radial range for targets with $20\,\mathrm{Myr} < \tau < 400\,\mathrm{Myr}$ (Genovali et al., 2014). Other young tracers such as OB stars (Kaufer et al., 1994; Daflon and Cunha, 2004; Bragança et al., 2019) and HII regions (Esteban et al., 2005; Balser et al., 2011) can be used to trace the [O/H] gradient over large regions of the Galaxy but, as for Cepheids, they cannot reveal the evolution over its history.

Low-mass field stars are ideal tracers, but there are many well-documented challenges

associated with obtaining reliable stellar ages for large samples. Ages may be estimated by comparison to isochrones, but they are sensitive to changes in model physics or temperature scale and are generally restricted to lower-luminosity phases of stellar evolution. For red giants which exhibit solar-like oscillations, asteroseismic analysis may be used to obtain precise and robust (though not model-independent) stellar ages (Soderblom, 2010; Chaplin and Miglio, 2013; Lebreton, Goupil, and Montalbán, 2014b). Anders et al. (2017b) demonstrated the potential of this approach with the CoRoGEE sample (Anders et al., 2017a), combining asteroseismic constraints from two fields observed by CoRoT (Baglin et al., 2006) with spectroscopy from APOGEE. The combination of asteroseismology and spectroscopy offers many advantages over classical tracers, as we can probe the full history of the disc over several kpc.

Kepler (Gilliland et al., 2010) represents the 'gold standard' in asteroseismic data, enabling ages to be determined to 10% precision (Montalbán et al., 2021). However, while the signature of radial migration can be seen in *Kepler* data (e.g. Figure 6 of Miglio et al. (2021)), they are restricted in spatial coverage to a single 105 $\deg^2$ area. In this work we utilise the results of the successor mission, K2 (Howell et al., 2014), which provides observations from all around the ecliptic plane, split into 20 campaigns each observed for around 80 days. Though the observation time per campaign was much shorter in duration than *Kepler* for a single field, the global oscillation frequencies are sufficient to place good constraints on the stellar mass, M_*, with which the age of low-mass red giants is tightly correlated. Combining these data with chemical abundances from APOGEE DR17 (Abdurro'uf et al., 2022), and *Gaia* DR3 (Gaia Collaboration et al., 2023c) unlocks the potential of asteroseismic ages for Galactic archaeology on a large scale.

In this work, we compile a catalogue of K2 targets with robust and homogeneously determined stellar parameters from asteroseismology. From this, we select members of the thin disc and measure the radial metallicity gradient as a function of age with two complementary techniques. We introduce our sample in Section 5.2 and describe our analysis in Sections 5.3 and 5.4. Section 5.5 contains a detailed discussion of our results and a comparison to the existing literature and theoretical predictions. Finally, our conclusions are presented in Section 5.6.

5.2 Observational constraints

In this section, we describe our sample of K2 solar-like oscillating red giants (Section 5.2.1), outline how the stellar and orbital parameters were inferred from the observables (Section 5.2.2), and how members of the thin disc were selected, utilising both the abundance and kinematic information (Section 5.2.3).

5.2.1 Asteroseismic, Spectroscopic and Astrometric Constraints

Our sample is based upon the catalogue of Willett et al. (in preparation; Chapter 4), which contains asteroseismic parameters from the pipelines of Mosser and Appourchaux (2009) and Elsworth et al. (2020), as well as spectroscopically derived abundances and radial velocities (RVs) from APOGEE DR17 (Abdurro'uf et al., 2022), and 5-parameter astrometric solutions from *Gaia* DR3 (Gaia Collaboration et al., 2023c).

In order to obtain a set of homogeneously constrained stellar ages, in this work we consider global asteroseismic parameters $\nu_{\rm max}$, the frequency of maximum oscillation power, and $\Delta\nu$, the large frequency separation, from the pipeline of Elsworth et al. (2020) only. This pipeline has been shown to produce fewer false positive detections (Mackereth et al., 2021) and the definition of $\Delta\nu$ (which varies between pipelines) is more similar to that used in the stellar parameter estimation code PARAM. The resulting sample is spread across K2 campaigns 1 – 8 and 10 – 18 which provides good coverage out to ≈ 3 kpc from the solar position.

The abundances used in this work are those produced by the APOGEE Stellar Parameters and Chemical Abundances Pipeline (ASPCAP; García Pérez et al., 2016). A full description of this pipeline as applied to APOGEE DR17 is given in Holtzman et al. (in preparation). We remove targets with `ASPCAPFLAG` containing `STAR_BAD` or `STAR_WARN`, and those with any `RV_FLAG` set.

We use five-parameter astrometric solutions $[\alpha, \delta, \varpi, \mu_\alpha, \mu_\delta]$ from *Gaia* DR3. Following L. Lindegren (2018), we remove targets with `ruwe` > 1.4 or which are marked as binaries by the `non_single_star` flag.

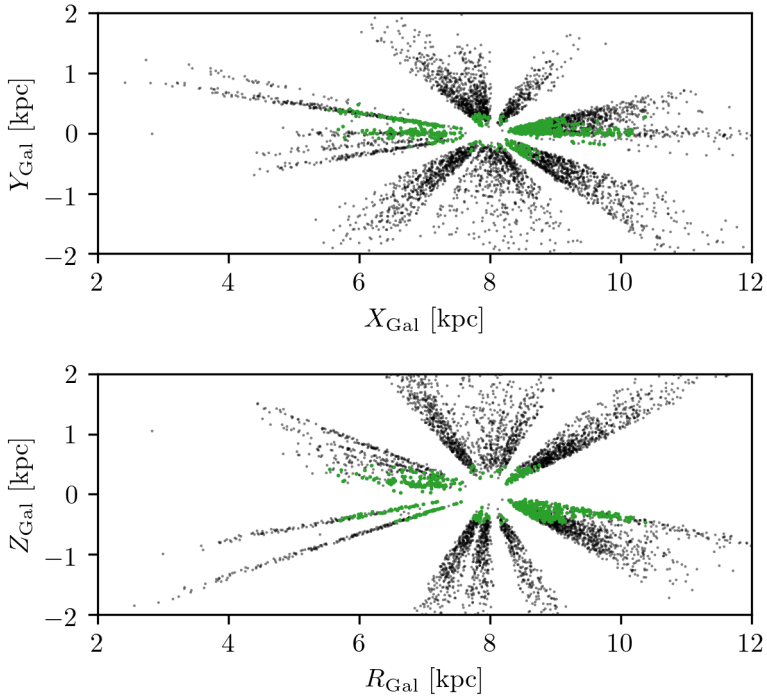


Figure 5.1: Location of stars in our sample in left-handed Galactocentric cartesian coordinates (top) and Galactocentric cylindrical coordinates (bottom). The green points show the stars in the thin disc, and the full sample is shown in the background (black points).

The final sample comprises 5885 targets, shown in Figure 5.1, with median metallicity uncertainty $\sigma_{\rm [Fe/H]} = 0.008$ dex. In practice, we enforce a lower limit of $\sigma_{\rm [Fe/H]} > 0.05$ dex and $\sigma_{T_{\rm eff}} > 50$ K during the inference of the stellar parameters (Section 5.2.2) because the pipeline uncertainties reflect only the internal errors. In addition, inflating the error on $T_{\rm eff}$ helps to mitigate the uncertainties associated with the descriptions of near-surface convection and outer boundary conditions in the stellar models. We use the ASPCAP $\sigma_{\rm [Fe/H]}$ in our analysis and the metallicity gradient, but show the negligible effect on our results of inflating the [Fe/H] uncertainty in Appendix B.1.

5.2.2 Inferred Stellar and Orbital Parameters

In this work we use the stellar parameters described in Chapter 4, specifically the mass, M_*, age, τ, and distance, D. These parameters are inferred using the PARAM code (da Silva et al., 2006; Rodrigues et al., 2014, 2017), which performs a Bayesian comparison to a grid of stellar models and returns full posterior information. Asteroseismic constraints are provided

by $\Delta\nu$ and $\nu_{\rm max}$ and we use the reference model grid (labelled G2) from the work of Miglio et al. (2021). We remove stars with $\nu_{\rm max}$ more than three standard deviations below 20 μHz, as asteroseismic inferences have not been extensively tested in this domain. A detailed discussion of the asteroseismic distances and how they compare to those from *Gaia* can be found in Khan et al. (2023).

Orbital parameters are obtained from the same source and here we use the guiding radius, $R_{\rm g}$, and maximum excursion from the Galactic plane $Z_{\rm max}$. They are computed using the fast orbit estimation method of Mackereth and Bovy (2018), implemented in `galpy` (Bovy, 2015). Throughout this work, we adopt the simple Milky Way potential `MWPotential2014` (Bovy, 2015) and, following this model, we assume the radial position of the Sun to be $R_{\rm Gal,\odot} = 8.0\,$kpc, where the circular velocity is $v_{\rm circ} = 220\,{\rm km\,s^{-1}}$ (Bovy et al., 2012). The additional solar motion is given by $[U, V, W]_\odot = [-11.1, 12.24, 7.25]{\rm km\,s^{-1}}$ (Schönrich, Binney, and Dehnen, 2010), and the Sun's vertical offset from the Galactic plane is $Z_{\rm Gal,\odot} = 20.8\,$pc (Bennett and Bovy, 2019).

For both the stellar and orbital parameters, we use the 68% credible interval throughout our analysis, and sometimes approximate the posteriors as Gaussian, taking half this interval as the standard deviation. The uncertainties on τ and $R_{\rm g}$ are shown in Figure 5.2.

5.2.3 Thin disc selection

In this work, we restrict our analysis to the thin disc, where the stellar orbits have been less disturbed by dynamical processes (either rapid 'non-adiabatic heating' which can be caused by interactions with other galaxies or scattering from giant molecular clouds, or 'adiabatic heating' from the secular evolution of the disc (Ting and Rix, 2019, and references therein)). The rest of the sample will be studied in future works where we explore other abundance gradients, vertical trends, and stars from the Galactic halo. We select thin disc members from our sample in two stages: first, we make a cut in the [α/M] abundance to remove the α-enhanced population, which is usually associated with the halo and thick disc (Figure 5.3). We use [α/M] as a proxy for [α/Fe]

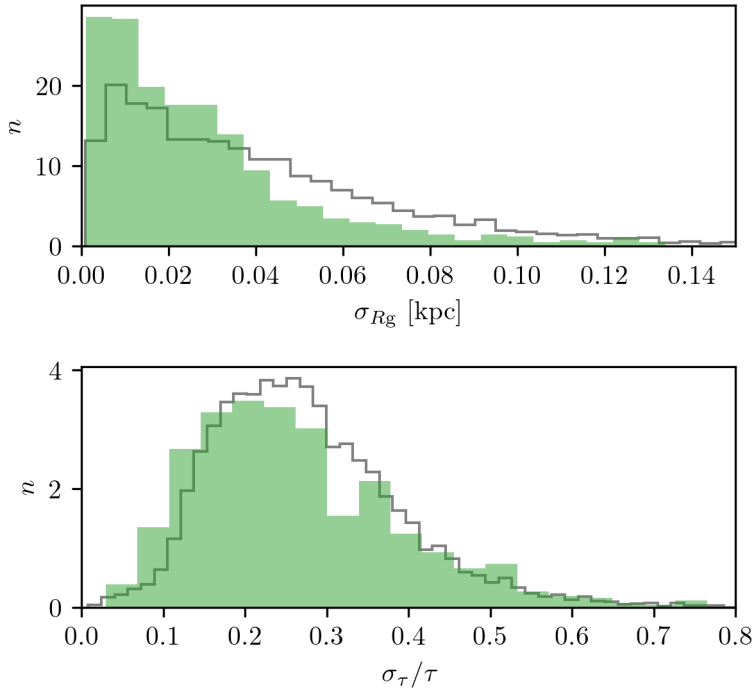


Figure 5.2: Distribution of the uncertainty on guiding radius (top) and fractional uncertainty on age (bottom) in the full sample (grey line) and thin disc (filled green). The area under each histogram integrates to one.

as the differences between them[2] are negligible. Second, we make a cut to retain stars with $Z_{\rm max} < 0.5$ kpc which are on kinematically cool orbits. This cut is chosen to be slightly wider than the scale height of the thin disc, to accommodate the flaring of the disc in the outer galaxy (Momany et al., 2006). Though this cut changes the metallicity distribution of our sample, our results are not very sensitive to its exact position (see Appendix B.2 for details).

Our thin disc sample contains a total of 668 stars and is shown in green in Figures 5.1, 5.2 and 5.3, with median uncertainties $\sigma_{\rm [Fe/H]} = 0.007$, $\sigma_\tau/\tau = 0.24$ and $\sigma_{R_{\rm g}} = 0.02$ kpc - though we remind the reader of the comment on $\sigma_{\rm [Fe/H]}$ in Section 5.2.1.

[2]defining [α/Fe] as an average of [X/Fe] for O, Mg, Si, S, and Ca

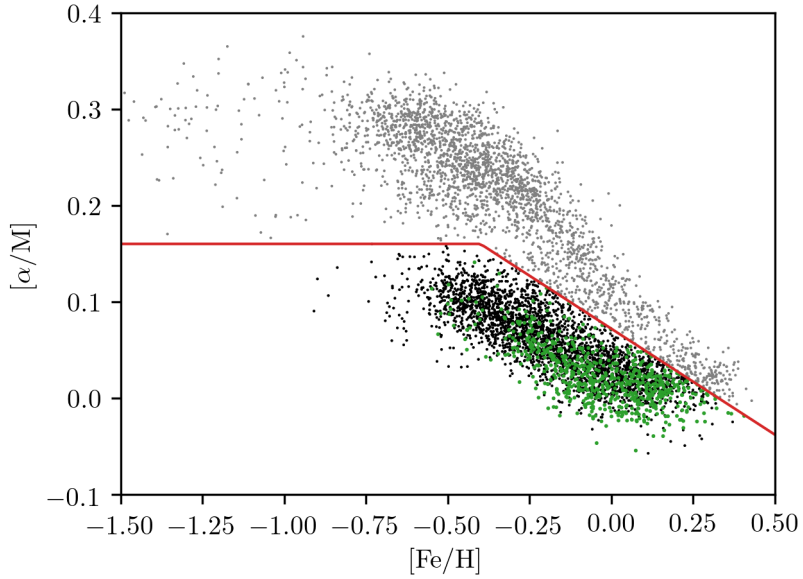


Figure 5.3: Average α element abundance [α/M] vs. [Fe/H]. The high- and low-α sequences were separated along the red line, with the high-α population (grey) removed from the analysis. of the remaining low-α population, stars with $Z_{\rm max} \geq 0.5\,$kpc were also removed (black). The final thin disc sample is shown in green.

5.3 The metallicity gradient in bins of age

We investigate the metallicity as a function of $R_{\rm g}$ across six bins in age:

$$\begin{aligned} \tau < 1\,\text{Gyr}, \qquad & 1\,\text{Gyr} \leq \tau < 2\,\text{Gyr}, \\ 2\,\text{Gyr} \leq \tau < 4\,\text{Gyr}, \qquad & 4\,\text{Gyr} \leq \tau < 6\,\text{Gyr}, \\ 6\,\text{Gyr} \leq \tau < 10\,\text{Gyr}, \qquad & 10\,\text{Gyr} \leq \tau \end{aligned}$$

where we use bins of increasing width to accommodate the wider posteriors at older ages. For ease of comparison, these bins are the same as those used by Anders et al. (2017b).

We utilise a Bayesian fitting procedure to constrain the metallicity gradient, using a 'linear + Gaussian spread' model. In physical terms, this means that we expect stars to be normally distributed about some line intrinsically, rather than having been drawn from a narrow relationship and subsequently scattered, so

$$[\text{Fe/H}] \sim \mathcal{N}(mR_{\rm g} + c, V). \tag{5.1}$$

This model has three parameters $\phi = m, c, V$, where m and c are the linear gradient and offset from [Fe/H] = 0 at $R_g = 0$, and V is the variance of the Gaussian, oriented perpendicular to the direction of the linear component. Using Bayes' theorem, the posterior probability density function (PDF) of these model parameters given some data d is

$$p(\phi|d) \propto p(\phi)p(d|\phi), \tag{5.2}$$

where $p(\phi)$ is the prior PDF of the model parameters and $p(d|\phi) = \mathcal{L}$ is the likelihood of observing the data, given the model.

Our fitting procedure follows Hogg, Bovy, and Lang (2010) and accounts for uncertainty on both R_g and [Fe/H] by utilising the full covariance matrix of each star i, ς_i, in the likelihood. In addition, we reparametrise the problem so that we do not directly constrain m and c, but rather the angle to the horizontal, $\cos(\theta) = 1/\sqrt{1+m^2}$, and $c_\perp = c\cos(\theta)$, which avoids our wide priors placing too much emphasis on gradients close to vertical. This gives a new set of parameters $\varphi = [\theta, c_\perp, V]$. Projecting ς_i to an orthogonal variance Σ_i^2, we may write the log-likelihood as:

$$\ln(\mathcal{L}) \propto -\frac{1}{2}\sum_i \left[\ln\left(\Sigma_i^2 + V\right) + \frac{\Delta_i^2}{\Sigma_i^2 + V}\right], \tag{5.3}$$

where Δ_i is the orthogonal displacement of star i from the line. We choose very wide, uniform priors on the parameters φ, requiring:

$$-\pi < \theta < \pi,$$
$$-10^3 < c_\perp < 10^3,$$
$$0 \leq V < 10^4.$$

We explore this parameter space by sampling according to the Markov Chain Monte Carlo (MCMC) algorithm, implemented in `emcee` (Foreman-Mackey et al., 2013). We use 32 walkers which each make 5000 steps, with a burn-in time which is dynamically determined to be 10 times the auto-correlation time (removing around 500 samples per walker). To account for

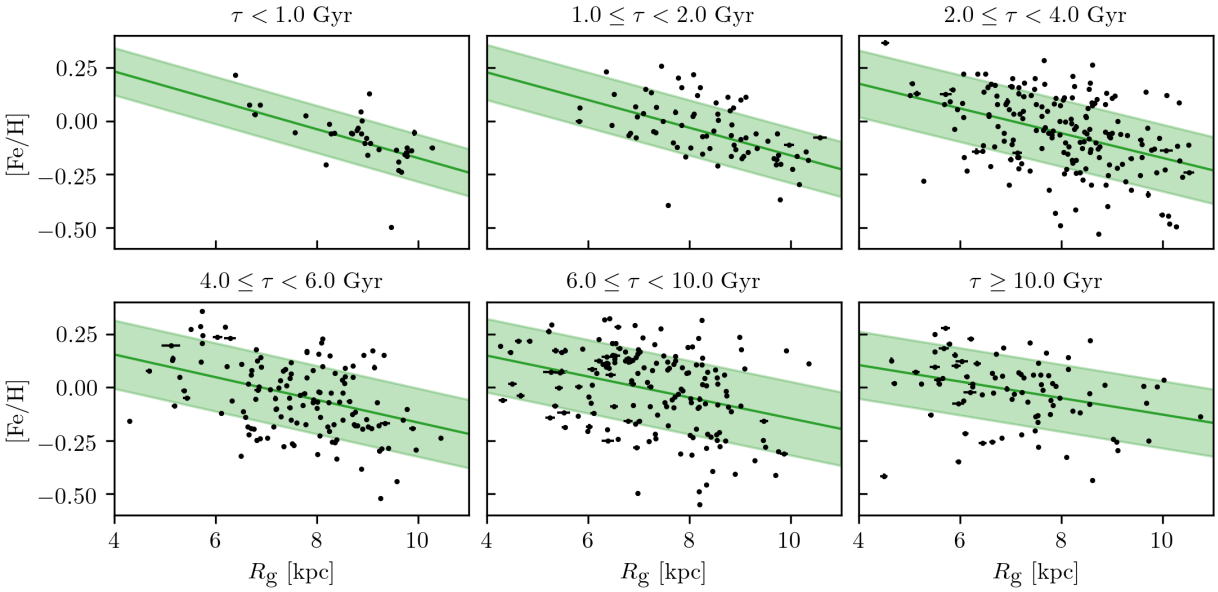


Figure 5.4: [Fe/H] vs. R_g in six bins of age. The thin disc sample is shown in black points, binned according to the median age of each star. The green line shows the best-fitting radial metallicity gradient from the MCMC analysis, with a filled region representing 1σ of the intrinsic spread.

the uncertainty on τ, we perform an overarching Monte Carlo (MC) analysis by repeating this procedure for 500 realisations of τ which are generated by approximating the posterior distribution from PARAM as Gaussian. This allows the stars to move between bins in each step of the MC. We combine all the post-burn-in samples and report the median and 68% credible interval as the best-fitting values of the parameters. The age uncertainty contributes approximately 30% to the overall error budget on these results. The lines corresponding to these values are shown in Figure 5.4, where the filled region indicates the intrinsic spread, $\sqrt{V}$, and the points appear in the bin to which the median age of the star belongs. An example corner plot showing the joint and marginal distributions of the fit parameters φ in one bin, for one realisation of τ, is shown in Figure 5.5.

We report the best fitting values of the gradient, m, metallicity offset at 8 kpc, $b = m \times 8 + c$, and [Fe/H] component of the spread $S = \sqrt{V}\cos(\theta)$ in the left-hand side of Table 5.1. The gradient flattens monotonically with age, and the spread is smallest for the youngest populations, increasing until $\tau \approx 10$ Gyr. The metallicity at 8 kpc is slightly sub-solar at all ages.

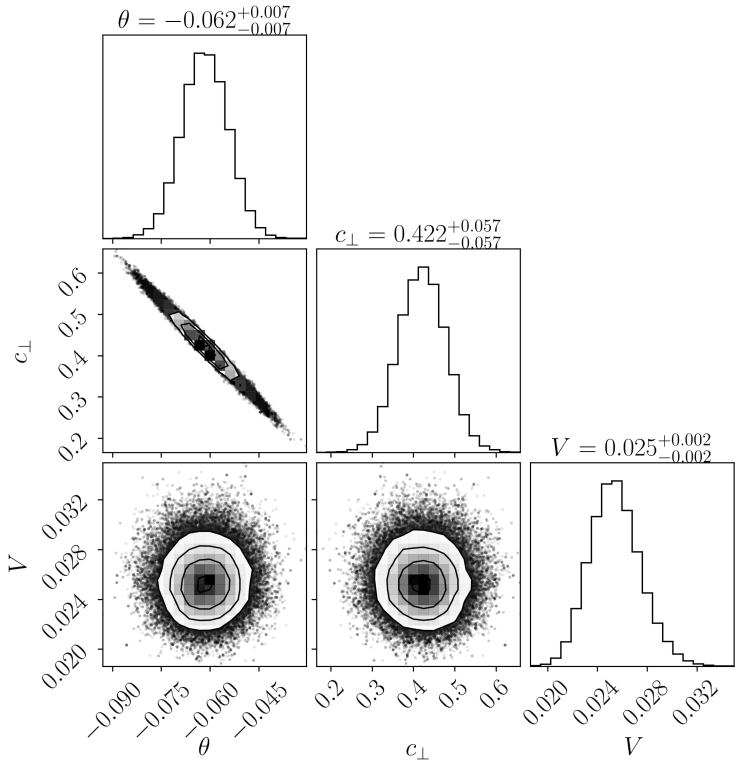


Figure 5.5: Corner plot (Foreman-Mackey, 2016) showing the joint and marginalised sampled posterior distributions of the fit parameters φ in the age bin $2\,\mathrm{Gyr} \leq \tau < 4\,\mathrm{Gyr}$ for one step in the MC (one realisation of τ).

Table 5.1: The median and 68% credible interval for each parameter from the MCMC analysis in bins of age (left) and the HBM, evaluated at the median age, $\tau_{\rm med}$ of each bin population (right); m is the gradient, b is the [Fe/H] offset at $R_{\rm g} = 8\,$kpc, and S is the component of the intrinsic spread in the [Fe/H] direction.

		MCMC Parameters				HBM Parameters		
bin range [Gyr]	$N_{\rm stars}$	m [dex/kpc]	b [dex]	S [dex]	$\tau_{\rm med}$ [Gyr]	m [dex/kpc]	b [dex]	S [dex]
$\tau < 1$	35	$-0.068^{+0.017}_{-0.016}$	$-0.039^{+0.022}_{-0.023}$	$0.111^{+0.015}_{-0.013}$	0.7	$-0.078^{+0.011}_{-0.011}$	$-0.022^{+0.016}_{-0.015}$	$0.115^{+0.010}_{-0.009}$
$1 \leq \tau < 2$	74	$-0.065^{+0.013}_{-0.013}$	$-0.033^{+0.015}_{-0.015}$	$0.130^{+0.012}_{-0.011}$	1.6	$-0.068^{+0.008}_{-0.007}$	$-0.034^{+0.010}_{-0.009}$	$0.130^{+0.007}_{-0.006}$
$2 \leq \tau < 4$	183	$-0.058^{+0.010}_{-0.010}$	$-0.058^{+0.011}_{-0.011}$	$0.157^{+0.008}_{-0.008}$	3.0	$-0.060^{+0.005}_{-0.005}$	$-0.044^{+0.006}_{-0.007}$	$0.145^{+0.005}_{-0.005}$
$4 \leq \tau < 6$	132	$-0.053^{+0.012}_{-0.012}$	$-0.060^{+0.016}_{-0.016}$	$0.160^{+0.011}_{-0.010}$	4.9	$-0.054^{+0.005}_{-0.005}$	$-0.052^{+0.007}_{-0.007}$	$0.157^{+0.004}_{-0.004}$
$6 \leq \tau < 10$	165	$-0.049^{+0.012}_{-0.011}$	$-0.048^{+0.016}_{-0.016}$	$0.173^{+0.011}_{-0.0010}$	7.6	$-0.048^{+0.006}_{-0.006}$	$-0.059^{+0.009}_{-0.009}$	$0.169^{+0.006}_{-0.006}$
$10 \leq \tau$	87	$-0.039^{+0.013}_{-0.013}$	$-0.051^{+0.020}_{-0.020}$	$0.158^{+0.012}_{-0.012}$	12.6	$-0.041^{+0.008}_{-0.008}$	$-0.067^{+0.012}_{-0.013}$	$0.184^{+0.010}_{-0.009}$

5.4 A hierarchical Bayesian approach

Reducing a dataset to a small number of bins can lead to misleading and sometimes unreliable results. In the specific context of this work, the intrinsic spread around the linear relationship carries essential information, so conflating it with a scatter caused by the mix of ages in a bin makes robust inference a challenge. This is compounded by the fact that the bins are wider, and therefore the populations are a worse approximation of mono-age, at older ages. In this section, we show that, with our large dataset and some simplifying assumptions, it is possible to remove the need for binning altogether.

To constrain the changes in the metallicity distribution with age we constructed a hierarchical Bayesian model (HBM). This allows the fit parameters to vary for each star (they are now the latent parameters), constrained by some population-level rule which describes how they vary with age. We reparameterise to describe the variation with $\log(\tau)$ instead because the increasing age uncertainty as a function of age makes the parameter space difficult to explore. In this case, we assume a linear relationship for m and b with $\log(\tau)$, and (since the spread must have a strictly non-negative value) S follows an exponential in $\log(\tau)$:

$$[\mathrm{Fe/H}] \sim \mathcal{N}(mR_{\mathrm{g}} + (b - 8m)\,, S^2); \tag{5.4}$$

$$\begin{aligned} m &= k_1 A_m \log(\tau) + k_2 B_m, \\ b &= k_3 A_b \log(\tau) + k_4 B_b, \\ S &= \exp(k_5 A_S \log(\tau) + k_6 B_S). \end{aligned}$$

The parameters $\Psi = A_m, B_m, A_b, B_b, A_S, B_S$ are the population-level hyperparameters and the constants k_i are introduced to rescale each to be close to unity, in order to increase the efficiency of our sampling. These simple relationships are a pragmatic choice, providing a test of the results from the binned analysis for a small number of hyperparameters.

Figure 5.6 shows the probabilistic graphical model corresponding to this analysis, where the dependencies between the hyperparameters, latent parameters and observables are indicated by arrows. Bayes' theorem now becomes:

$$p\left(\Psi, \phi | d\right) \propto p\left(\Psi\right) p\left(\phi | \Psi\right) p\left(d | \phi\right). \tag{5.5}$$

We choose minimally informative priors on the hyperparameters, Ψ, with each drawn from a normal of the form $\mathcal{N}(\mu, \sigma^2)$ such that:

$$\begin{aligned} A_m &\sim \mathcal{N}(3, 9), \quad & B_m &\sim \mathcal{N}(0, 9), \\ A_b &\sim \mathcal{N}(-3, 9), \quad & B_b &\sim \mathcal{N}(0, 9), \\ A_S &\sim \mathcal{N}(0, 25), \quad & B_S &\sim \mathcal{N}(0, 25), \end{aligned}$$

and, because the HBM is a generative model, we also require priors on R_g and $\log\left(\tau\right)$. We choose these to be broad and likelihood-dominated:

$$\begin{aligned} R_\mathrm{g} &\sim \mathcal{N}(8, 25) \\ \log\left(\tau\right) &\sim \mathcal{N}(0.7, 0.09). \end{aligned}$$

We explore this new parameter space with the No-U-Turn-Sampler (NUTS) variant of the MCMC algorithm (Hoffman and Gelman, 2011), implemented in `NumPyro` (Bingham et al., 2019; Phan, Pradhan, and Jankowiak, 2019), using five chains which each make a total of 15000 samples, 5000 of which are reserved for warm-up. We confirm model convergence by ensuring $\hat{r} < 1.04$ for all parameters (Gelman and Rubin, 1992).

The results for this analysis are shown in Figure 5.7, where the line indicates the median value of the posterior distribution and the filled band is the 68% credible interval, which is larger for younger and older stars where the data are sparser. For comparison, we show the results of the age-binned analysis, plotted against the median age of the population in each bin, with error

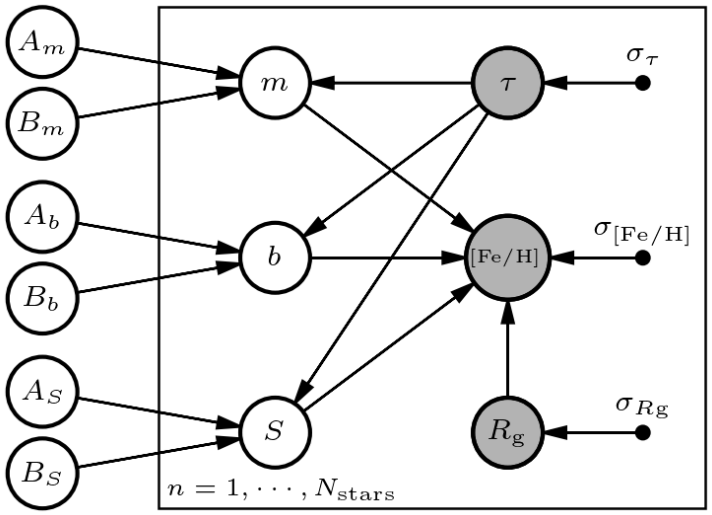


Figure 5.6: A probabilistic graphical model of the hierarchical Bayesian model (HBM). The properties of individual stars are shown inside the rectangle, and the hyperparameters are shown outside. Grey nodes represent observables and their respective observational uncertainties are given by the small black nodes.

bars which show the 68% credible interval. The results of the HBM at the median age of each bin population are reported in Table 5.1, and both sets of results are discussed more fully in the next section.

5.5 Discussion

We have shown results from two complementary methods to measure the radial metallicity gradient over the history of the MW's disc. In the next section, we discuss these results in more detail, as well as what can be learned from their comparison. We give special consideration to the oldest stars in Section 5.5.2 and comment on the possible biases present in our work in Section 5.5.3. Finally, in Section 5.5.4 we compare to predictions from theoretical models of chemo-dynamical evolution and set our work in the context of the literature.

5.5.1 Results of this work

Our sample of K2 oscillating red giants provides excellent coverage of a wide range of guiding radii and ages, which allows the metallicity evolution of the thin disc to be investigated. Using

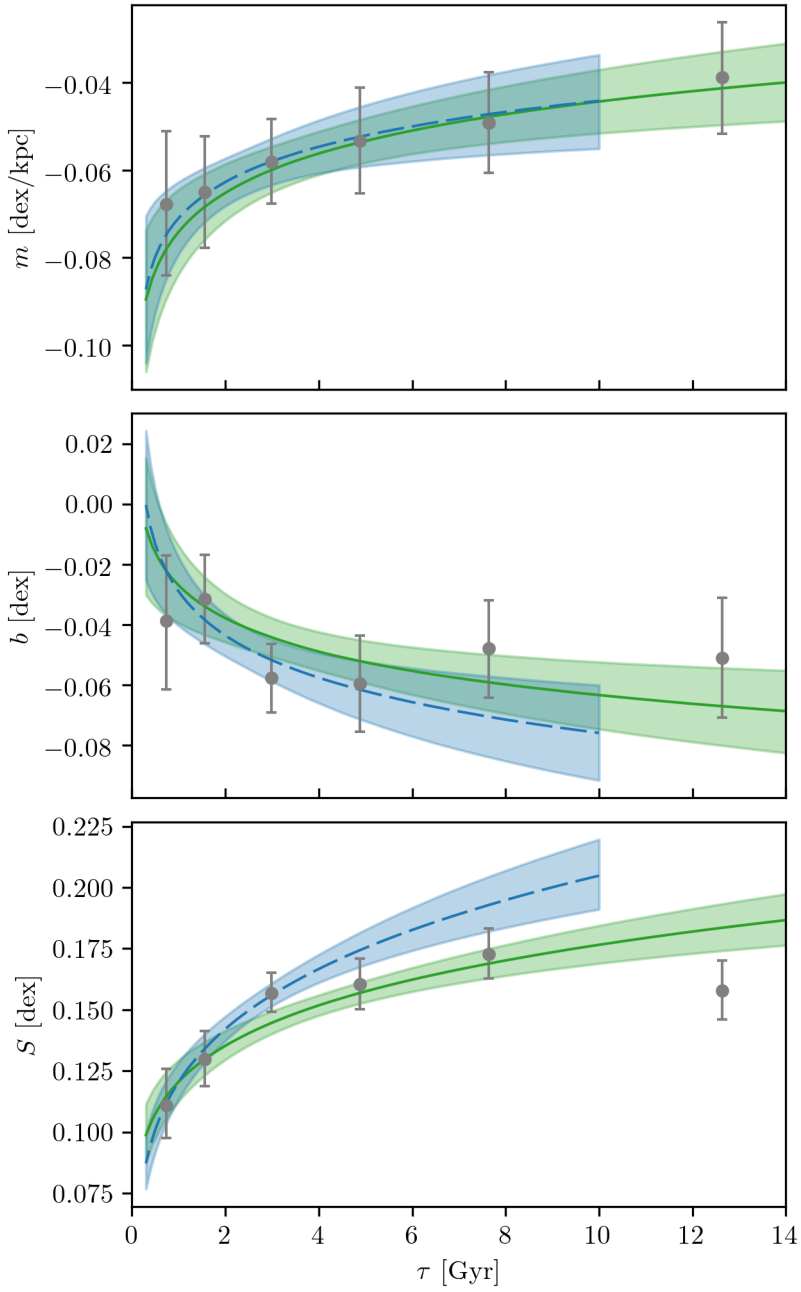


Figure 5.7: Evolution of the fit parameters as a function of stellar age. The grey points show the best-fitting value and 68% credible interval in each bin from the MCMC analysis (plotted against the median age of the population in the bin). The green line and filled region show the result and 68% credible interval from the HBM. The dashed blue line and filled region show the HBM result when stars older than 10 Gyr are excluded from the analysis.

hierarchical Bayesian analysis we obtain constraints which are free from the additional uncertainties introduced by binning. However, in this analysis, it is necessary to assume a functional form for the evolution of the fit parameters, and therefore the HBM does not have the freedom to trace all features of the data. In this way the MCMC analysis performed on the binned data and the HBM are complementary and it is useful to compare their results in detail.

As shown in Figure 5.7 and Table 5.1, the two methods agree very well (within 1σ) at all ages for the gradient and offset at 8 kpc of the radial metallicity relationship. The largest differences are in the stars younger than 2 Gyr, which may be due to the smaller sample size or the assumed functional forms within the HBM. We find that b is below solar metallicity at all ages, suggesting that the Sun was born closer to the Galactic centre than its current position, in agreement with Wielen, Fuchs, and Dettbarn (1996), Minchev, Chiappini, and Martig (2013), and Minchev et al. (2018) and Frankel et al. (2018).

There are more significant differences between the results for the intrinsic spread. This is not surprising because, in the MCMC analysis, the spread arising from the width of each bin and the sample size within each bin are conflated with the underlying physics. Overall the agreement between the methods suggests that the effects of the binning do not dominate. This verification is important as understanding this spread is an important step towards a measurement of the effects of churning (e.g. Haywood, 2008; Kubryk, Prantzos, and Athanassoula, 2015b), though quantifying the effects of radial migration is beyond the scope of this study. It seems likely that the difference in population size (Table 5.1) is the cause of the small fluctuations around the trend shown by the HBM, with slightly larger populations correlating with a larger spread. The deviation is largest in the population older than 10 Gyr and, while the smaller sample size in this bin is still relevant, these stars merit special consideration because they were likely born in an epoch prior to the formation of the thin disc.

5.5.2 Stars older than 10 Gyr

Models of the assembly history of the MW show that the Galactic disc formed $\approx$ 10 Gyr ago (e.g. Belokurov and Kravtsov, 2022). Therefore stars older than this were not born in the thin disc as

we know it today, and this bin contains the highest fraction of contaminants from the debris of mergers or other processes in the MW before the onset of disc formation. Since it is necessary to assume a functional form for the evolution of S, the HBM is not able to trace all features present in the data, so the difference between it and the binned result does not necessarily indicate an effect introduced by the binning. However, we can test the effect of the old population in the HBM by removing it and rerunning the analysis.

After removing stars with $\tau > 10$ Gyr, the HBM results for the slope and offset are consistent within their uncertainties (the blue lines in Figure 5.7), but we find a significantly steeper increase in the spread with age. This indicates that the reduced spread is, at least partly, a physical effect because the old population flattens the fit of the HBM overall. This could be a signature of the small radial extent and centrally concentrated star formation in that epoch of the MW. We also test whether the difference in these HBM results could be due to the larger uncertainty on the age of the older stars, but find that the effect is independent of the size of the age uncertainty.

There is a disagreement between these results and the intermediate age bins (4 Gyr $\leq \tau <$ 6 Gyr and 6 Gyr $\leq \tau <$ 10 Gyr), with the HBM predicting a larger spread, which is driven by the assumption in the HBM of linear dependence on $\log(\tau)$ and the steep increase in spread at young ages.

The age prior in PARAM is deliberately wide and uninformative, which means our sample contains some stars with median age greater than 13.6 Gyr. Since the age posteriors are wide, we do not remove these stars from our analysis, but we confirm that they are not dominating the result in the oldest bin by analysing them separately (Figure 5.8). We find that, though these stars do have a gradient which is significantly flatter than those with 10 Gyr $\leq \tau <$ 13.6 Gyr, the final fit in the bin is almost unaffected by their presence, being fully consistent to the result with the very old stars removed.

5.5.3 Possible sources of bias

In this work, we choose the guiding radius as our primary radial coordinate because it provides a robust estimate of the Galactocentric distance of the star over its whole orbit. For the same

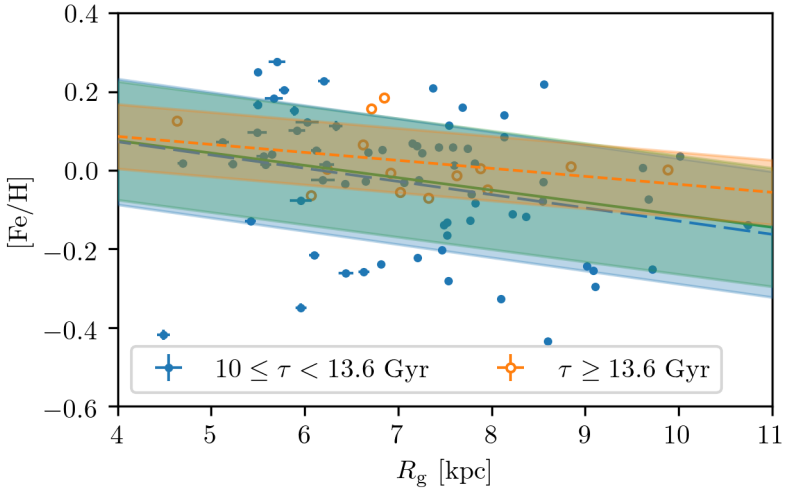


Figure 5.8: Results of the MCMC analysis for the oldest stars in our sample. The green line and filled region in the background show the result when including all stars with $\tau \geq 10$ Gyr, the long-dashed blue line and filled region (which are almost identical to the green) show the result of the analysis excluding stars with $\tau \geq 13.6$ Gyr, and the short-dashed orange line and filled region show the result based on only those stars.

sample, this will naturally tend to flatten the radial metallicity gradient because we observe a limited range of $R_{\rm Gal}$. In the inner Galaxy, it's only possible to observe stars with $R_g < R_{\rm Gal,\,min}$ if they are eccentric enough that their apocentre radius $R_{\rm ap} \geq R_{\rm Gal,\,min}$. We cannot observe stars on circular orbits with the same R_g because they never enter our observable region, so we spread our sample over a wider range of radii, without increasing the range in metallicity. We show this in Appendix B.3, Figures B.4 and B.5, where for $\tau > 2$ Gyr we do find a steeper gradient with $R_{\rm Gal}$. For $\tau < 2$ Gyr the effect is reversed, which is likely to be because the flattening effect of R_g is smaller due to the lower eccentricities of the younger population. The irregular distribution of the stars in $R_{\rm Gal}$ (Figure B.4) may then lead to a slight flattening of the gradient.

The equivalent argument can be made for stars with $R_g > R_{\rm Gal,\,max}$ and pericentre radius $R_{\rm pe} \leq R_{\rm Gal,\,max}$, but in our sample the two effects do not appear symmetrically: we have more stars with $R_g < R_{\rm Gal,min}$ than $R_g > R_{\rm Gal,\,max}$. The stellar density in the outer disc is lower, so we would see fewer of such stars in a spatially uniform sample, but we see roughly the same number of stars close to our radial limits ($R_{\rm Gal,\,min} \approx 5.5$ kpc, $R_{\rm Gal,\,max} \approx 10$ kpc). We can motivate the asymmetry by considering the probability of observing the 'inner' star ($R_g < R_{\rm Gal,\,min}$) while it is passing through the observable region, compared to the 'outer' star. As an example, our

sample contains one star with $R_g < 4$ kpc - i.e. which is observed more than 1.5 kpc away from its guiding radius. This means it has an eccentricity of $e \gtrsim 0.3$. An equivalent target in the outer disc with $R_g > 11.5$ kpc has $e \gtrsim 0.2$. Since low eccentricity stars dominate the population in the thin disc, it might seem surprising that we do not observe any stars with $R_g \gtrsim 10.5$ kpc. However, when we consider the probability of each star being in the part of its orbit where it is close enough to the solar position to be observable, as a fraction of its full orbit, we find that $P_{\mathrm{obs,\,inner}} \approx 2P_{\mathrm{obs,\,outer}}$. Given the small numbers involved, this is enough to explain the asymmetry in our sample.

Working in R_g may also introduce a kinematic bias since higher eccentricity stars tend to be older and thus more metal-poor. This could mean that we miss higher metallicity stars at low R_g and recover an overly flat gradient. Examining Figure 5.4, this does not appear to be the case, but as a test we repeat the HBM analysis, removing targets with $R_g < 5.5$ kpc. The result is shown in Figure B.6, where we see a slightly steeper gradient for stars older than 2 Gyr, but it is still fully consistent with the results from the full sample within the uncertainties.

5.5.4 Comparison to literature

In this section, we compare the results of our analysis to those from other studies based on field stars, Cepheid variables and OCs, as well as theoretical models.

Field stars and Cepheid Variables

Below we compare only to works with ages which are 'directly' inferred, either from comparison to isochrones or asteroseismology, similar to those used in this work. A comparison to the numerous age estimates available from machine learning methods is beyond the scope of this work and will be completed in a later study.

Nordström et al. (2004) and Casagrande et al. (2011) investigated the radial metallicity gradient in the Geneva-Copenhagen Survey (GCS). The large sample of local solar neighbourhood F and G dwarfs extends to ≈ 0.4 kpc from the solar position and has metallicity determinations based on Strömgren photometry and ages obtained from comparison to isochrones. Though the

precision of the ages is around 25%, they are subject to significant uncertainties arising from the calibration of the metallicity and temperature scales. The sample is dominated by young stars ($\tau \approx 2$ Gyr) due to the magnitude limits of the survey and its local volume, and between the works of Nordström et al. (2004) and Casagrande et al. (2011) the ages of many stars change by ≈ 1 Gyr as a result of changes to these calibrations.

Nordström et al. (2004) use the mean radius $R_\mathrm{m} = 0.5 \times (R_\mathrm{ap} + R_\mathrm{pe})$, extending their radial range to $6\,\mathrm{kpc} < R_\mathrm{m} < 9\,\mathrm{kpc}$, and find a gradient of -0.076 ± 0.014 dex/kpc for stars younger than 1.5 Gyr, and a steeper gradient of -0.099 ± 0.011 dex/kpc in an intermediate age population of $4\,\mathrm{Gyr} < \tau < 6\,\mathrm{Gyr}$. Their oldest population ($\tau > 10$ Gyr) is consistent with no gradient (0.028 ± 0.036 dex/kpc) and they suggest that this indicates that these stars are not thin disc members. We discuss the stars older than 10 Gyr present in our sample in Section 5.5.2.

Casagrande et al. (2011) improved on the age estimates of Nordström et al. (2004) and reanalysed the GCS sample to find a metallicity gradient with both R_m and R_g. They found a similar trend of a steeper gradient at intermediate ages than for the youngest stars, before flattening with age to a positive gradient in the older population. Their gradient with R_m is 0.05 dex/kpc – 0.01 dex/kpc less (in the sense of flattening a negative gradient) than Nordström et al. (2004) across the age range, and the main effect of switching to R_g is to soften the trend towards a steeper gradient at intermediate ages so that it is nearly flat.

Anders et al. (2017b) used a sample of around 400 red giants observed by CoRoT (from which they obtain asteroseismic age constraints) and APOGEE, with $6\,\mathrm{kpc} < R_\mathrm{Gal} < 13\,\mathrm{kpc}$ and $|Z_\mathrm{Gal}| < 0.3\,\mathrm{kpc}$. After applying a correction for the selection function (derived from comparison to a chemo-dynamical simulation) they find a gradient with R_Gal of $-0.058 \pm 0.008 \pm 0.003$ dex/kpc (statistical and systematic uncertainty) for $\tau < 1$ Gyr, steepening to $-0.066 \pm 0.007 \pm 0.002$ dex/kpc between 1 Gyr and 4 Gyr, before flattening to ≈ 0.03 dex/kpc between 6 Gyr and 10 Gyr.

Finally, Xiang et al. (2015) and Wang et al. (2019) and Vickers, Shen, and Li (2021) used large samples of main sequence turn-off and subgiant stars (0.3 million, with $8\,\mathrm{kpc} < R_\mathrm{Gal} < 11\,\mathrm{kpc}$; 0.94 million, with $7\,\mathrm{kpc} < R_\mathrm{Gal} < 11\,\mathrm{kpc}$; and 1.3 million, with $6\,\mathrm{kpc} < R_\mathrm{g} < 10\,\mathrm{kpc}$,

respectively) observed by LAMOST, with ages determined from isochrone comparisons. Xiang et al. (2015) and Wang et al. (2019) selected stars in slices of $|Z_{\rm Gal}|$ and investigated the gradient with $R_{\rm Gal}$. For stars close to the plane, both find the steepest gradient at intermediate ages (6 Gyr - 8 Gyr in Xiang et al. (2015) and 4 Gyr - 6 Gyr in Wang et al. (2019)), with younger and older stars showing shallower gradients. The gradients of Wang et al. (2019) are consistent with our results for the youngest and oldest stars, and steepen to ≈ -0.1 dex/kpc in between. Vickers, Shen, and Li (2021) select stars with low $Z_{\rm max}$ and α-abundance (similar to the procedure in this work) and find that the gradient with $R_{\rm g}$ flattens monotonically with age. Their results agree very well with this work at all ages.

Though most of the results described above agree with each other, and this work, within a few σ, they fall into two groups according to how the gradient varies with age. In this work and in Vickers, Shen, and Li (2021) the gradient flattens smoothly stellar age, while the other studies show a steeper gradient in intermediate-age stars of $\tau \approx 4$ Gyr than in the younger population (though this is least obvious in the $R_{\rm g}$ case of Casagrande et al. (2011)). comparisons are complicated by the different selection functions of each sample, but below we consider two other possible causes of this difference: the degree to which the population is contaminated by thick disc stars, and the choice of radial coordinate.

Considering first the contamination by thick disc stars, we refer to the works of Anders et al. (2014) (using $R_{\rm g}$ and $Z_{\rm max}$) and Hayden et al. (2014) (using $R_{\rm Gal}$ and $Z_{\rm Gal}$), in addition to Xiang et al. (2015) and Wang et al. (2019) and Vickers, Shen, and Li (2021), on the vertical dependence of the metallicity gradient. They all found that the radial metallicity gradient flattens with height above the Galactic plane. Including these thicker-disc stars could, therefore, flatten the overall gradient. This effect would be especially important in the younger population because the intrinsic scatter is low and, when working in $R_{\rm g}$ or $R_{\rm m}$, because the radial extent tends to be reduced due to the generally low eccentricities compared to the older stars. We show the effect of including stars with higher $Z_{\rm max}$ in Appendix B.2 where Figure B.2 shows a flatter gradient in the youngest age bin, more similar to previous studies, and Vickers, Shen, and Li (2021) also recover this effect for intermediate $Z_{\rm max}$ ($0.25\,{\rm kpc} < Z_{\rm max} < 0.75\,{\rm kpc}$). Though the

contamination of the GCS sample is likely to be small due to its small range in $R_{\rm Gal}$ and $Z_{\rm Gal}$, a few stars passing through the thin disc could be enough to cause this effect. The range of the Anders et al. (2017b) sample is larger and the selection for thin disc members is based on $Z_{\rm Gal}$, so stars on kinematically hot orbits which are currently close to the plane of the disc are still included. Since the studies of Anders et al. (2014) and Hayden et al. (2014) do not include age information, it is difficult to be sure that the flattening of the gradient in their results is driven by the distance from the plane, rather than an effect of the shift to older age distributions at a greater distance from the disc. However, Xiang et al. (2015) and Wang et al. (2019) and Vickers, Shen, and Li (2021) show this effect across a range of ages, and it will be investigated in our sample in a future study.

The choice of radial coordinate may also play a role: as described in Section 5.5.3, we would naively expect the change from $R_{\rm Gal}$ to $R_{\rm g}$ to flatten the observed metallicity gradient. We show the results of our analysis using $R_{\rm Gal}$ in Appendix B.3 where, for stars older than 3 Gyr, we do indeed see a steeper gradient. However, the gradient in the younger population is steeper in the $R_{\rm Gal}$ results, reproducing the effect seen in GCS and the works of Xiang et al. (2015) and Anders et al. (2017b) and Wang et al. (2019). As mentioned above, almost all of these stars have very low eccentricity, so the flattening effect of using $R_{\rm g}$ would be reduced, and it is possible that the uneven radial distribution (Figure B.4) in this small sample results in a steeper gradient overall.

Cepheid variables are good tracers of the present-day metallicity gradient as they provide a long radial baseline for targets which are 20 - 400 Myr old. Genovali et al. (2014) compiled a sample of 450 Cepheids with $4\,{\rm kpc} < R_{\rm Gal} < 19\,{\rm kpc}$ and found a gradient of -0.05 - $-0.06\,{\rm dex/kpc}$, depending on the sample used and the cut in $Z_{\rm Gal}$ applied, which is consistent with our MCMC results for the bin containing the youngest stars.

Open Clusters

There are many studies in which the radial metallicity gradient is constrained by observations of OCs (e.g. Magrini et al., 2009; Casamiquela et al., 2017, 2019; Spina et al., 2021; Myers et al., 2022; Netopil et al., 2022; Spina, Magrini, and Cunha, 2022; Gaia Collaboration et al.,

2023a) Here we mention just three recent examples, which benefit from advances in high-resolution spectroscopy, and both astrometry (for improving membership determination) and all-sky spectral analysis from *Gaia*.

Myers et al. (2022) use a sample of 85 OCs from the Open Cluster Chemical Abundances and Mapping survey (OCCAM), based on APOGEE DR17 abundances, with a radial range of $6\,\mathrm{kpc} < R_{\mathrm{Gal}} < 16\,\mathrm{kpc}$. They find a break in the radial metallicity relationship at around 12 kpc, recovering a gradient of $-0.073 \pm 0.002\,\mathrm{dex/kpc}$ inside and $-0.032 \pm 0.002\,\mathrm{dex/kpc}$ outside this radius.

Netopil et al. (2022) use 136 OCs compiled from various surveys and find that the relationship is well fit by a single line with gradient $-0.058\,\mathrm{dex/kpc}$ over a similar radial range in R_{Gal}. Their results are supported by photometric observations of a further 10 clusters, and they suggest that the appearance of a break in the relationship as seen in Myers et al. (2022) is strongly dependent on the specific objects included in the study, as well as the adopted distance scale.

Both these studies suffer to some extent from a fairly limited sample size, particularly in resolving the question of a break in the relationship. Spectral analysis from *Gaia* may now start to resolve this, for example, Gaia Collaboration et al. (2023a) have a sample of 503 clusters. However, they restrict their analysis of the metallicity gradient to $R_{\mathrm{Gal}} < 12\,\mathrm{kpc}$, so do not probe the region in question. They find a gradient of $-0.063 \pm 0.008\,\mathrm{dex/kpc}$ with R_{g} in the inner disc.

Investigating the evolution of the radial metallicity relationship with OCs presents an additional challenge, as the small samples must be broken into bins with few data in each, and the age range is restricted to a few Gyr at most. Gaia Collaboration et al. (2023a) and Netopil et al. (2022) divide their samples into 4 and 5 age bins, extending up to ≈ 5 and ≈ 7 Gyr respectively. In both cases, the gradient is found to increase as a function of age: the opposite of the trend observed in field stars. As proposed by Anders et al. (2017b) and Spina et al. (2021), this effect could be due to a survival bias for open clusters, as high metallicity clusters born in the inner disc are more likely to survive if they migrate outwards to Galactic regions where the potentials of the spiral arm and bar are weaker (see also Lynga and Palous, 1987). Low metallicity clusters from the outer disc which migrate towards the Galactic centre are more likely to be disrupted

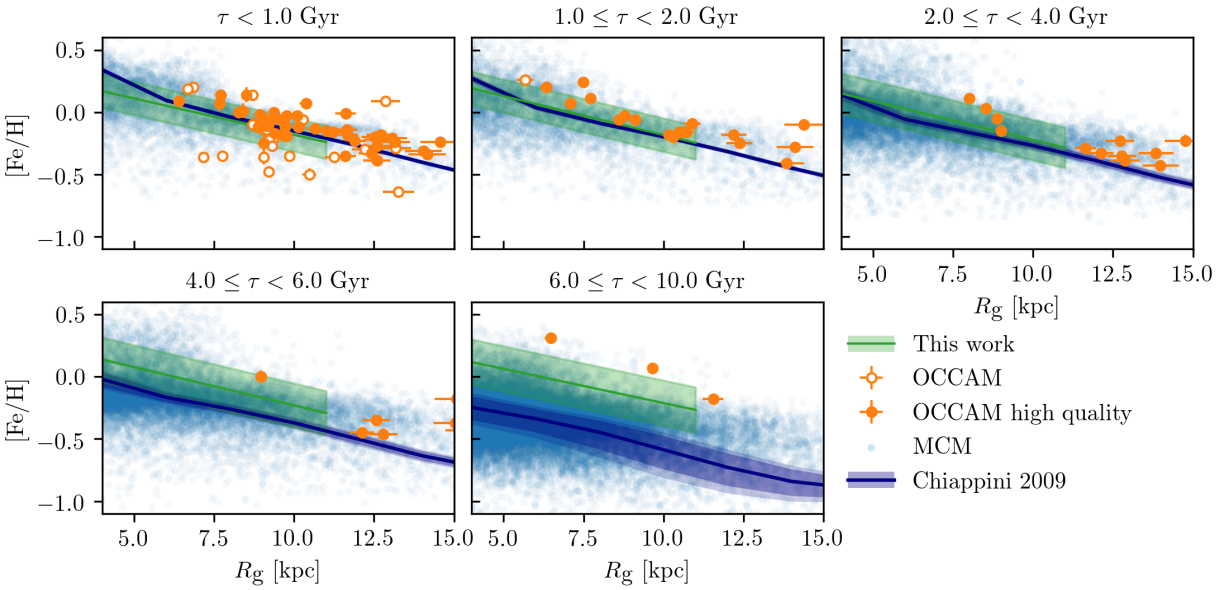


Figure 5.9: [Fe/H] vs. R_g in five bins of age. The orange and white points show the high-quality and plausible samples from the OCCAM survey (Myers et al., 2022), respectively. The blue points are the results of the MCM chemo-dynamical simulation (Minchev, Chiappini, and Martig, 2013, 2014), with the underlying chemical evolution model of Chiappini (2009) shown by the blue line and filled region. The green line shows the best-fitting radial metallicity gradient from the MCMC analysis of this work, with a filled region representing 1σ of the intrinsic spread.

and are, therefore, missing in the older population, which shows a steeper gradient as a result. We show the clusters used in the work of Myers et al. (2022) in Figure 5.9 because they use the same chemical abundances as employed in this work. The metallicity offset can be clearly seen in the $6\,\text{Gyr} \leq \tau < 10\,\text{Gyr}$ bin.

Models

Figure 5.9 also shows a comparison to the chemo-dynamical simulation of Minchev, Chiappini, and Martig (2013, 2014, hereafter MCM) and the underlying chemical evolution model (Chiappini, 2009). There is a great diversity of chemical evolution models and simulations (e.g. Schönrich and Binney, 2009a,b; Grand, Kawata, and Cropper, 2015; Kubryk, Prantzos, and Athanassoula, 2015a,b; Grisoni et al., 2017; Grisoni, Spitoni, and Matteucci, 2018; Vincenzo and Kobayashi, 2020; Spitoni et al., 2021) and we choose the MCM simulation to facilitate easy comparison with the works of Anders et al. (2017b), Casamiquela et al. (2017, 2019) and Myers et al. (2022). The model was computed in instantaneously mixed galactocentric annuli 2 kpc

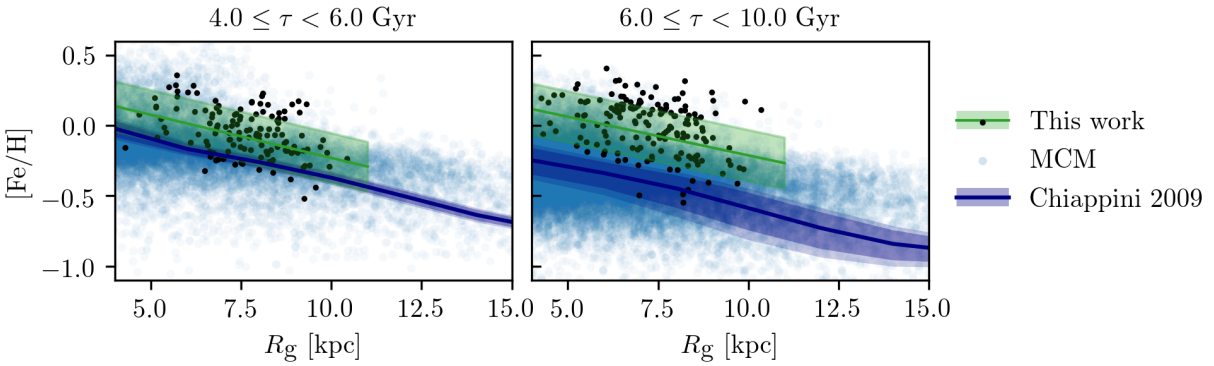


Figure 5.10: Same as Figure 5.9 for two age bins with the thin disc sample shown in black points, binned according to the median age of each star.

wide and for this plot, we interpolate between those annuli and transform from $R_{\rm Gal}$ to $R_{\rm g}$. The metallicity is scaled to reproduce the solar value at approximately the time and location of the Sun's birth (≈ 4 Gyr ago and $R_{\rm Gal} \approx 6$ kpc; Minchev, Chiappini, and Martig 2013). To allow a qualitative comparison to our results, the particles from the MCM are restricted to those with $Z_{\rm Gal} < 1$ kpc since the scale height of the simulated disc is larger than the MW's thin disc.

Our results are reasonably consistent with the chemical evolution model and MCM simulation at ages below ≈ 4 Gyr. In the older populations, the simulated particles show a more rapid flattening of the gradient, and an offset towards lower metallicities in the model becomes more apparent. This is likely due to the initial conditions of the models, as the thin disc is not pre-enriched in metals, giving a very metal-poor result at ages close to the start of disc formation. Our results, which are not subject to the metallicity bias which affects the older OCs, demonstrate that this very low metallicity is not a good representation of the thin disc's early state, and this effect is shown more clearly in comparison to the individual stars in our sample in Figure 5.10.

5.6 Conclusions

We have used the wide spatial and temporal coverage of the K2-APOGEE sample to study the evolution of the Milky Way's radial metallicity gradient in the range $4\,{\rm kpc} < R_{\rm g} < 11\,{\rm kpc}$ across the whole history of the thin disc. We find a gradient which flattens monotonically from $\approx -0.07\,{\rm dex/kpc}$ in stars of $\tau \approx 0.7\,{\rm Gyr}$ to $\approx -0.04\,{\rm dex\,kpc^{-1}}$ at $\tau \approx 12.6\,{\rm Gyr}$. The intrinsic

spread around this gradient, which is primarily caused by churning, increases with the age of the population until $\tau \approx 10\,\mathrm{Gyr}$. In older stars, the spread is slightly reduced, which we attribute to this population forming before the thin disc when star formation in the MW was very centrally concentrated. We also find that the metallicity of the solar neighbourhood has increased slightly over the last 5 Gyr to ≈ -0.04 dex, and that it is sub-solar throughout the history of the disc, indicating that the Sun migrated out from its birth radius to current position.

We have compared our results to other studies of field stars and explained the differences in our results in terms of the more robust selection of thin disc members and choice of guiding radius as the radial coordinate used in this work. We have also compared to recent studies of open clusters and have shown that older clusters appear to be subject to a survival bias, favouring those of higher metallicity. Finally, we have provided a qualitative comparison to the chemical evolution model of Chiappini (2009) and the chemo-dynamical simulation of Minchev, Chiappini, and Martig (2013, 2014). The most striking difference to our results is their much lower metallicity at ages above $\approx 6\,\mathrm{Gyr}$, which we attribute to the assumptions about the initial conditions in the model. Our results will facilitate new tests of the initial conditions and physics in models and simulations of MW evolution.

In the next decade, the ESA PLAnetary Transits and Oscillations of stars (PLATO) mission (Rauer et al., 2014) can potentially provide ages with 10% precision (Miglio et al., 2017) for a large sample of red giants. These data, combined with astrometry and spectroscopy from ongoing and planned surveys will allow the early evolution of the MW discs to be probed in detail and give a more precise measurement of the evolution of the metallicity gradient. These insights will throw new light on the open questions concerning the origin, strength and importance of radial migration in the Galactic archaeology fossil record.

Chapter 6

MILKY WAY HELIUM ENRICHMENT CONSTRAINED BY RC STARS

This chapter presents a draft copy of the paper with the above title. I confirm that all writing is my own, with editorial contributions from A. Miglio. The work presented is my own, with the exception of the computation of the stellar evolutionary models in MESA, which were provided by M. Tailo. Data are obtained from sources cited in the text.

6.1 Introduction and motivation

Initial chemical composition significantly affects all aspects of stellar structure and evolution. Therefore, the observable properties of resolved and integrated stellar populations are related to the abundances of helium and heavier elements in their member stars. The initial metal mass fraction, Z, can be constrained by spectroscopic observations, but the spectral features of helium are not observable at temperatures below $\sim 20\,000$ K. Low-mass stars, which are a valuable resource for studies of stellar evolution and the history of the Milky Way are below this temperature limit for most of their lifetimes and in advanced stages of evolution when the temperature does reach high enough, the helium abundance, Y at the stellar surface is no longer representative of the initial value.

In most cases, therefore, Y is estimated by indirect methods. Usually, a linear relationship between the enrichment of helium and metals in the interstellar medium (ISM) is assumed,

characterised by the enrichment ratio, $\Delta Y/\Delta Z$. Under this assumption, Y is estimated from $\Delta Y/\Delta Z$, Z, and the primordial helium abundance Y_p:

$$Y = \frac{\Delta Y}{\Delta Z} Z + Y_p. \tag{6.1}$$

Though assumption of a linear relationship is supported by some models of Galactic chemical evolution (e.g. Carigi and Peimbert, 2008; Vincenzo et al., 2019a), this is difficult to reconcile with the wide range of values ($\Delta Y/\Delta Z$ between ~ 1 and 5) found in the literature, using constraints from different observations (see Section 6.4.3). In particular, differences in helium enrichment have been found between stars in the multiple populations of some globular clusters (e.g. Lagioia et al., 2018; Milone et al., 2018) demonstrating that different enrichment histories are possible, at least in the case of these tightly-bound systems, and there are hints that the Galactic bulge may have experienced enhanced helium enrichment compared to the disc (Nataf and Gould, 2012). In addition, while Y_p is well constrained (Workman et al., 2022), the uncertainties on $\Delta Y/\Delta Z$ exceed 20% in many cases.

This lack of consensus is a significant problem, as an assumption of $\Delta Y/\Delta Z$ is required to make the computation of grids of stellar models tractable in many applications, across all scales of astrophysics. Of particular importance in the modern era of Galactic archaeology, is the effect on the age estimates of stars, which provide the chronological information from which the history of the MW is untangled. Indeed, Lebreton, Goupil, and Montalbán (2014a) found helium abundance and $\Delta Y/\Delta Z$ to be amongst the most significant sources of uncertainty on the duration of the main sequence (MS) – and, therefore, the age – in models of low-mass stars, with the stellar age at the turn-off varying by as much as 40 % for quite conservative changes in Y and $\Delta Y/\Delta Z$. This can be motivated by considering the approximate scaling of MS luminosity with mean molecular weight, μ, $L \propto \mu^{15/2}$ and the simple scaling of MS lifetime with luminosity and stellar mass, $\tau_{MS} \propto M/L$, from which we see that increasing Y by 0.02 leads to a $\sim$ 10% decrease in τ_{MS} (Kippenhahn, 2012). The precise effect of changing Y on the estimates of the stellar age is further complicated by the need to consider the full range of observables which are

used in grid-based modelling, and the fact that the scale of the effect changes as a function of metallicity (see Miglio et al., 2021).

In this work, we use the luminosity of red clump (RC) stars as a proxy for Y and so constrain $\Delta Y/\Delta Z$. The RC is formed of core helium-burning (CHeB) stars of sufficiently low mass that they have a degenerate core when they reach the tip of the red giant branch (RGB). The result is that helium ignition is delayed until the core reaches a critical mass, which depends only weakly on stellar mass and composition (Girardi, 2016). For this reason, the luminosity, L also depends weakly on the mass, M, and metallicity[1] of the stellar envelope, and small changes in L caused by differences in Y between stars can be observed.

For an RC star of given M and [Fe/H], increasing Y has two effects on the total luminosity. First, the μ is increased, resulting in higher internal temperatures during the ascent of the RGB, earlier ignition of the helium core and lower luminosity during the CHeB phase. However, the efficiency of hydrogen shell burning is increased, and this causes a corresponding increase in luminosity. For RC stars, which have sizeable envelopes, this effect dominates and we expect higher luminosities at higher helium abundances overall. In higher mass stars, the core mass during CHeB depends on the mass of the core during the MS, meaning that the luminosity is sensitive to overshooting during the MS, and the total stellar mass and [Fe/H].

In Figure 6.1 we show the evolutionary track of a 1 $M_\odot$, solar-metallicity model with $Y = 0.28$. The evolution from the MS to the tip of the RGB is shown in black, the CHeB phase in red (see Section 6.3.1 for the definition of this phase) and the rapid change in $T_{\rm eff}$ and L corresponding to the helium flash in grey. The inset plot shows a closer view of the RC, and the same phase for a track of $M = 1M_\odot$, [Fe/H] = 0, $Y = 0.31$ the ages of the stars in this phase are approximately 10 Gyr when $Y = 0.28$ and 8.5 Gyr for $Y = 0.31$. In Figures 6.2 and 6.3 we show selected (M, [Fe/H]) coordinates from the model grid used in this work (Section 6.3.1). We see that, though the luminosity is a function of the mass and metallicity, the helium abundance dominates these contributions. The luminosity also depends on how far through the

[1]Throughout this work we use iron abundance as a tracer for metallicity: $[{\rm Fe/H}] = \log_{10}(N_{\rm Fe}/N_{\rm H})_* - \log_{10}(N_{\rm Fe}/N_{\rm H})_\odot$, where $N_{\rm Fe}$ and $N_{\rm H}$ are the numbers of iron and hydrogen nuclei per unit volume of the stellar photosphere, respectively.

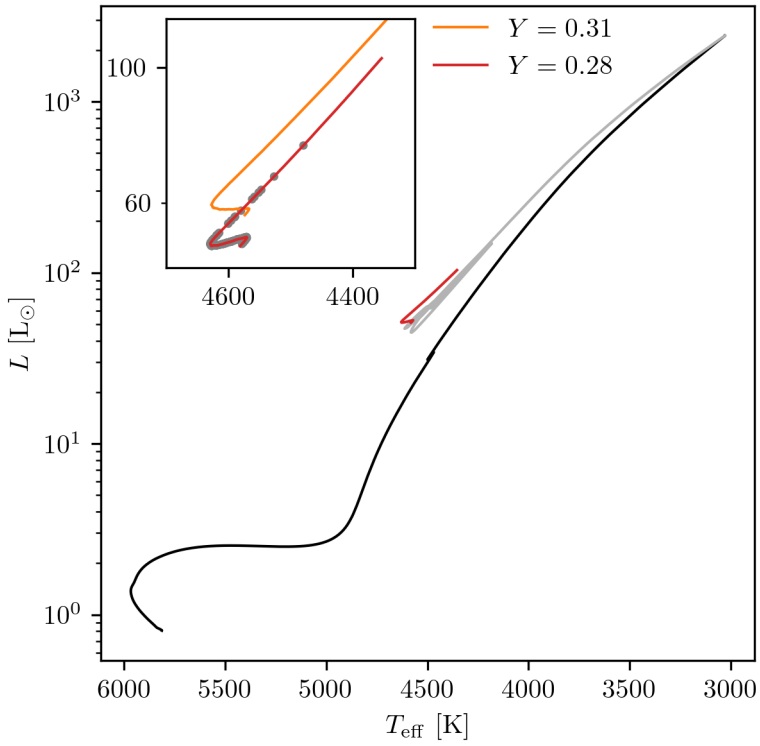


Figure 6.1: Main panel: the evolutionary track of a 1 $M_\odot$, solar metallicity model with $Y = 0.28$, showing the evolution from the MS to the tip of the RGB in black, the helium flash in grey and the CHeB phase in red. Inset panel: a closer view of the CHeB phase, and the same phase for a track of $Y = 0.31$. Grey points are positions of 100 EEPs (see Section 6.3.1) obtained by sampling the track uniformly in fractional age.

CHeB phase the star is, but because the evolution is much slower at the low-luminosity end of the track, the luminosity of a given $(M, [\mathrm{Fe/H}], Y)$ model is well characterised by the value there (see Section 6.3.1).

We use red giants observed by *Kepler* (Borucki et al., 2010; Gilliland et al., 2010), where the available asteroseismic information makes it possible to robustly separate CHeB and RGB stars and constrain the stellar mass. By comparing the very high-precision luminosities based on parallaxes from *Gaia* (Gaia Collaboration et al., 2016, 2023c) to a grid of stellar models of different helium abundance, we estimate Y and thus constrain $\Delta Y/\Delta Z$.

The rest of this paper is organised as follows: in Section 6.2 we introduce the observational data, and how RC stars are selected. Section 6.3 describes the model grid, our analysis and validation of our approach based on mock data. Our results are presented and discussed in Section 6.4, and a summary and conclusions are given in Section 6.5.

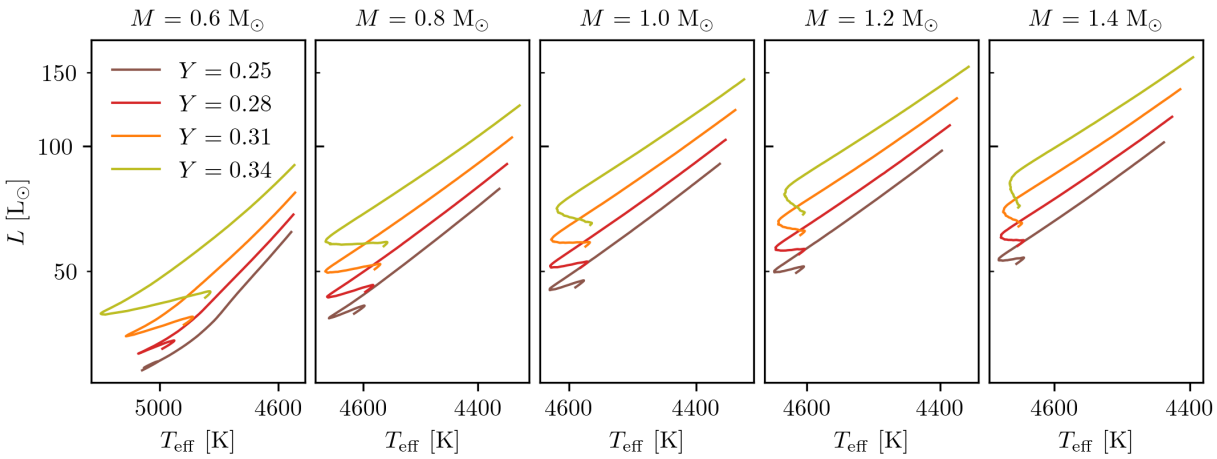


Figure 6.2: Evolutionary tracks of the CHeB phase for models of different M and Y, with [Fe/H] = 0.0. Models with $M = 0.6 M_\odot$ are excluded from our analysis as their luminosity distributions when sampled uniformly in fractional age, are not easily separable between the Y coordinates. The tracks are shown on separate axes for clarity, given the overlap in $T_{\rm eff}$.

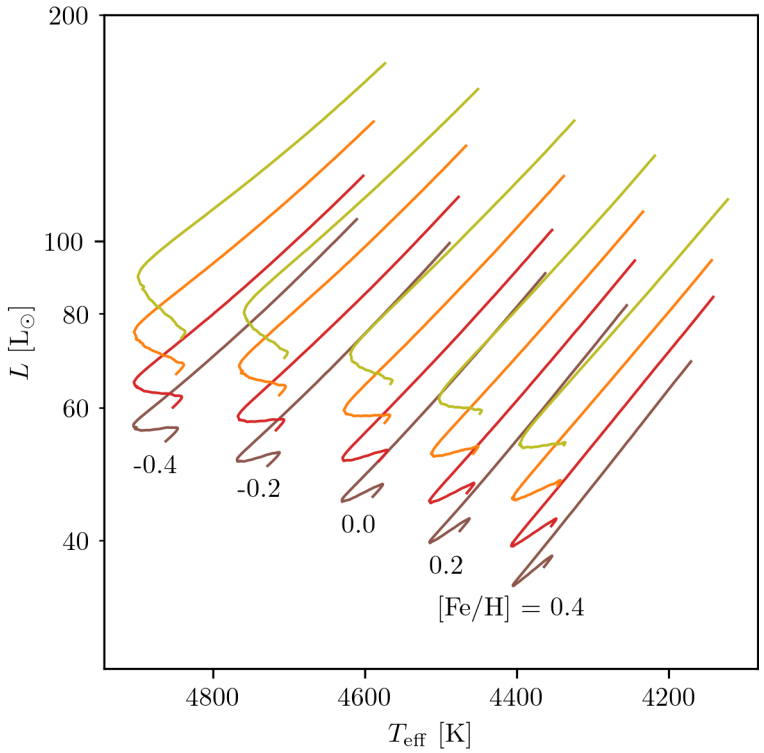


Figure 6.3: Evolutionary tracks of the CHeB phase for models of different [Fe/H] and Y, with $M = 1.0 M_\odot$.

6.2 Observational constraints

In this section, we describe our sample of *Kepler* solar-like oscillating red giants (Section 6.2.1), how members of the RC were selected, based on the asteroseismic information (Section 6.2.2), and outline how the stellar parameters were inferred from the observables (Section 6.2.3).

6.2.1 Asteroseismic, spectroscopic and astrometric constraints

Our sample is based upon the catalogue of Yu et al. (2018), which contains homogeneously determined asteroseismic parameters (the frequency of maximum oscillation power, $\nu_{\rm max}$, and large frequency separation, $\Delta\nu$) for 16000 red giants. Chapter 4 provides a crossmatch of this catalogue with the Apache Point Observatory Galactic Evolution Experiment (APOGEE) Data Release (DR) 17 (Majewski et al., 2017; Abdurro'uf et al., 2022), from which we obtain [Fe/H], α element abundance, $T_{\rm eff}$ and $\log g$, and *Gaia* DR3, which provides the parallax, ϖ of each source. The spectroscopically derived parameters are produced by the APOGEE Stellar Parameters and Chemical Abundances Pipeline (ASPCAP) (García Pérez et al., 2016), and a full description of this pipeline as applied to APOGEE DR17 is given in Holtzman et al. (in preparation). In our analysis, we remove target with the `ASPCAPFLAG` `STAR_BAD` or `STAR_WARN` set and also, following L. Lindegren (2018) targets with *Gaia* `ruwe` > 1.4 or marked by the `non_single_star` flag.

6.2.2 Red clump selection

From these observations, we identify members of the RC in two stages. First, we separate the CHeB stars from those ascending the RGB using the evolutionary state flag provided by Yu et al. (2018). From these stars, we isolate the 'true' RC (stars with degenerate-cored progenitors) from the higher mass secondary red clump (SRC) by requiring $\Delta\nu \leq 4.5\,\mu$Hz (Mosser et al., 2014). Figure 6.4 shows the appearance of this selection in the HRD.

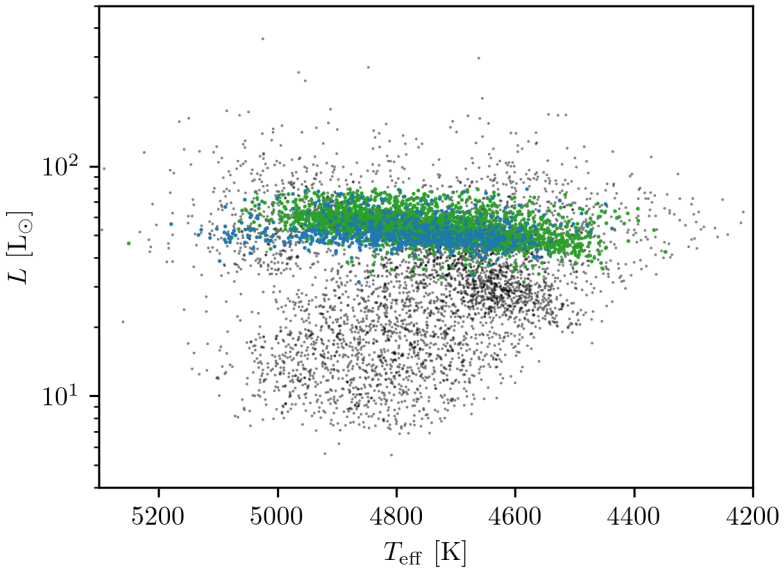


Figure 6.4: HRD showing stars flagged as RC members with low- (green) or high- (blue) α element abundance, compared to the full sample (black).

6.2.3 Stellar parameters

We use the luminosity provided in Chapter 4, which is computed from the *Gaia* parallax, requiring $\sigma_\varpi/\varpi > 5$, and using the bolometric corrections of Casagrande and VandenBerg (2014) and extinction from the `Bayestar19` dustmap (Green et al., 2014; Green et al., 2019). The parallax zero-point offset is corrected using the method of Lindegren et al. (2021), which Khan et al. (2023) found to work well in the *Kepler* field.

We estimate the stellar mass using the scaling relation

$$\frac{M}{M_\odot} = \frac{\nu_{\rm max}}{\nu_{\rm max,\odot}} \frac{L}{L_\odot} \left(\frac{T_{\rm eff}}{T_{\rm eff,\odot}} \right)^{\frac{-7}{2}}, \tag{6.2}$$

which provides a more robust estimate for these low-mass RC stars than the usual asteroseismic relation based on $\nu_{\rm max}$ and $\Delta\nu$, where the evolutionary state-dependent correction to the $\Delta\nu$ scaling is significant (Miglio et al., 2016). Other methods based on asteroseismology (e.g. the determination from PARAM included in Chapter 4) introduce a model dependence, which we seek to avoid here.

Finally, we consider α-enriched stars separately from the low-α sequence, using the sep-

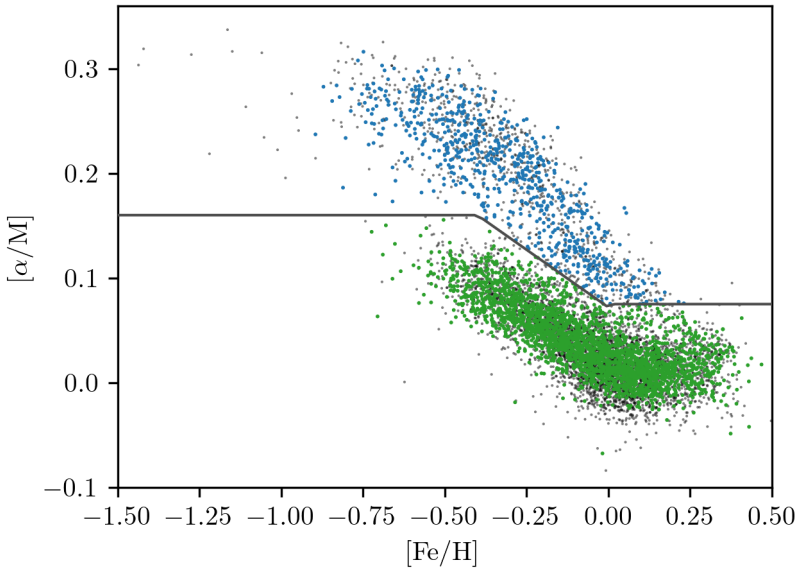


Figure 6.5: Average α element abundance [α/M] vs. [Fe/H]. The high- and low-α sequences were separated along the grey line. The colours are the same as Figure 6.4.

aration shown in Figure 6.5. These two populations are widely considered to have formed in different events (see Helmi, 2020, for a review) and, therefore, may show different helium enrichment histories. For the high-α stars [Fe/H] does not provide a good estimate of the total stellar metallicity so we rescale the observed value to the solar α abundance using the approach of Salaris, Chieffi, and Straniero (1993). Overall, we have 2603 low-α and 705 high-α RC stars. Distributions of some relevant stellar parameters and their uncertainties are shown in Figure 6.6.

6.3 Method

This section describes the steps to constrain $\Delta Y/\Delta Z$ for the observed stars by comparison to the model grid (Section 6.3.1) inference of Y (Section 6.3.2), fitting the inferred $Y(Z)$ relationship (Section 6.3.3) and validation of the approach with a mock dataset (Section 6.3.4).

6.3.1 Model grid

Our grid of stellar models is computed in MESA (Paxton et al., 2011, 2013, 2015, 2018, 2019; Jermyn et al., 2023), with dimensions $0.6 \leq M \leq 1.8\mathrm{M}_\odot$ in steps of $0.1\mathrm{M}_\odot$, and $-0.6 \leq$ [Fe/H] ≤ 0.5 in steps of 0.1 dex. At each (M, [Fe/H]) coordinate, we compute

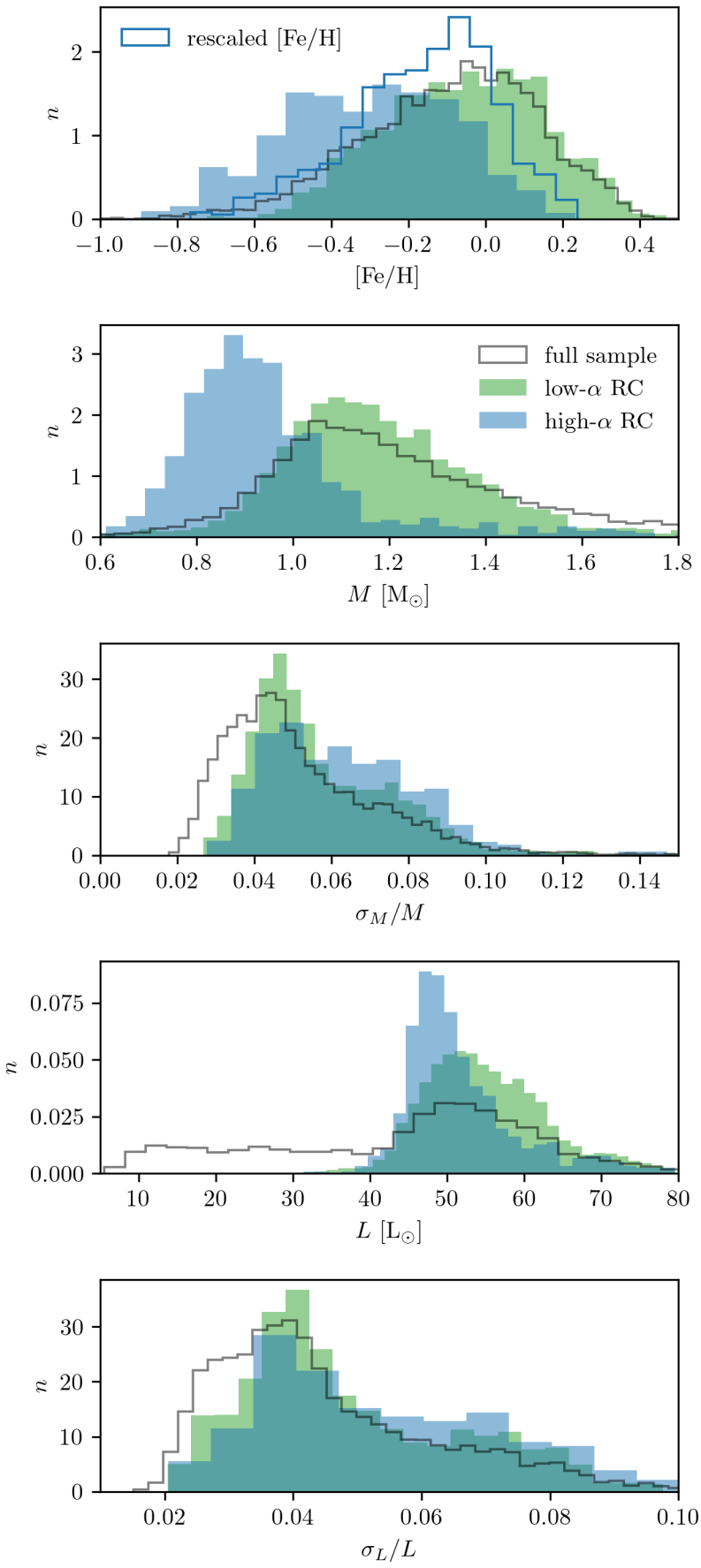


Figure 6.6: Distributions of selected observables and uncertainties in the low- (filled green) or high- (filled blue) α RC samples and the full sample (black). From top to bottom: [Fe/H], showing also the rescaled metallicity of the high-α population (dark blue; see Section 6.2.3), mass, fractional uncertainty on mass, luminosity, fractional uncertainty on luminosity. The young α-rich stars are visible in the high-α distribution as the long tail above $\sim 1.1\,M_\odot$.

models with different helium abundance: $Y = [0.25, 0.28, 0.31, 0.34]$, with solar-calibrated mass-fractions: $Y_\odot = 0.26317, Z_\odot = 0.01448$.

From the full evolutionary tracks, we extract the CHeB phase based on the central helium and carbon mass fractions: $0.001 < Y_c < 0.95 - Z, X_c^{C12} > 0.05$, where Z is computed from [Fe/H], Y and the hydrogen mass fraction, X, as:

$$Z = \frac{(1-Y)\,10^{[\mathrm{Fe/H}]+\log(X/Z)_\odot}}{1+10^{[\mathrm{Fe/H}]+\log(X/Z)_\odot}}. \tag{6.3}$$

We convert the selected phase of each track from the model points produced by MESA to 10000 'equivalent evolutionary phases' (EEPs) by sampling uniformly in the fractional age of the star

$$\mathcal{T} = \frac{\tau - \mathrm{ZAHB}}{\mathrm{TAHB} - \mathrm{ZAHB}}, \tag{6.4}$$

where τ is the stellar age and ZAHB and TAHB are the zero and terminal age of the star in the CHeB phase, interpolating linearly along the track (Figure 6.1). This process naturally produces most points at luminosities where the model predicts the slowest evolution and allows robust interpolation between tracks at different grid positions.

As shown in the top panel of Figure 6.7, the evolution is slowest at the low-L end of the track, with a rapid excursion toward high-L towards the end of the CHeB phase. The overall luminosity of a given RC track is well characterised by the median, and the distribution also features a long tail towards high-L, which overlaps the median of the distribution at the next Y coordinate.

To relate the helium abundance to the luminosity of an observed star, we rely on these luminosity distributions being distinguishable when accounting for all observational uncertainties. To facilitate this, we select the region of the model grid where the median luminosity, L^{50} is greater than the 84$^{\mathrm{th}}$-percentile, L^{84}, of the next distribution down in the Y plane: $L^{84}_{Y=25,28,31} < L^{50}_{Y=28,31,34}$. This selection removes all tracks with $M = 0.6$, three tracks with $M = 0.7$ and [Fe/H]=0.2 – 0.4, and a total of 17 tracks in the high-M, low-[Fe/H] corner of the grid. These regions of the M-[Fe/H] plane are less populated by our observational sample,

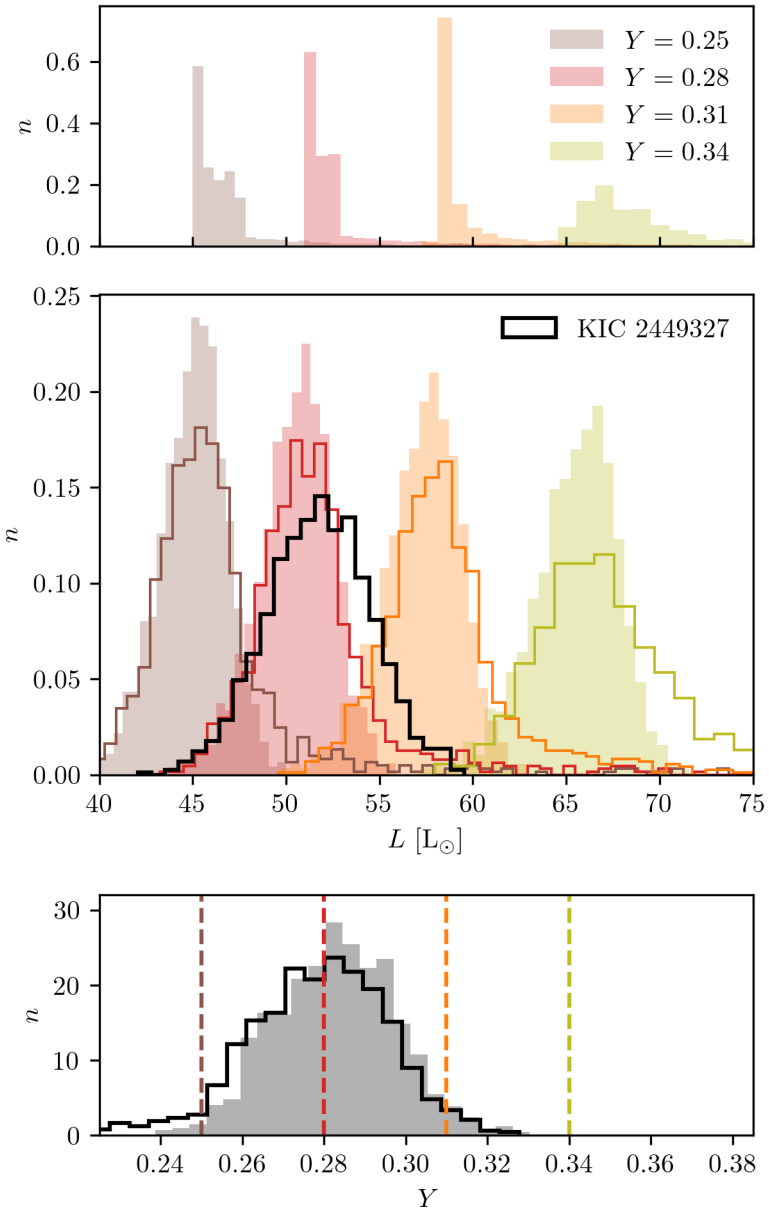


Figure 6.7: Luminosity distributions from model EEPs (top panel; see Section 6.3.1) and inferred from models including sources of uncertainty (middle panel). The middle panel shows the effect of the observational uncertainty on M and [Fe/H] (filled) and with the addition of unknown $\mathcal{T}$ (fine unfilled). The bold black distribution shows the luminosity realisations of KIC 2449327. The bottom panel shows the distribution of Y arising from the inclusion of the uncertainty on M and [Fe/H] (filled) and with the addition of unknown $\mathcal{T}$ (bold black). Vertical lines correspond to the Y values of the four models.

so this process does not significantly change the parameter space over which our results are constrained.

6.3.2 Helium abundance inference

The first step in the comparison of observed to modelled luminosity for a given star is to interpolate across the model grid to the observed values of M and [Fe/H]. We assign the star a random fractional age, and thus obtain four luminosity values from the models, corresponding to the four Y coordinates. We assume a linear function $L\,(Y)$ which we fit to the model points, and so obtain the value of Y corresponding to the observed L. The linear assumption is a pragmatic choice, but our results are not very sensitive to it .

We perform a Monte Carlo (MC) analysis by repeating these steps for 1000 realisations M, [Fe/H] and L, with a different assumption of $\mathcal{T}$ each time. For each star, we thus obtain a distribution of Y, formed of each step where the M and [Fe/H] realisations lie inside the valid region of the model grid. We compute Z from these samples following Equation 6.3. The median values of Y and Z for the low-α sample are shown in the top panel of Figure 6.8, coloured by stellar mass.

6.3.3 Analysis

For an individual star, the unknown fractional age has a significant effect on the uncertainty of our estimate of Y. This effect is demonstrated in Figure 6.7, and explained below. The top panel shows the luminosity distribution of the EEPs for models at $M = 1.0\mathrm{M}_{\odot}$, [Fe/H] = 0.0 dex, where the overall increase in L with Y is clearly visible, and the overlap between the distributions is quite small.

The filled distributions in the middle panel show the effect of the observational uncertainties on M and [Fe/H] for a single assumed fractional age $\mathcal{T} = 0.3$, generated by interpolation to realisations of the observed values corresponding to star KIC 2449327, which has $M = 0.97 \pm 0.06\mathrm{M}_{\odot}$, [Fe/H] = 0.0043 ± 0.0097. The effect is to broaden the L-distributions about their median value, increasing the overlap between the distributions at different values of Y.

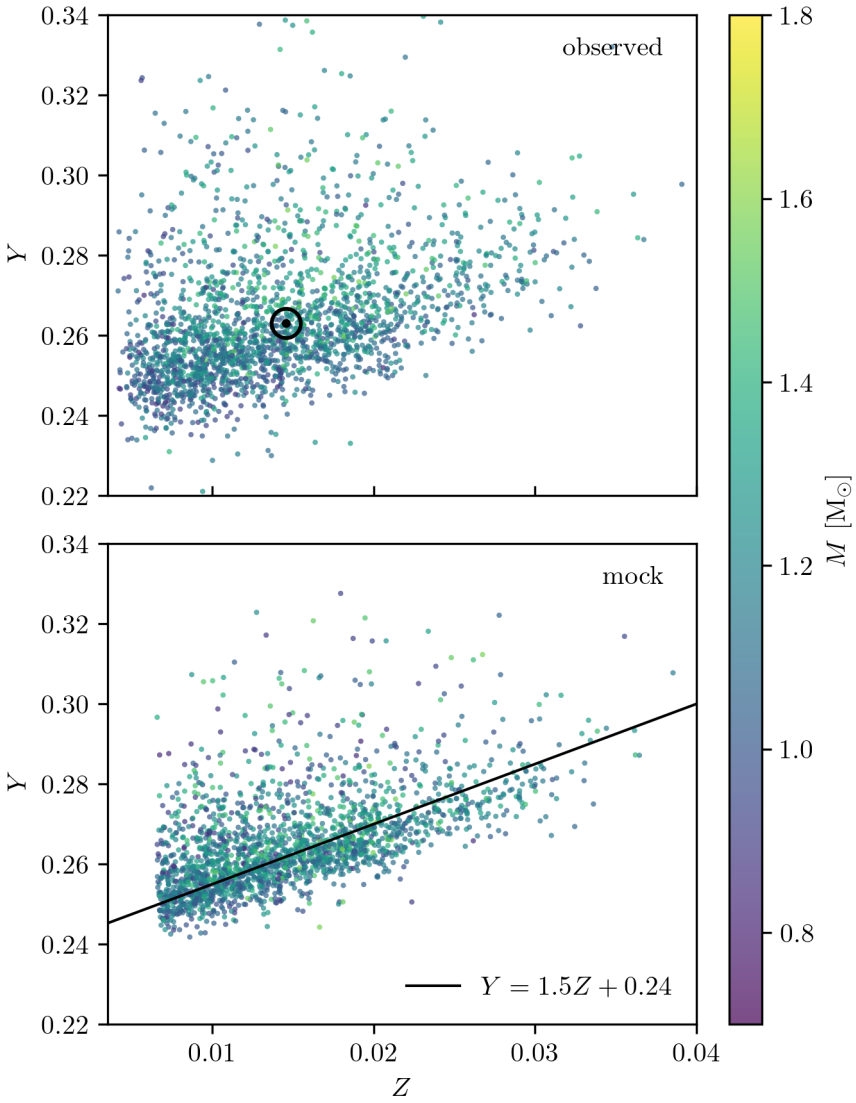


Figure 6.8: Median values of Y and Z inferred for observed (top) and mock (bottom) low-α datasets. The calibrated solar value $(Y_\odot, Z_\odot)$ is shown in the top panel by the black $\odot$ symbol, and the input relationship Y (Z) as the black line in the bottom panel.

The unfilled distributions in the foreground of the middle panel include the effect of unknown $\mathcal{T}$, as in this case each realisation has a different value of $\mathcal{T}$ assumed. The L-distributions now have more significant tails towards high-L, further reducing the separability between distributions at different Y. The black histogram shows the distribution of realisations of the observed L of KIC 2449327, and in our analysis we are effectively comparing this with the unfilled distributions corresponding to the models.

The effect on the inference of Y is shown in the bottom panel where, again, the filled distribution in the background corresponds to an assumed fractional age $\mathcal{T} = 0.3$, and the unfilled distribution in the foreground shows the full uncertainties. The effect of including the unknown $\mathcal{T}$ is to increase the uncertainty on Y by 30% for this star.

We can take advantage of the size of our sample to overcome this, by binning stars in [Fe/H]. It is safe to assume that any bin with a sufficiently large population provides a uniform sample of $\mathcal{T}$ in the observations and, therefore, the median value of Y (approximately corresponding to the median L of the population in the bin) provides a more robust and precise estimate of Y than is available for any single star. Figure 6.9 demonstrates this, showing the distribution of median luminosities of three bins in [Fe/H], for stars around $1\mathrm{M}_\odot$ from 1000 realisations of the observations. The precision of the estimate improves by a factor of the square root of the number of stars in the bin, and the average Y and Z of the bin around [Fe/H] = 0.0 agrees with the solar-calibrated values within 2σ.

Therefore, for each step in the MC analysis described in the previous section, we bin the realisation in [Fe/H] and, sometimes, M, and obtain distributions of the median Y and Z or each bin at each realisation. From these samples, we compute the mean and covariance matrix and use these values to fit the linear relation $Y(Z)$. Our fitting procedure follows Hogg, Bovy, and Lang (2010), accounting for the uncertainties on, and the correlation between, Y and Z.

Our model has two parameters $\phi = \Delta Y/\Delta Z, Y_p$ and, from Bayes' theorem, the posterior probability density function (PDF) for these parameters given some data, d is

$$p(\phi|d) \propto p(\phi)p(d|\phi), \tag{6.5}$$

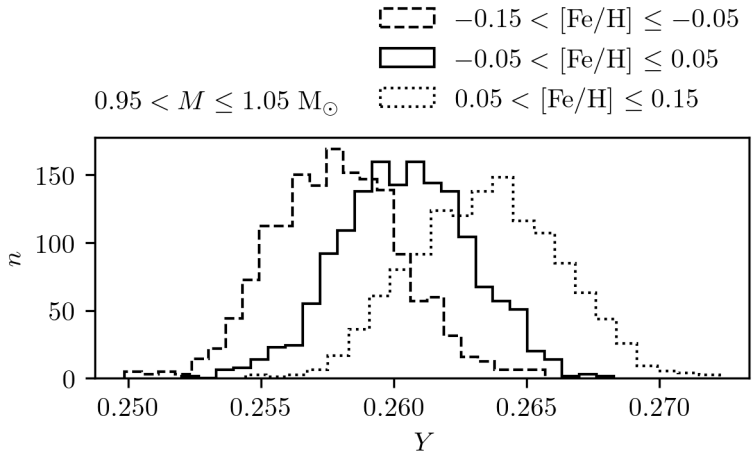


Figure 6.9: Distribution of median values of Y in three metallicity bins inferred from 1000 realisations of the observables.

where $p(\phi)$ is the prior PDF of the model parameters and $p(d|\phi) = \mathcal{L}$ is the likelihood of observing the data, given the model. We reparametrise the problem, to avoid wide priors placing too much emphasis on a gradient close to vertical, and so constrain instead the angle to the horizontal, $\cos(\theta) = 1/\sqrt{1+m^2}$, and $c_\perp = c\cos(\theta)$. This gives a new set of parameters $\varphi = \theta, c_\perp$ and, projecting the covariance matrix onto an orthogonal variance Σ_i^2, the log-likelihood may be written as

$$\ln(\mathcal{L}) \propto -\frac{1}{2}\sum_i \left[\ln \Sigma_i^2 + \frac{\Delta_i^2}{\Sigma_i^2}\right], \tag{6.6}$$

where Δ_i is the orthogonal displacement of star i from the line. We choose very wide, uniform priors on the parameters φ, requiring:

$$-\pi < \theta < \pi,$$
$$-10^3 < c_\perp < 10^3.$$

This new parameter space is explored by sampling according to the Markov Chain Monte Carlo (MCMC) algorithm, implemented in `emcee` (Foreman-Mackey et al., 2013), using 32 walkers which each makes 5000 steps, with a burn-in time which is dynamically determined to be 10 times the auto-correlation time.

The statistical uncertainty on the best fitting parameters is very small (< 5%), but there is an additional sensitivity to the binning scheme used. We test different numbers of bins in the M and [Fe/H] dimensions and validate our approach with a mock dataset, described below.

6.3.4 Validation with mock data

Our mock dataset is generated starting from the M and [Fe/H] of the observed stars. We enforce $\Delta Y/\Delta Z = 1.5$ and $Y_p = 0.24$, and calculate Y. We interpolate to (M, [Fe/H], Y) on the model grid and, assuming a random fractional age, obtain $L_{\rm mock}$ on which we assume an uncertainty of 4% (Figure 6.6). $L_{\rm mock}$ is then passed through the procedure described in the sections above, including calculating a new mass $M_{\rm mock}$ from the observed $\nu_{\rm max}$ and $L_{\rm mock}$.

In Figure 6.8 we show the median value of Y and Z obtained for each observed (top panel) and mock (bottom panel) star. The most obvious difference between the observed and mock results is a lack of stars at very low Z in the after case, because $L_{\rm mock}$ is not produced for values of Y outside of the model grid (i.e. $Y = 0.25; Z = 0.006$). There is also slightly less scatter in the mock results but, in general, the main features of the observations are reproduced well.

We find more scatter towards high Y than low, which is a result of the long tail towards high-L of the distributions shown in Figure 6.7: a more evolved star of $Y = 0.25$ may have the same luminosity as a less evolved star of $Y = 0.28$, but the probability of observing the latter is greater and the low-L evolution is slower. This means that for most values of $\mathcal{T}$, the observed L corresponds to the higher values of Y. In the mock data above $Z = 0.02$, we also see a slight tendency to underestimate Y compared to the input relationship (black line), and there are hints that this feature is also present in the observed results. The similarity of the results in the Y-Z plane indicates that a binning procedure found to be robust of the mock data should be reliable also for the observations.

We test different numbers of bins in [Fe/H] and also explore dividing the [Fe/H] bins further, according to stellar mass, allowing more mass bins in more populated regions of the [Fe/H] plane. We find good consistency when requiring $\sim$ 25 stars per bin, which is further improved when the bin population restriction is slightly relaxed to ensure the full range of Z is sampled,

by retaining less populated bins at the extrema. From this, the additional uncertainty on $\Delta Y/\Delta Z$ introduced by the sensitivity to the binning is estimated to be ± 0.05 in both the mock and observed datasets.

In general, the gradient is underestimated by $0.1 - 0.2$ compared to the imposed $\Delta Y/\Delta Z$, with a corresponding small overestimate of Y_p. Using larger bins tends to increase the deviation from the expected result and, though the input gradient can be reproduced by using more, smaller bins, the results are also more unstable.

6.4 Results and Discussion

In this section we discuss the results obtained from the low- and high-α populations (Sections 6.4.1 and 6.4.2) and set them in the context of the range of results in the literature in Section 6.4.3.

6.4.1 Low-α stars

Figure 6.10 shows the result obtained from one choice of bins, with bins of given [Fe/H] subdivided by M, requiring 25 stars per bin, where there are enough observations for multiple M bins. At high- and low-[Fe/H] where the data are sparser this restriction is relaxed, resulting in single bins with larger uncertainties. The points are plotted at the average Y and Z of the population in each bin, the error bars correspond to one standard deviation, and points are coloured according to the median M of the binned population. The fit arising from these bins is shown by the solid green line and has best fitting parameters $\Delta Y/\Delta Z = 1.29 \pm 0.05, Y_p = 0.2430 \pm 0.0008$, where we report the median and 64% credible interval and the uncertainties represent only the statistical error on the fit. The grey contours show the position of the median Y and Z of the individual stars (Figure 6.8), and we see that the bins follow the highest density ridge well, with a slight departure below $Z \approx 0.05$.

Figure 6.11 shows the same binning procedure, applied to the mock data. The solid black line shows the input relationship between Y and Z ($\Delta Y/\Delta Z_{\rm in} = 1.50, Y_{p,\rm in} = 0.24$), and the

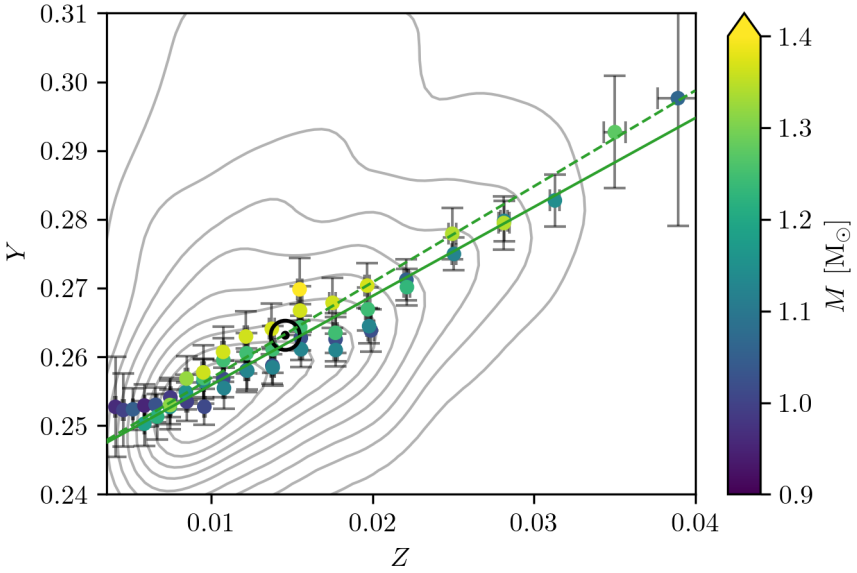


Figure 6.10: Results obtained from one set of bins for the observed low-α data. Bins plotted at the average Y and Z with 1σ error bars and are coloured by the median M of the binned population. Contours show the position of the median Y and Z for individual stars (top panel of Figure 6.8). The calibrated solar value $(Y_\odot, Z_\odot)$ is shown by the black $\odot$ symbol. The best fitting Y (Z) is shown by the solid green line, and with $\Delta Y/\Delta Z + 0.1$ by the dashed green line (see Section 6.4.1).

dashed line shows the fit constrained by the bins, where $\Delta Y/\Delta Z_{\rm mock} = 1.30 \pm 0.05, Y_{p,\,\rm mock} = 0.2443^{+0.0007}_{-0.0008}$. Given the good resemblance between the mock and observed data, we anticipate that the underestimation of $\Delta Y/\Delta Z$ in the mock results is similarly present in the observational result, but that Y_p is likely to be more robust, due to the larger number of points at low Z. The dashed line in Figure 6.10 shows the result of increasing the gradient by 0.1, for the same Y_p. This new line still agrees to $\sim 1\sigma$ with the bins, and provides a better agreement with $(Y_\odot, Z_\odot)$, shown by the black $\odot$ symbol.

At metallicities with multiple mass bins, we find a slight tendency towards higher Y at higher M, with the exception of the lowest mass ($M < 1\mathrm{M}_\odot$), i.e. oldest, stars at low Z, which form a very flat track in this plane. A similar effect is found in the mock data, excluding the more scattered appearance of the lowest mass bins, indicating that this effect is likely introduced by our analysis rather than an intrinsic property of the population.

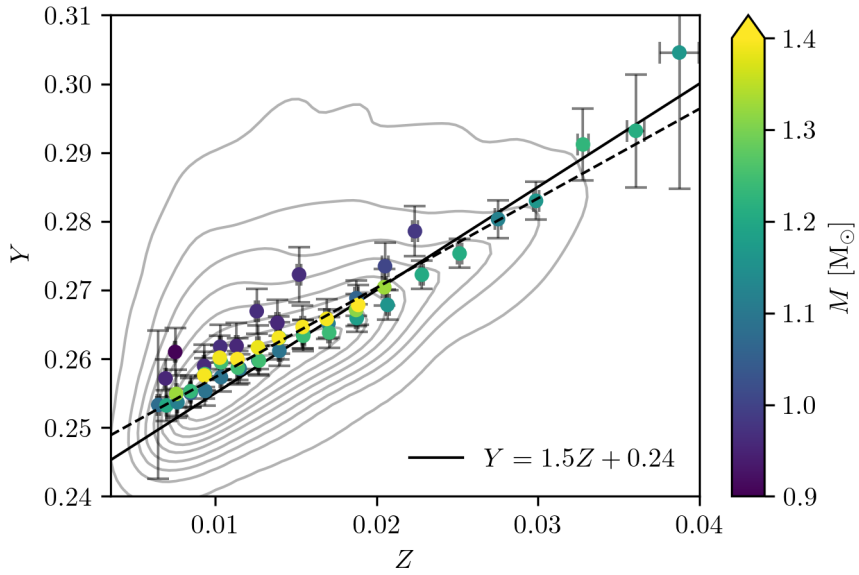


Figure 6.11: Same as Figure 6.10, but for the mock data. The input Y (Z) is shown by the solid black line and the best fitting result by the dashed black line.

6.4.2 High-α stars

In Figure 6.12, we show the results obtained from the high-α population, excluding stars with $M > 1.1\mathrm{M}_{\odot}$, which are likely members of the 'young α-rich' population and therefore may have enrichment histories which are affected by binary evolution Grisoni et al. (in preparation). Taking all of the bins together, we recover $\Delta Y/\Delta Z = 1.18 \pm 0.19, Y_p = 0.248 \pm 0.002$ (blue line). Not only are the statistical uncertainties larger than in the low-α case, but this fit is also less stable between bin choices, due to the lower number of stars and reduced extent on the Z-axis.

In this sample, there is a much clearer change in behaviour in bins of different mass (note the different scale of the colour bar). Bins with median mass $M \lessapprox 0.8\mathrm{M}_{\odot}$ follow a distinct track with a much steeper gradient ($\Delta Y/\Delta Z \approx 2.8 \pm 0.2, Y_p \approx 0.241 \pm 0.002$; dashed purple line), while the younger, higher mass, bins lie much closer to the relationship found in the low-α population (green line).

6.4.3 Comparison to literature

As mentioned in Section 6.1, there are a range of methods used to constrain $\Delta Y/\Delta Z$ in the literature, but there is little consensus between them. Comparison between these works is

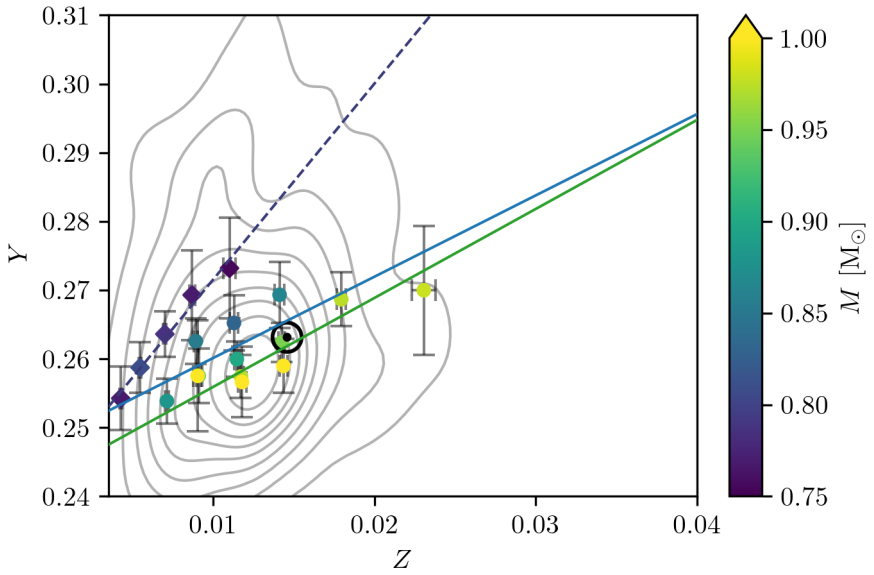


Figure 6.12: Same as Figure 6.10, but for the high-α sample. The five lowest mass bins are marked by diamonds. The best fitting Y (Z) for the whole high-α sample is shown by the blue line, the result from the low-α sample by the green line and an approximate fit to the lowest mass bins by the dashed purple line.

complicated by the fact that many assume different values of Y_p, $Y_\odot$ and $Z_\odot$, but these differences do not account for the full range of results. Many methods are also only available to a very limited (low) range of metallicities, presenting an additional challenge when constraining the Y (Z) relationship. Here we mention a few recent examples, based on a range of observations, to help place our work in context.

ISM helium abundance can be measured in Galactic and extragalactic HII regions, using optical (at low metallicities) and radio (for a wider range of Z) recombination lines. Izotov, Thuan, and Stasińska (2007) found $\Delta Y/\Delta Z = 2.38 \pm 0.45$ and $\Delta Y/\Delta Z = 2.19 \pm 0.39$ under different assumptions for the HeI emissivity, in 86 low-metallicity HII regions. Balser (2006) used the radio recombination lines to constrain the enrichment ratio over a wider range of metallicities, finding $\Delta Y/\Delta Z = 1.4 \pm 0.62$. Chiappini and Maciel (1994) also achieved a more extended metallicity range than optical HII region analysis alone, by including blue compact galaxies and planetary nebulae (PNe) in their sample, reaching $Z \sim 0.015$. They found that $\Delta Y/\Delta Z > 3$, with the exact value depending on the Z-range considered and the correction applied to the PNe data to account for contamination by the central star.

The spectral features of He are observable in B-stars, and Nieva and Przybilla (2012) used observations of 20 in the solar neighbourhood to define a 'cosmic standard' for the present-day abundance in the local ISM. The found $Y = 0.276, Z = 0.014 \pm 0.002$ which, extrapolating to $Y_p = 0.245$ (Workman et al., 2022) gives $\Delta Y/\Delta Z \sim 2.2$.

Brogaard et al. (2012) used detached eclipsing binaries in the open cluster NGC6791 to achieve very tight constraints on isochrone fits to the cluster population, obtaining a $Y = 0.3 \pm 0.01$. By extrapolating to $Y_p = 0.248$, and comparing to the solar abundance, they estimate $\Delta Y/\Delta Z = 1.4 \pm 0.1$.

$\Delta Y/\Delta Z$ can also be constrained by the structure of the HR diagram for low-MS K dwarfs, by modelling the width of the MS observed, which depends on Y amongst other stellar properties. Casagrande et al. (2007) used a sample of 105 local K dwarfs with accurate parallaxes to obtain $\Delta Y/\Delta Z = 2.1 \pm 0.9$ for targets above $\sim Z_\odot$. At lower metallicities, they found a steeper gradient was necessary to fit the observations, which would imply a very low value of Y_p. Gennaro, Prada Moroni, and Degl'Innocenti (2010) used a similar dataset, but found $\Delta Y/\Delta Z = 5.3 \pm 1.4$ when they corrected for systematic effects associated with a lack of accurate age constraints. They also showed that the sensitivity of the appearance of the K dwarf main sequence to Y is reduced at low metallicities, suggesting that the results are not reliable at $[\mathrm{Fe/H}] \lessapprox -0.3$.

Finally, asteroseismology can also be used to provide constraints. Verma et al. (2019) used the asteroseismic 'glitch' signature associated with He-ionisation in the stellar interior to constrain Y for 38 *Kepler* stars. They found $\Delta Y/\Delta Z = 1.226 \pm 0.849$ and $Y_p = 0.244 \pm 0.019$. Lyttle et al. (2021) took a statistical approach by using a hierarchical Bayesian model to constrain $\Delta Y/\Delta Z$, assuming first that such a linear relationship exists between Y and Z. Using a tight prior on $Y_p = 0.247$, they found $\Delta Y/\Delta Z = 1.05^{+0.28}_{-0.25}$.

6.5 Summary and conclusions

We have used the relationship between the luminosity and initial helium abundance of RC stars to constrain $\Delta Y/\Delta Z$. For low-mass, CHeB stars, the total luminosity is a function of the

stellar mass, metallicity, initial helium abundance and fractional age (of the CHeB phase). By comparison of precise *Gaia* luminosities for more than 2000 stars with *Kepler* constraints on mass and evolutionary phase to a grid of stellar evolutionary models, we estimate Y and Z in bins of [Fe/H] and mass.

For low-α stars, these bins show a tight, linear relationship between Y and Z, from which we estimate $\Delta Y/\Delta Z$ with $\sim$ 5% statistical uncertainty. We evaluate systematic effects in our analysis using a mock dataset and find a systematic underestimate of $\sim$ 0.1 in $\Delta Y/\Delta Z$. We therefore report $\Delta Y/\Delta Z = 1.29 \pm 0.07(\text{stat}) + 0.1(\text{sys})$, with $Y_p = 0.2430 \pm 0.0008(\text{stat})$, which is in agreement with independent measurements. Our result is also in good agreement with the solar-calibrated value.

We also investigate high-α stars, which show. more complex behaviour. Bins of higher mass (younger) stars agree well with the result obtained from the low-α population, while the older stars follow a clear, much steeper track in the Y-Z plane, with $\Delta Y/\Delta Z \approx 3$. These effects merit specific further investigation.

Our approach constrains $\Delta Y/\Delta Z$ with a larger population and higher precision than has been achieved previously, and we find no evidence of a break in the linear relationship which would lead to the recovery of very low-Y stars at low Z. Thorough characterisation of the systematic effects means that this result can now be used to reduce the uncertainty on stellar parameters (specifically ages) from model grids where a helium enrichment ratio is assumed. This method can also be applied to other asteroseismic datasets where a robust determination of the evolutionary state can be obtained including K2, using the evolutionary state based on machine learning (e.g. Hon, Stello, and Yu, 2017, 2018; Kuszlewicz, Hekker, and Bell, 2020), and the forthcoming PLATO mission (Rauer et al., 2014).

Chapter 7

SUMMARY AND OUTLOOK

In the preceding chapters, I have presented new results from the application of asteroseismology to Galactic archaeology, with the aim of achieving high temporal resolution studies of the Milky Way. This chapter provides a final summary of these results and some future prospects which were not already mentioned in the chapters' conclusions.

7.1 Summary

In Chapter 4 I described new catalogues of constraints on stellar and orbital parameters for more than 17000 stars, using asteroseismology from *Kepler*, K2 and TESS. I showed how high-precision *Gaia* luminosities can be used to identify stars with unreliable asteroseismic parameters, and that ages based on different observational constraints are suitable in different applications. I applied these catalogues in the context of Galactic archaeology and stellar evolution showing, in particular, that the age resolution from K2 is sufficient to recover expected trends in a range of planes, while extending to a wider range of mass, age and Galactic domains than are accessible to *Kepler* or TESS. I also demonstrated that these data can resolve the expected age difference between *in situ* and *ex situ* stars, and can be used to constrain population-average mass loss on the red giant branch.

In Chapter 5 I applied the K2 catalogue to the question of the thin disc radial metallicity gradient, as a function of stellar age. I found that the gradient flattens monotonically from

younger to older populations and that the metallicity of the solar neighbourhood has been slightly sub-solar throughout the history of the disc – indicating that the Sun is an outward migrator to its current position. These results provide further evidence for metallicity bias amongst older open clusters and, therefore, stronger constraints on the chemical and dynamical evolution of the disc.

In Chapter 6 I presented a new method to infer the initial helium abundance of low-mass core helium-burning stars using their luminosity. I used *Kepler* asteroseismology to obtain tight constraints on the stellar mass and a robust determination of the evolutionary state, and from the inferred helium abundances I constrained the helium-to-metal enrichment ratio with high statistical precision. I found that stars with low α-abundance show a tight, linear relationship between helium and metal abundance, which can be extrapolated to recover a primordial helium abundance which is consistent with independent determinations. The behaviour of high-α stars is more complex and motivates detailed further study.

7.2 Outlook

The conclusion sections of the chapters summarised here present some general future prospects for the work completed and mention opportunities with forthcoming data, so here I mention some specific next steps.

There are clearly many possible applications for the catalogues presented in Chapter 4, amongst which is a further investigation of the relationship between red giant branch mass loss and metallicity, which may help us to reconcile field stars with globular clusters (Tailo et al., 2021). In addition, a more detailed examination of the abundances of carbon and nitrogen as a function of stellar mass at low metallicities may provide new observational constraints for processes of thermohaline and rotational mixing (Charbonnel and Lagarde, 2010; Lagarde et al., 2019).

A natural extension of the work on the metallicity gradient in Chapter 5 is to apply the analysis to other abundance gradients to enable a more detailed comparison with models of

Galactic chemical evolution (Chiappini, Matteucci, and Romano, 2001; Cescutti et al., 2007). Furthermore, recent results on the inference of stellar birth radii indicate that it may be possible to recover the underlying evolution of the gradients, mitigating against the effects of radial migration (Lu et al., 2022; Ratcliffe et al., 2023).

Finally, the methods presented in Chapter 6 can be applied to K2 observations. Not only will this increase the sample size, but it will also allow the helium enrichment of different parts of the Galaxy to be compared. The main open question is that of evolutionary state determination, since 'traditional' methods used for *Kepler* cannot be reliably applied to the shorter-duration K2 observations. However, recent developments in machine learning techniques may hold a solution (Hon, Stello, and Yu, 2018; Kuszlewicz, Hekker, and Bell, 2020).

Asteroseismology has emerged as a powerful tool in the Galactic archaeologist's toolbox, complimenting the latest advances in astrometry and spectroscopy as we dig through the stellar fossil record. Future breakthroughs may be confidently expected from the continued analysis of available data and the release of new observations from ongoing and planned missions. The Galaxy may be *nothing but stars*[1], but from these stars we are uncovering the processes of Galactic and galaxy evolution, and writing a detailed history of the Milky Way.

[1] See Chapter 1

REFERENCES

Abadi, M. G. et al. (Nov. 2003). "Simulations of Galaxy Formation in a Λ Cold Dark Matter Universe. II. The Fine Structure of Simulated Galactic Disks". In: *ApJ* 597.1, pp. 21–34. DOI: 10.1086/378316. arXiv: astro-ph/0212282 [astro-ph].

Abdurro'uf et al. (Apr. 2022). "The Seventeenth Data Release of the Sloan Digital Sky Surveys: Complete Release of MaNGA, MaStar, and APOGEE-2 Data". In: *ApJS* 259.2, 35, p. 35. DOI: 10.3847/1538-4365/ac4414. arXiv: 2112.02026 [astro-ph.GA].

Aerts, C. (Jan. 2021). "Probing the interior physics of stars through asteroseismology". In: *Reviews of Modern Physics* 93.1, 015001, p. 015001. DOI: 10.1103/RevModPhys.93.015001. arXiv: 1912.12300 [astro-ph.SR].

Aller, L. H. (Jan. 1942). "The Spectra of the Emission Nebulosities in Messier 33." In: *ApJ* 95, p. 52. DOI: 10.1086/144372.

Anders, F. et al. (Apr. 2014). "Chemodynamics of the Milky Way. I. The first year of APOGEE data". In: *A&A* 564, A115, A115. DOI: 10.1051/0004-6361/201323038. arXiv: 1311.4549 [astro-ph.GA].

Anders, F. et al. (Jan. 2017a). "Galactic archaeology with asteroseismology and spectroscopy: Red giants observed by CoRoT and APOGEE". In: *A&A* 597, A30, A30. DOI: 10.1051/0004-6361/201527204. arXiv: 1604.07763 [astro-ph.GA].

Anders, F. et al. (Apr. 2017b). "Red giants observed by CoRoT and APOGEE: The evolution of the Milky Way's radial metallicity gradient". In: *A&A* 600, A70, A70. DOI: 10.1051/0004-6361/201629363. arXiv: 1608.04951 [astro-ph.GA].

Anders, F. et al. (Apr. 2023). "Spectroscopic age estimates for APOGEE red-giant stars: Precise spatial and kinematic trends with age in the Galactic disc". In: *arXiv e-prints*, arXiv:2304.08276, arXiv:2304.08276. DOI: 10.48550/arXiv.2304.08276. arXiv: 2304.08276 [astro-ph.GA].

Baglin, A. et al. (Jan. 2006). "CoRoT: a high precision photometer for stellar ecolution and exoplanet finding". In: *36th COSPAR Scientific Assembly*. Vol. 36, p. 3749.

Balser, D. S. (Dec. 2006). "The Chemical Evolution of Helium". In: *AJ* 132.6, pp. 2326–2332. DOI: 10.1086/508515. arXiv: astro-ph/0608436 [astro-ph].

Balser, D. S. et al. (Sept. 2011). "H II Region Metallicity Distribution in the Milky Way Disk". In: *ApJ* 738.1, 27, p. 27. DOI: 10.1088/0004-637X/738/1/27. arXiv: 1106.1660 [astro-ph.GA].

Belkacem, K. et al. (June 2011). "The underlying physical meaning of the ν_{max} - ν_c relation". In: *A&A* 530, A142, A142. DOI: 10.1051/0004-6361/201116490. arXiv: 1104.0630 [astro-ph.SR].

Belkacem, K. et al. (Dec. 2013). "On the Seismic Scaling Relations $\Delta\nu$ — ρ and ν_{max} — ν_c". In: *Progress in Physics of the Sun and Stars: A New Era in Helio- and Asteroseismology*. Ed. by H. Shibahashi and A. E. Lynas-Gray. Vol. 479. Astronomical Society of the Pacific Conference Series, p. 61. DOI: 10.48550/arXiv.1307.3132. arXiv: 1307.3132 [astro-ph.SR].

Belokurov, V. and A. Kravtsov (July 2022). "From dawn till disc: Milky Way's turbulent youth revealed by the APOGEE+Gaia data". In: *MNRAS* 514.1, pp. 689–714. DOI: 10.1093/mnras/stac1267. arXiv: 2203.04980 [astro-ph.GA].

Bennett, M. and J. Bovy (Jan. 2019). "Vertical waves in the solar neighbourhood in Gaia DR2". In: *MNRAS* 482.1, pp. 1417–1425. DOI: 10.1093/mnras/sty2813. arXiv: 1809.03507 [astro-ph.GA].

Bertin, G. and C. C. Lin (1996). *Spiral structure in galaxies : a density wave theory*. eng. Cambridge, Mass. ; London.

Bingham, E. et al. (2019). "Pyro: Deep Universal Probabilistic Programming". In: *J. Mach. Learn. Res.* 20, 28:1–28:6.

Binney, J. and S. Tremaine (2008). "Galactic dynamics". eng. In: Princeton series in astrophysics.

Binney, J. (Oct. 2012). "Actions for axisymmetric potentials". In: *MNRAS* 426.2, pp. 1324–1327. DOI: 10.1111/j.1365-2966.2012.21757.x. arXiv: 1207.4910 [astro-ph.GA].

Bird, J. C. et al. (Aug. 2013). "Inside out and Upside down: Tracing the Assembly of a Simulated Disk Galaxy Using Mono-age Stellar Populations". In: *ApJ* 773.1, 43, p. 43. DOI: 10.1088/0004-637X/773/1/43. arXiv: 1301.0620 [astro-ph.GA].

Borucki, W. J. et al. (Feb. 2010). "Kepler Planet-Detection Mission: Introduction and First Results". In: *Science* 327.5968, p. 977. DOI: 10.1126/science.1185402.

Bovy, J. (in preparation). *Dynamics and Astrophysics of Galaxies*. Princeton, N.J. ; Woodstock.

Bovy, J. (Feb. 2015). "galpy: A python Library for Galactic Dynamics". In: *ApJS* 216.2, 29, p. 29. DOI: 10.1088/0067-0049/216/2/29. arXiv: 1412.3451 [astro-ph.GA].

Bovy, J. et al. (Nov. 2012). "The Milky Way's Circular-velocity Curve between 4 and 14 kpc from APOGEE data". In: *ApJ* 759.2, 131, p. 131. DOI: 10.1088/0004-637X/759/2/131. arXiv: 1209.0759 [astro-ph.GA].

Bovy, J. et al. (Feb. 2016). "On Galactic Density Modeling in the Presence of Dust Extinction". In: *ApJ* 818.2, 130, p. 130. DOI: 10.3847/0004-637X/818/2/130. arXiv: 1509.06751 [astro-ph.GA].

Bragança, G. A. et al. (May 2019). "Radial abundance gradients in the outer Galactic disk as traced by main-sequence OB stars". In: *A&A* 625, A120, A120. DOI: 10.1051/0004-6361/201834554. arXiv: 1904.04340 [astro-ph.SR].

Brogaard, K. et al. (July 2012). "Age and helium content of the open cluster NGC 6791 from multiple eclipsing binary members. II. Age dependencies and new insights". In: *A&A* 543, A106, A106. DOI: 10.1051/0004-6361/201219196. arXiv: 1205.4071 [astro-ph.SR].

Brook, C. B. et al. (Sept. 2004). "The Emergence of the Thick Disk in a Cold Dark Matter Universe". In: *ApJ* 612.2, pp. 894–899. DOI: 10.1086/422709. arXiv: astro-ph/0405306 [astro-ph].

Brown, T. M. et al. (Oct. 2011). "Kepler Input Catalog: Photometric Calibration and Stellar Classification". In: *AJ* 142.4, 112, p. 112. DOI: 10.1088/0004-6256/142/4/112. arXiv: 1102.0342 [astro-ph.SR].

Buder, S. et al. (Sept. 2021). "The GALAH+ survey: Third data release". In: *MNRAS* 506.1, pp. 150–201. DOI: 10.1093/mnras/stab1242. arXiv: 2011.02505 [astro-ph.GA].

Burbidge, E. M. et al. (Jan. 1957). "Synthesis of the Elements in Stars". In: *Reviews of Modern Physics* 29.4, pp. 547–650. DOI: 10.1103/RevModPhys.29.547.

Camargo, D., C. Bonatto, and E. Bica (July 2015). "Tracing the Galactic spiral structure with embedded clusters". In: *MNRAS* 450.4, pp. 4150–4160. DOI: 10.1093/mnras/stv840. arXiv: 1505.01829 [astro-ph.GA].

Carigi, L. and M. Peimbert (Oct. 2008). "The Helium and heavy elements enrichment of the Galactic Disk". In: *Rev. Mexicana Astron. Astrofis.* 44, pp. 341–354. DOI: 10.48550/arXiv.0801.2867. arXiv: 0801.2867 [astro-ph].

Casagrande, L. and D. A. VandenBerg (Oct. 2014). "Synthetic stellar photometry - I. General considerations and new transformations for broad-band systems". In: *MNRAS* 444.1, pp. 392–419. DOI: 10.1093/mnras/stu1476. arXiv: 1407.6095 [astro-ph.SR].

Casagrande, L. et al. (June 2011). "New constraints on the chemical evolution of the solar neighbourhood and Galactic disc(s). Improved astrophysical parameters for the Geneva-Copenhagen Survey". In: *A&A* 530, A138, A138. DOI: 10.1051/0004-6361/201016276. arXiv: 1103.4651 [astro-ph.GA].

Casagrande, L. et al. (Dec. 2007). "The helium abundance and $\Delta Y/\Delta Z$ in lower main-sequence stars". In: *MNRAS* 382.4, pp. 1516–1540. DOI: 10.1111/j.1365-2966.2007.12512.x. arXiv: astro-ph/0703766 [astro-ph].

Casali, G. et al. (Sept. 2023). "Time evolution of Ce as traced by APOGEE using giant stars observed with the Kepler, TESS and K2 missions". In: *A&A* 677, A60, A60. DOI: 10.1051/0004-6361/202346274. arXiv: 2305.06396 [astro-ph.GA].

Casamiquela, L. et al. (Oct. 2017). "OCCASO - II. Physical parameters and Fe abundances of red clump stars in 18 open clusters". In: *MNRAS* 470.4, pp. 4363–4381. DOI: 10.1093/mnras/stx1481. arXiv: 1706.03656 [astro-ph.GA].

Casamiquela, L. et al. (Dec. 2019). "OCCASO - III. Iron peak and α elements of 18 open clusters. Comparison with chemical evolution models and field stars". In: *MNRAS* 490.2, pp. 1821–1842. DOI: 10.1093/mnras/stz2595. arXiv: 1909.05865 [astro-ph.GA].

Casamiquela, L. et al. (Aug. 2021). "Abundance-age relations with red clump stars in open clusters". In: *A&A* 652, A25, A25. DOI: 10.1051/0004-6361/202039951. arXiv: 2103.14692 [astro-ph.GA].

Cescutti, G. et al. (Feb. 2007). "Abundance gradients in the Milky Way for α elements, iron peak elements, barium, lanthanum, and europium". In: *A&A* 462.3, pp. 943–951. DOI: 10.1051/0004-6361:20065403. arXiv: astro-ph/0609813 [astro-ph].

Chaplin, W. J. and A. Miglio (Aug. 2013). "Asteroseismology of Solar-Type and Red-Giant Stars". In: *ARA&A* 51.1, pp. 353–392. DOI: 10.1146/annurev-astro-082812-140938. arXiv: 1303.1957 [astro-ph.SR].

Chaplin, W. J. et al. (Jan. 2020). "Age dating of an early Milky Way merger via asteroseismology of the naked-eye star ν Indi". In: *Nature Astronomy* 4, pp. 382–389. DOI: 10.1038/s41550-019-0975-9. arXiv: 2001.04653 [astro-ph.GA].

Charbonnel, C. and N. Lagarde (Nov. 2010). "Thermohaline instability and rotation-induced mixing. I. Low- and intermediate-mass solar metallicity stars up to the end of the AGB". In: *A&A* 522, A10, A10. DOI: 10.1051/0004-6361/201014432. arXiv: 1006.5359 [astro-ph.SR].

Chaussidon, M. (2007). "Formation of the Solar System: a Chronology Based on Meteorites". In: *Lectures in Astrobiology*. Ed. by M. Gargaud, H. Martin, and P. Claeys, p. 45. DOI: 10.1007/978-3-540-33693-8_2.

Chiappini, C. and W. J. Maciel (Aug. 1994). "Planetary nebulae and the helium-to-metals enrichment ratio". In: *A&A* 288, pp. 921–928.

Chiappini, C., F. Matteucci, and R. Gratton (Mar. 1997). "The Chemical Evolution of the Galaxy: The Two-Infall Model". In: *ApJ* 477.2, pp. 765–780. DOI: 10.1086/303726. arXiv: astro-ph/9609199 [astro-ph].

Chiappini, C. (Mar. 2009). "The chemical evolution of the Galactic thick and thin disks". In: *The Galaxy Disk in Cosmological Context*. Ed. by J. Andersen et al. Vol. 254, pp. 191–196. DOI: 10.1017/S1743921308027580.

Chiappini, C., F. Matteucci, and D. Romano (June 2001). "Abundance Gradients and the Formation of the Milky Way". In: *ApJ* 554.2, pp. 1044–1058. DOI: 10.1086/321427. arXiv: astro-ph/0102134 [astro-ph].

Christensen-Dalsgaard, J. (Jan. 2014). *Lecture Notes on Stellar Oscillations*. Fifth. University of Aarhus, Denmark: Unpublished manuscript.

Chrobáková, Ž., R. Nagy, and M. López-Corredoira (Aug. 2022). "Warp and flare of the Galactic disc revealed with supergiants by Gaia EDR3". In: *A&A* 664, A58, A58. DOI: 10.1051/0004-6361/202243296. arXiv: 2206.08230 [astro-ph.GA].

Cirasuolo, M. et al. (July 2014). "MOONS: the Multi-Object Optical and Near-infrared Spectrograph for the VLT". In: *Ground-based and Airborne Instrumentation for Astronomy V*. Ed. by S. K. Ramsay, I. S. McLean, and H. Takami. Vol. 9147. Society of Photo-Optical Instrumentation Engineers (SPIE) Conference Series, 91470N, 91470N. DOI: 10.1117/12.2056012.

Corbelli, E. and P. Salucci (Jan. 2000). "The extended rotation curve and the dark matter halo of M33". In: *MNRAS* 311.2, pp. 441–447. DOI: 10.1046/j.1365-8711.2000.03075.x. arXiv: astro-ph/9909252 [astro-ph].

Cresci, G. et al. (Oct. 2010). "Gas accretion as the origin of chemical abundance gradients in distant galaxies". In: *Nature* 467.7317, pp. 811–813. DOI: 10.1038/nature09451. arXiv: 1010.2534 [astro-ph.CO].

da Silva, L. et al. (Nov. 2006). "Basic physical parameters of a selected sample of evolved stars". In: *A&A* 458.2, pp. 609–623. DOI: 10.1051/0004-6361:20065105. arXiv: astro-ph/0608160 [astro-ph].

Daflon, S. and K. Cunha (Dec. 2004). "Galactic Metallicity Gradients Derived from a Sample of OB Stars". In: *ApJ* 617.2, pp. 1115–1126. DOI: 10.1086/425607. arXiv: astro-ph/0409084 [astro-ph].

Dalton, G. et al. (Dec. 2020). "Integration and early testing of WEAVE: the next-generation spectroscopy facility for the William Herschel Telescope". In: *Ground-based and Airborne Instrumentation for Astronomy VIII*. Ed. by C. J. Evans, J. J. Bryant, and K. Motohara. Vol. 11447. Society of Photo-Optical Instrumentation Engineers (SPIE) Conference Series, 1144714, p. 1144714. DOI: 10.1117/12.2561067.

Das, P., K. Hawkins, and P. Jofré (Apr. 2020). "Ages and kinematics of chemically selected, accreted Milky Way halo stars". In: *MNRAS* 493.4, pp. 5195–5207. DOI: 10.1093/mnras/stz3537. arXiv: 1903.09320 [astro-ph.GA].

Davies, G. R. and A. Miglio (Sept. 2016). "Asteroseismology of red giants: From analysing light curves to estimating ages". In: *Astronomische Nachrichten* 337.8-9, p. 774. DOI: 10.1002/asna.201612371. arXiv: 1601.02802 [astro-ph.SR].

de Jong, R. S. et al. (Sept. 2012). "4MOST: 4-metre multi-object spectroscopic telescope". In: *Ground-based and Airborne Instrumentation for Astronomy IV*. Ed. by I. S. McLean, S. K. Ramsay, and H. Takami. Vol. 8446. Society of Photo-Optical Instrumentation Engineers (SPIE) Conference Series, 84460T, 84460T. DOI: 10.1117/12.926239. arXiv: 1206.6885 [astro-ph.IM].

De Silva, G. M. et al. (May 2015). "The GALAH survey: scientific motivation". In: *MNRAS* 449.3, pp. 2604–2617. DOI: 10.1093/mnras/stv327. arXiv: 1502.04767 [astro-ph.GA].

de Zeeuw, T. (Sept. 1985). "Elliptical galaxies with separable potentials". In: *MNRAS* 216, pp. 273–334. DOI: 10.1093/mnras/216.2.273.

Deng, L.-C. et al. (July 2012). "LAMOST Experiment for Galactic Understanding and Exploration (LEGUE) — The survey's science plan". In: *Research in Astronomy and Astrophysics* 12.7, pp. 735–754. DOI: 10.1088/1674-4527/12/7/003. arXiv: 1206.3578 [astro-ph.GA].

Dobbs, C. L. et al. (Apr. 2010). "Simulations of the grand design galaxy M51: a case study for analysing tidally induced spiral structure". In: *MNRAS* 403.2, pp. 625–645. DOI: 10.1111/j.1365-2966.2009.16161.x. arXiv: 0912.1201 [astro-ph.GA].

Drimmel, R. (June 2000). "Evidence for a two-armed spiral in the Milky Way". In: *A&A* 358, pp. L13–L16. DOI: 10.48550/arXiv.astro-ph/0005241. arXiv: astro-ph/0005241 [astro-ph].

Drimmel, R., A. Cabrera-Lavers, and M. López-Corredoira (Oct. 2003). "A three-dimensional Galactic extinction model". In: *A&A* 409, pp. 205–215. DOI: 10.1051/0004-6361:20031070. arXiv: astro-ph/0307273 [astro-ph].

Elsworth, Y. et al. (Oct. 2020). "A Layered Approach to Robust Determination of Asteroseismic Parameters". In: *Research Notes of the American Astronomical Society* 4.10, 177, p. 177. DOI: 10.3847/2515-5172/abbf5a.

Esteban, C. et al. (Jan. 2005). "Carbon and Oxygen Galactic Gradients: Observational Values from H II Region Recombination Lines". In: *ApJ* 618.2, pp. L95–L98. DOI: 10.1086/426889. arXiv: astro-ph/0408397 [astro-ph].

Foreman-Mackey, D. (June 2016). "corner.py: Scatterplot matrices in Python". In: *The Journal of Open Source Software* 1, p. 24. DOI: 10.21105/joss.00024.

Foreman-Mackey, D. et al. (Mar. 2013). "emcee: The MCMC Hammer". In: *PASP* 125.925, p. 306. DOI: 10.1086/670067. arXiv: 1202.3665 [astro-ph.IM].

Frankel, N. et al. (Oct. 2018). "Measuring Radial Orbit Migration in the Galactic Disk". In: *ApJ* 865.2, 96, p. 96. DOI: 10.3847/1538-4357/aadba5. arXiv: 1805.09198 [astro-ph.GA].

Frankel, N. et al. (Oct. 2019). "The Inside-out Growth of the Galactic Disk". In: *ApJ* 884.2, 99, p. 99. DOI: 10.3847/1538-4357/ab4254. arXiv: 1909.07118 [astro-ph.GA].

Frankel, N. et al. (June 2020). "Keeping It Cool: Much Orbit Migration, yet Little Heating, in the Galactic Disk". In: *ApJ* 896.1, 15, p. 15. DOI: 10.3847/1538-4357/ab910c. arXiv: 2002.04622 [astro-ph.GA].

Gaia Collaboration et al. (Nov. 2016). "The Gaia mission". In: *A&A* 595, A1, A1. DOI: 10.1051/0004-6361/201629272. arXiv: 1609.04153 [astro-ph.IM].

Gaia Collaboration et al. (May 2021). "Gaia Early Data Release 3. Summary of the contents and survey properties". In: *A&A* 649, A1, A1. DOI: 10.1051/0004-6361/202039657. arXiv: 2012.01533 [astro-ph.GA].

Gaia Collaboration et al. (June 2023a). "Gaia Data Release 3. Chemical cartography of the Milky Way". In: *A&A* 674, A38, A38. DOI: 10.1051/0004-6361/202243511. arXiv: 2206.05534 [astro-ph.GA].

Gaia Collaboration et al. (June 2023b). "Gaia Data Release 3. Mapping the asymmetric disc of the Milky Way". In: *A&A* 674, A37, A37. DOI: 10.1051/0004-6361/202243797. arXiv: 2206.06207 [astro-ph.GA].

Gaia Collaboration et al. (June 2023c). "Gaia Data Release 3. Summary of the content and survey properties". In: *A&A* 674, A1, A1. DOI: 10.1051/0004-6361/202243940. arXiv: 2208.00211 [astro-ph.GA].

Galilei, G. (1610). *Sidereus nuncius*. DOI: 10.3931/e-rara-695.

Gallart, C. et al. (July 2019). "Uncovering the birth of the Milky Way through accurate stellar ages with Gaia". In: *Nature Astronomy* 3, pp. 932–939. DOI: 10.1038/s41550-019-0829-5. arXiv: 1901.02900 [astro-ph.GA].

García Pérez, A. E. et al. (June 2016). "ASPCAP: The APOGEE Stellar Parameter and Chemical Abundances Pipeline". In: *AJ* 151.6, 144, p. 144. DOI: 10.3847/0004-6256/151/6/144. arXiv: 1510.07635 [astro-ph.SR].

Gelman, A. and D. B. Rubin (Jan. 1992). "Inference from Iterative Simulation Using Multiple Sequences". In: *Statistical Science* 7, pp. 457–472. DOI: 10.1214/ss/1177011136.

Gennaro, M., P. G. Prada Moroni, and S. Degl'Innocenti (July 2010). "$\Delta Y/\Delta Z$ from the analysis of local K dwarfs". In: *A&A* 518, A13, A13. DOI: 10.1051/0004-6361/201014227. arXiv: 1005.0245 [astro-ph.GA].

Genovali, K. et al. (June 2014). "On the fine structure of the Cepheid metallicity gradient in the Galactic thin disk". In: *A&A* 566, A37, A37. DOI: 10.1051/0004-6361/201323198. arXiv: 1403.6128 [astro-ph.GA].

Gilliland, R. L. et al. (Feb. 2010). "Kepler Asteroseismology Program: Introduction and First Results". In: *PASP* 122.888, p. 131. DOI: 10.1086/650399. arXiv: 1001.0139 [astro-ph.SR].

Gilmore, G. and N. Reid (Mar. 1983). "New light on faint stars - III. Galactic structure towards the South Pole and the Galactic thick disc." In: *MNRAS* 202, pp. 1025–1047. DOI: 10.1093/mnras/202.4.1025.

Girardi, L. (Sept. 2016). "Red Clump Stars". In: *ARA&A* 54, pp. 95–133. DOI: 10.1146/annurev-astro-081915-023354.

Grand, R. J. J., D. Kawata, and M. Cropper (Mar. 2015). "Impact of radial migration on stellar and gas radial metallicity distribution". In: *MNRAS* 447.4, pp. 4018–4027. DOI: 10.1093/mnras/stv016. arXiv: 1410.3836 [astro-ph.GA].

Green, G. M. (June 2018). "dustmaps: A Python interface for maps of interstellar dust". In: *The Journal of Open Source Software* 3.26, p. 695. DOI: 10.21105/joss.00695.

Green, G. M. et al. (Dec. 2019). "A 3D Dust Map Based on Gaia, Pan-STARRS 1, and 2MASS". In: *ApJ* 887.1, 93, p. 93. DOI: 10.3847/1538-4357/ab5362. arXiv: 1905.02734 [astro-ph.GA].

Green, G. M. et al. (Mar. 2014). "Measuring Distances and Reddenings for a Billion Stars: Toward a 3D Dust Map from Pan-STARRS 1". In: *ApJ* 783.2, 114, p. 114. DOI: 10.1088/0004-637X/783/2/114. arXiv: 1401.1508 [astro-ph.GA].

Grisoni, V., E. Spitoni, and F. Matteucci (Dec. 2018). "Abundance gradients along the Galactic disc from chemical evolution models". In: *MNRAS* 481.2, pp. 2570–2580. DOI: 10.1093/mnras/sty2444. arXiv: 1805.11415 [astro-ph.GA].

Grisoni, V. et al. (Dec. 2017). "The AMBRE project: chemical evolution models for the Milky Way thick and thin discs". In: *MNRAS* 472.3, pp. 3637–3647. DOI: 10.1093/mnras/stx2201. arXiv: 1706.02614 [astro-ph.GA].

Guzik, J. A. (Dec. 2013). "Challenges in Solar and Stellar Model Physics". In: *Fifty Years of Seismology of the Sun and Stars*. Ed. by K. Jain et al. Vol. 478. Astronomical Society of the Pacific Conference Series, p. 351.

Hall, O. J. et al. (July 2021). "Weakened magnetic braking supported by asteroseismic rotation rates of Kepler dwarfs". In: *Nature Astronomy* 5, pp. 707–714. DOI: 10.1038/s41550-021-01335-x. arXiv: 2104.10919 [astro-ph.SR].

Hawkins, K. et al. (Dec. 2014). "On the relative ages of the α-rich and α-poor stellar populations in the Galactic halo". In: *MNRAS* 445.3, pp. 2575–2588. DOI: 10.1093/mnras/stu1910. arXiv: 1409.3431 [astro-ph.GA].

Hawkins, K. et al. (Oct. 2015). "Using chemical tagging to redefine the interface of the Galactic disc and halo". In: *MNRAS* 453.1, pp. 758–774. DOI: 10.1093/mnras/stv1586. arXiv: 1507.03604 [astro-ph.GA].

Hayden, M. R. et al. (May 2014). "Chemical Cartography with APOGEE: Large-scale Mean Metallicity Maps of the Milky Way Disk". In: *AJ* 147.5, 116, p. 116. DOI: 10.1088/0004-6256/147/5/116. arXiv: 1311.4569 [astro-ph.GA].

Hayden, M. R. et al. (Aug. 2015). "Chemical Cartography with APOGEE: Metallicity Distribution Functions and the Chemical Structure of the Milky Way Disk". In: *ApJ* 808.2, 132, p. 132. DOI: 10.1088/0004-637X/808/2/132. arXiv: 1503.02110 [astro-ph.GA].

Haywood, M. (Aug. 2008). "Radial mixing and the transition between the thick and thin Galactic discs". In: *MNRAS* 388.3, pp. 1175–1184. DOI: 10.1111/j.1365-2966.2008.13395.x. arXiv: 0805.1822 [astro-ph].

Hegedűs, V. et al. (Feb. 2023). "Comparative analysis of atmospheric parameters from high-resolution spectroscopic sky surveys: APOGEE, GALAH, Gaia-ESO". In: *A&A* 670, A107, A107. DOI: 10.1051/0004-6361/202244813. arXiv: 2211.03416 [astro-ph.SR].

Hekker, S. and J. Christensen-Dalsgaard (June 2017). "Giant star seismology". In: *A&A Rev.* 25.1, 1, p. 1. DOI: 10.1007/s00159-017-0101-x. arXiv: 1609.07487 [astro-ph.SR].

Helmi, A. (Aug. 2020). "Streams, Substructures, and the Early History of the Milky Way". In: *ARA&A* 58, pp. 205–256. DOI: 10.1146/annurev-astro-032620-021917. arXiv: 2002.04340 [astro-ph.GA].

Helmi, A. et al. (Oct. 2018). "The merger that led to the formation of the Milky Way's inner stellar halo and thick disk". In: *Nature* 563.7729, pp. 85–88. DOI: 10.1038/s41586-018-0625-x. arXiv: 1806.06038 [astro-ph.GA].

Herschel, W. (Jan. 1785). "On the Construction of the Heavens." In: *Philosophical Transactions of the Royal Society of London Series I* 75, pp. 213–266.

Hoffman, M. D. and A. Gelman (Nov. 2011). "The No-U-Turn Sampler: Adaptively Setting Path Lengths in Hamiltonian Monte Carlo". In: *arXiv e-prints*, arXiv:1111.4246, arXiv:1111.4246. DOI: 10.48550/arXiv.1111.4246. arXiv: 1111.4246 [stat.CO].

Hogg, D. W., J. Bovy, and D. Lang (Aug. 2010). "Data analysis recipes: Fitting a model to data". In: *arXiv e-prints*, arXiv:1008.4686, arXiv:1008.4686. DOI: 10.48550/arXiv.1008.4686. arXiv: 1008.4686 [astro-ph.IM].

Hon, M., D. Stello, and J. Yu (Aug. 2017). "Deep learning classification in asteroseismology". In: *MNRAS* 469.4, pp. 4578–4583. DOI: 10.1093/mnras/stx1174. arXiv: 1705.06405 [astro-ph.SR].

— (May 2018). "Deep learning classification in asteroseismology using an improved neural network: results on 15 000 Kepler red giants and applications to K2 and TESS data". In: *MNRAS* 476.3, pp. 3233–3244. DOI: 10.1093/mnras/sty483. arXiv: 1802.07260 [astro-ph.IM].

Hon, M., D. Stello, and J. C. Zinn (May 2018). "Detecting Solar-like Oscillations in Red Giants with Deep Learning". In: *ApJ* 859.1, 64, p. 64. DOI: 10.3847/1538-4357/aabfdb. arXiv: 1804.07495 [astro-ph.SR].

Horta, D. et al. (Apr. 2023). "The chemical characterization of halo substructure in the Milky Way based on APOGEE". In: *MNRAS* 520.4, pp. 5671–5711. DOI: 10.1093/mnras/stac3179. arXiv: 2204.04233 [astro-ph.GA].

Howell, S. B. et al. (Apr. 2014). "The K2 Mission: Characterization and Early Results". In: *PASP* 126.938, p. 398. DOI: 10.1086/676406. arXiv: 1402.5163 [astro-ph.IM].

Hubble, E. P. (Mar. 1929). "A spiral nebula as a stellar system, Messier 31." In: *ApJ* 69, pp. 103–158. DOI: 10.1086/143167.

Hubble, E. (1982). *The realm of the nebulae*. eng. New Haven ; London.

Huber, D. et al. (Dec. 2011). "Testing Scaling Relations for Solar-like Oscillations from the Main Sequence to Red Giants Using Kepler Data". In: *ApJ* 743.2, 143, p. 143. DOI: 10.1088/0004-637X/743/2/143. arXiv: 1109.3460 [astro-ph.SR].

Huber, D. et al. (May 2016). "The K2 Ecliptic Plane Input Catalog (EPIC) and Stellar Classifications of 138,600 Targets in Campaigns 1-8". In: *ApJS* 224.1, 2, p. 2. DOI: 10.3847/0067-0049/224/1/2. arXiv: 1512.02643 [astro-ph.SR].

Ibata, R. A. et al. (Feb. 1997). "The Kinematics, Orbit, and Survival of the Sagittarius Dwarf Spheroidal Galaxy". In: *AJ* 113, pp. 634–655. DOI: 10.1086/118283. arXiv: astro-ph/9612025 [astro-ph].

Iben Icko, J. (Nov. 1964). "The Surface Ratio of N^{14} to C^{12} during Helium Burning." In: *ApJ* 140, p. 1631. DOI: 10.1086/148077.

— (Feb. 1967). "Stellar Evolution.VI. Evolution from the Main Sequence to the Red-Giant Branch for Stars of Mass 1 M_{sun}, 1.25 M_{sun}, and 1.5 M_{sun}". In: *ApJ* 147, p. 624. DOI: 10.1086/149040.

Izotov, Y. I., T. X. Thuan, and G. Stasińska (June 2007). "The Primordial Abundance of ^{4}He: A Self-consistent Empirical Analysis of Systematic Effects in a Large Sample of Low-Metallicity H II Regions". In: *ApJ* 662.1, pp. 15–38. DOI: 10.1086/513601. arXiv: astro-ph/0702072 [astro-ph].

Jermyn, A. S. et al. (Mar. 2023). "Modules for Experiments in Stellar Astrophysics (MESA): Time-dependent Convection, Energy Conservation, Automatic Differentiation, and Infrastructure". In: *ApJS* 265.1, 15, p. 15. DOI: 10.3847/1538-4365/acae8d. arXiv: 2208.03651 [astro-ph.SR].

Johnston, K. V. et al. (Oct. 1999). "Constraining the History of the Sagittarius Dwarf Galaxy Using Observations of Its Tidal Debris". In: *AJ* 118.4, pp. 1719–1726. DOI: 10.1086/301037. arXiv: astro-ph/9906457 [astro-ph].

Jurić, M. et al. (Feb. 2008). "The Milky Way Tomography with SDSS. I. Stellar Number Density Distribution". In: *ApJ* 673.2, pp. 864–914. DOI: 10.1086/523619. arXiv: astro-ph/0510520 [astro-ph].

Kaufer, A. et al. (Sept. 1994). "The galactic abundance gradients traced by B-type stars." In: *A&A* 289, pp. 740–748.

Khan, S. et al. (Sept. 2023). "Investigating Gaia EDR3 parallax systematics using asteroseismology of Cool Giant Stars observed by Kepler, K2, and TESS. I. Asteroseismic distances to 12 500 red-giant stars". In: *A&A* 677, A21, A21. DOI: 10.1051/0004-6361/202346196. arXiv: 2304.07158 [astro-ph.SR].

Kippenhahn, R. (2012). *Stellar structure and evolution / Rudolf Kippenhahn, Alfred Weigert, Achim Weiss.* eng. Heidelberg ; London.

Kjeldsen, H. and T. R. Bedding (Jan. 1995). "Amplitudes of stellar oscillations: the implications for asteroseismology." In: *A&A* 293, pp. 87–106. DOI: 10.48550/arXiv.astro-ph/9403015. arXiv: astro-ph/9403015 [astro-ph].

Kormendy, J. and J. Kennicutt Robert C. (Sept. 2004). "Secular Evolution and the Formation of Pseudobulges in Disk Galaxies". In: *ARA&A* 42.1, pp. 603–683. DOI: 10.1146/annurev.astro.42.053102.134024. arXiv: astro-ph/0407343 [astro-ph].

Kubryk, M., N. Prantzos, and E. Athanassoula (Aug. 2015a). "Evolution of the Milky Way with radial motions of stars and gas. I. The solar neighbourhood and the thin and thick disks". In: *A&A* 580, A126, A126. DOI: 10.1051/0004-6361/201424171. arXiv: 1412.0585 [astro-ph.GA].

— (Aug. 2015b). "Evolution of the Milky Way with radial motions of stars and gas. II. The evolution of abundance profiles from H to Ni". In: *A&A* 580, A127, A127. DOI: 10.1051/0004-6361/201424599. arXiv: 1412.4859 [astro-ph.GA].

Kuszlewicz, J. S., S. Hekker, and K. J. Bell (Oct. 2020). "Clumpiness: time-domain classification of red giant evolutionary states". In: *MNRAS* 497.4, pp. 4843–4856. DOI: 10.1093/mnras/staa2155. arXiv: 2007.10921 [astro-ph.SR].

L. Lindegren (Aug. 2018). "Re-normalising the astrometric chi-square in Gaia DR2". Technical Note. GAIA-C3-TN-LU-LL-124.

Lagarde, N. et al. (Jan. 2019). "The Gaia-ESO Survey: impact of extra mixing on C and N abundances of giant stars". In: *A&A* 621, A24, A24. DOI: 10.1051/0004-6361/201732433. arXiv: 1806.01868 [astro-ph.SR].

Lagioia, E. P. et al. (Apr. 2018). "The Hubble Space Telescope UV Legacy Survey of Galactic Globular Clusters - XII. The RGB bumps of multiple stellar populations". In: *MNRAS* 475.3, pp. 4088–4103. DOI: 10.1093/mnras/sty083. arXiv: 1801.03395 [astro-ph.SR].

Lamb, H. (1932). *Hydrodynamics / by Sir Horace Lamb*. eng. Cambridge.

Larson, R. B. (July 1976). "Models for the formation of disc galaxies." In: *MNRAS* 176, pp. 31–52. DOI: 10.1093/mnras/176.1.31.

Lebreton, Y., M. J. Goupil, and J. Montalbán (Nov. 2014a). "How accurate are stellar ages based on stellar models?. I. The impact of stellar models uncertainties". In: *EAS Publications Series*. Ed. by Y. Lebreton, D. Valls-Gabaud, and C. Charbonnel. Vol. 65. EAS Publications Series, pp. 99–176. DOI: 10.1051/eas/1465004. arXiv: 1410.5336 [astro-ph.SR].

— (Nov. 2014b). "How accurate are stellar ages based on stellar models?. II. The impact of asteroseismology". In: *EAS Publications Series*. Ed. by Y. Lebreton, D. Valls-Gabaud, and C. Charbonnel. Vol. 65. EAS Publications Series, pp. 177–223. DOI: 10.1051/eas/1465005. arXiv: 1410.5337 [astro-ph.SR].

Leung, S.-C. and K. Nomoto (Nov. 2021). "Type Ia Supernovae and their Explosive Nucleosynthesis: Constraints on Progenitors". In: *arXiv e-prints*, arXiv:2111.14795, arXiv:2111.14795. DOI: 10.48550/arXiv.2111.14795. arXiv: 2111.14795 [astro-ph.HE].

Liddle, A. R. (2015). *An introduction to modern cosmology / Andrew Liddle*. eng. Third edition. ISBN: 9781118690277.

Lin, C. C. and F. H. Shu (Aug. 1964). "On the Spiral Structure of Disk Galaxies." In: *ApJ* 140, p. 646. DOI: 10.1086/147955.

Lindegren, L. et al. (May 2021). "Gaia Early Data Release 3. Parallax bias versus magnitude, colour, and position". In: *A&A* 649, A4, A4. DOI: 10.1051/0004-6361/202039653. arXiv: 2012.01742 [astro-ph.IM].

Lu, Y. et al. (Dec. 2022). "There is No Place Like Home – Finding Birth Radii of Stars in the Milky Way". In: *arXiv e-prints*, arXiv:2212.04515, arXiv:2212.04515. DOI: 10.48550/arXiv.2212.04515. arXiv: 2212.04515 [astro-ph.GA].

Luger, R. et al. (Sept. 2018). "An Update to the EVEREST K2 Pipeline: Short Cadence, Saturated Stars, and Kepler-like Photometry Down to Kp = 15". In: *AJ* 156.3, 99, p. 99. DOI: 10.3847/1538-3881/aad230. arXiv: 1702.05488 [astro-ph.IM].

Lynga, G. and J. Palous (Dec. 1987). "The local kinematics of open star clusters." In: *A&A* 188, pp. 35–38.

Lyttle, A. J. et al. (Aug. 2021). "Hierarchically modelling Kepler dwarfs and subgiants to improve inference of stellar properties with asteroseismology". In: *MNRAS* 505.2, pp. 2427–2446. DOI: 10.1093/mnras/stab1368. arXiv: 2105.04482 [astro-ph.SR].

Mackereth, J. T. and J. Bovy (Nov. 2018). "Fast Estimation of Orbital Parameters in Milky Way-like Potentials". In: *PASP* 130.993, p. 114501. DOI: 10.1088/1538-3873/aadcdd. arXiv: 1802.02592 [astro-ph.GA].

Mackereth, J. T. et al. (Oct. 2019a). "Dynamical heating across the Milky Way disc using APOGEE and Gaia". In: *MNRAS* 489.1, pp. 176–195. DOI: 10.1093/mnras/stz1521. arXiv: 1901.04502 [astro-ph.GA].

Mackereth, J. T. et al. (Jan. 2019b). "The origin of accreted stellar halo populations in the Milky Way using APOGEE, Gaia, and the EAGLE simulations". In: *MNRAS* 482.3, pp. 3426–3442. DOI: 10.1093/mnras/sty2955. arXiv: 1808.00968 [astro-ph.GA].

Mackereth, J. T. et al. (Apr. 2021). "Prospects for Galactic and stellar astrophysics with asteroseismology of giant stars in the TESS continuous viewing zones and beyond". In: *MNRAS* 502.2, pp. 1947–1966. DOI: 10.1093/mnras/stab098. arXiv: 2012.00140 [astro-ph.GA].

Magrini, L. et al. (Jan. 2009). "The evolution of the Galactic metallicity gradient from high-resolution spectroscopy of open clusters". In: *A&A* 494.1, pp. 95–108. DOI: 10.1051/0004-6361:200810634. arXiv: 0812.0854 [astro-ph].

Magrini, L. et al. (Apr. 2016). "Metallicity gradients in local Universe galaxies: Time evolution and effects of radial migration". In: *A&A* 588, A91, A91. DOI: 10.1051/0004-6361/201527799. arXiv: 1602.02529 [astro-ph.GA].

Majewski, S. R. et al. (Sept. 2017). "The Apache Point Observatory Galactic Evolution Experiment (APOGEE)". In: *AJ* 154.3, 94, p. 94. DOI: 10.3847/1538-3881/aa784d. arXiv: 1509.05420 [astro-ph.IM].

Marshall, D. J. et al. (July 2006). "Modelling the Galactic interstellar extinction distribution in three dimensions". In: *A&A* 453.2, pp. 635–651. DOI: 10.1051/0004-6361:20053842. arXiv: astro-ph/0604427 [astro-ph].

Martig, M. et al. (Mar. 2016). "Red giant masses and ages derived from carbon and nitrogen abundances". In: *MNRAS* 456.4, pp. 3655–3670. DOI: 10.1093/mnras/stv2830. arXiv: 1511.08203 [astro-ph.SR].

Massari, D., H. H. Koppelman, and A. Helmi (Oct. 2019). "Origin of the system of globular clusters in the Milky Way". In: *A&A* 630, L4, p. L4. DOI: 10.1051/0004-6361/201936135. arXiv: 1906.08271 [astro-ph.GA].

Masseron, T. and G. Gilmore (Oct. 2015). "Carbon, nitrogen and α-element abundances determine the formation sequence of the Galactic thick and thin discs". In: *MNRAS* 453.2, pp. 1855–1866. DOI: 10.1093/mnras/stv1731. arXiv: 1503.00537 [astro-ph.SR].

Matteucci, F. and P. Francois (Aug. 1989). "Galactic chemical evolution : abundance gradients of individual elements." In: *MNRAS* 239, pp. 885–904. DOI: 10.1093/mnras/239.3.885.

Matteuzzi, M. et al. (Mar. 2023). "Red horizontal branch stars: An asteroseismic perspective". In: *A&A* 671, A53, A53. DOI: 10.1051/0004-6361/202245746. arXiv: 2301.08761 [astro-ph.SR].

Miglio, A. et al. (Jan. 2012). "Asteroseismology of old open clusters with Kepler: direct estimate of the integrated red giant branch mass-loss in NGC 6791 and 6819". In: *MNRAS* 419.3, pp. 2077–2088. DOI: 10.1111/j.1365-2966.2011.19859.x. arXiv: 1109.4376 [astro-ph.SR].

Miglio, A. et al. (Sept. 2016). "Detection of solar-like oscillations in relics of the Milky Way: asteroseismology of K giants in M4 using data from the NASA K2 mission". In: *MNRAS* 461.1, pp. 760–765. DOI: 10.1093/mnras/stw1555. arXiv: 1606.02115 [astro-ph.SR].

Miglio, A. et al. (July 2017). "PLATO as it is : A legacy mission for Galactic archaeology". In: *Astronomische Nachrichten* 338.6, pp. 644–661. DOI: 10.1002/asna.201713385. arXiv: 1706.03778 [astro-ph.SR].

Miglio, A. et al. (Jan. 2021). "Age dissection of the Milky Way discs: Red giants in the Kepler field". In: *A&A* 645, A85, A85. DOI: 10.1051/0004-6361/202038307. arXiv: 2004.14806 [astro-ph.GA].

Milone, A. P. et al. (Dec. 2018). "The Hubble Space Telescope UV legacy survey of galactic globular clusters - XVI. The helium abundance of multiple populations". In: *MNRAS* 481.4, pp. 5098–5122. DOI: 10.1093/mnras/sty2573. arXiv: 1809.05006 [astro-ph.SR].

Minchev, I. (July 2016). "Constraining the Milky Way assembly history with Galactic Archaeology. Ludwig Biermann Award Lecture 2015". In: *Astronomische Nachrichten* 337.7, p. 703. DOI: 10.1002/asna.201612366. arXiv: 1701.07034 [astro-ph.GA].

Minchev, I., C. Chiappini, and M. Martig (Oct. 2013). "Chemodynamical evolution of the Milky Way disk. I. The solar vicinity". In: *A&A* 558, A9, A9. DOI: 10.1051/0004-6361/201220189. arXiv: 1208.1506 [astro-ph.GA].

— (Dec. 2014). "Chemodynamical evolution of the Milky Way disk. II. Variations with Galactic radius and height above the disk plane". In: *A&A* 572, A92, A92. DOI: 10.1051/0004-6361/201423487. arXiv: 1401.5796 [astro-ph.GA].

— (Sept. 2016). "Milky Way chemo-dynamics in the era of Gaia". In: *Astronomische Nachrichten* 337.8-9, p. 944. DOI: 10.1002/asna.201612404. arXiv: 1601.01313 [astro-ph.GA].

Minchev, I. et al. (Dec. 2012). "Radial migration does little for Galactic disc thickening". In: *A&A* 548, A127, A127. DOI: 10.1051/0004-6361/201219714. arXiv: 1205.6475 [astro-ph.GA].

Minchev, I. et al. (Dec. 2018). "Estimating stellar birth radii and the time evolution of Milky Way's ISM metallicity gradient". In: *MNRAS* 481.2, pp. 1645–1657. DOI: 10.1093/mnras/sty2033. arXiv: 1804.06856 [astro-ph.GA].

Momany, Y. et al. (May 2006). "Outer structure of the Galactic warp and flare: explaining the Canis Major over-density". In: *A&A* 451.2, pp. 515–538. DOI: 10.1051/0004-6361:20054081. arXiv: astro-ph/0603385 [astro-ph].

Monari, G. et al. (Mar. 2017). "Tracing the Hercules stream with Gaia and LAMOST: new evidence for a fast bar in the Milky Way". In: *MNRAS* 466.1, pp. L113–L117. DOI: 10.1093/mnrasl/slw238. arXiv: 1610.05342 [astro-ph.GA].

Montalbán, J. et al. (Jan. 2021). "Chronologically dating the early assembly of the Milky Way". In: *Nature Astronomy* 5, pp. 640–647. DOI: 10.1038/s41550-021-01347-7. arXiv: 2006.01783 [astro-ph.GA].

Morel, T. et al. (Feb. 2021). "Testing abundance-age relations beyond solar analogues with Kepler LEGACY stars". In: *A&A* 646, A78, A78. DOI: 10.1051/0004-6361/202039212. arXiv: 2011.04481 [astro-ph.SR].

Mosser, B. (Feb. 2015). "Stellar oscillations - I - The adiabatic case". In: *EAS Publications Series*. Vol. 73-74. EAS Publications Series, pp. 3–110. DOI: 10.1051/eas/1573002. arXiv: 1509.08077 [astro-ph.SR].

Mosser, B. and T. Appourchaux (Dec. 2009). "On detecting the large separation in the autocorrelation of stellar oscillation times series". In: *A&A* 508.2, pp. 877–887. DOI: 10.1051/0004-6361/200912944. arXiv: 0909.0782 [astro-ph.SR].

Mosser, B. et al. (July 2010). "Red-giant seismic properties analyzed with CoRoT". In: *A&A* 517, A22, A22. DOI: 10.1051/0004-6361/201014036. arXiv: 1004.0449 [astro-ph.SR].

Mosser, B. et al. (Dec. 2014). "Mixed modes in red giants: a window on stellar evolution". In: *A&A* 572, L5, p. L5. DOI: 10.1051/0004-6361/201425039. arXiv: 1411.1082 [astro-ph.SR].

Moya, A. et al. (Apr. 2022). "Stellar dating using chemical clocks and Bayesian inference". In: *A&A* 660, A15, A15. DOI: 10.1051/0004-6361/202141125. arXiv: 2201.05228 [astro-ph.SR].

Myers, N. et al. (Sept. 2022). "The Open Cluster Chemical Abundances and Mapping Survey. VI. Galactic Chemical Gradient Analysis from APOGEE DR17". In: *AJ* 164.3, 85, p. 85. DOI: 10.3847/1538-3881/ac7ce5. arXiv: 2206.13650 [astro-ph.GA].

Nataf, D. M. (June 2016). "The Controversial Star-Formation History and Helium Enrichment of the Milky Way Bulge". In: *PASA* 33, e023, e023. DOI: 10.1017/pasa.2015.38. arXiv: 1509.00023 [astro-ph.SR].

Nataf, D. M. and A. P. Gould (June 2012). "Reconciling the Galactic Bulge Turnoff Age Discrepancy with Enhanced Helium Enrichment". In: *ApJ* 751.2, L39, p. L39. DOI: 10.1088/2041-8205/751/2/L39. arXiv: 1112.1072 [astro-ph.GA].

Netopil, M. et al. (Jan. 2022). "The Galactic metallicity gradient shown by open clusters in the light of radial migration". In: *MNRAS* 509.1, pp. 421–439. DOI: 10.1093/mnras/stab2961. arXiv: 2110.11893 [astro-ph.GA].

Nieva, M. .-. and N. Przybilla (Mar. 2012). "Present-day cosmic abundances. A comprehensive study of nearby early B-type stars and implications for stellar and Galactic evolution and interstellar dust models". In: *A&A* 539, A143, A143. DOI: 10.1051/0004-6361/201118158. arXiv: 1203.5787 [astro-ph.SR].

Nordström, B. et al. (May 2004). "The Geneva-Copenhagen survey of the Solar neighbourhood. Ages, metallicities, and kinematic properties of ~14 000 F and G dwarfs". In: *A&A* 418, pp. 989–1019. DOI: 10.1051/0004-6361:20035959. arXiv: astro-ph/0405198 [astro-ph].

Pagel, B. E. J. (2009). *Nucleosynthesis and chemical evolution of galaxies / Bernard Pagel.* eng. Cambridge.

Pagel, B. E. J. and M. G. Edmunds (Jan. 1981). "Abundances in stellar populations and the interstellar medium in galaxies". In: *ARA&A* 19, pp. 77–113. DOI: 10.1146/annurev.aa.19.090181.000453.

Paxton, B. et al. (Jan. 2011). "Modules for Experiments in Stellar Astrophysics (MESA)". In: *ApJS* 192.1, 3, p. 3. DOI: 10.1088/0067-0049/192/1/3. arXiv: 1009.1622 [astro-ph.SR].

Paxton, B. et al. (Sept. 2013). "Modules for Experiments in Stellar Astrophysics (MESA): Planets, Oscillations, Rotation, and Massive Stars". In: *ApJS* 208.1, 4, p. 4. DOI: 10.1088/0067-0049/208/1/4. arXiv: 1301.0319 [astro-ph.SR].

Paxton, B. et al. (Sept. 2015). "Modules for Experiments in Stellar Astrophysics (MESA): Binaries, Pulsations, and Explosions". In: *ApJS* 220.1, 15, p. 15. DOI: 10.1088/0067-0049/220/1/15. arXiv: 1506.03146 [astro-ph.SR].

Paxton, B. et al. (Feb. 2018). "Modules for Experiments in Stellar Astrophysics (MESA): Convective Boundaries, Element Diffusion, and Massive Star Explosions". In: *ApJS* 234.2, 34, p. 34. DOI: 10.3847/1538-4365/aaa5a8. arXiv: 1710.08424 [astro-ph.SR].

Paxton, B. et al. (July 2019). "Modules for Experiments in Stellar Astrophysics (MESA): Pulsating Variable Stars, Rotation, Convective Boundaries, and Energy Conservation". In: *ApJS* 243.1, 10, p. 10. DOI: 10.3847/1538-4365/ab2241. arXiv: 1903.01426 [astro-ph.SR].

Phan, D., N. Pradhan, and M. Jankowiak (Dec. 2019). "Composable Effects for Flexible and Accelerated Probabilistic Programming in NumPyro". In: *arXiv e-prints*, arXiv:1912.11554, arXiv:1912.11554. DOI: 10.48550/arXiv.1912.11554. arXiv: 1912.11554 [stat.ML].

Poggio, E. et al. (Mar. 2020). "Evidence of a dynamically evolving Galactic warp". In: *Nature Astronomy* 4, pp. 590–596. DOI: 10.1038/s41550-020-1017-3. arXiv: 1912.10471 [astro-ph.GA].

Pontoppidan, K. M. et al. (Sept. 2022). "The JWST Early Release Observations". In: *ApJ* 936.1, L14, p. L14. DOI: 10.3847/2041-8213/ac8a4e. arXiv: 2207.13067 [astro-ph.IM].

Quinn, P. J., L. Hernquist, and D. P. Fullagar (Jan. 1993). "Heating of Galactic Disks by Mergers". In: *ApJ* 403, p. 74. DOI: 10.1086/172184.

Randich, S. et al. (Oct. 2022). "The Gaia-ESO Public Spectroscopic Survey: Implementation, data products, open cluster survey, science, and legacy". In: *A&A* 666, A121, A121. DOI: 10.1051/0004-6361/202243141. arXiv: 2206.02901 [astro-ph.GA].

Ratcliffe, B. et al. (Oct. 2023). "Unveiling the time evolution of chemical abundances across the Milky Way disc with APOGEE". In: *MNRAS* 525.2, pp. 2208–2228. DOI: 10.1093/mnras/stad1573. arXiv: 2305.13378 [astro-ph.GA].

Rauer, H. et al. (Nov. 2014). "The PLATO 2.0 mission". In: *Experimental Astronomy* 38.1-2, pp. 249–330. DOI: 10.1007/s10686-014-9383-4. arXiv: 1310.0696 [astro-ph.EP].

Reid, M. J. et al. (Mar. 2014). "Trigonometric Parallaxes of High Mass Star Forming Regions: The Structure and Kinematics of the Milky Way". In: *ApJ* 783.2, 130, p. 130. DOI: 10.1088/0004-637X/783/2/130. arXiv: 1401.5377 [astro-ph.GA].

Reimers, D. (Jan. 1975). "Circumstellar absorption lines and mass loss from red giants." In: *Memoires of the Societe Royale des Sciences de Liege* 8, pp. 369–382.

Renaud, F., Á. Segovia Otero, and O. Agertz (Nov. 2022). "The merger-starburst connection across cosmic times". In: *MNRAS* 516.4, pp. 4922–4931. DOI: 10.1093/mnras/stac2557. arXiv: 2209.03983 [astro-ph.GA].

Ricker, G. R. et al. (Jan. 2015). "Transiting Exoplanet Survey Satellite (TESS)". In: *Journal of Astronomical Telescopes, Instruments, and Systems* 1, 014003, p. 014003. DOI: 10.1117/1.JATIS.1.1.014003.

Robertson, B. E. et al. (May 2023). "Identification and properties of intense star-forming galaxies at redshifts z > 10". In: *Nature Astronomy* 7, pp. 611–621. DOI: 10.1038/s41550-023-01921-1. arXiv: 2212.04480 [astro-ph.GA].

Rodrigues, T. S. et al. (Dec. 2014). "Bayesian distances and extinctions for giants observed by Kepler and APOGEE". In: *MNRAS* 445.3, pp. 2758–2776. DOI: 10.1093/mnras/stu1907. arXiv: 1410.1350 [astro-ph.SR].

Rodrigues, T. S. et al. (May 2017). "Determining stellar parameters of asteroseismic targets: going beyond the use of scaling relations". In: *MNRAS* 467.2, pp. 1433–1448. DOI: 10.1093/mnras/stx120. arXiv: 1701.04791 [astro-ph.SR].

Roman, N. G. (Nov. 1950). "A Correlation Between the Spectroscopic and Dynamical Characteristics of the Late F - and Early G - Type Stars." In: *ApJ* 112, p. 554. DOI: 10.1086/145367.

Salaris, M., A. Chieffi, and O. Straniero (Sept. 1993). "The alpha -enhanced Isochrones and Their Impact on the FITS to the Galactic Globular Cluster System". In: *ApJ* 414, p. 580. DOI: 10.1086/173105.

Schönrich, R. and J. Binney (June 2009a). "Chemical evolution with radial mixing". In: *MNRAS* 396.1, pp. 203–222. DOI: 10.1111/j.1365-2966.2009.14750.x. arXiv: 0809.3006 [astro-ph].

— (Nov. 2009b). "Origin and structure of the Galactic disc(s)". In: *MNRAS* 399.3, pp. 1145–1156. DOI: 10.1111/j.1365-2966.2009.15365.x. arXiv: 0907.1899 [astro-ph.GA].

Schönrich, R., J. Binney, and W. Dehnen (Apr. 2010). "Local kinematics and the local standard of rest". In: *MNRAS* 403.4, pp. 1829–1833. DOI: 10.1111/j.1365-2966.2010.16253.x. arXiv: 0912.3693 [astro-ph.GA].

Searle, L. and R. Zinn (Oct. 1978). "Composition of halo clusters and the formation of the galactic halo." In: *ApJ* 225, pp. 357–379. DOI: 10.1086/156499.

Searle, L. (Sept. 1971). "Evidence for Composition Gradients across the Disks of Spiral Galaxies". In: *ApJ* 168, p. 327. DOI: 10.1086/151090.

Sellwood, J. A. and J. J. Binney (Nov. 2002). "Radial mixing in galactic discs". In: *MNRAS* 336.3, pp. 785–796. DOI: 10.1046/j.1365-8711.2002.05806.x. arXiv: astro-ph/0203510 [astro-ph].

Sellwood, J. A. and R. G. Carlberg (July 1984). "Spiral instabilities provoked by accretion and star formation". In: *ApJ* 282, pp. 61–74. DOI: 10.1086/162176.

Soderblom, D. R. (Sept. 2010). "The Ages of Stars". In: *ARA&A* 48, pp. 581–629. DOI: 10.1146/annurev-astro-081309-130806. arXiv: 1003.6074 [astro-ph.SR].

Sparke, L. S. and J. S. Gallagher (2007). *Galaxies in the universe : an introduction*. eng. Cambridge.

Spergel, D. et al. (Mar. 2015). "Wide-Field InfrarRed Survey Telescope-Astrophysics Focused Telescope Assets WFIRST-AFTA 2015 Report". In: *arXiv e-prints*, arXiv:1503.03757, arXiv:1503.03757. DOI: 10.48550/arXiv.1503.03757. arXiv: 1503.03757 [astro-ph.IM].

Spina, L. et al. (May 2021). "The GALAH survey: tracing the Galactic disc with open clusters". In: *MNRAS* 503.3, pp. 3279–3296. DOI: 10.1093/mnras/stab471. arXiv: 2011.02533 [astro-ph.GA].

Spina, L., L. Magrini, and K. Cunha (Jan. 2022). "Mapping the Galactic Metallicity Gradient with Open Clusters: The State-of-the-Art and Future Challenges". In: *Universe* 8.2, p. 87. DOI: 10.3390/universe8020087. arXiv: 2202.00463 [astro-ph.GA].

Spitoni, E. et al. (Mar. 2021). "APOGEE DR16: A multi-zone chemical evolution model for the Galactic disc based on MCMC methods". In: *A&A* 647, A73, A73. DOI: 10.1051/0004-6361/202039864. arXiv: 2101.08803 [astro-ph.GA].

Steinmetz, M. et al. (Aug. 2020a). "The Sixth Data Release of the Radial Velocity Experiment (RAVE). I. Survey Description, Spectra, and Radial Velocities". In: *AJ* 160.2, 82, p. 82. DOI: 10.3847/1538-3881/ab9ab9. arXiv: 2002.04377 [astro-ph.SR].

Steinmetz, M. et al. (Aug. 2020b). "The Sixth Data Release of the Radial Velocity Experiment (RAVE). II. Stellar Atmospheric Parameters, Chemical Abundances, and Distances". In: *AJ* 160.2, 83, p. 83. DOI: 10.3847/1538-3881/ab9ab8. arXiv: 2002.04512 [astro-ph.SR].

Stephan, E. (Aug. 1881). "Nébuleuses découvertes et observées à l'Observatoire de Marseille". In: *Astronomische Nachrichten* 100.14, p. 209. DOI: 10.1002/asna.18811001402.

Tailo, M. et al. (May 2021). "Mass-loss law for red giant stars in simple population globular clusters". In: *MNRAS* 503.1, pp. 694–703. DOI: 10.1093/mnras/stab568. arXiv: 2102.12146 [astro-ph.SR].

Tailo, M. et al. (June 2022). "Asteroseismology of the multiple stellar populations in the globular cluster M4". In: *A&A* 662, L7, p. L7. DOI: 10.1051/0004-6361/202243721. arXiv: 2205.06645 [astro-ph.SR].

Tassoul, M. (Aug. 1980). "Asymptotic approximations for stellar nonradial pulsations." In: *ApJS* 43, pp. 469–490. DOI: 10.1086/190678.

Thielemann, F. .-. et al. (Apr. 2011). "What are the astrophysical sites for the r-process and the production of heavy elements?" In: *Progress in Particle and Nuclear Physics* 66.2, pp. 346–353. DOI: 10.1016/j.ppnp.2011.01.032.

Ting, Y.-S. and H.-W. Rix (June 2019). "The Vertical Motion History of Disk Stars throughout the Galaxy". In: *ApJ* 878.1, 21, p. 21. DOI: 10.3847/1538-4357/ab1ea5. arXiv: 1808.03278 [astro-ph.GA].

Toomre, A. (Jan. 1977). "Mergers and Some Consequences". In: *Evolution of Galaxies and Stellar Populations*. Ed. by B. M. Tinsley and D. C. Larson Richard B. Gehret, p. 401.

Ulrich, R. K. (July 1986). "Determination of Stellar Ages from Asteroseismology". In: *ApJ* 306, p. L37. DOI: 10.1086/184700.

Verma, K. et al. (Mar. 2019). "Helium abundance in a sample of cool stars: measurements from asteroseismology". In: *MNRAS* 483.4, pp. 4678–4694. DOI: 10.1093/mnras/sty3374. arXiv: 1812.02751 [astro-ph.SR].

Vickers, J. J., J. Shen, and Z.-Y. Li (Dec. 2021). "The Flattening Metallicity Gradient in the Milky Way's Thin Disk". In: *ApJ* 922.2, 189, p. 189. DOI: 10.3847/1538-4357/ac27a9. arXiv: 2109.09250 [astro-ph.GA].

Villalobos, Á. and A. Helmi (Dec. 2008). "Simulations of minor mergers - I. General properties of thick discs". In: *MNRAS* 391.4, pp. 1806–1827. DOI: 10.1111/j.1365-2966.2008.13979.x.

Vincenzo, F. et al. (Oct. 2019a). "He abundances in disc galaxies. I. Predictions from cosmological chemodynamical simulations". In: *A&A* 630, A125, A125. DOI: 10.1051/0004-6361/201935886. arXiv: 1905.08309 [astro-ph.GA].

Vincenzo, F. and C. Kobayashi (July 2020). "Stellar migrations and metal flows - Chemical evolution of the thin disc of a simulated Milky Way analogous galaxy". In: *MNRAS* 496.1, pp. 80–94. DOI: 10.1093/mnras/staa1451. arXiv: 2004.08050 [astro-ph.GA].

Vincenzo, F. et al. (July 2019b). "The Fall of a Giant. Chemical evolution of Enceladus, alias the Gaia Sausage". In: *MNRAS* 487.1, pp. L47–L52. DOI: 10.1093/mnrasl/slz070. arXiv: 1903.03465 [astro-ph.GA].

Wang, C. et al. (Jan. 2019). "Metallicity distributions of mono-age stellar populations of the Galactic disc from the LAMOST Galactic spectroscopic surveys". In: *MNRAS* 482.2, pp. 2189–2207. DOI: 10.1093/mnras/sty2797. arXiv: 1810.05958 [astro-ph.GA].

Warfield, J. T. et al. (Mar. 2021). "An Intermediate-age Alpha-rich Galactic Population in K2". In: *AJ* 161.3, 100, p. 100. DOI: 10.3847/1538-3881/abd39d. arXiv: 2102.03377 [astro-ph.GA].

Wegg, C., O. Gerhard, and M. Portail (July 2015). "The structure of the Milky Way's bar outside the bulge". In: *MNRAS* 450.4, pp. 4050–4069. DOI: 10.1093/mnras/stv745. arXiv: 1504.01401 [astro-ph.GA].

White, S. D. M. and M. J. Rees (May 1978). "Core condensation in heavy halos: a two-stage theory for galaxy formation and clustering." In: *MNRAS* 183, pp. 341–358. DOI: 10.1093/mnras/183.3.341.

Wielen, R., B. Fuchs, and C. Dettbarn (Oct. 1996). "On the birth-place of the Sun and the places of formation of other nearby stars". In: *A&A* 314, p. 438.

Willett, E. et al. (Aug. 2023). "The evolution of the Milky Way's thin disc radial metallicity gradient with K2 asteroseismic ages". In: *MNRAS*. DOI: 10.1093/mnras/stad2374. arXiv: 2307.14422 [astro-ph.GA].

Workman, R. L. et al. (Aug. 2022). "Review of Particle Physics". In: *Progress of Theoretical and Experimental Physics* 2022.8, 083C01, p. 083C01. DOI: 10.1093/ptep/ptac097.

Xiang, M.-S. et al. (Aug. 2015). "The evolution of stellar metallicity gradients of the Milky Way disk from LSS-GAC main sequence turn-off stars: a two-phase disk formation history?" In: *Research in Astronomy and Astrophysics* 15.8, 1209, p. 1209. DOI: 10.1088/1674-4527/15/8/009. arXiv: 1505.08063 [astro-ph.GA].

Yanny, B. et al. (Aug. 2009). "Tracing Sagittarius Structure with SDSS and SEGUE Imaging and Spectroscopy". In: *ApJ* 700.2, pp. 1282–1298. DOI: 10.1088/0004-637X/700/2/1282. arXiv: 0905.4502 [astro-ph.GA].

Yu, J. et al. (June 2018). "Asteroseismology of 16,000 Kepler Red Giants: Global Oscillation Parameters, Masses, and Radii". In: *ApJS* 236.2, 42, p. 42. DOI: 10.3847/1538-4365/aaaf74. arXiv: 1802.04455 [astro-ph.SR].

Zhao, G. et al. (June 2012). "LAMOST Spectral Survey". In: *arXiv e-prints*, arXiv:1206.3569, arXiv:1206.3569. DOI: 10.48550/arXiv.1206.3569. arXiv: 1206.3569 [astro-ph.IM].

Appendix A

APPENDIX TO CHAPTER 4

A.1 Asteroseismic pipeline comparison for K2 targets

Figure A.1 shows a comparison of the asteroseismic parameters obtained for K2 stars from the independent BHM and COR pipelines, relative to their combined uncertainty. In general, the pipelines agree at the 2σ level.

A.2 Identifying nyquist-affected $\nu_{\rm max}$

Figure A.2 shows stars removed from the K2-BHM-APOGEE sample due to cuts on the asteroseismic parameters as red points. Targets with $\nu_{\rm max} + 3\sigma_{\nu_{\rm max}} < 20\,\mu$Hz and $\Delta\nu \geq 21\,\mu$Hz are rejected, as described in Section 4.2.1.

A.3 Comparing $\Delta\nu$ and L results in *Kepler* and TESS

Figures A.3 and A.4 show the stellar mass and radius obtained from scaling relations for *Kepler* and TESS stars, with stars flagged as having unreliable $\Delta\nu$ according to the definition in Section 4.3.1 highlighted (red points). In comparison to Figure 4.4, we see a greatly reduced number of stars highlighted by this flag, as a result of the increased duration of the observations.

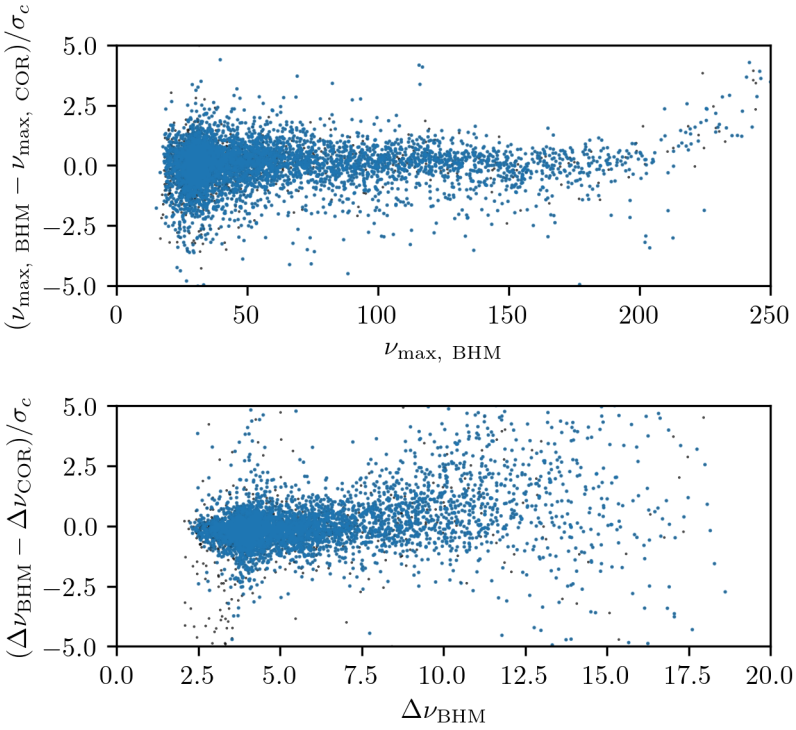


Figure A.1: Difference between $\nu_{\rm max}$ (*top*) and $\Delta\nu$ (*bottom*) from independent BHM and COR pipelines, relative to combined uncertainty. Stars with reliable ages are shown in the foreground with blue points. Stars with reliable data but which do not pass our tests on age are shown as black points in the background.

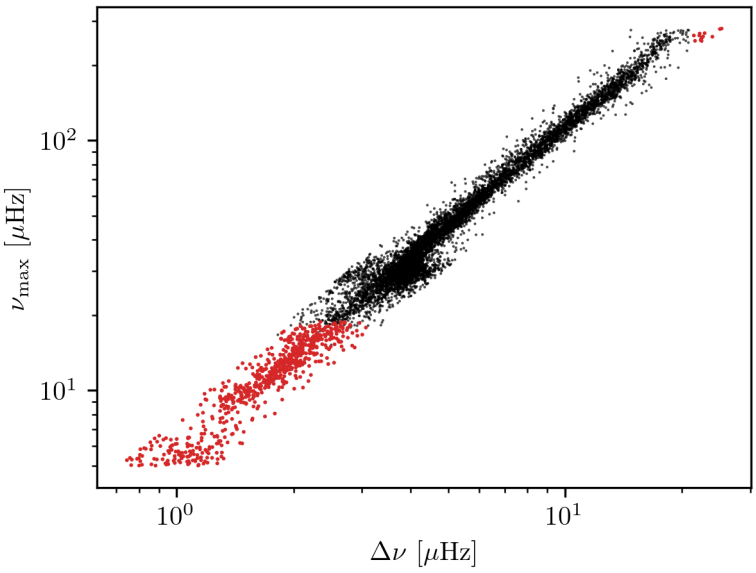


Figure A.2: $\nu_{\rm max}$ vs. $\Delta\nu$ for the K2-BHM-APOGEE sample. Stars removed as a result of the cuts described in Section 4.2.1 are shown in red.

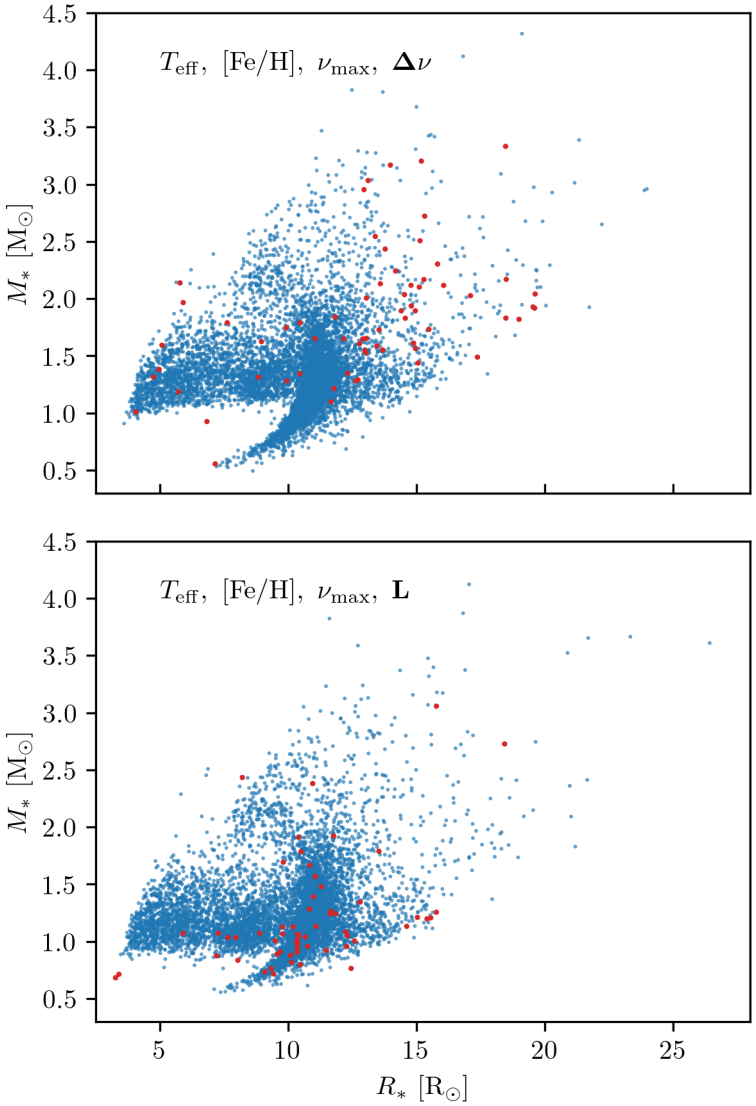


Figure A.3: Same as Figure 4.4, but for *Kepler* targets.

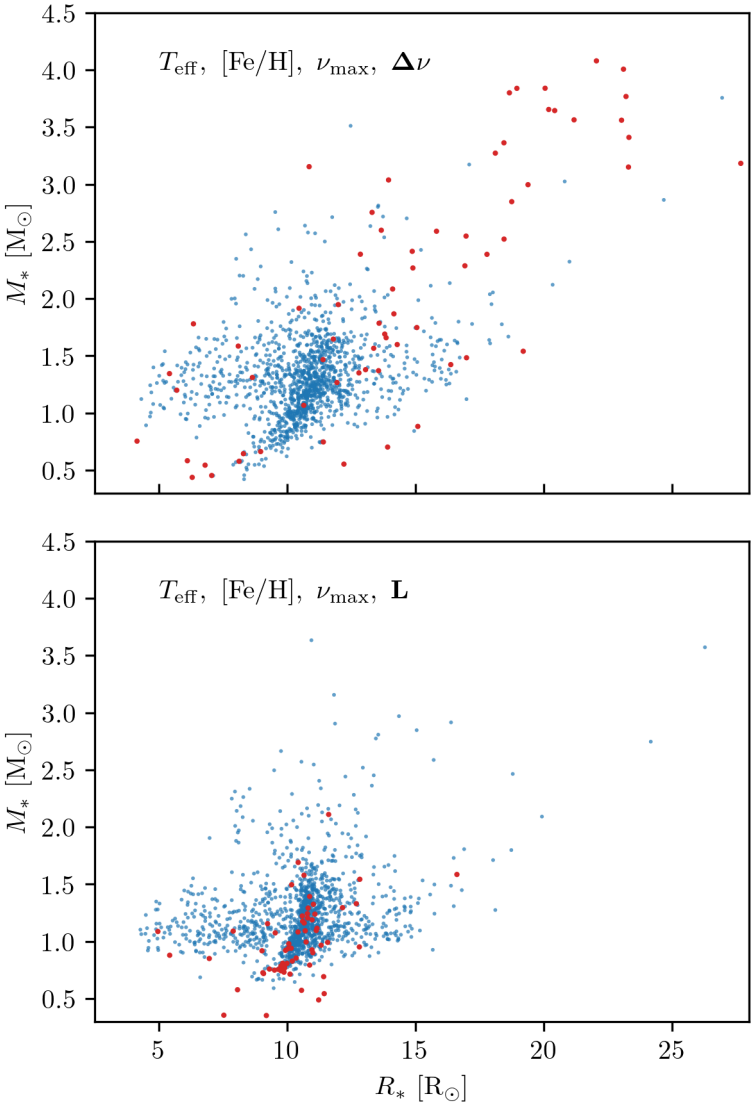


Figure A.4: Same as Figure 4.4, but for TESS targets.

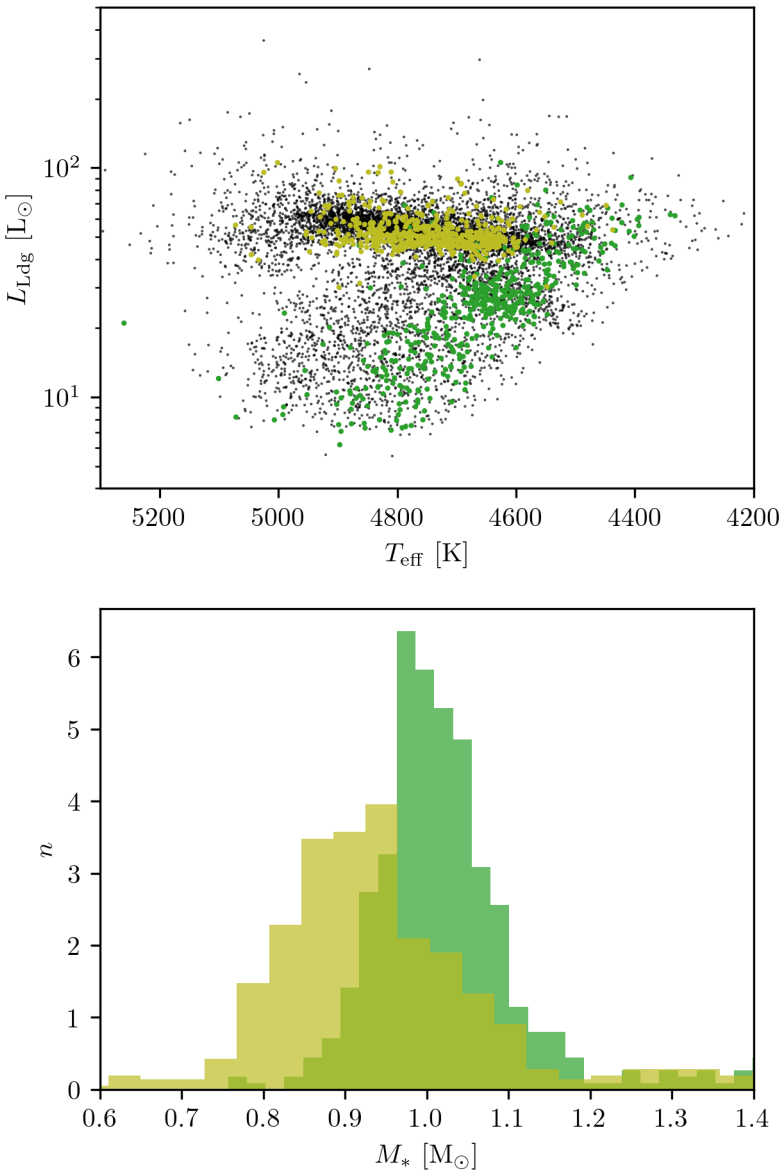


Figure A.5: Same as Figure 4.18, but for *Kepler* targets.

A.4 Mass loss in *Kepler*

Figure A.5 shows the selection (*top*) and mass distributions (*bottom*) of stars in the RGB and CHeB populations of the *Kepler* sample. We find that CHeB stars have lost $\sim 0.1 M_\odot$, consistent with the K2 sample shown in Figure 4.18.

Appendix B

APPENDIX TO CHAPTER 5

B.1 Effect of [Fe/H] error inflation

As described in Chapter 4, during the PARAM runs to constrain the stellar parameters used in this work, the uncertainty on [Fe/H] from APOGEE DR17 was inflated to 0.05 dex for all stars with a reported uncertainty below this value. In our subsequent analysis of the metallicity gradient, we use the published values of uncertainty, but here we show the results obtained from the HBM if we follow the same inflation procedure. The evolution and uncertainties for the gradient and offset are almost unchanged from our original analysis and are not shown here, and Figure B.1 shows that, though the intrinsic spread is slightly decreased, it is still fully consistent within uncertainties.

B.2 Sensitivity to the $Z_{\rm max}$ cut

In this section, we show the sensitivity of our results to the cut in $Z_{\rm max}$ used to identify thin disc members. Figure B.2 summarises the results of the MCMC and HBM analysis under different conditions. The gradient (*top panel*) recovered with a wider ($Z_{\rm max} \leq 1.0$ kpc) or narrower ($Z_{\rm max} \leq 0.3$ kpc) range of $Z_{\rm max}$ is consistent with our original analysis within the uncertainties. Decreasing the $Z_{\rm max}$ range does not significantly change the [Fe/H] offset at 8 kpc (*middle panel*), but the result from the wider cut shows significantly lower metallicity. This is consistent with

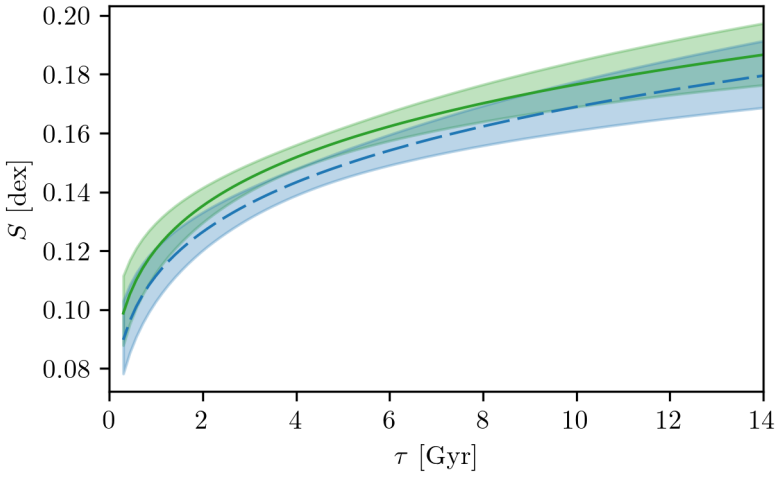


Figure B.1: The [Fe/H] component of the intrinsic spread constrained by our HBM using the published [Fe/H] uncertainties (green) or inflating them as in Chapter 4 (dashed blue).

the wider range of metallicities in this sample (Figure B.3). The intrinsic spread (*bottom panel*) of the three samples is more sensitive to the $Z_{\rm max}$ cut, but the relationship between the MCMC and HBM result is the same in a given sample.

B.3 Effect of $R_{\rm g}$ or $R_{\rm Gal}$

In this section, we provide further detail on the sensitivity of our results to the radial coordinate and range used in the analysis.

First, we show the results of our analysis using $R_{\rm Gal}$ rather than $R_{\rm g}$. Figure B.4 shows the results in bins of age, where the uneven radial distribution caused by the K2 field placement can be clearly seen. Figure B.5 summarises the results from the MCMC and HBM analysis, where in general all parameters agree within their uncertainties. The exception is the HBM result for the [Fe/H] offset at 8 kpc, which is likely a result of the populations clumping up in $R_{\rm Gal}$.

We also test the sensitivity of our result to stars with $R_{\rm g} < R_{\rm Gal,\,min}$ (see Section 5.5.3 for details). Excluding these stars does result in a slightly steeper gradient at $\tau > 1$ Gyr, but the two results are consistent within uncertainties. The offset and intrinsic spread are almost unchanged in the new samples and are not shown here. This indicates that our results are not biased by the choice of $R_{\rm g}$ as the radial coordinate in our analysis.

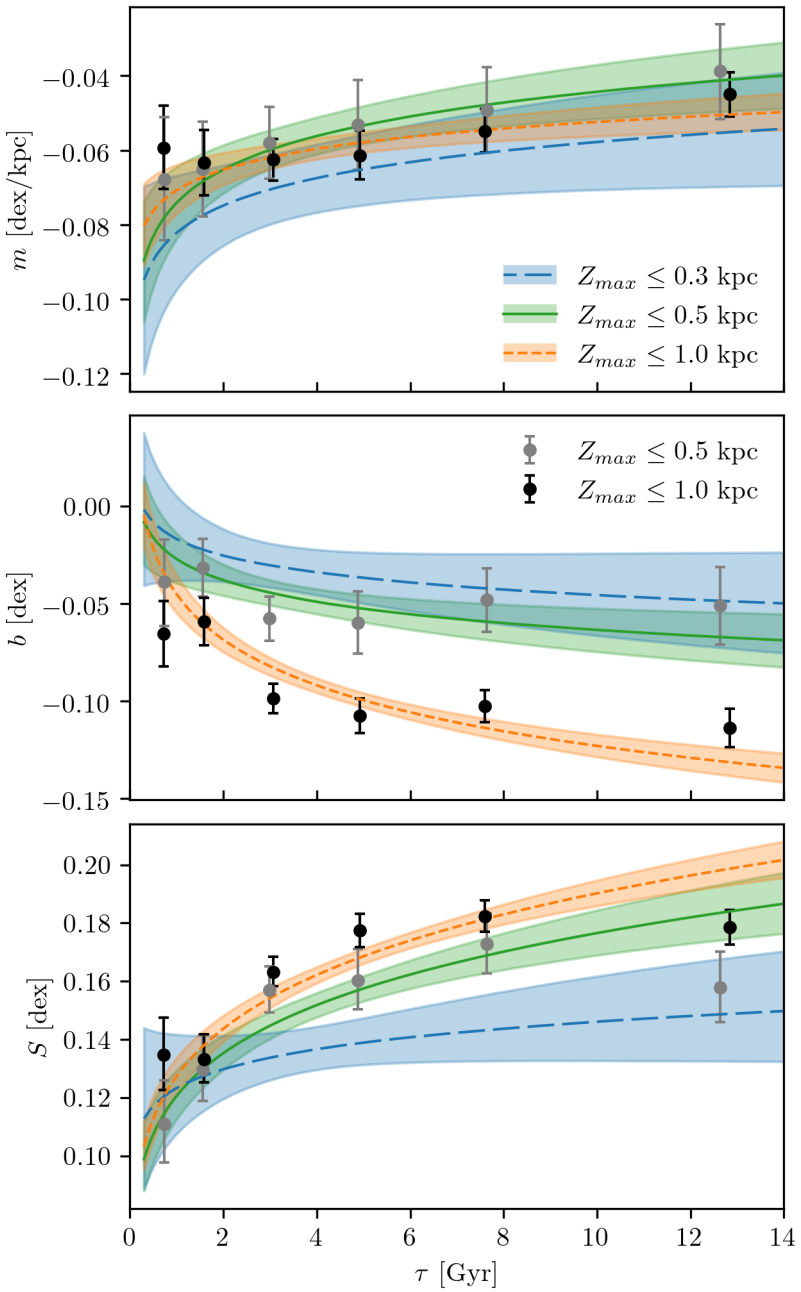


Figure B.2: Evolution of the fit parameters as a function of stellar age. The grey points and green line and filled region show the best-fitting value and 68% credible interval in each bin from the MCMC analysis (plotted against the median age of the population in the bin) and the result and 68% credible interval from the HBM from the original analysis. The black points and short-dashed orange line and filled region show the same but for a sample including stars with a wider range of Z_{max}. The long-dashed blue line and filled region show the HBM result for a narrower Z_{max} range.

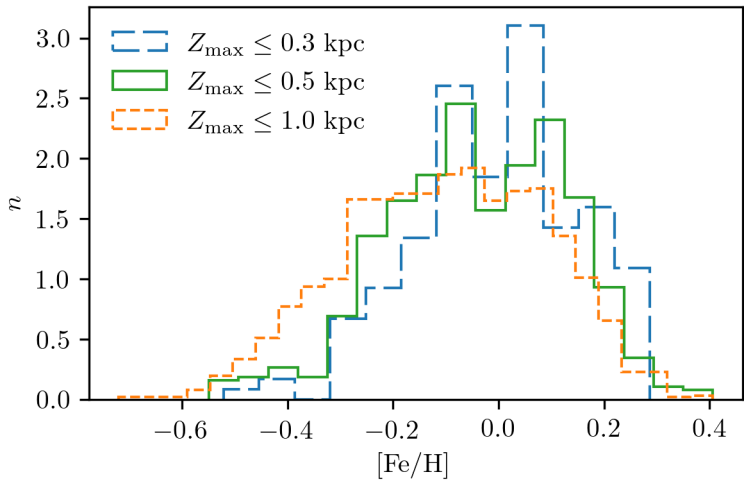


Figure B.3: [Fe/H] distributions for samples including stars with a wider (short-dashed orange) or narrower (long-dashed blue) range of $Z_{\rm max}$ than the original analysis (green). The area under each histogram integrates to one.

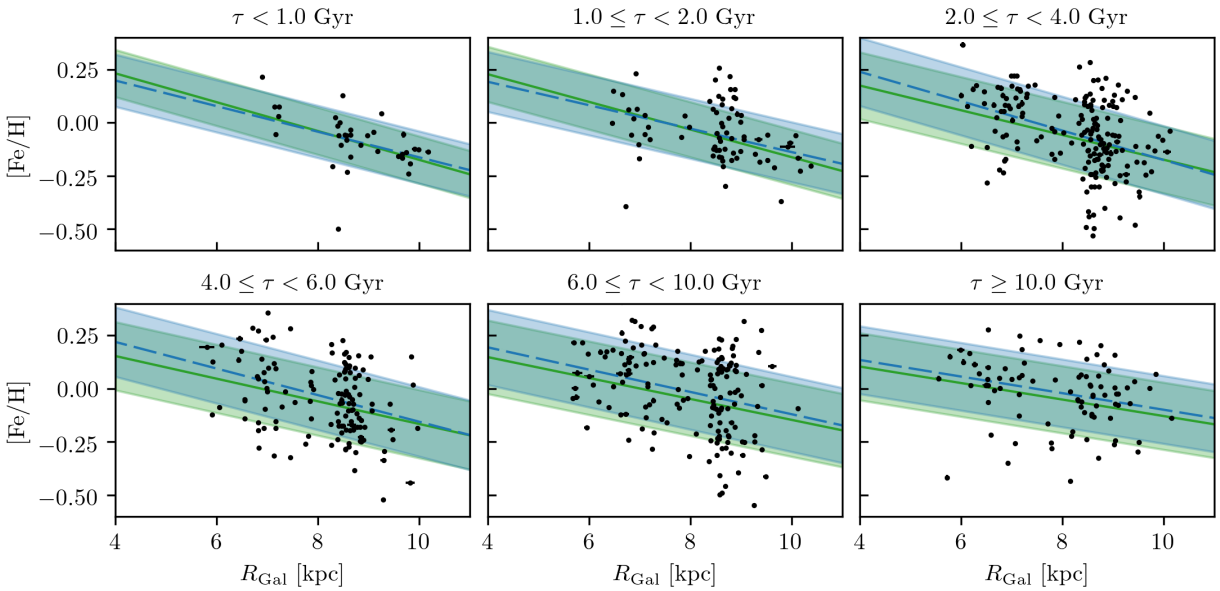


Figure B.4: [Fe/H] vs. $R_{\rm Gal}$ in six bins of age. The thin disc sample is shown in black points, binned according to the median age of each star. The dashed blue line and filled region show the results from the MCMC analysis using $R_{\rm Gal}$. For comparison, the green line and filled region show the results using $R_{\rm g}$ (plotted against $R_{\rm g}$).

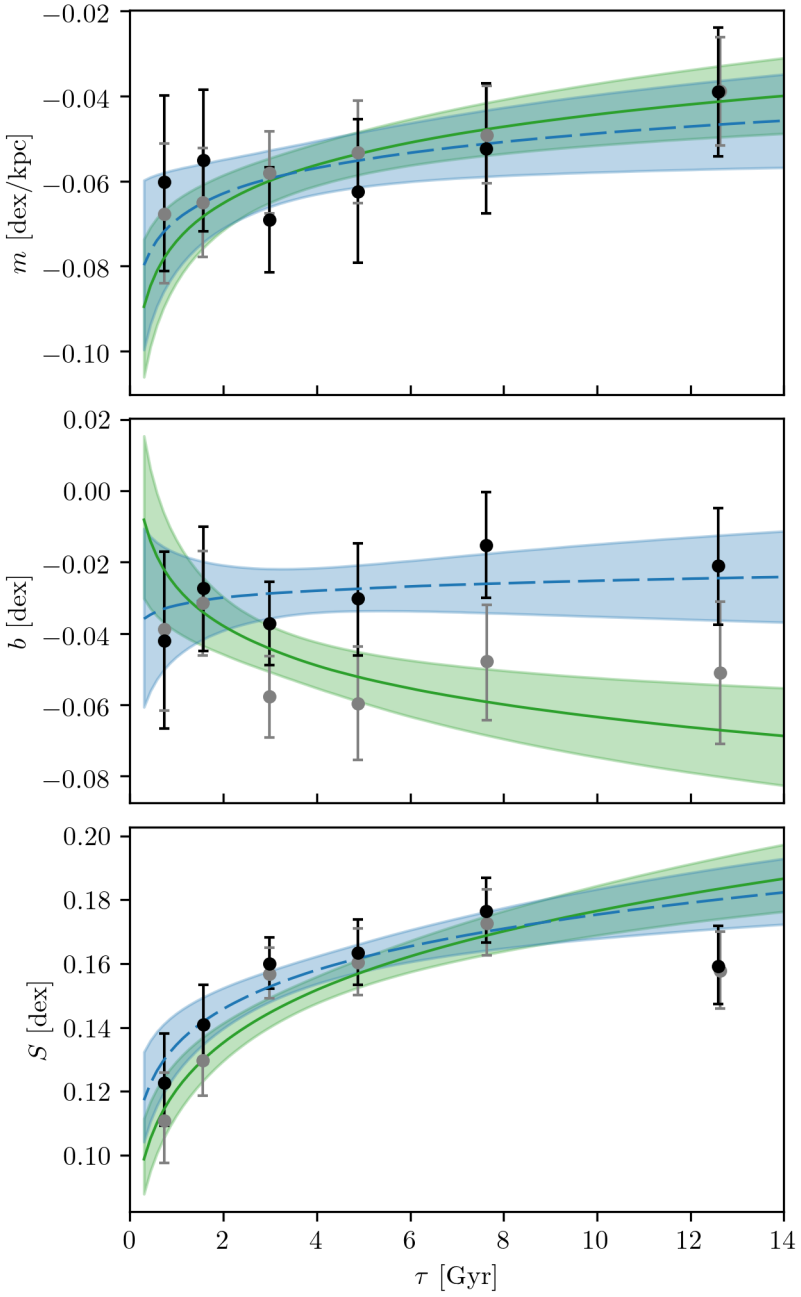


Figure B.5: Evolution of the fit parameters as a function of stellar age. The grey points and green line and filled region show the best-fitting value and 68% credible interval in each bin from the MCMC analysis (plotted against the median age of the population in the bin) and the result and 68% credible interval from the HBM from the original analysis using R_g. The black points and dashed blue line and filled region show the same using R_{Gal}.

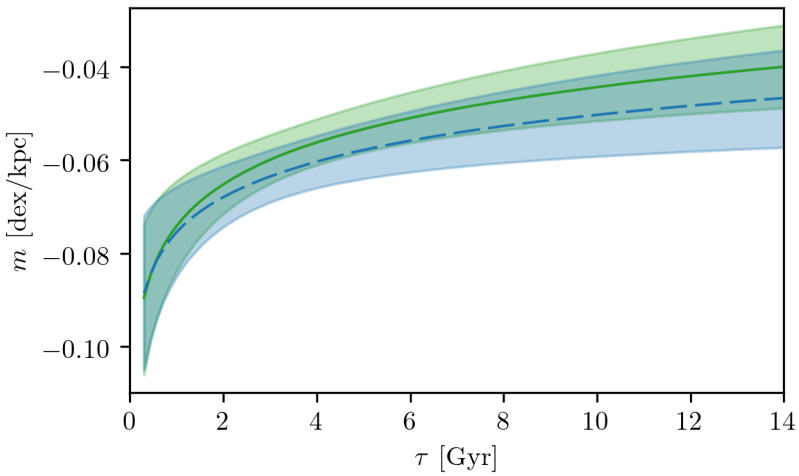


Figure B.6: Evolution of the gradient with age for the full sample (green) and excluding stars with $R_{\rm g} < R_{\rm Gal,\,min}$ (dashed blue).